Technische Universität München
TUM School of Engineering and Design

Fundamental Methods for Real-Time Hybrid Substructuring with Contact: Enabling Testing of Prosthetic Feet

Christina Olga Insam

Vollständiger Abdruck der von der TUM School of Engineering and Design der Technischen Universität München zur Erlangung des akademischen Grades einer

Doktorin der Ingenieurwissenschaften (Dr.-Ing.)

genehmigten Dissertation.

Vorsitz: Prof. Dr.-Ing. Veit Senner

Prüfer*innen der Dissertation:

1. Prof. dr.ir. Daniel J. Rixen
2. Assoc. Prof. Dr. Eleni Chatzi
3. Prof. Richard Christenson, Ph.D.

Die Dissertation wurde am 15. März 2022 bei der Technischen Universität München eingereicht und durch die TUM School of Engineering and Design am 31. August 2022 angenommen.

Abstract

The gait pattern of prosthesis wearers differs from that of able-bodied humans. For example, higher energy consumption, asymmetry and increased loading are observed. For a targeted improvement of existing prostheses, the dynamic interplay between a human and the prosthesis needs to be well comprehended. An appropriate method to analyze the dynamics is Real-Time Hybrid Substructuring (RTHS), where the prosthesis is tested on a test bench and the amputee is co-simulated in real-time. In this thesis, the foundation is laid for testing prosthetic feet using RTHS. For this purpose, control schemes are first compared that allow safe and accurate testing of systems with contact. Specifically, Iterative Learning Control as a feedforward controller, in combination with Normalized Passivity Control, is proposed and experimentally investigated. A key research question in RTHS is the fidelity assessment of the experiments. This thesis proposes a novel approach called *Fidelity Assessment based on Convergence and Extrapolation (FACE)*. The presentation and analysis of the method is done using virtual RTHS tests, as well as experimental RTHS tests. Additionally, an RTHS test was conducted, where the human is modeled using the Virtual Pivot Point model and the prosthesis tested on the test bench. In this test, one gait cycle is completed and the results reveal that the dynamic interplay between an amputee and a prosthesis can be emulated. By this work, not only the feasibility and potential to test prostheses are demonstrated, but also methods are presented that represent an advance for various RTHS applications in the field of actuator control and fidelity assessment.

Zusammenfassung

Das Gangbild von Prothesenträgern unterscheidet sich von dem gesunder Menschen u.a. durch einen erhöhten Energieverbrauch, Asymmetrie und erhöhte Belastungen. Für eine gezielte Verbesserung bestehender Prothesen muss das Verständnis über das dynamische Zusammenspiel von Mensch und Prothese verbessert werden. Eine geeignete Methodik zur Analyse dieser Dynamik stellt Real-Time Hybrid Substructuring (RTHS) dar. Hierbei wird die Prothese am Prüfstand getestet und der Amputierte in Echtzeit co-simuliert. In dieser Arbeit werden die Grundlagen für das Testen von Fußprothesen mittels RTHS geschaffen. Dazu werden zunächst verschiedene Regelstrategien verglichen, die ein sicheres und genaues Testen von Systemen mit Kontakt ermöglichen. Konkret wird die Verwendung von Iterative Learning Control als Vorsteuerungsmethode in Kombination mit Normalized Passivity Control vorgestellt und experimentell untersucht. Eine zentrale Forschungsfrage in RTHS ist die Genauigkeitsbewertung von Versuchen. Diese Arbeit stellt einen neuartigen Ansatz namens *Fidelity Assessment based on Convergence and Extrapolation (FACE)* vor. Die Vorstellung und Analyse der Methodik findet sowohl an virtuellen RTHS Versuchen als auch an experimentellen RTHS Tests statt. Zuletzt wird ein RTHS Versuch durchgeführt, in welchem der Mensch mittels Virtual Pivot Point Modell simuliert und die Prothese am Prüfstand getestet wird. Die Ergebnisse eines Schritts legen dar, dass das dynamische Zusammenspiel von Mensch und Prothese mittels RTHS nachgebildet werden kann. Durch diese Arbeit werden nicht nur die Machbarkeit und das Potential dieser visionären Testmethode aufgezeigt, sondern auch Methoden vorgestellt, die einen Fortschritt für verschiedenste RTHS Anwendungen im Bereich der Aktorregelung und der Genauigkeitsanalyse bedeuten.

Acknowledgement

Als ich Ende 2017 die Zusage für eine Stelle als Wissenschaftliche Mitarbeiterin am Lehrstuhl für Angewandte Mechanik erhalten habe, war meine Freude groß: Ich wusste, dass ich in der bevorstehenden Zeit mein fachliches Verständnis vertiefen kann, interessante und lehrreiche Diskussionen führen werde sowie spannende und anspruchsvolle Forschungsfragen erarbeite.

Zurückblickend auf die vergangenen Jahre kann ich sagen, dass meine Vorstellungen nicht nur erfüllt, sondern bei weitem übertroffen wurden und eine tolle, unvergessliche und ja, auch intensive Lebensphase hinter mir liegt. Aber es sind nicht nur die wissenschaftlichen Fragestellungen und die damit verbundenen Aufgaben, die die letzten Jahre so besonders gemacht haben, sondern vor allem die Menschen, die mich begleitet und unterstützt haben.

Ein besonderer Dank gilt meinem Doktorvater Prof. dr. ir. Daniel Rixen für die Unterstützung, den intensiven fachlichen Austausch und auch die menschliche Förderung. Du vermittelst uns Freude an der Forschung und schaffst eine inspirierende und freundliche Atmosphäre, die uns Raum gibt, unsere Ideen einzubringen und umzusetzen. Dies alles hat maßgeblich zum Gelingen dieser Arbeit beigetragen.

Ich danke zudem den Mitgliedern der Prüfungskommission, Prof. Dr. Veit Senner für die Übernahme des Vorsitzes sowie Prof. Dr. Eleni Chatzi und Prof. Dr. Richard Christenson für die Übernahme der Gutachten. Teile der Forschungsarbeiten sind im Rahmen des DFG-Projekts „Robuste Regelung und Genauigkeitsbewertung von Real-Time Hybrid Substructuring von Kontaktproblemen“ (RI2451/14-1) entstanden. Ich bedanke mich für die Förderung der Deutschen Forschungsgemeinschaft.

Herzlich bedanken möchte ich mich bei allen Kollegen mit denen ich während meiner Zeit zusammenarbeiten durfte und viele Freunde gewinnen konnte. Ich danke euch für die tolle Zusammenarbeit, die positive Energie, euer offenes Ohr und eure Motivation. Die Zeit am Lehrstuhl wird mir in bester Erinnerung bleiben. Insbesondere gilt Dr.-Ing. habil. Thomas Thümmel ein großer Dank, der mich als Studentin für die Forschungstätigkeiten am Lehrstuhl begeistert und während meiner Promotion in allen Belangen unterstützt hat. Außerdem möchte ich mich bei meinem Mentor Dr.-Ing. Felix Schranner für die hilfreichen Tipps, die Unterstützung und das Interesse bedanken. Für das Gelingen der vorliegenden Arbeit war auch die Zusammenarbeit mit den zahlreichen Student*innen als studentische Hilfskräfte oder im Rahmen von Bachelor-, Semester- und Masterarbeiten von entscheidender Bedeutung. Danke für euer Interesse und Engagement, die tolle Zusammenarbeit und viele anregende Diskussionen. Mein besonderer Dank gilt außerdem den fleißigen Korrekturlesern für die gründliche Durchsicht dieser Dissertation.

Schließlich danke ich meinen engen Freunden, meiner Familie, insbesondere meiner Mama Helga, meinem Papa Franz und meinen Geschwistern Franz und Sophia, sowie meinem Freund Dominik. Danke, dass ihr mich immer unterstützt, Freude und Sorge mit mir teilt und ich auf euch zählen kann. Ohne eure große Unterstützung wäre das alles nicht möglich. Danke, dass ihr mich begleitet.

Garching, September 2022 *Christina Insam*

Contents

Nomenclature

Variables written in bold denote vectors and scalar quantities are written in regular typeface. Variables in frequency domain are indicated by upper case letters and the Laplace variable is $s = j\omega$.

Operators

$\dot{(\cdot)}$	...	time derivative
$\ddot{(\cdot)}$	...	second time derivative
∇	...	gradient
$\tilde{(\cdot)}$	...	filtered
$\hat{(\cdot)}$	...	reference/correct value

Greek Symbols

α	...	damping coefficient in NPC
$\alpha_{(\cdot)}$	...	angle between leg and ground (gait models)
β	...	proportional gain in ILC
γ	...	derivative gain in ILC
γ_{LMS}	...	regularization term in AFF
γ_{VPP}	...	angle between the leg and the connection foot-point to VPP in the VPP model
δ	...	small value in the AFF implementation
ΔT	...	sample time/synchronization time step
Δz_{max}	...	defines the magnitude of the suspension in Part I
μ_{LMS}	...	adaptation gain in AFF
ν_{LMS}	...	leakage factor in AFF
ϕ_{pm}	...	phase margin
ϕ_{VPP}	...	trunk orientation of the VPP model
Φ	...	rotation of the Stewart Platform about the X axis
Ψ	...	rotation of the Stewart Platform about the Z axis
τ	...	scalar representation of the delay in the RTHS loop
τ_{add}	...	additional delay used in the FACE method
τ_{crit}	...	critical delay where RTHS loop becomes unstable
τ_{FEI}	...	equivalent time delay (FEI index)
$\tau_{\mathrm{h,n}}$	...	total hip torque in the VPP model for $n = \{L, R\}$
$\tau_{\mathrm{VPP,n}}$	...	hip torque in the VPP model by the VPP controller for $n = \{L, R\}$
Θ	...	rotation of the Stewart Platform about the Y axis
$\boldsymbol{\Theta}$	...	vector with FIR coefficients in AFF
ω_{bw}	...	actuator bandwidth
ω_c	...	corner frequency of the identified Stewart Platform leg transfer behavior
ω_{dyn}	...	eigenfrequency of the dynamical system
ω_{pm}	...	frequency of phase margin

Superscripts

$(\cdot)^{\mathrm{c}}$	...	during contact
$(\cdot)^{\mathrm{f}}$	...	frequency domain value
$(\cdot)^{\mathrm{NUM\text{-}TS}}$	...	from the numerical part to the transfer system
$(\cdot)^{\mathrm{r}}$	...	reference quantity
$(\cdot)^{\mathrm{TS\text{-}EXP}}$	...	from the transfer system to the experimental part
$(\cdot)'$	...	real/achieved quantity

Subscripts

$(\cdot)_{\mathrm{ACT}}$	...	actuation system
$(\cdot)_{\mathrm{CoP}}$	...	Center of Pressure (Part III)
$(\cdot)_{\mathrm{diss}}$	...	dissipated
$(\cdot)_{\mathrm{error}}$	...	error (energy or power)
$(\cdot)_{\mathrm{ext}}$	...	by external forces
$(\cdot)_{\mathrm{EXP}}$	...	experimental part
$(\cdot)_{\mathrm{FP}}$	...	foot point (Part III)
$(\cdot)_{\mathrm{FTS}}$	...	force/torque sensor
$(\cdot)_{\mathrm{h}}$	...	hip (Part III)
$(\cdot)_{i}$	...	leg of the Stewart Platform, $i = 1...6$
$(\cdot)_{\mathrm{int}}$	...	interface
$(\cdot)_{\mathrm{IFP}}$	...	interface point
$(\cdot)_{j}$	...	iteration of the ILC scheme
$(\cdot)_{k}$	...	discrete time instant
$(\cdot)_{L}$	...	left leg/foot
$(\cdot)_{\mathrm{l}}$	...	weighted by l (FEI index)
$(\cdot)_{\mathrm{m}}$	...	measured
$(\cdot)_{\mathrm{min}}$	...	minimum achievable
$(\cdot)_{\mathrm{max}}$	...	maximum
$(\cdot)_{n}$	...	indicates both feet/legs, $n = \{L, R\}$
$(\cdot)_{\mathrm{NUM}}$	...	numerical part
$(\cdot)_{\mathrm{pred}}$	...	predicted with the FACE method
$(\cdot)_{\mathrm{r}}$	...	relative error
$(\cdot)_{\mathrm{ref}}$	...	reference error
$(\cdot)_{R}$	...	right leg/foot
$(\cdot)_{\mathrm{tot}}$	...	total
$(\cdot)_{\mathrm{track}}$	...	tracking
$(\cdot)_{\mathrm{TD}}$	...	touch down
$(\cdot)_{\mathrm{TO}}$	...	take off
$(\cdot)_{\mathrm{u}}$	...	upper leg of the modeled amputee
$(\cdot)_{\mathrm{VPP}}$	...	VPP model (Part III)
$(\cdot)_{\perp}$	...	perpendicular to the leg axis of the VPP model
$(\cdot)_{\parallel}$	...	parallel to the leg axis of the VPP model
$(\cdot)_{0}$	...	initial value (at $t = 0\,\mathrm{s}$)
$(\cdot)_{\infty}$	...	final value ($t \rightarrow \infty$)

Latin Symbols

a	...	peak magnitude
A_{FEI}	...	amplitude error indicator (FEI index)
b	...	leg length of the Stewart Platform
$c_{(\cdot)}$	...	constant coefficient
C	...	feedback controller
d	...	damping
e	...	error
E	...	energy
f	...	frequency
f_{d}	...	prescribed frequency of the suspension
f_{eq}	...	equivalent frequency (FEI index)
f_{j}	...	feedforward signal in iteration j (ILC)
$f_{\mathrm{Q,cut}}$	...	cutoff frequency robustness filter (ILC)
F	...	force
F_{d}	...	damping force by NPC
F_{o}	...	open loop transfer function
F_{s}	...	spring force
g	...	gravitational constant or gap
G	...	transfer function
G_{P}	...	damping scaling value of NPC
h	...	height
$h(\cdot)$	...	functional interrelationship (FACE)
h_{f}	...	height of the prosthetic foot
i	...	leg index of Stewart Platform, $i = 1...6$
j	...	imaginary unit or iteration of the ILC scheme
J	...	cost function
J_{VPP}	...	moment of inertia of the VPP model
k	...	stiffness
$K_{(\cdot)}$	...	controller parameter (e.g. K_{Pp}, K_{Pv}, K_{Iv})
l	...	spring length in Part I and Part III
l_{ff}	...	distance between foot point and toes (prosthetic foot)
l_{h}	...	distance between the heel and the foot point (prosthetic foot)
L	...	learning function of ILC

m	...	mass
M	...	torque
n_t	...	number of samples in one RTHS test
N_FIR	...	number of coefficients of the AFF
P	...	plant transfer function
$P_{(\cdot)}$	...	power
q	...	measure of the Quantity of Interest
Q	...	robustness filter (ILC)
r	...	set-point trajectory
s	...	Laplace variable
$S_{(\cdot)}$	...	sensitivity functions in ILC ($S_\mathrm{f,in}$, S_in)
t	...	time
t_end	...	time span of the RTHS test
t_pause	...	pause time during successive ILC iterations
T	...	time constant
T_o	...	complementary sensitivity
u	...	feedforward signal of AFF
x	...	direction/location or CoM movement of the walking model
X	...	translation of the Stewart Platform in workspace
$\boldsymbol{X}$	...	workspace of the Stewart Platform
y	...	direction or CoM movement of the walking model
Y	...	translation of the Stewart Platform in workspace
Z	...	translation of the Stewart Platform in workspace
$\boldsymbol{z}$, z	...	interface displacement
z_d	...	prescribed movement of the suspension (Part I)

Abbreviations

AFF	...	Adaptive Feedforward Filters
ANN	...	Artificial Neural Network
CoM	...	center of mass
CoP	...	Center of Pressure
CoR	...	Coefficient of Restitution
COT	...	Cost of Transport
CSI	...	control-structure interaction
DDE	...	Delay Differential Equation
DoF	...	Degree of Freedom
DSP	...	Digital Signal Processor
DSS	...	Dynamically Substructured System
EEI	...	Energy Error Indicator
EoM	...	Equation of Motion
FACE	...	Fidelity Assessment based on Convergence and Extrapolation
FBS	...	Frequency Based Substructuring
FEI	...	Frequency Evaluation Index
FF	...	feedforward
FFT	...	fast Fourier transform
FIR	...	Finite Impulse Response
FMCH	...	Force Modulated Compliant Hip
FRF	...	Frequency Response Function
FTS	...	force/torque sensor
FXLMS	...	filtered-x least-mean-squares
GRF	...	Ground Reaction Force
HiL	...	Hardware-in-the-Loop
HSEM	...	Hybrid Simulation Error Monitor
IFP	...	interface point
ILC	...	Iterative Learning Control
LMS	...	least-mean-squares
MDOF	...	multiple degree of freedom system
MSD	...	mass-spring-damper
NPC	...	Normalized Passivity Control
NMS	...	Neuromuscular-Skeletal
PC	...	passivity controller
PD	...	proportional-derivative
PI	...	proportional-integral
PO	...	passivity observer
PSD	...	Pseudo-Dynamic
PSI	...	Predictive Stability Indicator
QoI	...	Quantity of Interest
RTHS	...	Real-Time Hybrid Substructuring
RMS	...	root-mean-square
RLS	...	recursive-least-squares
SDOF	...	single degree of freedom system
SLIP	...	Spring Loaded Inverted Pendulum
TCP	...	tool center point
TD	...	touch down
TDPC	...	time domain passivity control
TO	...	take off
VFF	...	velocity feedforward
vRTHS	...	virtual Real-Time Hybrid Substructuring
VP	...	Virtual Pendulum
VPP	...	Virtual Pivot Point

Chapter 1

Introduction

The loss of a body part changes life suddenly: On the one hand, everyday activities become major challenges and on the other hand, the loss also represents a major psychological burden. The causes for the necessity of an amputation are manifold and include vascular diseases, cancer, infections, trauma or accidents [32, 74, 139, 234]. Almost 50,000 amputations of the foot were performed in 2019 in Germany [209]. By prosthetic fitting, an attempt is made to emulate the functionality of the lost body part and thereby enables the patient to resume an independent everyday life. Prostheses exist for different body parts. This thesis focuses on the lower extremities, viz. foot prostheses. Despite great advances in the design of prostheses, the complex role of the missing body parts is difficult to emulate and differences between amputees and able-bodied humans can be observed. For example, the gait pattern of foot prosthesis wearers differs, which is directly noticeable in greater energy consumption and altered forces (e.g. in the ankle, knee and hip). Over time, the excessive loading and compensation of lost functionalities lead to osteoarthritis, osteopenia, osteoporosis and back pain. [32, 74, 154, 193] For a targeted development and further improvement of prosthetic feet, the dynamic interplay between an amputee and the prosthesis needs to be well understood. One option is to observe amputees in locomotion laboratories and ask them for feedback. However, this approach is time-consuming, subjective, not repeatable and possibly unsafe for the wearer. Hence, a robot-based test method is desirable that not only eliminates these disadvantages, but can also be applied in the early development phase.

A neat strategy to investigate the dynamics of complex systems is Real-Time Hybrid Substructuring (RTHS). In this method, parts of the dynamical system are tested experimentally while the remainder of the system is simulated numerically. Coupling the individual substructures in real-time provides the dynamic behavior of the full dynamical system. The application of RTHS for prostheses testing could therefore be a suitable choice. In RTHS, the amputee is modeled and the prosthetic foot tested on the test bench to emulate the dynamic interplay. The principle is visualized in fig. 1.1. The vision at the Chair of Applied Mechanics is to investigate the applicability of RTHS to test prosthetic feet and establish it as a testing method.

1.1 Objective and Outline

The objective of this thesis is to

lay the foundation for testing prosthetic feet using Real-Time Hybrid Substructuring such that, in the future, this testing method can be realized.

Successful testing of prosthetic feet using RTHS requires that the methods developed for RTHS are advanced enough to replicate complex system behavior with high fidelity. Hence,

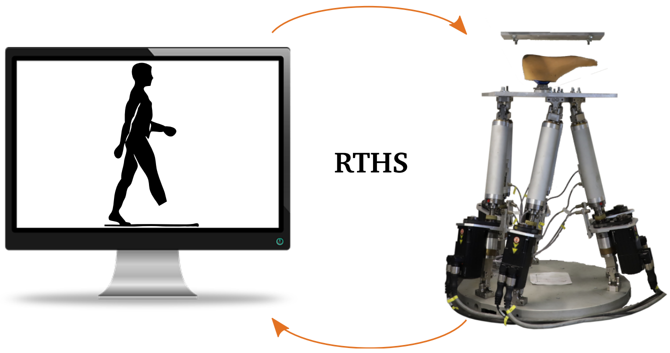

Figure 1.1: When a prosthetic foot is tested with RTHS, the amputee is modeled and simulated numerically. The amputee is coupled with the tested prosthetic foot to analyze the gait dynamics of the prosthesis wearer. The coupling is done by exchanging displacement/velocity and force information at the interface (ankle). In this visualization, the prosthetic foot is moved by a Stewart Platform. (Image of the amputee adapted from [179]; figure adapted from [105].)

objective fulfillment includes building an understanding of the current state-of-the-art of RTHS, determining necessary steps and removing any barriers. Based on a literature review, three major tasks were identified as essential for the success of prostheses testing with RTHS. These are reflected in the structure of this thesis as individual parts. A visualization is given in fig. 1.2, where each of the topics is represented as a pillar necessary to support the roof with the vision to test prostheses using RTHS.

After this introductory chapter, the thesis commences with the fundamentals of Real-Time Hybrid Substructuring (RTHS) in chapter 2. This chapter is not only intended to give non-specialists a smooth start into this topic, but also to make researchers acquainted with the view on RTHS used in and required for the understanding of this thesis. Subsequently to that, three parts follow. These form the supporting pillars for the success of prostheses testing using RTHS (cf. fig. 1.2).

Part I focuses on *Actuator Control* for RTHS systems with contact. The stability of RTHS tests with contact is jeopardized due to the rapid change of system dynamics at the transition from contact to non-contact and vice versa. An actuator control scheme is proposed with the objective to enable safe, stable and robust testing as well as high fidelity testing of RTHS systems with contact. Specifically, Iterative Learning Control is introduced as feedforward control scheme because it requires only little model knowledge and is applicable to a wide variety of RTHS setups/dynamical systems. Iterative Learning Control is furthermore combined with Normalized Passivity Control for improved stability and robustness. An experimental benchmark study assesses the efficiency of the proposed scheme in comparison with Velocity Feedforward and Adaptive Feedforward Filters as feedforward control schemes. The dynamical system used for these investigations is a one-dimensional dynamical system with contact as represented in the depiction of the first pillar in fig. 1.2.

A key issue in the RTHS community is the *Fidelity* assessment, represented as the second pillar in fig. 1.2. Often, a reference solution is not available against which the RTHS result can be validated. This is also the case when it comes to testing of prosthetic feet using RTHS. Still, a fidelity measure is required that assesses how much the errors in the RTHS setup deteriorate the test accuracy. In Part II, a method called *Fidelity Assessment based on Convergence and Extrapolation (FACE)* is developed, which is a fundamentally different approach from literature to determine the test fidelity. In this method, the reference solution is estimated using several test results with different settings. The methodology is described and elaborated on the basis of examples of structural vibrations. The FACE method is evaluated by simulated and experimental analysis of linear systems as well as of the system with contact from Part I.

With respect to the visionary application of prostheses testing with RTHS, a *Proof-of-*

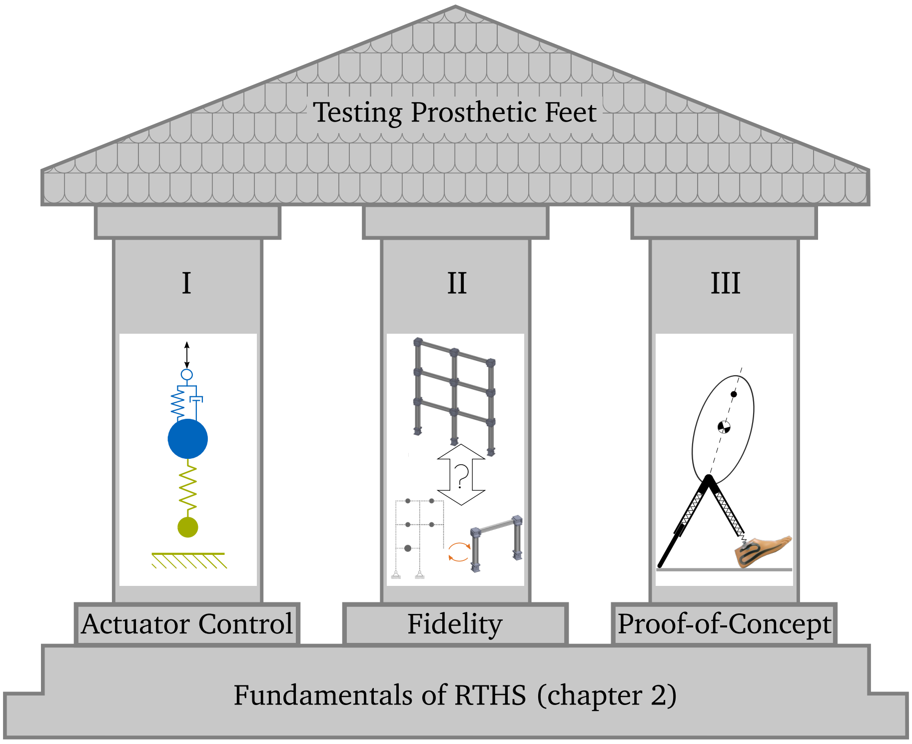

Figure 1.2: This PhD thesis sets the basis for testing of prosthetic feet using RTHS. Three important topics have been identified to be essential for the achievement of this visionary test method: actuator control, fidelity assessment (part of the depiction from [205]) and a proof-of-concept (prosthetic foot 1D35 by Ottobock, © by Ottobock). Each of these topics is represented by a pillar and elaborated in this dissertation. The methods developed in Part I and Part II are applicable to a wide range of RTHS applications and are not limited to the idea of testing prosthetic feet.

Concept is performed in Part III (third pillar in fig. 1.2). Therein, the objective is to perform a first RTHS test with a simulated amputee and an experimentally tested prosthetic foot. This is to show that the human gait dynamics can be emulated using an RTHS test. Part III presents state-of-the-art testing techniques and motivates the application of RTHS for testing prosthetic feet. This part also introduces human gait characteristics, models used to describe human gait and how an amputee can be modeled using these models. An RTHS test, where one gait cycle is performed, is conducted and the results are qualitatively analyzed.

Since each of the three parts deals with different topics, the state-of-the-art as well as the references to related work are given at the beginning of each part. Furthermore, all required methods, the results and a conclusion are described for each part individually. Each part is thus self-contained and a general summary of the thesis is given in chapter 19. This chapter gives also an outlook on possible future research directions.

The vision of testing prosthetic feet using RTHS is highly ambitious and much research is needed before this will be possible. This is indicated in the figure by the many roof tiles that need to be joined together.

1.2 Scientific Contributions

This PhD thesis contributes to scientific advances in the field of RTHS with contact. In particular, the methods proposed in Parts I and II are applicable to a wide range of RTHS setups and dynamical systems. Part III presents a novel application of RTHS, namely testing prosthetic feet with RTHS. Novel scientific contributions of this work are:

- The application of Iterative Learning Control (ILC) to improve the tracking performance of the actuator in RTHS is proposed in chapter 6. A convergence condition is set up which helps the user to determine the hyper-parameters of the ILC implementation. To a large extend, this was published in [107, 108].
- The applicability of Normalized Passivity Control (NPC, proposed by Peiris et al. [171]) to RTHS with contact is investigated in chapter 5, parts of which have been published in [104]. NPC was furthermore combined with ILC for a one-dimensional system with contact in chapter 6, which is based on publication [108].
- Chapter 11 proposes the FACE method, which is a novel method for fidelity assessment that is fundamentally different from the existing accuracy measures found in literature. The FACE method is applicable to a large variety of dynamical systems and the efficacy of this method is analyzed for the vibration response of dynamical systems in chapter 12. The method is published in [110].
- The first ever RTHS test with a prosthetic foot is performed in Part III. Specifically, a model of an amputee based on the Virtual Pivot Point (VPP) model is derived and one gait cycle performed. The results are published in [105].

Chapter 2

Fundamentals of Real-Time Hybrid Substructuring (RTHS)

Testing of components is an essential step during the development process to ensure that requirements are met [127]. In many engineering applications, not only the correct function of a component needs to be verified, but also its dynamic behavior has to be investigated. For example, the dynamic interaction of structural components can lead to noise, vibration, and harshness (NVH). This is not only unwanted and needs to be reduced in order to meet a high quality standard, but can also lead to safety-critical component failure.

There are several methods to investigate the dynamics of a mechanical system: Finite Element Modeling or multibody simulation offer a purely computational analysis of structural parts. In contrast, experimental modal analysis is a purely experimental approach. Numerical simulation is a safe approach with high repeatability and the modeling of linear elastic parts is well understood and reliable. However, modeling of nonlinear behavior, such as e.g. geometric nonlinearities or contact phenomena, is still challenging [177, 187]. A further drawback is the long computation time of extensive Finite Element Models, which might take up to many hours even on high-performance computers. Experimental Testing, in turn, is an appropriate method to investigate complex dynamical systems reliably without the need to identify system properties or take assumptions. However, setting up test benches is time-consuming, full-scale testing of large structural systems is not viable and system properties cannot be changed easily in an experimental setup. This is where Real-Time Hybrid Substructuring (RTHS) comes into play, which is a hybrid approach combining the benefits of both, numerical simulation and experimental testing. In RTHS, parts of the dynamical system under test are tested experimentally and form the *Experimental Part* whereas the rest of the system is simulated numerically, designated the *Numerical Part*[1]. The principle is illustrated in fig. 2.1. The experimental part typically comprises critical components from which the correct function should be verified or parts that are cumbersome to model (e.g. due to

[1]The terms *part*, *substructure* and *component* are used interchangeably.

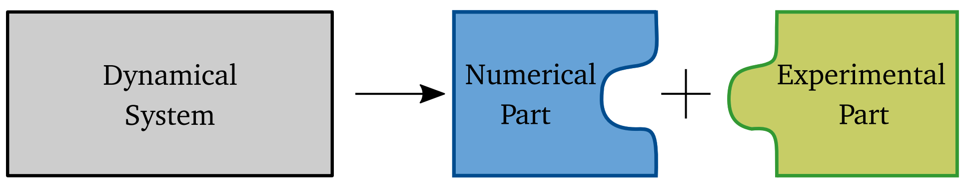

Figure 2.1: Basic idea of RTHS: A dynamical system (overall system) is split into a numerically simulated and an experimentally tested part. A co-simulation is performed to analyze the dynamic behavior.

nonlinearities, uncertainty in model parameters) [64]. The numerical part, conversely, comprises parts that are dynamically well understood, not yet available as hardware, or too large to be tested at full scale. Furthermore, system properties such as mass, damping, stiffness, geometry or material of the numerical part can easily be changed and their influence on the dynamic behavior of the overall system can be investigated. The computational and experimental dynamics analyses are performed in a co-simulation, meaning that information is exchanged between them in real-time and the dynamic interaction between the numerical and experimental part is considered. This makes RTHS an efficient and cost-effective way to investigate components already during the early development stage. RTHS offers the possibility to test components in full scale and with realistic in-service conditions, i.e. reproduce the dynamic conditions that the parts will experience in the later application. [19, 25, 37, 176]

Definition 1 (Overall System) *This denotes the coupled dynamical system, i.e. the dynamical system that is investigated. In the realm of RTHS, the overall system is split into the numerical and the experimental part.*

For introductory material on RTHS, the reader is referred to [158], [190], or e.g. the following publications [19, 144, 176].

2.1 Methodology

The idea of Hybrid Simulation, viz. the combination of numerical and experimental analysis, was first proposed by Hakuno et al. [88]. Due to limitations in computing power, real-time control and sensory equipment, first tests had to be conducted on extended time scale and were called Pseudo-Dynamic (PsD) testing [33, 216]. Since PsD testing is only appropriate if rate-dependent effects like damping play a minor role in the dynamics of the overall system, the need for RTHS arose. Thanks to the technological progress, the first successful implementations of RTHS could be reported in the 1990s by e.g. Nakashima et al. [156, 157], Horiuchi et al. [100] and Darby et al. [46]. For a detailed overview about the history of RTHS, the interested reader is referred to [155].

In literature, one can find different names in lieu of Real-Time Hybrid Substructuring that all refer to the same methodology: Real-Time Hybrid Simulation/Testing, Real-Time Substructuring, Real-Time Dynamic Substructuring/Testing as well as Model-in-the-Loop and (mechanical-level) Hardware-in-the-Loop [23, 59, 64, 164, 176, 226]. In this thesis, the naming RTHS is applied because it captures all ideas of the method: *Real-Time* indicates that the test execution and substructure coupling is in real-time, *Hybrid* refers to the combination of numerical and experimental dynamic analysis methods and *Substructuring* implies that the overall system is split into several parts that are investigated independently. Note that the concept of Hardware-in-the-Loop (HiL) can itself be classified into mechanical-level HiL, which is basically RTHS (see [64, 164]), power-level HiL and signal-level HiL. In the latter approach, signals are exchanged between the numerical and experimental parts rather than mechanical quantities. Common applications are in the automotive and aerospace industry. Signal-level HiL poses different research challenges than RTHS and is therefore not considered subsequently [112, 146].

As mentioned before, there needs to be a data exchange between the numerical and experimental parts to couple them, i.e. to investigate their dynamic interaction. This is called co-simulation [191]. Note that a general RTHS setup can comprise multiple experimental substructures [158, 192]. However, for the remainder of this thesis, the case of having one numerical and one experimental part is considered.

Definition 2 (Co-Simulation) *Implies that the computations and measurements are executed for each substructure independently. Information is exchanged in real-time between the substructures at discrete synchronization time steps to couple them.*

Since the substructures exchange energy with each other—as they would also do if they were coupled in the real setup (overall system)—variables describing flow and effort need to be exchanged at the interface. These are displacement/velocity and force information in RTHS. The data exchange is performed by the *Transfer System*, which consists of a controlled actuator, position/velocity sensors, force/torque sensors (FTS) and a Digital Signal Processor (DSP). The task of the transfer system is to achieve equilibrium and compatibility at the interfaces between the numerical and experimental part. Therefore, all necessary translational and rotational characteristics between the substructures need to be replicated and multiple actuators might be necessary. [48, 158]

2.1.1 Signal Flow

The basic signal flow, which is commonly applied, is position-based coupling and described in the following. In contrast, force-based coupling is the rarely used alternative (see [15, 181] for more details). A visualization of position-based coupling in RTHS is given in fig. 2.2. As

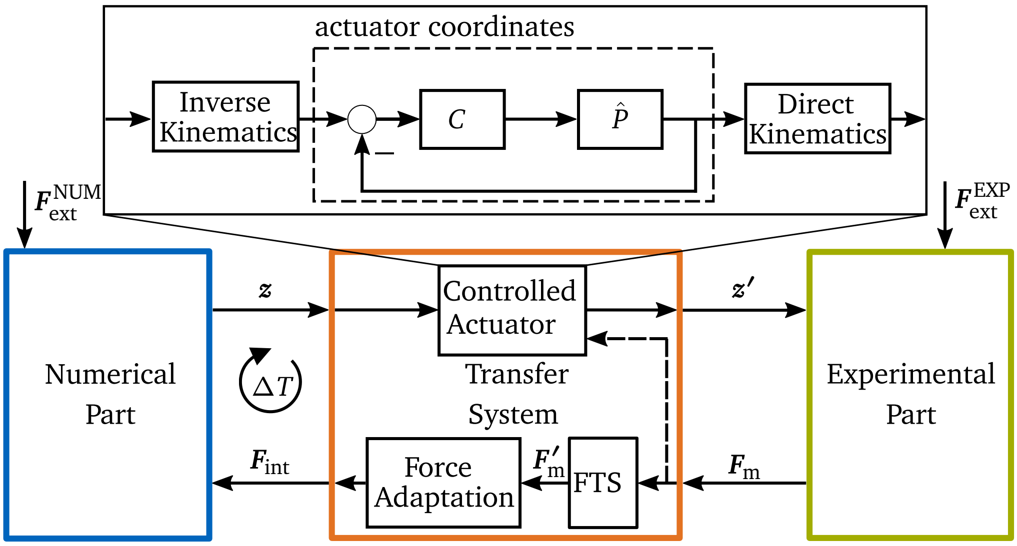

Figure 2.2: The signal flow in position-based RTHS. The coupled loop consists of the numerical part (in blue), the transfer system (in orange) and the experimental part (in green). The force/torque sensor is denoted by FTS.

can be seen in the figure, the RTHS setup forms a closed feedback loop [145]. The numerical simulation contains a model of the numerical part. This can be a closed-form analytical solution or a non-analytical computational model, such as a Finite Element Model or a multibody simulation [192]. Any external forces exciting the numerical substructure are denoted by $\boldsymbol{F}_{\text{ext}}^{\text{NUM}}$. The equations of motion are solved by a numerical time integration algorithm[2] that outputs the interface displacements $\boldsymbol{z}$. The displacement command $\boldsymbol{z}$ is sent to a controlled actuator. In many applications, hydraulic actuators are used, but also electric or pneumatic actuators can be employed. Depending on the experimental setup, i.e. how the actuator is oriented with respect to the interface Degrees of Freedom (DoFs), a kinematic transformation into the actuator coordinates (joint space) is necessary. The controlled actuator can be seen

[2] The selection of numerical time integration schemes is not further detailed here and can be found in i.a. [15, 24, 35, 39, 202].

as an inner control loop in the outer RTHS loop. In fig. 2.2, the special case where the actuator with transfer function $\hat{P}$ is controlled by a feedback controller with transfer function C is visualized. In an RTHS setup, however, any choice of controller can be suitable (feedforward and/or feedback) and different control schemes will be presented in Part I. The achieved displacement is denoted by $\boldsymbol{z}'$, which is the motion that the interface of the experimental part undertakes. It results from the dynamics of the controlled actuators and the kinematics of the arranged actuators (indicated with *direct kinematics* in the figure). The experimental part is mounted with its interface to the end effector of the actuator system[3] and reacts to this displacement and potential external forces $\boldsymbol{F}_{\text{ext}}^{\text{EXP}}$ with measurable forces $\boldsymbol{F}_{\text{m}}$. These forces can originate from strains, rate-dependent damping and inertial forces depending on the dynamic characteristics of the experimental substructure. The FTS, which is mounted at the end-effector of the actuator, measures the interface forces $\boldsymbol{F}_{\text{m}}'$. The interface forces can be processed by e.g. a filter or coordinate transformation, which is denoted by the force adaptation block in fig. 2.2. The (possibly processed) interface forces $\boldsymbol{F}_{\text{int}}$ result and are used as input to the numerical simulation in the next time step. [158] For the sake of clarity, the DSP, which is part of the transfer system (in orange), is not visualized in fig. 2.2.

The computations in the numerical part, the discrete sample time of the controlled actuator and the sample time of the force measurement may all be different and appropriate for the respective subsystem. However, there is the need for a synchronization time step ΔT at which information is exchanged, i.e. the coupling performed [18, 99, 233].

Notation in the Remainder of the Thesis

Figure 2.2 shows the general case of an RTHS setup where the interface consists of multiple DoFs and possibly also of multiple controlled actuators to represent the necessary interface translations/rotations. This means that the displacement and force quantities that are exchanged between the substructures are vectors. In Part I and Part II of this thesis, the interface is one-dimensional and therefore the exchanged quantities are scalars. In Part III, three DoFs (two translations, one rotation) are needed. All derivations in Part I and II are generally valid and not restricted to the one-dimensional case.

Furthermore, the applications and derivations in Part I and Part II will consider the case where all computations/measurements of the substructures are performed with the same time step, namely the synchronization time step ΔT. In Part III, in turn, the step size of the numerical time integration step and the force measurement is five times smaller than ΔT.

2.1.2 Physical Components

The transfer system and the experimental part make up the physical components of an RTHS setup. Since they are in dynamic interaction with each other, too, the achieved displacement of the actuator $\boldsymbol{z}'$ depends on the interaction between them. This is visualized in fig. 2.3, where both the transfer system and the experimental part are illustrated as mass-spring-damper (MSD) systems. If the transfer system can be regarded as stiff compared to the experimental part, the achieved displacement solely depends on the dynamic characteristics of the actuator $\hat{P}$ and the respective controller C. Often, however, the experimental part and the transfer system dynamically interact with each other and thus the achieved displacement is considerably influenced. This is known as control-structure interaction (CSI) and described for hydraulic actuators in [59]. The dashed arrow in fig. 2.2 indicates this dynamic interaction.

[3] In some cases, a direct control of the experimental interface locations is not possible. An idea to bypass this problem, which is based on the concept of transmission simulator from dynamic substructuring, is presented in [15].

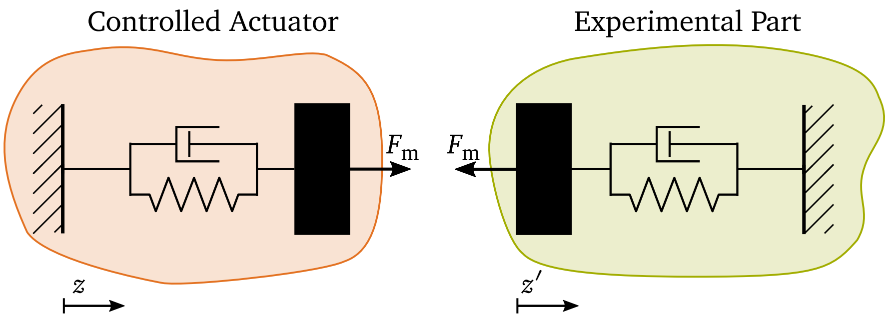

Figure 2.3: Visualization of the dynamic interaction between the controlled actuator and the experimental part. The dynamics of both are simplified as a linear MSD system.

2.2 Delay in RTHS

As mentioned above, the transfer system should achieve compatibility ($\boldsymbol{z}' = \boldsymbol{z}$) and equilibrium ($\boldsymbol{F}_\mathrm{m} + \boldsymbol{F}_\mathrm{int} = 0$) between the numerical and experimental substructure in order to represent their dynamic interaction realistically. However, in a real RTHS setup, there are several error sources that lead to desynchronization at the interface. Two of these error sources are the frequency-dependent time delay and the frequency-independent time lag[4]. On the one hand, time delays are introduced by frequency-dependent dynamics, such as the actuator delay ($\boldsymbol{z}' \neq \boldsymbol{z}$) or the transfer dynamics of the FTS. On the other hand, time lag is introduced by e.g. communication, computation as well as A/D and respectively D/A conversion. [37, 38, 42, 137] In the following, the term *delay* is used to describe the aggregation of all sources of time delay and time lag.

Definition 3 (Tracking Performance) *By tracking performance we denote the set-point tracking between the desired command*[5] z *and the real achieved displacement* z'*. The error is calculated as* $g = z - z'$ *and often referred to as gap. In case of perfect tracking, the condition of compatibility is fulfilled at the interface between the numerical and experimental substructure.*

Due to desynchronization at the interface and violation of the compatibility/equilibrium conditions, the RTHS setup distorts the investigated dynamics and the test accuracy is affected.

Definition 4 (Distortion) *If additional dynamics or other errors are introduced in the RTHS loop, the investigated dynamic interaction between the numerical and experimental part is changed. This means that the observed dynamics of the RTHS test differ from the dynamics of the overall system. A reason might be any introduced dynamics by the transfer system that lead to a violation of compatibility and equilibrium at the interface.*

More importantly, this delay can lead to instability of the test. RTHS test stability is indispensable in order to perform safe tests—for the user and for the used hardware.

Definition 5 (Stability) *The RTHS loop forms a feedback coupling that can become unstable in the presence of destabilizing factors (delay, unstable numerical time integration, measurement noise, ...). Instability means that the energy in the RTHS setup increases and leads to growing oscillation amplitudes in the actuator command. Instability of coupled RTHS tests should not be mixed-up with instability of the controlled actuator (inner loop): Even with a stably and robustly controlled actuator, RTHS instability can occur.*

[4] For now, other sources of error are disregarded. They are detailed in chapter 10.

[5] In case of force-based coupling rather than position-based coupling, the desired/real quantities would be forces.

Whether delay leads to instability and how much delay is tolerated before a test becomes unstable does not only depend on the amount of delay, but also on the dynamics of the investigated system and its partitioning into numerical and experimental part[6]. As a rule of thumb, the RTHS stability is less susceptible to delay the higher the damping in the overall system and the less stiffness in the experimental part. Furthermore, a test is less sensitive when the investigated system dynamics are slow[7]. In literature, one can find various methods to assess the stability of RTHS tests. Many of them consider the sum of all time delays and time lags as a constant time lag value τ for their studies [42, 136, 144]. The reasoning is that many tests are performed in a small frequency range, where the frequency-dependent dynamics do not change or the phase shows a linear roll-off. Furthermore, e.g. [144, 192] showed that only the sum of the delay/lag values matters, but not their individual values, if linear systems are considered. Reducing all delays to a scalar value τ enables an analysis at which critical value τ_{crit} a test becomes unstable. The analysis methods include control theoretical approaches such as an investigation of the closed loop poles [38], the phase margin [15, 42] or the root locus plot [41]. Based on Delay Differential Equations (DDE) some approaches can be found in [101, 135, 227]. Furthermore, the following literature studies the susceptibility of RTHS tests to time delay and gives recommendations about suitable choices of partitioning [28, 126, 134–137]. All these presented approaches require a known or at least an approximated dynamic representation of the experimental part, which is—according to the problem statement of RTHS—generally not available.

2.2.1 The Concept of Stability Margin

The concept of stability margin is commonly used in linear control theory to evaluate the robustness of a closed loop system. To apply this concept, the transfer function of the open loop system is plotted. Then, the phase is read at the frequency where the magnitude crosses one, i.e. 0 dB (location indicated by a vertical line in the magnitude plot of the following figures). The distance between that phase value and −180° implies the degree of robustness (phase margin indicated by a vertical line in the phase plot of fig. 2.4). The reason is that if the magnitude of the oscillation at a certain frequency is larger than one and the phase delay larger than −180° (half period), the oscillation of the system is stirred up. If the phase margin is ϕ_{pm} (in degree) at a frequency ω_{pm} (in rad/s), then the maximum allowed additional time delay is $\tau_{\text{crit}} = \frac{2 \cdot \pi \cdot \phi_{\text{pm}}}{360 \cdot \omega_{\text{pm}}}$ before the closed loop system becomes unstable. This concept is also applicable to the RTHS feedback loop if the individual substructures are linear [16].

Definition 6 (Robustness) *The closer an RTHS setup is to its stability boundary, the less robust it is. Robustness is a measure for how sensitive an RTHS setup is to any destabilizing factors, such as disturbances like measurement noise or additional delays. The notion of robustness is closely related to safety of the test.*

2.2.2 Mass vs. Spring Experimental Part

The effect of delay on the RTHS stability and how much delay is tolerated depends on the system dynamics and the partitioning into numerical/experimental part. In particular, the effect of a mass and a spring in the experimental part can be opposite. The investigations of linear MSD systems e.g. in [28, 41, 75, 134, 226] show that, in general, stiffness in the

[6] Note that even if a test remains stable, bad actuator tracking leads to inaccuracy of the test and therefore should be compensated for (see chapter 3).

[7] These are general rules deduced from literature and their validity could also be experienced in the course of this research.

experimental part has generally a destabilizing effect, while mass has a stabilizing effect. Both statements indicate the tendency, but are only true within certain bounds[8].

To visualize the effect of delay on the stability margin of an RTHS test with a spring experimental part, a simple example is shown in fig. 2.4. The figure shows the case where a linear MSD system (numerical part) is coupled to a spring (experimental part) for the case of an ideal actuator and with a time lag of $\tau = 0.005\,\mathrm{s}$. The vertical lines of the phase response indicate the stability margin. The higher the stability margin, the more additional delay is permitted before the test becomes unstable [15]. In this case, where the experimental part consists only of a spring, the delay leads to a decreased stability margin (14.6° to 3.8° at 6 Hz) and thus less robustness ($\tau_{crit} = 0.007\,\mathrm{s}$ to $\tau_{crit} = 0.002\,\mathrm{s}$).

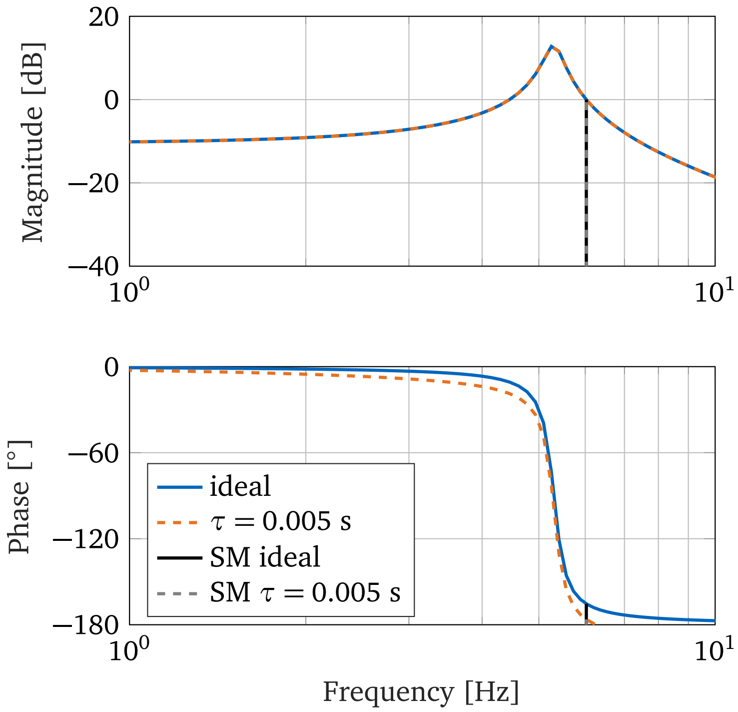

Figure 2.4: Bode diagram showing the influence of delay on the stability margin of the RTHS test for a stiffness experimental part. The ideal dynamics (solid, blue line) of the overall system and the dynamics including a pure time delay of $\tau = 0.005\,\mathrm{s}$ (dashed, orange line) are shown. The construction of the stability margin (SM) is indicated by the vertical lines.

This example demonstrates that additional delay leads to decreased robustness in case of a spring experimental part. In case of a mass experimental part, the phase margin increases in the presence of actuator delay. The reason for the different effect of delay when the experimental mass consists of a mass or a spring can be explained using a representation in the complex plane. Figure 2.5 shows the forces on the mass of an oscillating MSD system (spring stiffness k, damping constant d and mass m, eigenfrequency ω_0). A delay τ rotates the force components. In case the inertia forces are delayed, which is the case when the mass is in the experimental substructure, a positive damping component is gained. This, in turn, increases the RTHS test robustness. In case the spring forces are delayed, though, the rotation of the force vector creates a negative damping contribution and hence destabilizes the RTHS setup.

[8] For example, [28] reports that if $k_{\mathrm{EXP}} < 0.06k_{\mathrm{NUM}}$ or $m_{\mathrm{EXP}} < 0.06m_{\mathrm{NUM}}$ for a system with 3 % critical damping, the test is in a region of unconditional stability. This means that the test is stable regardless of any time delay. Furthermore, if the resonance frequencies of the numerical and experimental part match, i.e. $\frac{k_{\mathrm{NUM}}}{m_{\mathrm{NUM}}} = \frac{k_{\mathrm{EXP}}}{m_{\mathrm{EXP}}}$, the test is also unconditionally stable. The fact that RTHS setups with mass in the experimental part tolerate larger time delays is only true if $m_{\mathrm{EXP}} < m_{\mathrm{NUM}}$. If $m_{\mathrm{EXP}} > m_{\mathrm{NUM}}$, a position-based RTHS coupling tolerates no delay at all.

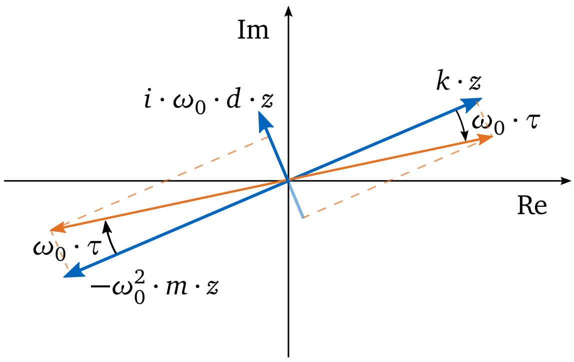

Figure 2.5: The forces on the mass in an MSD system are represented in the complex plane (blue). In the presence of a delay τ, the complex force vectors are delayed (orange), which corresponds to a clockwise rotation.

In the present section, the influence of time delay was discussed. For the sake of completeness it should be mentioned that there are also other sources of errors and uncertainty in an RTHS setup that lead to inaccuracy of the test. These are discussed in Part II.

2.3 Test Fidelity

RTHS aims at emulating the true dynamic behavior of the overall system, which is called the *reference solution* [134, 238]. The reference solution can either be a full experimental test or a full numerical simulation of the overall system. However, in many engineering applications, the generation of the reference solution is impractical and the main reason why RTHS is employed in the first place. On the one hand, pure numerical modeling might be inappropriate due to complex dynamic behavior (nonlinearity, contact, unknown material properties) of the experimental part. On the other hand, a full-scale test of the experimental part might require huge laboratories as well as the existence of all parts and not all of them might be manufactured yet. If possible, the reference solution should be obtained from a full experimental test of the overall system. This is because there are less assumptions involved compared to a pure numerical simulation of the overall system.

Definition 7 (Fidelity) *How well the true dynamic behavior of the overall system (reference solution) is emulated by the RTHS test is called fidelity. A high fidelity corresponds to a good emulation of the system dynamics and a high test confidence.*

The fidelity can be measured by different quantities (e.g. time and frequency domain) and is detailed in Part II. In general, these measures investigate how well the test replicates the Quantity of Interest (QoI).

Definition 8 (Quantity of Interest (QoI)) *The purpose of an RTHS test is to investigate e.g. the system dynamics, function of parts and possible failure of components, which is called the QoI. This can be a physical quantity such as e.g. a displacement, stress, force, temperature, frequency response, etc. or a parameter that evaluates the function of a component. The QoI does not necessarily need to be at the interface but can also be an internal DoF of either the numerical or experimental part. [191, 232]*

2.4 RTHS from Different Perspectives

The RTHS principle and the effects observable in RTHS experiments can be viewed as a dynamic substructuring problem and also as a control theoretical task. This section aims at linking these views together. This is to establish the connection to RTHS for readers who are more familiar with one of the perspectives.

2.4.1 Dynamic Substructuring Perspective

Analyzing system dynamics by splitting the overall system into several substructures is not only found in RTHS, but also in dynamic substructuring. This includes coupling of either several numerical or experimental substructures or the coupling of experimental and analytical models [7, 50, 67, 79]. Even though dynamic substructuring poses different research questions, readers from this field might better understand the content of this thesis if a few relations are given.

In frequency-based substructuring, which considers the substructuring problem in frequency domain, the substructures are commonly denoted by *Substructure A* and *Substructure B* (see the illustration in fig. 2.6). These correspond to the numerical and experimental part. The RTHS test is supposed to emulate the overall system dynamics, which comprises substructures A and B. The transfer system, which is substructure C, should perfectly transmit the dynamics between A and B, i.e. should be ideally stiff and $z' = z$. In a real RTHS setup, however, not only the dynamics of substructures A and B are involved, but also some additional interface dynamics, which are represented as *Substructure C* (corresponds to the transfer system in RTHS). Any additional dynamics of substructure C change the dynamic response when substructures A and B are coupled. For example, El Mahmoudi et al. [60] include bushings at the interface between two substructures A and B. The bushings are modeled as spring-damper elements (stiffness $k^{(\mathrm{Bush})}$, damping $c^{(\mathrm{Bush})}$) with an admittance $\frac{1}{k^{(\mathrm{Bush})}+c^{(\mathrm{Bush})}(i\omega)}$. From this equation, it can be seen that the influence of the bushing (substructure C) on the dynamics of the coupled substructures A and B is zero if the impedance $k^{(\mathrm{Bush})} + c^{(\mathrm{Bush})}(i\omega) \rightarrow \infty$. In the RTHS loop, delays (see section 2.2) lead to $z' \neq z$ at a certain time step, which corresponds to a finite rather than infinite impedance of the transfer system.

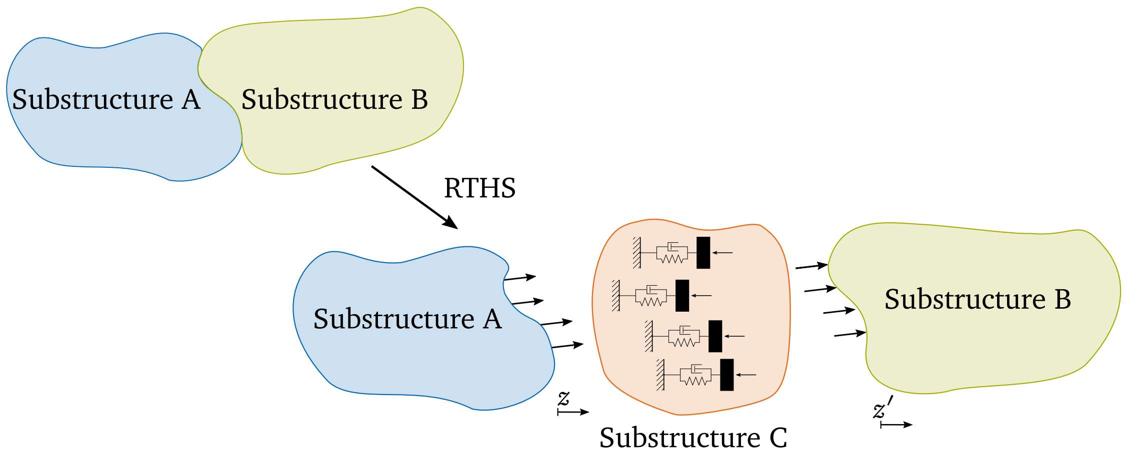

Figure 2.6: RTHS in the notation of dynamic substructuring.

2.4.2 Control Theoretical Perspective

Just as the mechanical perspective before, there might be readers who feel themselves more acquainted with control theory. The block diagram representing RTHS is shown in fig. 2.7.

The correct transfer function of the numerical part is denoted by $\hat{G}_{\text{NUM}}$ and of the experimental part with $\hat{G}_{\text{EXP}}$. The actuator (transfer function $\hat{P}$) is controlled by a feedback controller C, yielding the transfer function $\hat{G}_{\text{ACT}} = \frac{z'(s)}{z(s)} = \frac{C\cdot\hat{P}}{1+C\cdot\hat{P}}$ of the controlled actuator.

The denominator of a closed loop transfer function provides information about the characteristic dynamics of the system. For the RTHS loop as shown in fig. 2.7, the denominator of the sensitivity function writes $1+\hat{G}_{\text{NUM}}\cdot\hat{G}_{\text{ACT}}\cdot\hat{G}_{\text{EXP}}\cdot\hat{G}_{\text{FTS}}$. In case of a perfect transfer system (i.e., $\hat{G}_{\text{ACT}}=\hat{G}_{\text{FTS}}=1$), the reference dynamics result[9] and the characteristic equation writes $1+\hat{G}_{\text{NUM}}\cdot\hat{G}_{\text{EXP}}$. However, in a general RTHS system, the characteristic equation contains the dynamics of the transfer system. From this it is clear that any dynamics of the transfer system directly influence the RTHS result. Furthermore, these characteristic dynamics can be unstable, which results in the test instability discussed in section 2.2.

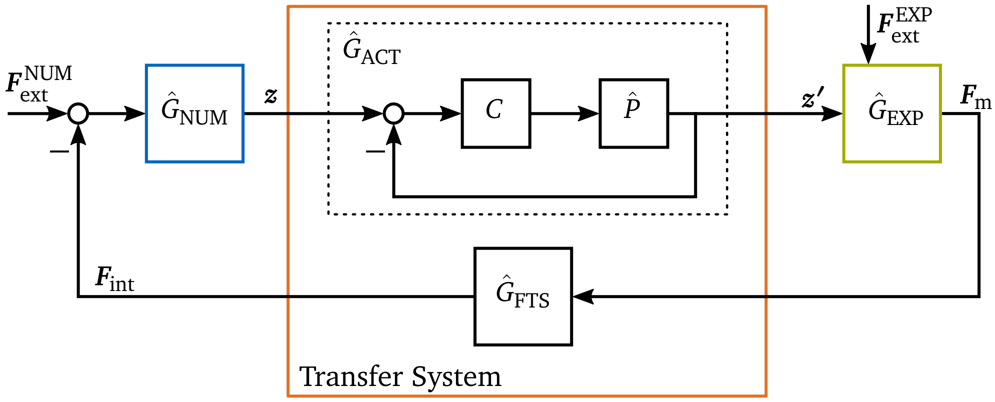

Figure 2.7: Representation of the RTHS loop as control loop. For the sake of clarity, any coordinate transformations, force adaptations and the DSP are omitted in this figure. $\hat{G}_{\text{NUM}}$ and $\hat{G}_{\text{EXP}}$ are the true transfer functions of the numerical and experimental part.

2.5 Applications and Current Research

Nowadays applications of RTHS range from civil engineering, where structural behavior under natural-hazards is investigated, to the automotive and aerospace sector, robotics, manufacturing systems and medical applications. This section gives a brief summary about them, but does not claim to be exhaustive.

Applications in civil engineering include testing of buildings under earthquake loads, testing of tall buildings under wind loads, investigation of structural components in case of fire and testing of road/rail bridges under wind and wave loads [98, 228, 243]. Furthermore, aerodynamic forces are often emulated using RTHS, see e.g. [176], and wind turbine blades are analyzed [26, 37, 123, 191]. In the automotive sector, e.g., semiactive MacPherson suspension systems [65], active safety vehicle systems [208] or vehicle axles [165] have been tested using RTHS. Further, the pantograph-catenary interaction of the power supply of trains was i.a. investigated in [64]. In the aerospace sector, [91] looked into spacecraft parachute deployment and i.a. [22, 132] probed the rendezvous and docking of satellites in space. Biomechanical analyses of hip and knee endoprostheses have been performed by [78, 93].

Even though RTHS is already applied as testing procedure in some engineering applications, there are still many open research questions. MECHS (Multi-Hazard Engineering Collaboratory for Hybrid Simulation), which is an NSF-funded Research Coordination Network, aims at pushing the frontiers of Hybrid Simulation and foster the exchange of knowledge

[9] This also assumes that the model of the numerical part and the time integration scheme are accurate.

and codes. In 2019, they set up a Research Agenda [142] that displays the current research status and the required research to further advance the field of application. The following outlined research questions aim at providing an overview about the various research activities on RTHS but are not considered in this thesis. Modeling of the numerical part is of huge importance in RTHS. As the applications are becoming more complex, the need for accurate numerical models that can still be solved in real-time rises. Model Order Reduction or black box modeling via Neural Networks are approaches that can be found in literature [18, 83]. Associated to the correct modeling of the numerical parts, suitable numerical time integration schemes are needed [44]. For the last decades, RTHS has mainly be considered from a deterministic perspective. Over the last few years, the focus shifts to frameworks including parameter uncertainty and the investigation of uncertainty/error propagation through the RTHS loop [1–3, 192]. A further research topic is about distributed RTHS, where experimental parts are at different laboratories around the world and RTHS tests are performed. Details about this idea can be found i.a. in [29, 124].

A large research focus is also put on the transfer system control and the compensation of the actuator dynamics [142]. The methods developed in this track address the stability and accuracy problem described in section 2.2. Current limitations include the implementation complexity as they often need a system identification of the actuator used and their limited versatility when it comes to testing of nonlinear experimental parts. This research question is the focus of Part I. Furthermore, fidelity assessment is of huge importance so that confidence is gained in the methodology. The tracks that have been considered so far to handle the assessment of RTHS tests and a novel methodology are presented in Part II.

Part I

Actuator Control for RTHS with Contact

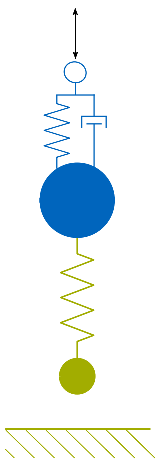

Chapter 3

Contact and Actuator Control in RTHS: an Introduction

As discussed in section 2.2, the dynamics of the transfer system influence the test fidelity and stability. Generally, the vast part of the delay in an RTHS system comes from the controlled actuator while the dynamics of the FTS and the DSP can be considered fast [144]. This is because the internal dynamics of the FTS and DSP are often much faster than the dynamics of the investigated overall system or the controlled actuator. Since the test result should be of high fidelity, there is a special research focus on minimizing the spurious dynamics introduced by the actuator into the coupling loop. Particularly for testing impact-contact scenarios, which is also the case in the visionary RTHS application of prostheses testing, existing actuator control/dynamics compensation schemes are not fully sophisticated and their application is cumbersome. Part I deals with actuator control for RTHS applications with impact-contact scenarios and is not limited to the application of prostheses testing.

3.1 Contact Problems

In nature as well as in engineering, there are many processes that are dominated by contact. The phenomena comprising contact are manifold and depend on the length and time scale and can be viewed from nanoscale to macroscopic level. Contact phenomena can be beneficial and indispensable, e.g. when animals and humans exploit the dynamic interaction with the ground while walking and running. The dynamic phenomena can also be detrimental, though, as contact affects the vibratory response of the systems undergoing contact. Considering the local interface dynamics, effects like friction, stick-slip and wear can be observed. These local effects influence the dynamic response of the contact partners and can induce unwanted vibrations. In many technical applications, high customer requirements must be met and the induced dynamics that can lead to noise, vibration, and harshness (NVH) are unwanted and must be reduced. [14, 115, 177, 245] The basic principles of contact mechanics can be found in [14, 115].

When contact occurs, two or more contact partners are involved. At the contact boundary, i.e. where the respective parts touch each other, a dynamic interaction takes place between them. This means that the dynamical properties of the contact partners instantaneously complement each other. The dynamic interaction of the contact partners can lead to changes in the resonance frequency, the excitation of a resonance and also energy dissipation at the contact interface. If the relative velocity between the contact partners and the rate of loading is high (short time scale), a stress-wave can result that propagates through the components. This phenomenon is known as impact. [115]

Due to the complexity of contact phenomena, modeling of contact is challenging [23, 177]. For example, the dynamic properties of the contact partners must be known accurately as well as the exact surface shape and geometry and the impact velocity. Nevertheless, the high technical demands of novel products need to be met in a cost-effective manner and testing the dynamic interaction between the contact partners already in the early development stage is indispensable. An appropriate choice can be RTHS for the reasons outlined in chapter 2. The first application of RTHS with contact can be found in Veerasamy and Hubbar [224]. Since then, several RTHS setups have been built to simulate spacecraft docking and on-orbit servicing (see [5] for an overview). Using RTHS for such simulations in aerospace does not only enable the investigation of contact dynamics without the need of computational modeling, but also offers the possibility to investigate the dynamics realistically under zero-gravity conditions as in space. The researchers encountered stability issues when performing RTHS with contact and report that the type of actuator used is key for the success of such tests. For example, a high actuator bandwidth [23] and a fast cycle time [22, 132] are desirable. Furthermore, Ma et al. [132] report that the use of impedance control would be beneficial but cannot be implemented in industrial robots due to the inaccessibility of the required signals. They implemented admittance control instead and incorporated active (virtual) and passive (mechanical) compliant parts in the RTHS setup to enable stable RTHS tests [241, 242].

A further application in the aerospace sector is the investigation of Air-to-Air Refuelling [23], albeit this work uses PsD testing rather than RTHS due to limited actuator bandwidth. In the transportation sector, the contact between a pantograph and the overhead line (power supply) of a train is e.g. investigated in [64, 213]. In these applications, the contact phenomenon is defined by brief duration with high rate of loading/unloading and abrupt acceleration and deceleration patterns. These RTHS applications with contact are depicted in fig. 3.1.

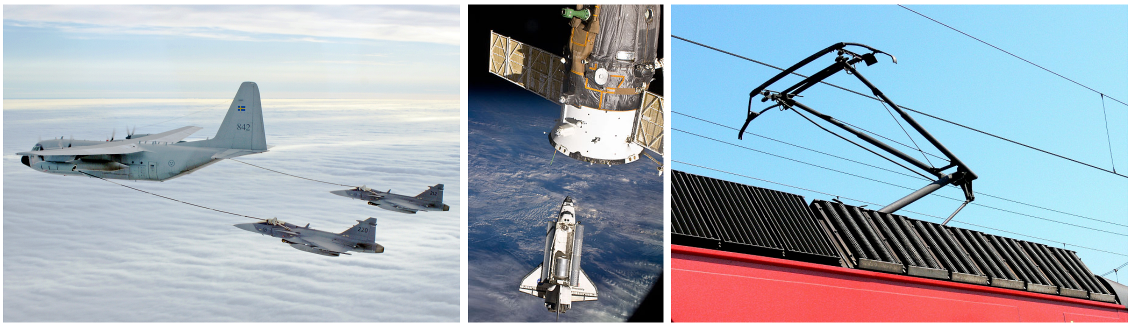

Figure 3.1: Example engineering applications with contact, where an investigation of the dynamics using RTHS would be desirable. The left picture shows Air-to-Air Refuelling (©Milan Nykodym) [163]. In the middle, the docking of a spacecraft to a space station is visualized [159] and on the right, a pantograph for power supply of trains is depicted.

3.2 Requirements on Actuator Control for RTHS with Contact

As outlined in section 2.2, there is a need for effective actuator dynamics compensation. Based on the research agenda from MECHS [142], a literature survey and the intended application of RTHS tests with contact, the following requirements can be formulated for the actuator control[1] (this list is inspired by [137, 138, 142, 206]):

[1]These requirements are set for all kinds of RTHS setups and are not limited to RTHS with contact.

- **Accurate tracking:** A good tracking performance (cf. definition on p. 9) is vital for a high fidelity test result. A good control scheme compensates for all uncertainties of the control plant and performs the desired motion with minimum discrepancies for a large frequency range. This is also known as high controller bandwidth (magnitude 0 dB and phase delay constant).

- **Data-based approach:** The control scheme should be applicable without the need for an analytical model or a system identification neither of the actuator nor the experimental part.

- **Simple and straightforward:** This requirement indicates the necessity for a simple implementation with only few tuning parameters that can be tuned in a straightforward manner. The implementation effort should preferably be as little as possible.

- **Widely applicable:** Despite the simple implementation, the scheme should be applicable to a wide range of RTHS setups. Firstly, this includes that many kinds of dynamical systems can be investigated properly: For example, nonlinear and discontinuous dynamics as well as unpredictable component failure and complex dynamic bifurcation need to be reproduced safely and accurately. Secondly, the control scheme should be applicable to a wide range of robots (also industrial robots, where often not all signals can be tapped), actuation systems and to existing facilities. Therefore, an appropriate control scheme should not interfere with the existing control scheme and ought to work for different types of command signals (acceleration, velocity, displacement).

- **Stability:** Requirements on stability do not only include the stability of the controlled actuator itself, but also stability of the RTHS loop (cf. definition on p. 9). Stability of the controlled actuator itself can, in particular, be an issue for purely feedforward controlled actuators and is independent of the RTHS loop. Stability of the RTHS loop, in turn, depends on the amount of uncertainties in the RTHS loop and the sensitivity of the RTHS test (in general, depending on the dynamical system properties). An appropriate control scheme is able to maintain test stability under any circumstances to protect the user and the hardware setup from damage. For example, testing of lightly damped systems, which have a small stability margin and are highly sensitive to delay and uncertainty, ought to be feasible [77].

- **Robustness:** This requirement goes hand in hand with the requirement on stability and refers to the test stability in the presence of uncertainties (cf. definition on p. 10). Even in the presence of unpredictable component failure or destabilizing factors, the test execution needs to remain safe.

Definition 9 (Bandwidth) *Bandwidth defines the frequency (ω_{bw}) up to which the controlled actuator is able to perform a movement with minimum discrepancies. This means that the magnitude of the transfer function is* $\approx 0\,\mathrm{dB}$ *and the phase delay is constant within this frequency band.*

3.3 Overview about State-of-the-Art

Over the past two decades, plenty of methods have been proposed to improve the actuator tracking performance and compensate for any unwanted dynamics that distort the RTHS result. Many of them still suffer from limitations and do not fulfill all requirements outlined in section 3.2. This chapter aims at giving a broad overview about various proposed techniques but does not claim completeness.

Short Recap about Control Theory

Control schemes can be classified into *feedforward* and *feedback* controllers and they often complement each other to achieve the goal of robust and agile actuator tracking. Feedforward controllers determine the plant input based on the desired command (here: z) and therefore shape the command input response, i.e. the dynamics with which the actuator follows the desired trajectory. If the dynamic behavior of the plant (here: actuator $\hat{P}$) is perfectly known, one can find a feedforward controller that uses the inverted dynamics $\hat{P}^{-1}$ and perfect reference tracking can be achieved, i.e. $\hat{P}^{-1} \cdot \hat{P} = 1$. In reality, however, there are modeling errors and disturbances which can lead to instability of the controlled plant. An additional feedback controller can eliminate this problem. The input to a feedback controller is the error between the desired and the achieved value (here e.g. position error $g = z - z'$) and can deal with uncertainties. The parameters of the feedback controller determine the dynamic response to disturbances. [69] Even though the sole use of a feedback controller is more robust compared to a feedforward controller, the tracking performance is limited [223]. Hence, the combined use of both is recommended, especially for RTHS, where tight actuator tracking is required [175].

3.3.1 Actuator Delay Compensation

The first and probably most prominent publication in this field is by Horiuchi et al. [98, 100]. In this work, the actuator delay is modeled as a pure time lag τ (rather than a frequency-dependent delay). The key idea is illustrated in fig. 3.2a and is as follows: First, a polynomial fit is performed at time t on a predefined number of previous displacement commands ($t - \tau$, $t - 2\tau$, ...). Then, using this polynomial, an extrapolation is performed to predict the actuator command ahead this delay value (time $t + \tau$). The predicted value $z(t + \tau)$ is sent to the actuator instead of the calculated command z, which is the output of the numerical simulation. A major limitation of this basic compensation scheme is that the real transfer behavior of the actuator is frequency-dependent and can only in a limited frequency range be regarded as constant. Furthermore, the polynomial degree needs to be selected appropriately. This basic implementation has been improved i.a. by Darby et al. [47] and Wallace et al. [227] to estimate the time lag during the RTHS test. A comparison of these delay compensation schemes is given in [217]. Nevertheless, the scheme has several limitations and is restricted to low-frequency movements where the actuator delay is small relative to the period of the vibrations to be controlled.

To overcome these limitations, model-based feedforward/feedback control has been applied [34, 68, 175]. The block diagram is given in fig. 3.2b. In this scheme, a system identification of the plant $\hat{P}$ is performed and an approximate model P is identified. The inverse of that model is used as feedforward controller and complements a feedback controller C, which can e.g. be a PID controller [34]. For model-based feedforward control, a dynamic model of the actuator P needs to be available or identified beforehand. To achieve high performance, the transfer behavior must be modeled accurately. The modeling process is cumbersome, though. Often, linear time-invariant transfer function models are used. These are in general not sufficient, because the actual dynamic behavior is nonlinear and friction effects or transient dynamics might be present. Furthermore, the real achieved displacement z' depends on the dynamic interaction between the actuator and the experimental part (see explanation in section 2.1.2). If the actuator cannot be regarded as stiff compared to the experimental part, the time-consuming system identification needs to be performed with the experimental specimen mounted on the actuator. This means that for each experimental specimen that should be tested with RTHS, the system identification needs to be performed again. Furthermore, this implies that model-based feedforward/feedback control is not applicable if the dynamic properties of the experimental part change during the system identification. The application of RTHS with contact poses a further difficulty in the modeling process of the actuator since the dynamics change abruptly at the instant of contact and a single transfer function model might not be sufficient to guarantee high fidelity RTHS tests.

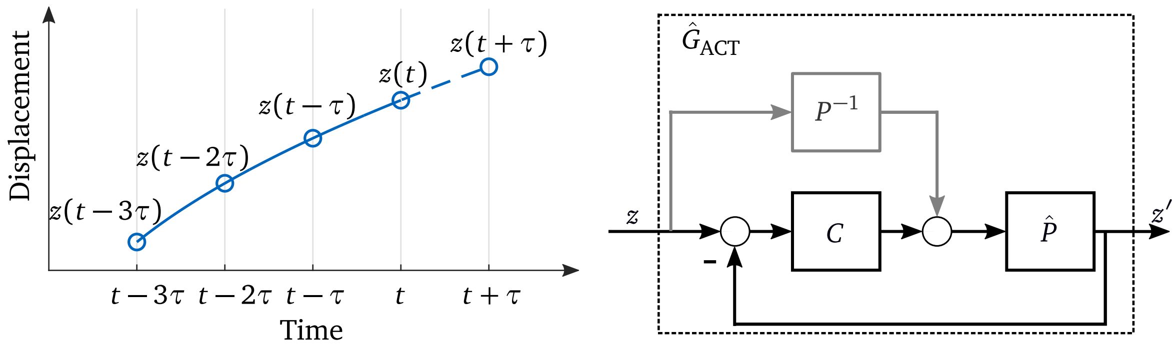

(a) The principle of polynomial extrapolation. Figure adapted from [98].

(b) Model-based feedforward/feedback control.

Figure 3.2: This figure illustrates two common delay compensation schemes used in RTHS.

The requirements on the modeling process can be relaxed by the application of adaptive controllers. Here, the idea is to adapt the identified model parameters or controller parameters continuously during run-time. The adaptation process is based on a cost function, which is e.g. the tracking error (gap g). An algorithm (e.g. least-mean-squares algorithm) is employed to minimize this cost function [17, 25, 40, 55, 206]. In the work of Bartl et al. [15, 17], adaptive feedforward filters (AFF) are used and the implementation could achieve perfect interface synchronization ($g \approx 0$) even for RTHS tests with transient dynamics. The investigation of RTHS tests with continuous dynamics proved the efficacy of AFF, but the applicability to RTHS tests with discontinuities such as contact has not been investigated yet. Similar to the model-based feedforward/feedback control, a difficulty might be the change of the system dynamics at the moment of contact.

Further advanced actuator control schemes include the combination of sliding mode controllers in combination with an adaption layer [133] and the use of model predictive control [221]. Both publications discuss the robustness of these schemes and the ability to control nonlinear plants that are subject to external disturbances and model uncertainties. Since these schemes are not dealt with in this thesis, the interested reader is directly referred to these publications.

Looking back to the requirements from section 3.2, shortcomings of the existing actuator control schemes can be summarized as follows:

- Most of the control schemes rely on a precise identification of the actuator dynamics interacting with the experimental specimen. This contradicts the desire of a data-based and simple approach. The system identification process requires the right equipment, advanced knowledge and is time consuming. Furthermore, there are many tunable parameters that complicate the applicability of these schemes.

- The example applications often include linear continuous dynamical systems and their applicability to more complex dynamical systems (nonlinearity, discontinuity) has not been investigated. Using these methods for RTHS with contact is assumed to be complicated and not straightforward. This is because the actuator alternates between moving the experimental part freely and pushing it against a surface, which changes the dynamic interaction between the actuator and the experimental part (change of $\hat{G}_{\mathrm{ACT}} = \frac{Z'(s)}{Z(s)}$). Special transition strategies might be required to avoid parasitic dynamics [214].

- Most of the existing control methods cannot be used for out-of-the-box actuators (e.g., industrial robots) and their corresponding control system. This is because out-of-the-box actuators do not offer the signals at the interface that are required for many of the methods and often the sampling rate is lower than needed for RTHS. The sampling rate of out-of-the-box robots is often 250 Hz, while many RTHS experiments are performed with $> 1000\,\text{Hz}$. For future applications and a simple workflow, actuator control schemes that do not interfere with the existing actuator controller are favorable.

3.3.2 Robustness of RTHS Tests

The actuator delay compensation schemes presented above (section 3.3.1) consider the actuator tracking performance. All of them try to achieve compatibility at the interface between the numerical and experimental substructure and positively affect the test fidelity. Nevertheless, if the RTHS setup is highly sensitive, test instability can still occur in case of slightly imperfect dynamics compensation [77]. None of the presented schemes observe the test stability and therefore they do not intervene or stop the RTHS test in case of instability. Only a few attempts to improve robustness and prevent instability can be found in literature. Gawthrop et al. [77] propose two model-free approaches, namely to enhance the numerical substructure by additional damping (damping raises the stability margin, see section 2.2) and secondly to use a phase lead transfer function. Apart from these approaches, also the concept of passivity-based control has been applied to RTHS. This scheme is commonly applied e.g. in teleoperation or the control of haptic interfaces [70, 89, 188, 189, 240].

In the realm of passivity-based control, a network of subsystems is considered from an energetic point of view. Passivity states that a system does not generate energy. This is sufficient to guarantee stability, because the definition of stability is that the system output energy remains bounded if the energy input is bounded [89]. Passivity-based control schemes embed this principle: They monitor the system energy, more precisely, the power-flow between the subsystems of the network. If instability is detected, they interfere with the system and dissipate spuriously added energy to maintain stability.

Definition 10 (Passivity) *A system (network of subcomponents) is passive if it does not generate energy. Passivity is a sufficient condition for stability. Passivity-based control schemes interfere with the system, i.e. dissipate spuriously added energy, when an energy increase is detected.*

Passivity-based control schemes are employed when time delays are present, such as for example in teleoperation. Teleoperation systems are used to control haptic devices in remote environments, such as e.g. undersea, in space or to handle hazardous material [160]. The basic signal flow between the involved parts is illustrated in fig. 3.3. Here, a user operates an input device to control a remote robot and interact with the environment. Force feedback from the input device helps the user to control the robot. A key challenge in teleoperation is to maintain stability in the presence of destabilizing factors, such as time-varying communication delays[2] or uncertain dynamics of the remote environment [70]. Passivity-based control proved to be successful and maintains stability of teleoperation systems. A comparison of fig. 2.2 and fig. 3.3 reveals that the problem structure of teleoperation systems and RTHS as well as the sources of uncertainties and destabilizing factors are similar. Therefore, the application of passivity-based control to RTHS can be a useful means to enable safe testing. First investigations of passivity-based control in RTHS have been performed in e.g. [53, 104, 171, 172]. The implementations are described in detail in chapter 5. The term *fidelity* in RTHS corresponds to the measure of *transparency* in teleoperation. Transparency denotes

[2] The time delays become particularly large in case of long distances between the user and the slave robot.

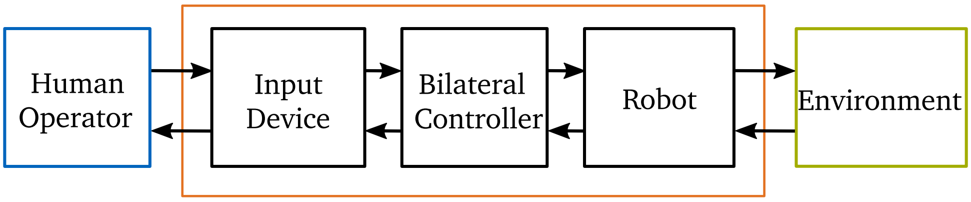

Figure 3.3: Basic signal flow in teleoperation. In comparison with an RTHS loop, the user can be regarded as the numerical part (blue), the master, controller and slave robot as the transfer system (orange) and the interaction with the remote environment as the experimental part (green). Adapted from [160].

the degree to which the true interaction forces with the remote environment are fed back to the user.

A main shortcoming of the presented robustness schemes is that they distort the investigated dynamics. Hence, their application introduces a trade-off between fidelity and robustness [77]. In this work, passivity-based control schemes will be considered henceforth since they only interfere in case test stability is jeopardized. Until now, the applications of passivity-based control to RTHS mainly consider linear and nonlinear systems. While passivity-based control schemes guarantee test stability, they cannot improve the actuator tracking performance. Consequently, a combination of passivity-based control schemes with a powerful delay compensation scheme is desirable.

3.4 Objective of Part I

RTHS should become more versatile and general, and thus applicable to a broader range of problems, e.g. dynamic systems including contact. For the reasons outlined above, there is the need for actuator dynamics compensation schemes that fulfill the requirements defined in section 3.2. More specifically, a powerful control scheme ought to be set up that tackles the challenges of **stability** (robustness in the presence of destabilizing factors) and **fidelity** (actuator tracking accuracy). The main focus lies on RTHS systems with contact. The developed scheme should require no or only little knowledge about the dynamics of the actuator system (no system identification) to make the methods as versatile and simple to use as possible. Part I aims at attaining such a powerful control scheme and investigates the applicability of Normalized Passivity Control, Iterative Learning Control and Adaptive Feedforward Filters.

The remainder of Part I is organized as follows: Chapter 4 presents the investigated dynamical system, which is a one-dimensional mass-spring-damper system experiencing contact. Furthermore, the physical RTHS setup comprising a controlled Stewart Platform as actuator, a force/torque sensor and a digital signal processor as well as the experimental part is introduced. A simulation environment, i.e. a digital twin of the experimental RTHS setup, is developed and serves as a safe test environment for the proposed algorithms. This chapter also presents the reference solution and the definition of accuracy and fidelity measures that are used for the assessment of the proposed method.

In order to guarantee test stability, the concept of passivity-based control schemes is investigated in chapter 5. Firstly, an introduction to the energy/power flow in an RTHS system is given. After that, passivity-based control schemes that have been applied to RTHS are presented and Normalized Passivity Control (NPC) is applied to the presented RTHS system with contact. The influence of the tunable parameters as well as the ability to maintain stability are discussed at the end of chapter 5.

Iterative Learning Control (ILC) is presented in chapter 6. First, an introduction is given together with some common applications. Then, ILC is applied to RTHS and the success of ILC in an RTHS setup is discussed using the derived convergence condition. Different ILC methods are applied to RTHS and the advantages and disadvantages are presented.

As stated above, Adaptive Feedforward Filters (AFF) have proven to compensate actuator dynamics effectively in the work of [15]. The principle of AFF as well as its application to RTHS with contact are investigated in chapter 7.

Chapter 8 brings all parts together and a benchmark is presented where ILC, AFF and NPC are combined and compared. Furthermore, ILC is combined with velocity feedforward, which is a simple feedforward control approach. A critical discussion is given and the strengths and weaknesses of the schemes are presented in detail.

A summary of Part I is given in chapter 9 that evaluates the proposed actuator dynamics compensation methods based on the requirements.

Chapter 4

RTHS System with Contact and Hardware Setup

This chapter is partly based on the author's publications [102–104, 107, 108]. The students Mert Göldeli and Lisa Kühn contributed as research assistants to the identification of the Stewart Platform's dynamic behavior and the parameter tuning for the cascaded controller, respectively.

This chapter aims at introducing the used dynamical system with contact as well as the RTHS setup at the Chair of Applied Mechanics, Technical University of Munich. The research in Part I deals with the method development for the actuator dynamics compensation for RTHS with contact. Even though the vision at the Chair of Applied Mechanics is to test prosthetic feet using RTHS, such a complex RTHS setup would not be suitable for basic research in this field. Hence, the investigations in this part are performed with a one-dimensional system. This choice is based on the thought that if observable (dynamic) effects or anomalies cannot be explained for a simple dynamical system, the study of a more complex RTHS system is not viable.

4.1 Dynamical System with Contact

The following requirements are set for the choice of the academic dynamical system used in this part:

- **Availability of reference solution:** To validate the efficacy of the proposed methods, a reference solution needs to be available (see section 2.3).
- **Simple:** This requirement relates to the idea that all effects should be explainable. Even though many real-world contact phenomena are three-dimensional, the choice is a one-dimensional dynamical system with one interface DoF. The advantage is that simple computational methods exist for one-dimensional contact (perpendicular to contact surface) and thus a reference solution can be obtained. Furthermore, one-dimensional contact already offers the investigation of changing dynamics. In the future, it is intended to investigate the presented methods for three-dimensional contact tasks and to include i.a. friction and stick-slip effects.
- **Relation to prosthetic feet:** Our vision is to set up an RTHS test for prosthetic feet, which is a highly complex intention. Albeit strongly simplified, this idea should be integrated in the choice of the dynamical system. This also implies that the contact stiffness should be in a similar range as for the contact between a prosthetic foot and

the ground. The ground can be assumed to be rigid, i.e. the contacting environment is stiff compared to the test component[1].

- **Possibility of modification:** The efficacy (tracking accuracy and robustness) of control schemes is only given if they work for different dynamical system properties, such as RTHS setups with different sensitivities and stability margins. Therefore, the dynamical system should be easily modifiable such that e.g. the case of low damping can be investigated.

4.1.1 Geometry of the Dynamical System and RTHS Split

The one-dimensional mass-spring-damper (MSD) system illustrated in fig. 4.1 fulfills the defined requirements. In this system, the upper suspension performs a cosine trajectory $z_\mathrm{d}/\dot{z}_\mathrm{d}$ such that the lower mass contacts the ground intermittently. The whole motion is characterized by the alternating *flight phase* and *contact phase* (from touch-down until lift-off). The magnitude of the cosine trajectory is $\frac{h_0+\Delta z_\mathrm{max}}{2}$, where h_0 is the maximum distance between the lower mass and the ground, Δz_max is a scalar value and the frequency in Hertz is given by f_d.

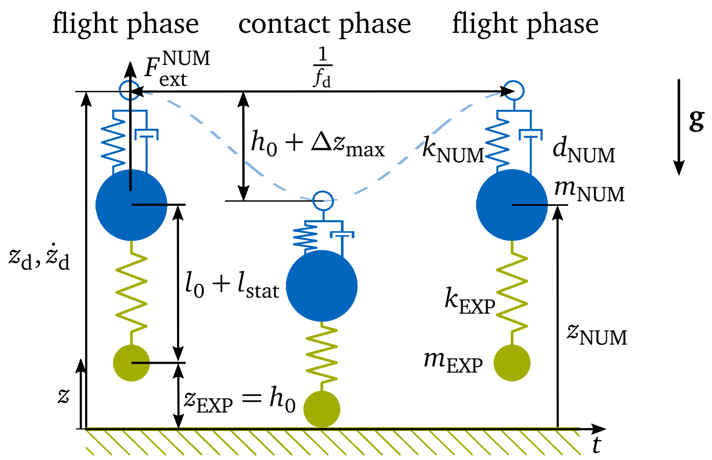

Figure 4.1: Dynamical reference system, which was investigated using RTHS. The upper mass, the suspension and the spring-damper-element form the numerical part (blue). The experimental part is formed by the spring between the masses, the lower mass and the ground. Adapted from [108].

The dynamical system needs to be split into a numerically simulated and an experimentally tested part for the application of RTHS. Regarding the goal of this study and the later application to more complex dynamical systems, the contact scenario is tested experimentally, here. The experimental part (green in the figure) comprises the lower spring and mass (k_EXP, m_EXP) as well as the ground. The remaining system, which consists of the upper MSD system (m_NUM, k_NUM and d_NUM) and the moving suspension (z_d, $\dot{z}_\mathrm{d}$) forms the numerical part (in blue)[2]. Initially, the system is at rest with the upper mass being at a height of $z_\mathrm{NUM} = h_0+l_0+l_\mathrm{stat}$ (size of the masses neglected, l_0 resting spring length), where $l_\mathrm{stat} = \frac{m_\mathrm{EXP}\cdot g}{k_\mathrm{EXP}}$ is the static deflection of the lower spring due to the gravitational forces. The dimensions of

[1]Obviously, amputees do not only walk on flat and rigid ground, but also e.g. on sand, gravel, mats, stairs and ramps. This kind of complexity can be added in future research when the RTHS test case of walking on even and solid ground works reliably.

[2]Note that the discontinuity, i.e. the change of system equations, occurs in the experimental part and not in the numerical part. Therefore, there is no need to deal with any discontinuities of the system equations in the numerical simulation. The contact event will only change the input force to the numerical simulation discontinuously, which does not destabilize the numerical simulation.

the numerically simulated part are irrelevant to the dynamics and are thus not specified. Furthermore, there is a constant external force $F_{\text{ext}}^{\text{NUM}} = (m_{\text{NUM}} + m_{\text{EXP}}) \cdot g$ acting on the numerical mass. The ground exerts an external force $F_{\text{ext}}^{\text{EXP}}$ on the experimental mass during contact.

Biomechanical Motivation

The numerical subsystem can also be interpreted as a mass following the prescribed trajectory according to a proportional-derivative (PD) control law. This is because the proportional part acts on position errors $z_{\text{d}} - z_{\text{NUM}}$ (counterpart spring) and the derivative part on velocity errors $\dot{z}_{\text{d}} - \dot{z}_{\text{NUM}}$ (counterpart damper). In humanoid robotics, the center of mass (CoM) trajectory is often prescribed and controlled with a PD controller to achieve the walking pattern [236]. Thus, in a very simplified representation, a walking human can be illustrated as in the dynamical system in fig. 4.1. In this case, the upper MSD system represents the human with all masses concentrated in the CoM and the lower mass-spring-system contacting the ground imitates the prosthetic foot.

4.1.2 Dynamical Properties

Part of the objective is to develop a control scheme that is robust and thus able to stably perform RTHS tests. For example, RTHS setups that have only little damping or that are unfavorably partitioned possess a small stability margin and are hence extremely sensitive to smallest uncompensated actuator dynamics [77, 137]. For this purpose, two different parameter sets are sought, where one has a small stability margin (highly sensitive) and one that is more robust and permits larger delays.

For the presented dynamical system, the dynamic interaction between the numerical and experimental part is a lot stronger during the contact phase (larger interface forces F_{int}) than during the flight phase. Hence, the contact phase is more critical regarding test stability and is considered for the stability analysis. Here, the concept of stability margin presented in section 2.2 is used. The analysis makes use of the assumption that, during the contact phase, the mass m_{EXP} does not move ($z_{\text{EXP}} = \dot{z}_{\text{EXP}} = \ddot{z}_{\text{EXP}} = 0$). The open loop transfer function of the dynamical system in the RTHS setup writes $F_o(s) = \frac{F_{\text{m}}(s)}{F_{\text{int}}} = \frac{k_{\text{EXP}}}{m_{\text{NUM}} s^2 + d_{\text{NUM}} s + k_{\text{NUM}}}$. The frequency response of the open loop transfer function $F_o(s)$ is obtained by setting the Laplace variable $s = j\omega$ and can be seen in fig. 4.2. The specific parameter values are given in table A.2 in the appendix. While the system with higher damping ($d_{\text{NUM}} = 200\,\text{kg/s}$) has a stability margin of 62°, which corresponds to a critical delay value of $\tau_{\text{crit}} = 0.0284\,\text{s}$, the RTHS setup with lower damping ($d_{\text{NUM}} = 50\,\text{kg/s}$) requires tight actuator tracking as the critical delay value is $\tau_{\text{crit}} = 0.0058\,\text{s}$.

In general, an RTHS test has a QoI (cf. definition on p. 12). For the presented dynamical system, the displacement of the interface z_{NUM} is selected to be the QoI. Hence, for this specific example, the actuator command is $z = z_{\text{NUM}}$ and the RTHS result is equal to the achieved interface displacement, i.e. $z' = z'_{\text{NUM}}$.

4.2 Physical Setup

The whole physical test setup includes the transfer system and the experimental part. The transfer system itself is composed of an actuator, a force/torque sensor (FTS), an encoder and a Digital Signal Processor (DSP). The mass-spring system and the ground form the experimental part. The respective components are described next. The transfer system components are shown in fig. 4.3.

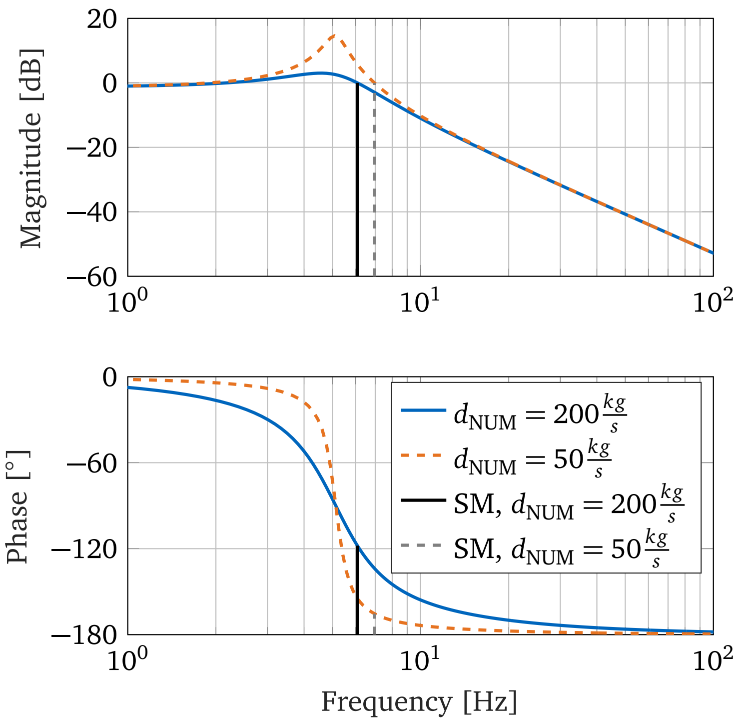

Figure 4.2: Bode diagram of the open loop transfer function. The influence of the damping parameter d_{NUM} on the stability margin of the closed loop RTHS test can be analyzed with this Bode diagram. The vertical lines indicate the construction of the stability margin (SM).

4.2.1 Stewart Platform

In this work, an in-house built *Stewart Platform* (also called *Gough-Stewart Platform* or *Hexapod*) is used as an actuator [84, 211]. Originally, it was built at the University of Duisburg-Essen and set up in the 2000s at the Technical University of Munich by Riebe [183]. Stewart Platforms consist of six actuated legs that connect a (usually) fixed base plate and an upper plate. The legs are connected via universal joints to the upper and lower platform. The tool center point (TCP), which is attached to the upper platform, can be moved along three translational (X, Y, Z) and three rotational (Φ, Θ, Ψ) DoFs by actuation of the legs. Due to the closed loop kinematic chain between the lower platform and the upper motion platform, Stewart Platforms belong to the class of parallel manipulators (in contrast to serial manipulators). Advantages of parallel manipulators include a high load capacity, high rigidity and relating thereto high positioning accuracy and high achievable dynamics. A downside is the limited workspace in contrast to serial robots. [174, 204]

Each leg of the Stewart Platform[3] used is driven by an electric motor (G423-414, MOOG GmbH, Germany) with a servo amplifier (L180-310A-A2, MOOG GmbH, Germany) [147, 148]. The motors are connected to a spindle drive by belts. The spindle rotation changes the respective leg length. The Stewart Platform is controlled with a decentralized cascaded controller, i.e. each leg is controlled individually [183]. The basic control principle is visualized in fig. 4.4. Therefore, the motion command for the TCP (work space coordinates $\boldsymbol{X} = \{X, Y, Z, \Phi, \Theta, \Psi\}$) needs to be transformed to the individual leg commands (joint space coordinates) by an inverse kinematics module. The length of leg i, where $i = 1...6$, is denoted by b_i. Cascaded control schemes are commonly used to control electric motors [215]. The whole controller consists of three cascaded control loops, where the dynamics of the inner

[3]The height of the Stewart Platform in the depicted configuration is about 0.7 m.

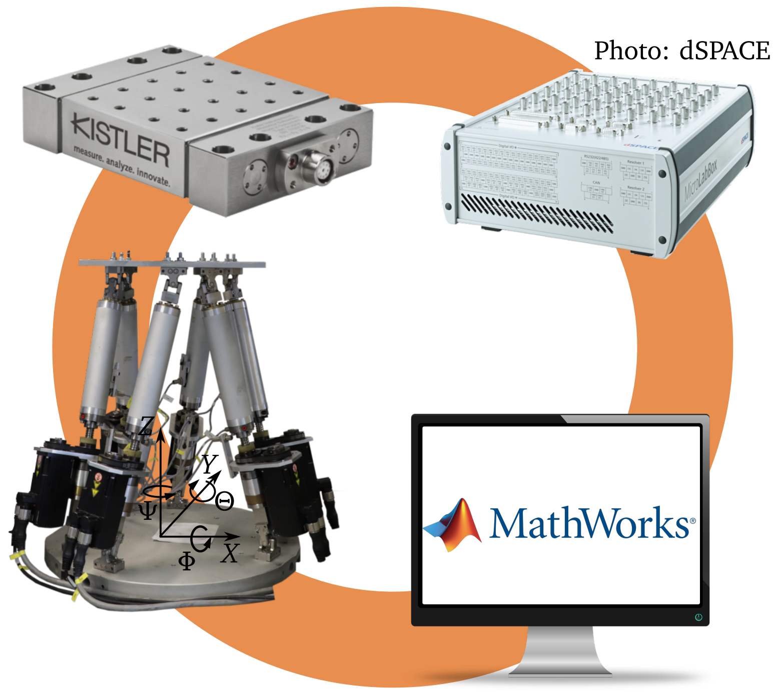

Figure 4.3: In this RTHS setup, the transfer system consists of a Stewart Platform as actuator and a Kistler Multicomponent Dynamometer as FTS. Furthermore, the real-time application is realized with a MicroLabBox from dSPACE (©Copyright 2020: dSPACE GmbH) and MATLAB®/Simulink®(version 2016b, The MathWorks Inc., USA).

loops are faster. The innermost loop is a current controller with transfer function G_i that is implemented on the servo amplifiers. This is a proportional-integral (PI) controller. Due to the high sampling rate and the lack of accessibility of the signals, the assumption $G_\mathrm{i} \approx 1$ is taken. The middle loop is a velocity controller, which is a proportional-integral (PI) controller with transfer function G_v. The position errors are controlled by a proportional (P) controller with transfer function G_p in the outermost loop. The real achieved displacement $\boldsymbol{X}'$ results from the dynamics of the actuators $\hat{P}_i$ and the kinematics (denoted by *Direct Kinematics* in the figure). In this control approach, any coupling between legs or friction forces are considered as disturbances. The controller parameters are summarized in appendix A and an applicable tuning procedure is described in [183].

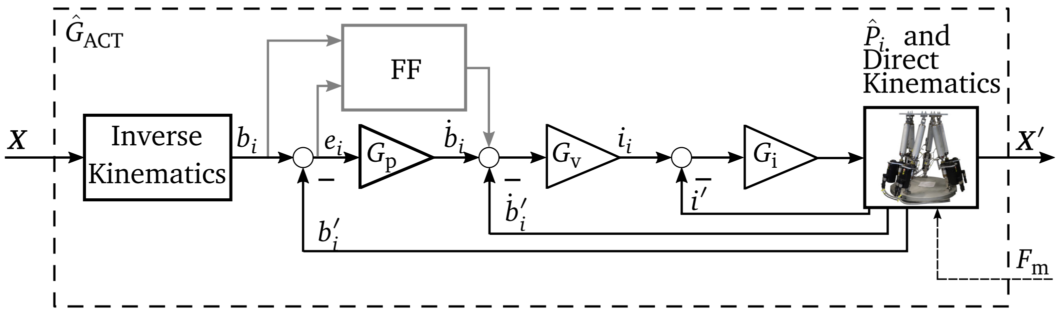

Figure 4.4: The Stewart Platform is controlled with a decentralized cascaded controller for current, velocity and position. External forces acting on the Stewart Platform are denoted by F_m.

The cascaded control scheme is a feedback control scheme and can be extended by a feedforward (FF) controller for improved command input response. The input of an FF controller can either be the desired leg position b_i ($i = 1...6$) or the position error $e_i = b_i - b'_i$. The FF signal can be injected on velocity level, as shown in fig. 4.4, on current level (after G_v) or on position level (before G_p). If not indicated otherwise, the FF signal is injected on velocity level in this work. A simple but effective implementation of an FF controller is called *velocity feedforward (VFF)* [214]. Here, the FF input is the desired leg position and the FF block contains a time derivative. Therefore, the output of the position controller G_p is enhanced by the desired leg velocity.

For details about the implemented safety features and kinematic relations (direct and inverse kinematics) the interested reader is referred to [174, 194]. The above implementation assumes that the motion from the electric motors is directly transmitted to the TCP position/orientation $\boldsymbol{X}'$ without any backlash of the belt, spindle drive or the universal joints. The validity of this assumption was investigated in this work using externally mounted eddy current sensors that measured the motion of the upper plate. These measurements were compared to the results from direct kinematics using the encoder measurements from the motors. Since the results match well, the backlash is negligible.

4.2.2 Force/Torque Sensor and Encoders

A further important component in the measurement chain is the FTS. For all experiments presented in this thesis, a Multicomponent Dynamometer (Type 9129AA, Kistler Instrumente AG, Switzerland) is used in conjunction with a charge amplifier (Type 5080A, Kistler Instrumente AG, Switzerland) [117]. It includes four three-component force sensors that are built of quartz and possess piezoelectric properties, which means that they respond to loads by measurable electrical charges. All measured signals are processed and the resulting forces/moments (six DoFs) can be tapped from the charge amplifier. Due to the measuring principle, such FTSs are well suited to measure highly dynamic processes, but measuring of constant loads is limited. The dynamic behavior of the FTS was identified using the data acquisition system Siemens Simcenter SCADAS Mobile and impact hammer measurements. The results can be seen in appendix B and summarized as follows: the magnitude and phase response show ideal transfer behavior in the frequency range of interest (up to 1000 Hz), i.e. $\hat{G}_{\text{FTS}} = 1$ is assumed for the remainder of the thesis.

Resolvers are used (G3L15, MOOG GmbH, Germany) to measure the angle of each electric motor. These measurements and the transmission ratio of the spindle drive to the leg stroke (5 mm stroke per revolution) yield the actuator lengths b'_i ($i = 1...6$). The resolvers have a resolution of 2048 pulses per revolution. Converted with the transmission ratio of the spindle drive to the leg stroke, the resolution is 2.4 μm [183]. Using direct kinematics, the translations and orientations of the upper plate, i.e. at the TCP, are determined.

4.2.3 Digital Signal Processor

The real-time application is operated from a host PC (operating system *Windows 10*), where the numerical simulation and implementation of the control are done using MATLAB®/Simulink® (version R2016b, The MathWorks Inc., USA). A MicroLabBox dS1202 from dSPACE is used as DSP and controlled from the host PC via ControlDesk® (version 6.0). Based on the dynamic specifications of the DSP, the internal dynamics are much faster than the investigated process (e.g. ΔT or the dynamics of the controlled Stewart Platform), and the assumption is taken that no time lag (D/A or A/D conversion) or dynamics of the dSPACE platform have to be considered.

4.2.4 Full Experimental Setup

The full RTHS setup for the dynamical system presented in section 4.1 is shown in fig. 4.5. The setup comprises the numerical simulation (NUM), the transfer system with the parts presented in section 4.2.1, section 4.2.2 and section 4.2.3 as well as the experimental spring-mass system (EXP). The experimental part consists of a 3D printed plastic (PLA) half sphere, a compression spring (type VD-319 [87]) and an aluminum plate ("ground").

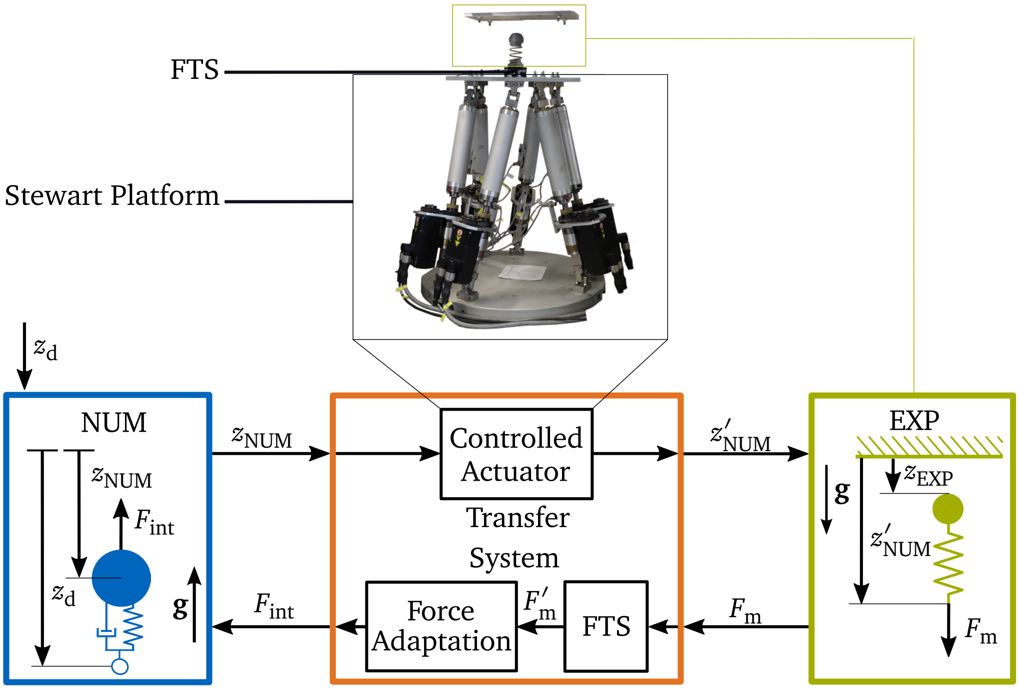

Figure 4.5: The used experimental setup for the RTHS tests. For the sake of simplicity, the inverse and direct kinematics block are omitted in the figure. Adapted from [108].

Compared to fig. 4.1, the experimental part is mounted upside down on the Stewart Platform. This is because it is easier to compensate the measured forces than turning the Stewart Platform upside down (e.g. mounting on a stiff frame): the gravitational effects are compensated by adapting the measured force by $F_{\text{int}} = F'_{\text{m}} + 2 \cdot m_{\text{EXP}} \cdot g$. Before an experiment is conducted, the experimental mass is brought to the position $z_{\text{EXP}} = h_0$. Because of the linear displacement-force-characteristics of the used compression spring, the measured forces during the test are the same as if the experimental part was hanging.[4] Since the measurement noise is higher than the inertia forces of the experimental part during the flight phase, the force is only measured when contact is detected and else set to $F_{\text{int}} = m_{\text{EXP}} \cdot g$.

4.3 Digital Twin: Virtual RTHS Setup

To set up a safe test environment for the method development, the full experimental RTHS setup is simulated. Performing purely simulated RTHS tests, i.e. where the transfer system and the experimental part are also simulated, is called *virtual RTHS* or *vRTHS*. For that purpose, a system identification of all involved parts has to be performed.

[4] This statement holds if bending of the spring can be neglected.

4.3.1 System Identification of the Transfer System

The dynamics of the transfer system are dominantly determined by the controlled Stewart Platform and the dynamics of the FTS and the DSP can be neglected, as outlined in section 4.2.2 and section 4.2.3. A transfer function model P_i of each leg $i = 1...6$ (true dynamic behavior $\hat{P}_i$) needs to be found.

The block diagram in fig. 4.6 illustrates the system identification procedure of the Stewart Platform. The system identification of an actuator can either be performed open- or closed loop, i.e. with the feedback controller switched off or on. Here, a closed loop approach is pursued because open loop identification should only be used for stable systems. Note that, even though the feedback controller is active, just the transfer behavior of the legs P_i is identified if the correlation between the excitation signal and the plant output is high. As a rule of thumb, the coherence must be $> 75\,\%$. Next, the excitation signal must be chosen and possible choices are e.g. Gaussian white noise, pseudo random signals, sine sweep/chirp signals and segmented multi-sine. The excitation must be able to excite all frequencies of interest sufficiently. [129]

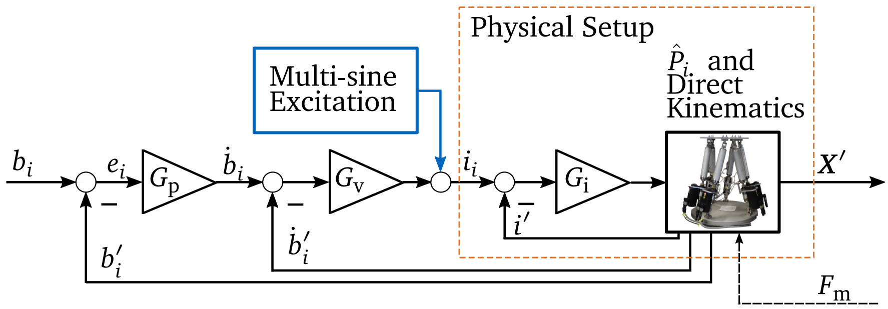

Figure 4.6: The system identification of the Stewart Platform was performed with a multi-sine signal injected on current level.

In this work, a segmented multi-sine signal was selected, which is a signal composed of multiple sine signals with different frequencies. The advantage compared to a sine sweep, for example, is that individual frequencies are excited for a longer time duration [129]. The whole frequency range of interest was divided into frequency bands and the system identification was performed for each of the frequency bands. Here, the frequency range of interest was up to 100 Hz. The frequency spacing was 0.5 Hz and the frequency band was split into 10 smaller bands, i.e. $[0.5, 10], [10.5, 20], ..., [90.5, 100]$ Hz. The signal was injected behind the velocity controller G_v, which is the closest accessible position to the Stewart Platform. Following the reasoning in section 4.2.1, the dynamics of the current controller are neglected ($G_i \approx 1$). The transfer behavior of each leg $i = 1...6$ writes

$$\hat{P}_i = \hat{P}_i(s) = \frac{B'_i(s)}{I(s)}, \tag{4.1}$$

with $B'_i(s)$ and $I_i(s)$ being the frequency domain representations of b'_i and i_i. The Laplace variable is denoted by s (frequency response $s = j\omega$). The measurements for the six legs were performed subsequently and each 10 Hz-band was excited for 200 s.

The measured transfer function $\hat{P}_i$ and the approximation P_i from motor current to leg length are shown representatively for one leg in fig. 4.7. Similar dynamic behavior can be observed for the other legs. When approximating a measured transfer function, the degree (number of zeros and poles) has to be defined. For the measured frequency range (up to

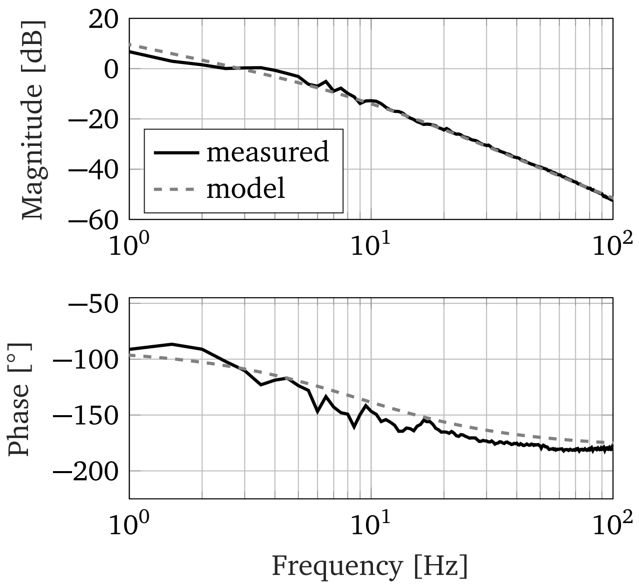

Figure 4.7: The measured transfer function (black, solid line) and the approximated transfer function (gray, dashed line) from motor current to leg length are shown for leg $i = 2$.

100 Hz), the dynamic behavior of the Stewart Platform used is approximated with

$$\hat{P}_i(s) \approx P_i(s) = \frac{k_i}{s \cdot (T_i \cdot s + 1)} = \frac{k_i \cdot \omega_{c,i}}{s \cdot (s + \omega_{c,i})}\ \text{, with}\ \ \omega_{c,i} = \frac{1}{T_i}. \tag{4.2}$$

Viewing this transfer function from a mechanical perspective, this implies that the Stewart Platform resembles a mass-damper system[5]. This interpretation is reasonable because the Stewart Platform possesses a high mass that is pushed by the motor torques (inertia part) and is highly damped (friction, ...). In the considered frequency range, no further dynamics such as the eigenfrequencies of the electric loops (e.g. current control) take effect, as these are high frequency dynamics. The identified transfer functions are listed in table 4.1 for each leg $i = 1...6$. The identified transfer functions can be used for system theoretical investigations

Table 4.1: Summary of the leg transfer functions from motor current to leg length of the Stewart Platform $i = 1...6$.

	$i=1$	$i=2$	$i=3$	$i=4$	$i=5$	$i=6$
P_i	$\frac{1011}{s\cdot(s+122.9)}$	$\frac{1053.1}{s\cdot(s+55.5)}$	$\frac{1123.5}{s\cdot(s+54.7)}$	$\frac{780.9}{s\cdot(s+55.3)}$	$\frac{988.1}{s\cdot(s+66.2)}$	$\frac{1070.9}{s\cdot(s+59)}$

and vRTHS simulations. When using these transfer functions, one has to keep the following limitations in mind:

- Friction is not considered and not identified but rather approximated by viscous damping [183].
- The given transfer functions are linear and any kind of nonlinearity is not considered.
- The influence of external forces (F_m) on the displacement b_i' and the damping is neglected.

[5]The inertia of a mass is proportional to the acceleration, i.e. s^2 in the Laplace domain, and damping forces are proportional to the velocity (s).

- Due to the closed kinematic chain of the Stewart Platform, there is coupling between the legs. This coupling is not considered, neither in the control nor in the identification of the transfer behavior. This assumption is approximately valid since this Stewart Platform is designed for minimum dynamic coupling (arrangement of actuators) [183].
- The system dynamics have only been identified in a frequency range up to 100 Hz. Hence, any effects with higher frequency content should not be interpreted.

4.3.2 System Identification of the Experimental Part

To simulate the experimental part for the vRTHS simulation, the dynamic behavior must be identified. The experimental part consists of a spring [87], a mass and the ground. As the true spring stiffness can differ from that given in the data sheet, a quasi-static identification was performed. The experimental part was mounted on the Stewart Platform and deformed in steps of 0.1 mm. This test revealed that the behavior is linear in the considered frequency range with a spring constant of $k_{\mathrm{EXP}} = 8650\,\mathrm{N/m}$. The mass of the experimental part (spring, mounting and half sphere) is $m_{\mathrm{EXP}} = 0.38\,\mathrm{kg}$. The model includes the following assumptions:

- There is no damping in the experimental part.
- The mass of the experimental part is concentrated in the center of the half sphere.
- The spring is linear and has the same static and dynamic spring stiffness. Due to the linear elastic behavior, the static deflection l_{stat} is negligible.
- There is no friction present between the mounting and the spring. This is ensured by the mounting that has as little contact surface with the spring as possible.
- The spring is only axially deformed and there is no bending. This assumption is valid following video recordings with a high-speed camera.

Contact Modeling

In addition to the dynamic properties of the experimental part itself, the impact-contact scenario needs to be modeled to set up the digital twin. Two possibilities to solve the discontinuous dynamics are the penalty method and the conservation of momentum in combination with the coefficient of restitution (CoR).

In the penalty method, the ground is modeled using a spring-damper element exerting forces on the mass acting against the penetration. For the investigated case, the ground stiffness is set to $10^9\,\mathrm{N/m}$ and the damping to $500\,\mathrm{kg/s}$. The magnitude of the stiffness is based on the Young's modulus of aluminum. The damping value is tuned such that the experimental mass comes to rest on the ground after a short time, which corresponds to the observations with the high-speed camera. In the second approach, the conservation of momentum equation is solved at the instant of impact. The CoR is set to 0, which corresponds to a perfectly inelastic impact, and 0.73, which is a typical value for the impact between plastic and aluminum.

Figure 4.8 shows the results of a vRTHS test using these different methods for contact modeling. In particular, the simulated displacement z_{NUM} of the numerical mass is visualized. Contact occurs at $\approx 1\,\mathrm{s}$ and the transition from the contact to the flight phase at $\approx 3\,\mathrm{s}$. All simulation approaches show good agreement and reveal that the momentum of the experimental mass is very small and the impact on the numerical part little. High-speed camera measurements of the experimental impact-contact scenario show that the experimental mass m_{EXP} sticks to the ground immediately after the first impact. This fosters the statement that

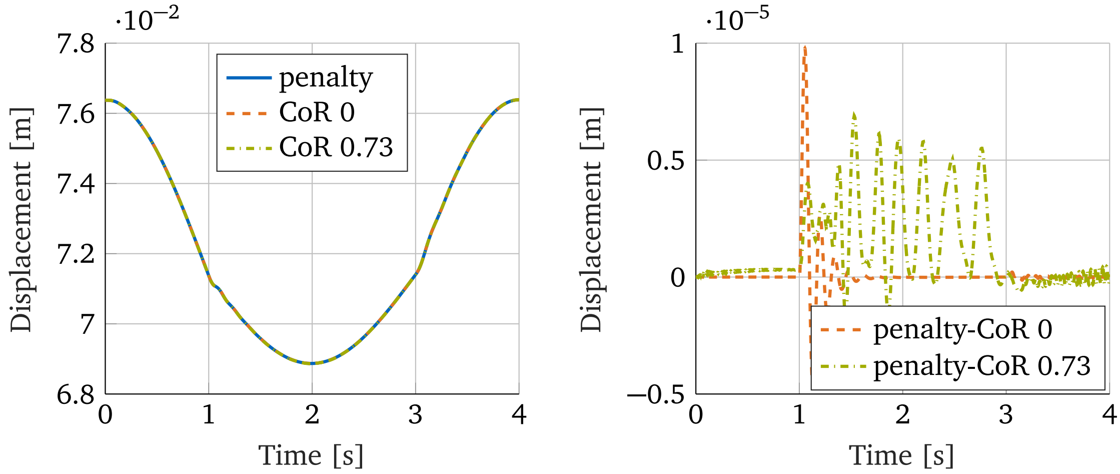

(a) The penalty method (blue, solid line) and the conservation of momentum with a CoR of 0 (orange, dashed line) and 0.73 (green, dash-dotted line) are used.

(b) The differences between the solutions z_{NUM} of the penalty method and the conservation of momentum with CoR of 0 (orange, dashed line) and the difference between the penalty method and the conservation of momentum with CoR 0.73 are shown.

Figure 4.8: Comparison of different modeling strategies to calculate the impact-contact scenario of the dynamical system (fig. 4.1). The parameters are given as stated in table A.2, where $h_0 = 0.005\,\text{m}$ and $d_{\text{NUM}} = 150\,\text{kg/s}$ were used.

the spring forces of k_{EXP} pushing the mass on the ground are larger than the (change of) momentum of the experimental mass due to impact that rebounds the mass.

The digital twin of the RTHS setup presented in this section was used for first investigations of the control schemes presented in Part I and also in Part II. Using this vRTHS simulation, different approaches can be implemented and tested in a safe environment before they are applied to the real RTHS test. In general, the results of the vRTHS tests correspond well to the real RTHS tests. Therefore, if not indicated otherwise, only the results from the real RTHS tests are shown.

4.4 Measures for the Success of the RTHS Test

In this part, the intention is to improve the actuator tracking performance and investigate the influence on the test fidelity. To evaluate and compare different actuator control schemes, measures are needed to quantify the remaining errors.

The actuator tracking performance measures the difference between the commanded and real achieved displacement, i.e.

$$e_{\text{track}} = z_{\text{NUM}} - z'_{\text{NUM}} \tag{4.3}$$

for the given application. The relative root-mean-square (RMS) tracking error is defined as

$$e_{\text{track,rel}} = \frac{RMS(z_{\text{NUM}} - z'_{\text{NUM}})}{MAX\left(|z_{\text{NUM}}|\right)}. \tag{4.4}$$

The RMS value of a variable ξ is defined as $RMS(\xi) = \sqrt{\frac{1}{n_t}\sum_{i=1}^{n_t}(\xi(k))^2}$, where $\xi(k)$ denotes the value at time step t_k. In eq. (4.4), the RMS error is normalized by the maximum absolute value of the displacement command. A common assumption is that a better tracking performance leads to a better fulfillment of the compatibility condition and thus higher fidelity.

Reference Solution of the Investigated Dynamical System
To measure the fidelity, a similar measure is set up using the reference solution of the QoI, which is the displacement of the numerical mass. In this work, the reference solution $z^{\mathrm{r}}_{\mathrm{NUM}}$ is obtained from a pure numerical simulation of the overall dynamical system[6]. The numerical simulation uses the dynamic parameters identified in section 4.3.2 (dynamics of transfer system ideal) and the penalty method for contact-impact simulation. Since the force measurement is deactivated during the flight phases in the real RTHS setup, this is also done in the reference simulation. This means that the dynamic interaction between the numerical and experimental part is not considered during the flight phase. In particular, this means that the oscillation of the experimental mass after lift-off is neglected (no damping in the experimental part).

Similar to eq. (4.3), the reference error between the RTHS test and the reference solution writes

$$e_{\mathrm{ref}} = z^{\mathrm{r}}_{\mathrm{NUM}} - z'_{\mathrm{NUM}} \tag{4.5}$$

and the relative RMS reference error is defined as

$$e_{\mathrm{ref,rel}} = \frac{RMS(z^{\mathrm{r}}_{\mathrm{NUM}} - z'_{\mathrm{NUM}})}{MAX\left(|z^{\mathrm{r}}_{\mathrm{NUM}}|\right)}. \tag{4.6}$$

The smaller the reference error, the higher the fidelity.

These accuracy measures are used throughout Part I. In Part II, further measures are explained and used for the accuracy assessment of RTHS tests.

[6]A discussion of the reference solution is described in section 2.3

Chapter 5

Test Stability and Robustness

This chapter is partly based on the author's publications [104, 108]. The software implementation of the NPC scheme has been performed in the semester thesis by Doris Zhou and fine tuned by Arian Kist. The measurements shown in this chapter have been performed by Arian Kist as research assistant.

The objective of Part I is to develop an actuator control scheme that enables stable and high fidelity RTHS tests of dynamical systems with contact. This chapter focuses on test stability. In particular, passivity-based control is presented to increase test robustness (cf. definition on p. 10), i.e. maintain test stability also if unpredictable disturbances occur. For this purpose, the notion of RTHS stability is set up based on the consideration of energy/power flow in the RTHS setup. After that, passivity-based control schemes, especially Normalized Passivity Control (NPC), are introduced and the applicability to RTHS with contact investigated.

5.1 Energy and Power Flow

Whenever components dynamically interact with each other, they exchange energy. For example, when thinking of substructures A and B (as in section 2.4.1), energy can be transferred from A to B and vice versa while the overall energy of the dynamical system (A and B together) remains constant[1]. In the presence of transfer system dynamics (substructure C), i.e. when the compatibility and/or equilibrium conditions are violated, the energy transfer between the substructures is impaired and energy is either generated or dissipated. One of the key questions in RTHS is how to determine the test stability of an ongoing[2] RTHS test. The system energy of an RTHS setup is an appropriate indicator for test stability (see the concept of passivity in section 3.3.2). Following the definition of Galmez and Fermandois [75], the energy of the coupled system increases exponentially in case of instability. The power flow of an RTHS setup is depicted in fig. 5.1. The energy of the numerical part (kinetic and potential energy) changes due to work done by external forces, which is denoted by the external power $P_{\mathrm{ext}}^{\mathrm{NUM}}$. Furthermore, energy dissipation occurs due to mechanical effects such as friction and damping and also if the used time integration scheme is not energy conserving. The dissipated power is denoted by $P_{\mathrm{diss}}^{\mathrm{NUM}}$. Lastly, there is a power exchange between the numerical part with the transfer system due to the interface forces and velocities $P^{\mathrm{NUM\text{-}TS}}$.

[1]The energy of the coupled dynamical system remains constant if there are no external forces or energy dissipation (friction, damping, ...).

[2]Offline stability indicators are briefly outlined in section 2.2.

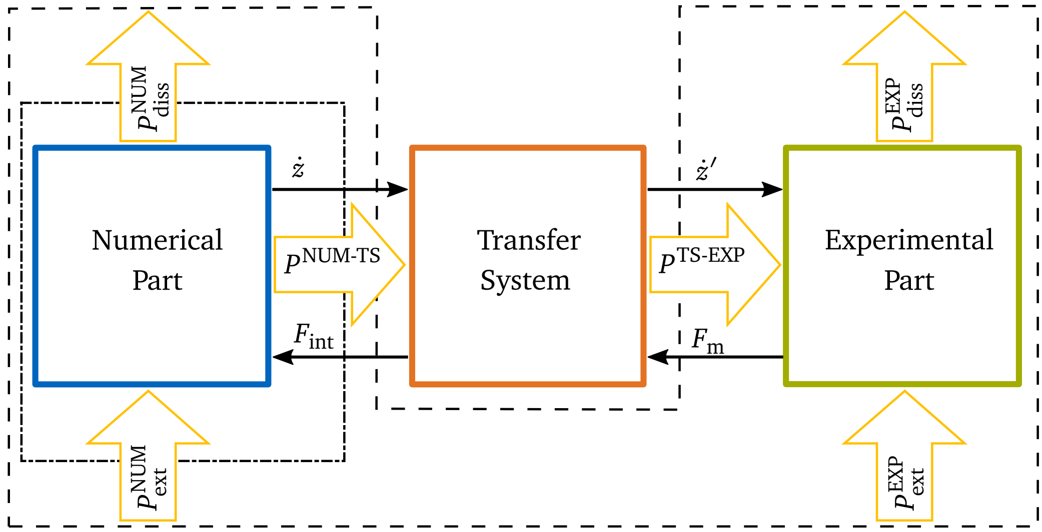

Figure 5.1: Power exchange in RTHS between the numerical part, the transfer system and the experimental part. For energy considerations of an RTHS setup, either the dashed system boundary (coupled system) or the dash-dotted system boundary (numerical part) can be taken.

The energy of the experimental part, in turn, changes by the power input from the transfer system and the external forces $\left(P^{\text{TS-EXP}}\right.$ and $\left.P^{\text{EXP}}_{\text{ext}}\right)$ and mechanical power dissipation $\left(P^{\text{EXP}}_{\text{diss}}\right)$.[3] While the energy of the numerical part can be calculated at each time step, the energy of the experimental part is generally not available. Passivity-based control schemes dissipate energy when the passivity condition is violated, i.e. an energy increase of the system is detected (cf. definition on p. 24). In RTHS, two different system considerations can be pursued to determine the RTHS test stability, namely observing (i) the energy of the numerical part (dash-dotted system boundary in fig. 5.1) or (ii) the energy of the coupled dynamical system (dashed system boundary).

The energy balance of the numerical part (i) is observed in the publications by [53, 75]. Following these considerations, the test stability is jeopardized when the energy in the numerical part increases more than the energy input by the external force. De Stefano et al. [53] propose the use of a passivity-based controller to dissipate the amount of energy by which the energy of the numerical part increased. The approach by Galmez and Fermandois [75] is more conservative and suggests that energy dissipation is not necessary until the energy increase also surpasses the amount of dissipated energy $\left(\int P^{\text{NUM}}_{\text{diss}}\right)$.

The second approach (ii), which considers the coupled dynamical system, is i.a. used in [119, 171]. Here, the difference between the power flowing from the numerical part to the transfer system $\left(P^{\text{NUM-TS}}\right)$ and the power flowing from the transfer system into the experimental part $\left(P^{\text{TS-EXP}}\right)$ are observed.[4] Any difference between these power flows changes the energy of the coupled system. In this consideration, a passivity-based control scheme interferes if $P^{\text{TS-EXP}} > P^{\text{NUM-TS}}$. Using these system boundaries can also be seen as monitoring the energy flow through the transfer system. If the transfer system outputs more energy than was supplied to it (and initially stored), energy is introduced and the passivity constraint violated.

In comparison, both viewpoints have their advantages and disadvantages. Approach (i) is able to include energy dissipation/generation due to numerical time integration. However, only the numerical part is considered and an energy increase of the experimental part and

[3] In the special case when an active component such as e.g. an active vibration controller is tested as hardware, the energy of the experimental part also changes. Nevertheless, an energy increase due to the investigated dynamical system does not influence the RTHS test stability.

[4] Note that the quantities $P^{\text{NUM-TS}}$ and $P^{\text{TS-EXP}}$ can be positive or negative, depending on the net power flow.

thus the coupled dynamical system is unobservable. Approach (ii), in turn, considers the energy of the coupled dynamical system and detects any energy increase due to transfer system dynamics. Energy increase due to external forcing or numerical time integration is not determined here. Hence, only an energy increase is detected with approach (ii), but not whether the test really becomes unstable.

As outlined in section 2.2.2, the effects of a mass vs. stiffness experimental part are different in the presence of delay. The general tendency is that increased experimental stiffness and decreased experimental mass lead to test instability. This is also visible when looking at the system energy. For a system with only a mass in the experimental part, $P^{\text{NUM-TS}} > P^{\text{TS-EXP}}$ can be observed in the presence of delay. In contrast, $P^{\text{NUM-TS}} < P^{\text{TS-EXP}}$ in case of a stiffness experimental part.

5.2 Passivity Control in RTHS

As briefly introduced in section 3.3.2, the structures of RTHS and teleoperation systems resemble each other. In teleoperation, many different PC schemes have been proposed to stabilize the closed loop system. To name a few examples, there is the scattering and wave variable approach [8, 160], the tele-impedance control [122] and time domain passivity control (TDPC) [89]. To take advantage of the comprehensive research and literature, the application of passivity-based control to RTHS is reasonable. So far, TDPC has been applied to RTHS, which was proposed by Hannaford and Ryu [89] and later improved and extended by Ryu et al. [188, 189]. The algorithm of TDPC comprises a passivity observer (PO) and a passivity controller (PC). The PO monitors the system energy and triggers the PC when energy/power is generated, i.e. the condition of passivity is violated. The PC introduces a variable-rate virtual damper to dissipate the added amount of energy/power. The advantage of TDPC over other passivity-based control schemes is that its efficacy is independent of the real delay and the used model [122]. Commonly, the whole dynamical system can be viewed as multiple subsystems forming a network and exchanging energy/power between them. If all subsystems are passive, they form a passive network. Hence, it is sufficient to ensure passivity of each of the involved subsystems.

Different implementations can be chosen when using TDPC for RTHS. For the PO, the system boundaries have to be selected (see section 5.1) and it has to be chosen whether the energy or the power is monitored. The PC can be implemented in impedance or admittance causality. In impedance causality, the variable-rate virtual damper acts on the measured feedback forces and in admittance causality on the velocity command. A classification of the state-of-the-art implementations depending on the used PO is given in table 5.1.

Table 5.1: Passivity observers in the state-of-the-art implementations of TDPC.

System boundary	Energy	Power
Numerical part (i)	De Stefano et al. [53]	—
Coupled system (ii)	Krenn et al. [118, 119] Peiris et al. [172]	Peiris et al. [171]

Monitoring power errors has the advantages that the PC reacts in a more agile manner and that no integration is necessary to retrieve the energy error from the power error [171, 240]. Hence, in this work, the approach by Peiris et al. [171] is applied. Their approach is called Normalized Passivity Control (NPC) and implements an augmentation of the measured feedback force, i.e. it is in impedance causality. Following the investigations in [118], also the admittance causality proves successful and could be applied.

5.3 Normalized Passivity Control (NPC)

This section presents Normalized Passivity Control (NPC) proposed by Peiris et al. [171]. The main structure of the NPC implementation is visualized in fig. 5.2. In this implemen-

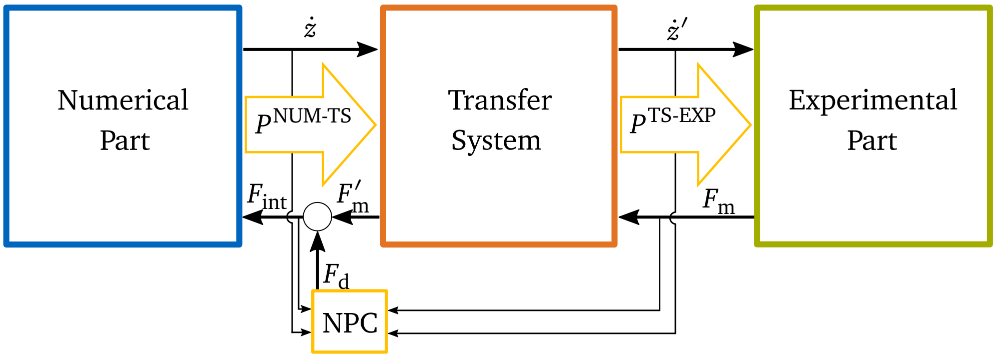

Figure 5.2: NPC monitors the power flow at the two ports of the transfer system and augments the measured force by an additional damping force F_{d} (impedance causality), i.e. $F_{\text{int}} = F'_{\text{m}} + F_{\text{d}}$, in case energy is erroneously added to the coupled system. For the sake of clarity, any further force adaptation and power flows into/out of the numerical and the experimental part are omitted. Figure adapted from [104, 108].

tation, the PO monitors the power flow from the transfer system to the coupled system, i.e. the numerical and experimental part (approach (ii) in section 5.1). Ideally, compatibility and equilibrium are fulfilled at the interface between the numerical and experimental part and $P^{\text{NUM-TS}} = P^{\text{TS-EXP}}$, where

$$P^{\text{NUM-TS}} = F_{\text{int}} \cdot \dot{z} \tag{5.1}$$

$$P^{\text{TS-EXP}} = F_{\text{m}} \cdot \dot{z}' \approx F'_{\text{m}} \cdot \dot{z}'. \tag{5.2}$$

Since the true restoring force F_{m} cannot be determined, the assumption $F'_{\text{m}} = F_{\text{m}}$ has to be made. The energy of the coupled system increases in case $P^{\text{TS-EXP}} > P^{\text{NUM-TS}}$ and the erroneously introduced power can be written as

$$\begin{aligned} P_{\text{error}} &= P^{\text{TS-EXP}} - P^{\text{NUM-TS}} \\ &= F'_{\text{m}} \cdot \dot{z}' - F_{\text{int}} \cdot \dot{z} > 0. \end{aligned} \tag{5.3}$$

The PO triggers the PC, which outputs an additional damping force F_{d} if $P_{\text{error}} > 0$. This damping force is always $F_{\text{d}} > 0\,\text{N}$ and reduces the power error:

$$P_{\text{error}} = F'_{\text{m}} \cdot \dot{z}' - (F'_{\text{m}} + F_{\text{d}}) \cdot \dot{z}. \tag{5.4}$$

The force $F_{\text{int}} = F'_{\text{m}} + F_{\text{d}}$ is used as interface force for the numerical simulation. In NPC, the damping force $F_{\text{d}}(t_k)$ at time step t_k is calculated as:

$$F_{\text{d}}(t_k) = \alpha(t_k) \cdot \dot{z}(t_k) \qquad \text{and} \qquad \alpha(t_k) = G_{\text{P}} \cdot \frac{\tilde{P}_{\text{error}}(t_{k-1})}{|\tilde{P}_{\text{tot}}(t_k)|} \quad \text{if } P_{\text{error}} > 0. \tag{5.5}$$

Here, the time-varying damping constant α is calculated based on the power error normalized by the magnitude of the total power throughput $P_{\text{tot}} = P^{\text{NUM-TS}} + P^{\text{TS-EXP}}$ and a damping scaling value G_{P}. The tilde operator $\tilde{\bullet}$ denotes that the power error and the total power throughput are low-pass filtered to smoothen the force output F_{d}. Without the normalization of P_{error}, the damping force F_{d} is high in experiments with high force/displacement amplitudes and hence leads to over-zealous damping and loss of test fidelity [171].

In general, higher values of the damping scaling value G_P introduce higher damping forces and thus a higher amount of power error can be damped. However, large damping forces also lead to a high distortion (cf. definition on p. 9) of the test results because the equilibrium condition is violated. Hence, the tuning of G_P is a trade-off between stability and fidelity.

The choice of the time constants of the low-pass filters determines the frequencies of the power error that are damped. High values of the low-pass filter imply a low cut-off frequency. This leads to smooth changes of the output force, but decreased responsiveness. The energy excess from frequencies above the cut-off frequency is not damped and must be accounted for later, when they also make lower frequencies unstable. With low time constants (cut-off frequency high), the dissipative force F_d is more volatile with higher magnitudes and a higher responsiveness at the same time.

Advantages of NPC include that only little understanding of the investigated dynamical system is necessary to perform stable tests. Furthermore, NPC only interferes when the transfer system introduces energy and thus RTHS test stability is jeopardized. Since NPC does not include information about the past except for the introduced delay and smoothing by the low-pass filters, the responsiveness is high. High agility is necessary for RTHS with contact, where the system dynamics change rapidly at the instant of impact.

5.4 Application of NPC to RTHS with Contact

The applications in [171] include dynamical systems with continuous dynamics and impacts in the numerical substructure. Hence, the applicability to RTHS with contact (discontinuity in the experimental part) needs to be investigated. For this purpose, the RTHS setup presented in chapter 4 is used.

5.4.1 RTHS Test Stability

The test stability depends on the dynamical properties of the investigated system and the transfer system dynamics. In section 4.1.2, a damping value of $d_{\mathrm{NUM}} = 50\,{}^{\mathrm{kg}}/_{\mathrm{s}}$ was identified to require tight actuator tracking and $d_{\mathrm{NUM}} = 200\,{}^{\mathrm{kg}}/_{\mathrm{s}}$ permits delays up to $0.0284\,\mathrm{s}$. As presented in section 4.2.1, the Stewart Platform used is controlled with a cascaded control scheme and velocity feedforward (VFF) can be activated to improve the tracking performance. RTHS experiments for $d_{\mathrm{NUM}} = 50\,{}^{\mathrm{kg}}/_{\mathrm{s}}$ with and without VFF are illustrated in fig. 5.3 (other parameters as given in table A.2). Note that NPC was switched off. The case of pure feedback control is visualized in fig. 5.3a. Here, the test can be regarded as unstable without NPC because the interface oscillations and the power error grow during the contact phase. Enhancing the feedback controller with VFF, which is shown in fig. 5.3b, leads to a stable RTHS test due to the better actuator tracking performance[5]. The better actuator tracking performance is also visible in the magnitude of the power error, which is much smaller in the RTHS experiment with VFF (note that the axes in the figures without/with VFF are differently scaled). The plots also visualize the active and passive phases during the RTHS tests, i.e. when $P_{\mathrm{error}} > 0$ and $P_{\mathrm{error}} \leq 0$, respectively. As can be seen in the figures, both active and passive phases are present in both RTHS tests, even though the test with VFF would be considered as a stable test from the user view. In case these RTHS tests are enhanced with NPC, additional dissipative forces would be introduced during the active phases.

[5] Test stability without VFF is e.g. given for $d_{\mathrm{NUM}} = 200\,{}^{\mathrm{kg}}/_{\mathrm{s}}$ and test instability with VFF for $d_{\mathrm{NUM}} = 5\,{}^{\mathrm{kg}}/_{\mathrm{s}}$.

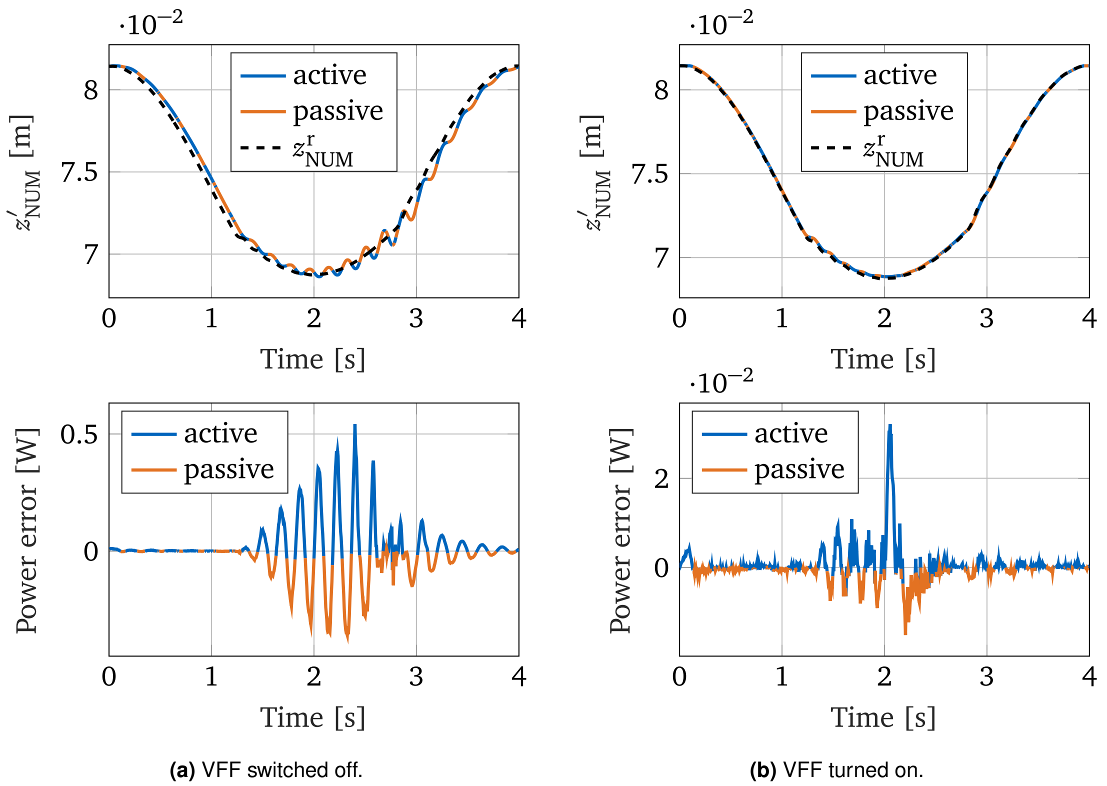

Figure 5.3: The interface displacements and the power errors are shown for RTHS tests with $d_{NUM} = 50\,{}^{kg}/_{s}$. The active phases are visualized in blue and the passive phases in orange.

During the contact phase, which is between the touch-down and the take off, i.e. $t \in [t_{TD}, t_{TO}]$, the amount of introduced energy error is

$$E^{c}_{error} = \int_{t_{TD}}^{t_{TO}} P_{error}(t)\ dt \approx \sum_{t_{TD}}^{t_{TO}} P_{error}(t_k) \cdot \Delta T. \tag{5.6}$$

Here, the continuous time integration is approximated using a sum over the discrete time measurement points. For the two RTHS tests, the values are $E^{c}_{error} = 3.5 \cdot 10^{-3}\,\mathrm{J}$ without VFF and $E^{c}_{error} = -1.54 \cdot 10^{-5}\,\mathrm{J}$ with VFF. Similar to the sign convention of the power error, a positive E^{c}_{error} indicates test instability and $E^{c}_{error} < 0\,\mathrm{J}$ indicates test stability. However, one has to pay attention using these values because the test without VFF exhibits a highly undesirable behavior, but the energy error E^{c}_{error} has only a slightly positive value. This is because the positive and negative contributions of the power error sum almost up to zero and therefore do not capture the degree of instability properly.

Even though the test with VFF (fig. 5.3b) is a stable RTHS test, the measure P_{error} detects many active phases, where NPC would turn on, because the transfer system introduces energy. Hence, P_{error} is overcautious and detects supposedly instability even if the test remains stable. However, to the author's knowledge, no better online measures of RTHS stability exist in literature. Thus, the influence of NPC in stable tests needs to be investigated (see section 5.4.4).

5.4.2 Influence of Low-Pass Filters

The low-pass filters used to filter the power error and the total power throughput in eq. (5.5) have a transfer behavior of $\frac{1}{T_{error} \cdot s+1}$ and $\frac{1}{T_{tot} \cdot s+1}$. For each specific application, the appropriate values of the time constants T_{error} and T_{tot} have to be found. Hence, RTHS experiments[6] were conducted where both time constants took the values $\{0.01, 0.1, 1\}$ s and all combinations were investigated. The general influence of the low-pass filters on the damping force F_{d} (by the NPC) is shown in fig. 5.4 for the cases where both time constants took the same value. The shown results illustrate the explanation from section 5.3, namely that longer time constants reduce the magnitude of the introduced damping force F_{d} and the responsiveness of the NPC. Viewing the measured interface forces ($F_{\text{int}} = F'_{\text{m}} + F_{\text{d}}$) shows that the magnitude of the damping forces is small and only slightly larger than the measurement noise. This figure also reveals that the measured interface forces lag behind the reference solution $F^{\text{r}}_{\text{int}}$ due to the bad actuator tracking performance without VFF.

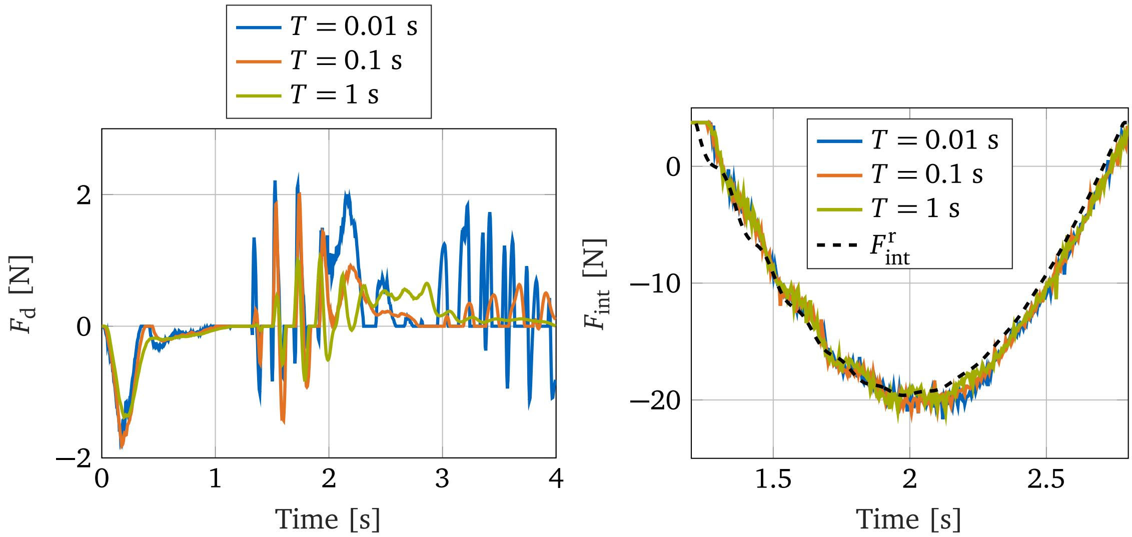

Figure 5.4: The variation of the time constants $T_{\text{error}} = T_{\text{tot}} = T$ influences the volatility of the additional damping force F_{d}. The resulting interface force $F_{\text{int}} = F'_{\text{m}} + F_{\text{d}}$ is shown on the right during the contact phase. The RTHS experiments were performed without VFF, $d_{\text{NUM}} = 50\,\text{kg/s}$ and $G_{\text{P}} = 1600\,\text{kg/s}$ (remaining parameters are given in table A.2).

Finding the most appropriate time constants for a specific RTHS experiment is challenging, as there are no explicit rules on how to select them. In the presented RTHS test with contact, the time constants $T_{\text{error}} = 0.1\,\text{s}$ and $T_{\text{tot}} = 0.01\,\text{s}$ are selected. These parameters lead to high responsiveness, which is considered necessary for RTHS tests with contact. In case a reference solution is available, as in this experiment, the time constants can also be optimized by investigation of the relative RMS reference error eq. (4.6). The selected time constants lead to a high fidelity. Nevertheless, the choice is not unique and e.g. also $T_{\text{error}} = T_{\text{tot}} = 0.1\,\text{s}$ would be an appropriate—neither significantly better nor worse—choice for this RTHS system.

5.4.3 Influence of Damping Scaling Parameter

Apart from the low-pass filters, also the damping scaling value G_{P} must be tuned by hand to achieve RTHS test stability. The value is experiment specific and determines the magnitude of the introduced damping force F_{d} by the NPC. As mentioned above, the appropriate choice is important and involves a trade-off between stability (high values of G_{P}) and fidelity (low values of G_{P}). Therefore, the influence of G_{P} on the RTHS system with contact needs to be investigated. RTHS tests were performed with $G_{\text{P}} = \{0, 400, 800, 1600, 3200\}\ \frac{\text{kg}}{\text{s}}$ and the

[6] Such investigations have also been performed using the vRTHS setup and similar results could be observed.

results are shown in fig. 5.5. As discussed above and can be seen in the figure, the test is unstable without NPC. The NPC manages to stabilize the test, i.e. dampen the undesired oscillations that occur during the contact phase.

The energy error during the whole test E_{error} and the amount of dissipated energy E_{diss} (by NPC) are determined with

$$E_{\text{error}} = \int_0^{t_{\text{end}}} P_{\text{error}}(t) \ \mathrm{d}t \approx \sum_0^{t_{\text{end}}} P_{\text{error}}(t_k) \cdot \Delta T \text{ and} \tag{5.7}$$

$$E_{\text{diss}} = \sum_0^{t_{\text{end}}} F_{\text{d}}(t_k) \cdot \dot{z} \cdot \Delta T, \tag{5.8}$$

where t_{end} denotes the length of the RTHS test (here $t_{\text{end}} = \frac{1}{f_{\text{d}}}$). The energy error and dissipated energy are depicted on the lower left of fig. 5.5. From the figure it can be inferred that the higher force values F_{d} for higher values of G_{P} lead to more dissipated energy E_{diss}. Accordingly, the energy error E_{error} decreases by the amount E_{diss} that is dissipated by NPC. For high values of G_{P}, still a considerable amount of energy error can be seen. This is due to the bad actuator tracking and the fact that compatibility and equilibrium are not fulfilled. Even though NPC manages to stabilize the test, it does not improve the actuator tracking performance and therefore $E_{\text{error}} > 0\,\text{J}$. Note that the relatively low value of the energy error without NPC (at $G_{\text{P}} = 0\,\text{kg/s}$) results from the oscillations of the power error around zero (compare to fig. 5.3a) and does not capture the test instability properly.

Furthermore, the relative RMS reference error (eq. (4.6)) is shown on the lower right of fig. 5.5. For small values of G_{P}, the fidelity increases due to the stabilization of the test. However, when G_{P} increases further, the damping force F_{d} falsifies the investigated system dynamics too much and the reference error increases. The optimum damping scaling value G_{P} is large enough to stabilize the RTHS test but as small as possible to distort the output as little as possible.

A detailed analysis of the influence of G_{P} on this RTHS system with contact is given in [104].

5.4.4 NPC in Stable RTHS Tests

The passivity controller should only interfere if test stability is jeopardized. In the implementation, the PO uses the power error P_{error} as indicator. However, this indicator is overcautious and therefore NPC sometimes also interferes when the test would remain stable (see e.g. fig. 5.3b). Hence, the detrimental influence of NPC in stable tests needs to be investigated.

Figure 5.6 shows RTHS tests where the system with $d_{\text{NUM}} = 50\,\text{kg/s}$ is investigated with VFF and thus is stable. The damping forces F_{d} by the NPC are shown at the top of fig. 5.6. The higher G_{P}, the higher the magnitude of the additional damping forces. Nevertheless, the magnitude remains small compared to the measurement noise of the FTS and in relation to the magnitude in the tests without VFF (cf. fig. 5.4). The RTHS system is detected as being active, i.e. $P_{\text{error}} > 0\,\text{W}$ and $F_{\text{d}} \neq 0\,\text{N}$, only at few time instants. The energy error E_{error} is, compared to the test without VFF, much smaller. This is due to the better tracking. Similar to fig. 5.5, the dissipated energy E_{diss} reduces the energy error (lower left figure in fig. 5.6). Due to the good actuator tracking, also the relative RMS reference error is very small. Since this test is stable without NPC, the $e_{\text{ref,rel}}$ increases for all values $G_{\text{P}} > 0\,\text{kg/s}$. The increase of the reference error is very small, though, compared to fig. 5.5 without VFF.

To summarize, when NPC is applied to stable tests, additional damping forces F_{d} are introduced. Nevertheless, the influence can be regarded as negligible since the transfer system is barely active.

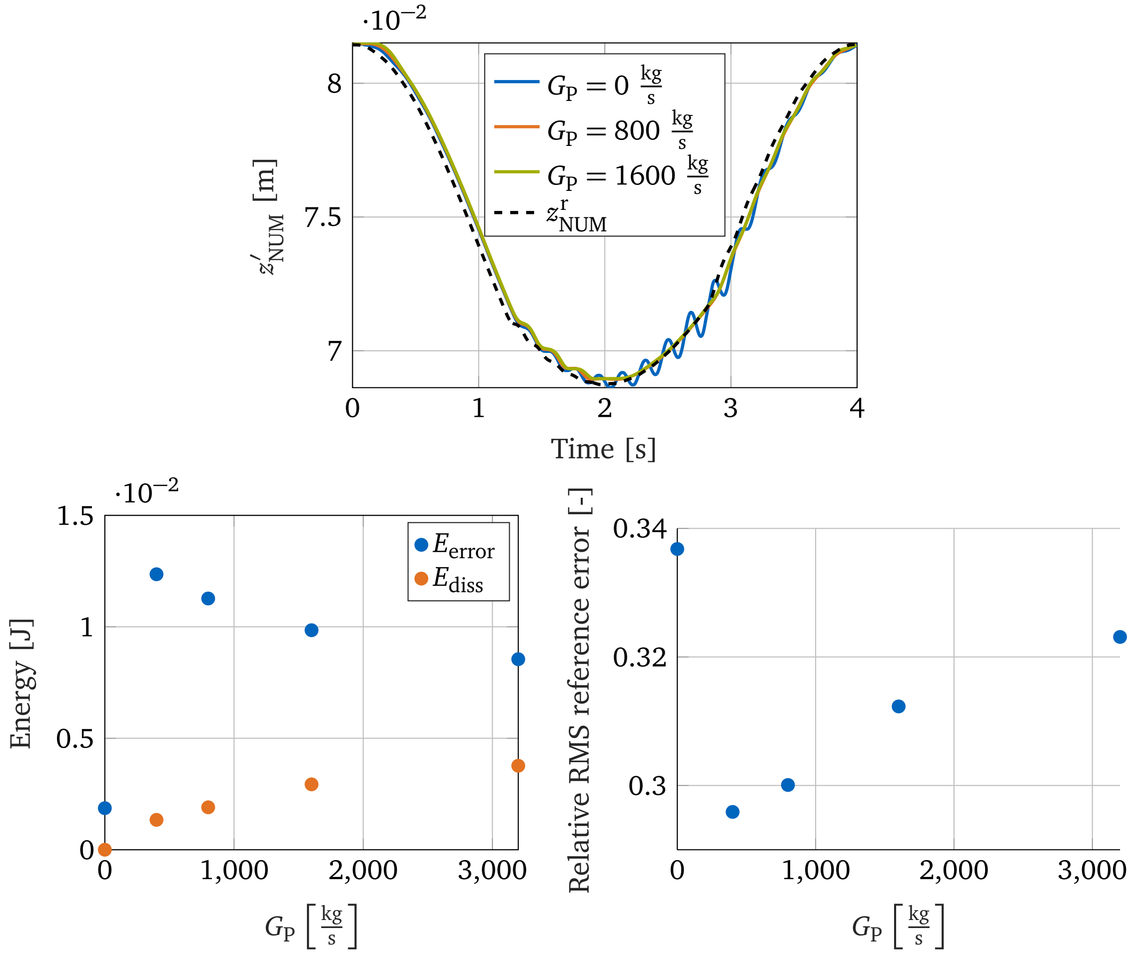

Figure 5.5: The damping scaling value directly influences the magnitude of the damping force F_d and its influence on the interface trajectory, error and damping energy as well as the relative RMS reference error is shown. The RTHS experiments were performed without VFF, $d_\mathrm{NUM} = 50\,\mathrm{kg/s}$ and $T_\mathrm{error} = T_\mathrm{tot} = 0.1\,\mathrm{s}$ (remaining parameters are given in table A.2).

5.4.5 Discussion

NPC is a simple method to perform stable RTHS tests with little system knowledge and no assumption about linearity [171]. For optimum results in terms of stability and fidelity, the time constants of the low-pass filters T_error and T_tot as well as the damping scaling value G_P need to be tuned. The choice of the time constants is ambiguous and depends on the investigated system dynamics. For the RTHS setup with contact, short time constants are preferred. The optimum parameter G_P is crucial for a good performance of the NPC. In a new RTHS setup, the following procedure is suggested to appropriately choose G_P: The underlying idea of TDPC[7] is that the PC dissipates the amount of power error $P_\mathrm{error}(t_k)$ in each time step t_k. This condition can be written as

$$F_\mathrm{d} \cdot \dot{z} \overset{!}{=} P_\mathrm{error} \tag{5.9}$$

$$G_\mathrm{P} \cdot \frac{P_\mathrm{error}}{|P_\mathrm{tot}|} \cdot \dot{z}^2 = P_\mathrm{error} \quad \text{and solved for } G_\mathrm{P} \tag{5.10}$$

$$G_\mathrm{P} = \frac{|P_\mathrm{tot}|}{\dot{z}^2} \approx \frac{|F'_\mathrm{m} \cdot (\dot{z}' + \dot{z})|}{\dot{z}^2} \approx \frac{|2 \cdot F'_\mathrm{m} \cdot \dot{z}'|}{\dot{z}^2} \tag{5.11}$$

[7] One approach found in literature on PC is to set $F_\mathrm{d}(t_k) = \frac{P_\mathrm{error}(t_k)}{\dot{z}(t_k)}$ [240]. However, using this approach instead of NPC in experiments resulted in forces F_d that were orders of magnitude larger than F_m and very volatile.

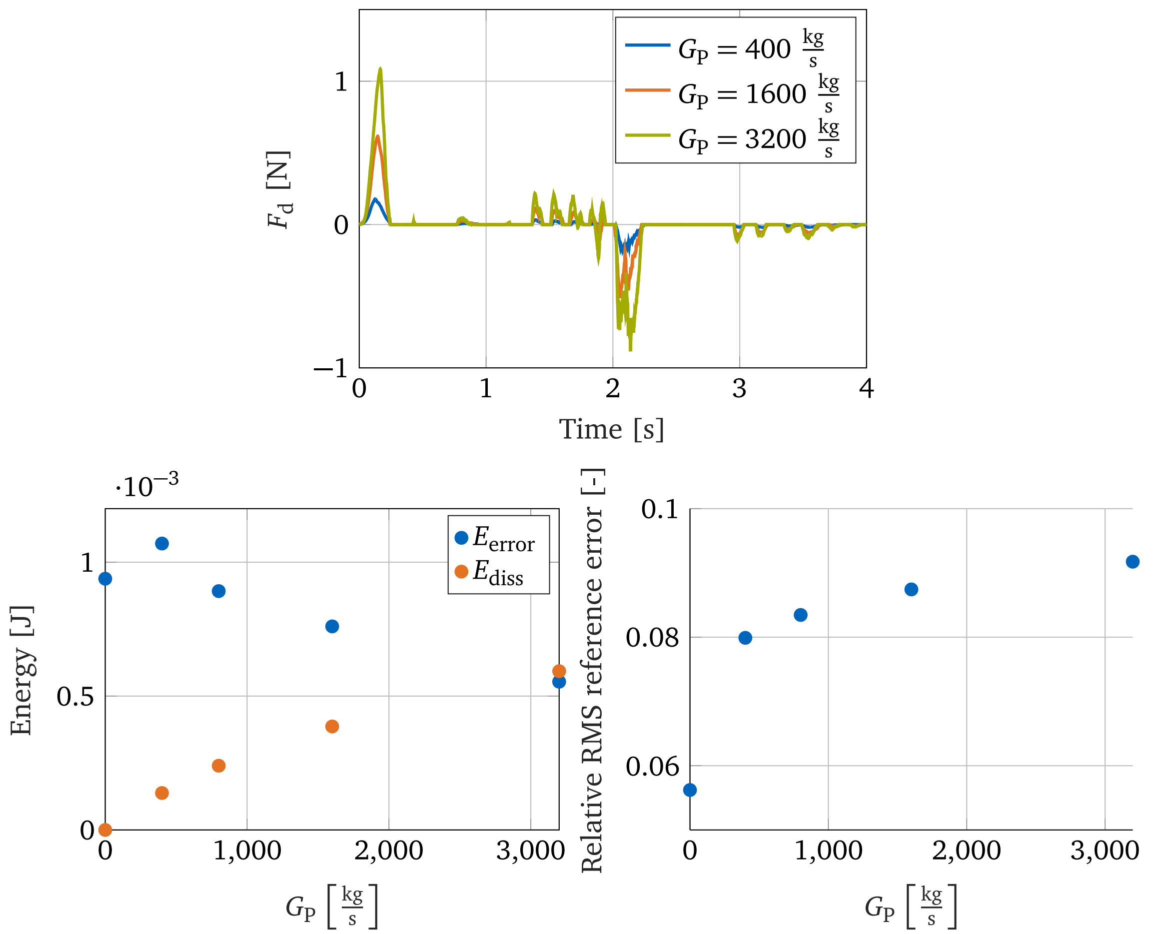

Figure 5.6: The influence of NPC is investigated for a stable RTHS test, where the system with $d_{NUM} = 50\,\mathrm{kg/s}$ was investigated with VFF switched on. The damping force F_d, the energy error and the dissipated energy as well as the relative RMS reference error are shown. The system parameters were $T_{error} = T_{tot} = 0.1\,\mathrm{s}$ and the remaining parameters are given in table A.2.

when the low-pass filtering is omitted. Equation (5.11) can be evaluated using the expected interface forces and displacements, which gives a good initial guess for G_P. In case this value is higher than the optimum value and dampens too much (deterioration of fidelity), it can gradually be reduced until the sweet spot for the trade-off stability vs. fidelity is found. In general, the value should be as small as possible to prevent nonlinear distortion but high enough to ensure stability. The parameters that are used in the remainder of Part I are $T_{error} = 0.1\,\mathrm{s}$, $T_{tot} = 0.01\,\mathrm{s}$ and $G_P = 1600\,\mathrm{kg/s}$, which are also summarized in table A.3.

Even though NPC is able to stabilize RTHS tests, the tracking accuracy is unaffected. In order to increase the test fidelity, the tracking accuracy needs to be improved by an adequate control scheme. In case of perfect tracking, or rather when the compatibility and equilibrium conditions are fulfilled, the transfer system (interface) is energy conservative and does neither introduce nor dissipate energy.

Chapter 6

Iterative Learning Control (ILC)

This chapter is partly based on the author's publications [103, 107, 108]. The students Tobias Klotz, Arian Kist and Henri Schwalm contributed to the final implementation of the ILC scheme during their student theses. The derivation of the convergence condition has been published in [108, 194]. The measurements shown in this chapter have been performed by Arian Kist as research assistant.

Human progress is based on the ability to learn. Many skills are established by repetition and learning from failure [85]. For example, a basketball player learns how to score by repeatedly shooting, observing the motion path of the ball and adapting the body movement. The concept of learning during a task that is performed repeatedly is also the key idea in *Iterative Learning Control (ILC)*.

6.1 Introduction to ILC

Many robots/actuation systems need to perform the identical or similar motion task many times in a row. ILC can be used in such applications. In ILC, information from previous trials is exploited to improve the tracking accuracy and reject repeating disturbances [31]. The idea is that ILC controllers learn to generate a feedforward control signal that approximately inverts the plant dynamics[1]. This is achieved by monitoring the tracking error in each iteration. Therefore, ILC can be viewed as a controller in trial domain (iterations j), rather than in time domain (time steps t_k) [31, 56, 166]. The feedback in trial domain enables the use of the whole trajectory of the previous iteration(s) $j-1$ to generate the feedforward signal at time t_k in iteration j. This leads to the anticipating properties of ILC [61, 149].

The first publications on ILC date back to the 1970s and include the work of Cryer et al. [45] and Uchiyama et al. [222]. Often, also the work of Arimoto et al. [9] is considered to be the origin of ILC. In this work, the control signal in iteration j is updated based on the control signal from iteration $j-1$ and the time-derivative of the tracking error from iteration $j-1$. Since then, numerous publications with different ILC implementations have been developed. Nowadays, the application of ILC can be found in industrial robotic structures [61, 162], the motion control of inkjet printers [230] and applications that require high precision, such as silicon wafer production [57] and nanopositioning atomic force microscopy [52].

The basic signal flow of ILC is depicted in fig. 6.1, where the ILC enhances a feedback controller C. The iteration-invariant reference trajectory is denoted by r (specifically $r(t)$)

[1] In the example with the basketball player from the beginning, the feedforward control signal corresponds to the body movement. The plant dynamics comprise the flight path (gravity, mass and drag of ball, distance) and the basket.

and the iteration-variant actuator motion with y_j. The tracking accuracy is measured with $e_j = r - y_j$. The error signal of the whole trajectory j is processed by a learning function L. Together with the feedforward signal during iteration j, the feedforward signal for the successive iteration $j+1$ is formed. For enhanced robustness, a robustness filter Q is often used. Hence, the update law writes

$$f_{j+1} = Q \cdot (L \cdot e_j + f_j). \tag{6.1}$$

ILC can be used in conjunction with a feedback controller, as depicted in fig. 6.1, or as a standalone controller. In that case, the existing controller is replaced from the second iteration onward.

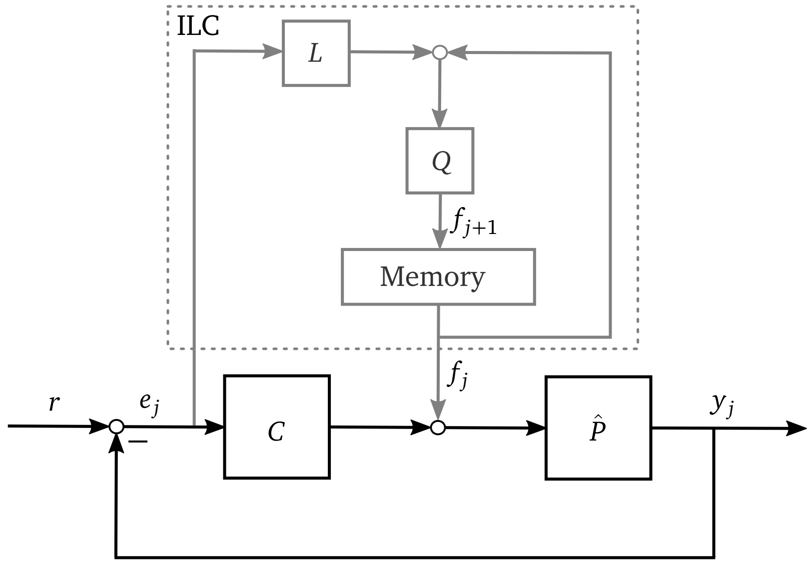

Figure 6.1: The block diagram of ILC (in gray) in combination with a feedback controller C is visualized. In ILC, the tracking error $e_j = r - y_j$ of iteration j is processed to generate a feedforward signal f_{j+1} in the next iteration.

Requirements on the successful implementation of basic ILC are [71, 149, 161, 229]:

- The reference set-point trajectory is iteration-invariant.
- The system states are the same for all iterations, i.e. they must be reset between iterations.
- The system dynamics must be iteration-invariant.
- Each iteration must have a fixed length.
- There must be an input with which the reference trajectory can be followed.

Over the past decades, research has been conducted to drop some of the assumptions and make ILC more widely applicable.

6.1.1 ILC Approaches

Many different ILC approaches have been proposed. They can be classified into first order and higher order algorithms depending on the number of past iterations that are included in the calculation of the feedforward signal. A further distinction can be made into linear and nonlinear ILC, fixed and adaptive algorithms, time domain vs. frequency domain analysis or whether assumptions about the plant are necessary. [149] The most commonly used learning functions L are the PD-type learning function, plant inversion, H_∞ techniques and the quadratically optimal design [31]. The simplest choice is the PD-type learning function which can be applied to systems with only little knowledge about the system dynamics. In PD-type learning, the learning function L consists of a proportional part β and a derivative part γ. The feedforward signal writes

$$f_{j+1} = Q \cdot (\beta \cdot e_j + \gamma \cdot \dot{e}_j + f_j). \tag{6.2}$$

Plant inversion methods require a model P of the plant dynamics and the learning function is chosen as $L = P^{-1}$. While the convergence property of this scheme, i.e. the learning progress, is usually very good, the performance and robustness heavily rely on accurate models. Both the H_∞ and quadratic optimal design approaches require a sophisticated implementation procedure [31]. Albeit simple, PD-type ILC is efficient and is therefore used in the remainder of this thesis.

6.1.2 Success of ILC

Like in other control approaches, stability is an important feature of an ILC implementation. In contrast to other control techniques, where the time domain is considered, asymptotic stability needs to be considered in the iteration domain in ILC. In ILC, convergence is given if f_j converges towards a fixed, bounded signal for $j \to \infty$ [31]. In iteration domain, the condition of asymptotic stability does not ensure monotonic convergence, which is $||e_{j+1}|| < ||e_j||$.[2] As described i.a. in[61, 166], monotonic convergence is desired because bad transient learning behavior might occur otherwise. Bad transients mean that errors grow up to multiple orders of magnitude higher than the initial value before converging to the final, lower value. The relation between the errors in two successive iterations j and $j+1$ can be expressed as

$$e_{j+1} = Q \cdot (1 - \hat{P} \cdot S \cdot L) \cdot e_j, \tag{6.3}$$

when no external disturbances are present. Here, the plant is represented by the transfer function $\hat{P}$ that is controlled with a feedback controller C and the sensitivity of the system $S = (1 + C\hat{P})^{-1}$ [51]. Monotonic convergence and asymptotic stability are guaranteed when the operator mapping between e_j and e_{j+1} contracts all frequencies, i.e.

$$\left| Q(e^{i\omega})(1 - \hat{P}(e^{i\omega})S(e^{i\omega})L(e^{i\omega})) \right| < 1 \; \forall \omega. \tag{6.4}$$

This condition means that the frequency response function (FRF) needs to stay below 0 dB for all frequencies. For all frequencies with a magnitude greater than 0 dB, the error increases from iteration to iteration. The robustness filter Q is used to cut those frequencies and also to increase robustness. Robustness means that convergence can be obtained even in the presence of disturbances, model uncertainties and high-frequency noise. Without Q, even little model errors could lead to instability. Hence, the choice of Q is often a low-pass filter with a cutoff frequency $f_{\mathrm{Q,cut}}$. Possible choices are Butterworth filters or zero-phase filters. [30, 61]

After convergence, a final error of

$$e_\infty = \frac{1 - Q}{1 - Q(1 - \hat{P}SL)} \cdot \mathrm{e}_1 \tag{6.5}$$

remains, with e_1 being the error in the first iteration [149]. This equation reveals that a final error of zero can theoretically be achieved if $Q = 1$. So, a careful tuning of the cutoff frequency $f_{\mathrm{Q,cut}}$ is essential and a trade-off between minimum final error and robustness. In

[2] The error can e.g. be measured as an RMS error or in the L2-norm [61, 130, 166].

case of noise and non-repeating disturbances or changing initial conditions, ILC converges to a range around e_∞ [149].

In literature, there are no commonly applicable guidelines about the proper selection of the L and Q filter available and a tuning procedure needs to be performed. In general, L must be chosen such that eq. (6.4) is a contraction mapping. Small learning gains lead to slower convergence and increased robustness [30, 61, 130]. A recommended tuning procedure is to start with a high cutoff frequency $f_{\mathrm{Q,cut}}$ of Q. If no convergence is achieved, an FRF of the error signal can be made to find the parasitic frequencies. The Q filter is then tuned to erase them [61, 130]. For good performance and small remaining errors, the bandwidth of the Q filter should be as high as possible. In case of P-type ILC (PD-type with $\gamma = 0$), the learning filter is suggested to be in the range $L \in (\frac{1}{4}, 1)$ [130].

Side note: A closely related approach is called Repetitive Control (RC). In contrast to ILC, the system is not reset between the trials [130].

6.2 Application of ILC to RTHS

Comparing the requirements for the actuator control for RTHS with contact (cf. section 3.2) with the properties of ILC (see section 6.1), one can see that ILC could be a suitable control technique for the actuator in RTHS. Throughout the ILC iterations, the **actuator tracking** performance is increased when the ILC scheme converges monotonically. Next, only signals are used by ILC to generate an appropriate feedforward signal that inverts the plant dynamics, but not the inverse transfer function is sought. This makes ILC a **data-based approach**. If, for example, the PD-type ILC implementation is selected, the implementation is **simple and straightforward** with only few tuning parameters. In ILC, the feedforward signal is learned for each time step t_k of a motion trajectory and does not try to identify the plant dynamics. As long as the dynamics remain the same for a certain time step t_k throughout the iterations j, ILC can deal with any nonlinearities and discontinuities. Hence, ILC is particularly suited for system dynamics with contact because the changing system dynamics (contact – non-contact) are inherently included in the generation of the feedforward signal and do not need to be incorporated in the implementation. Depending on the actuation system used, the injection of the feedforward signal f_j after the feedback controller C (see fig. 6.1) might not be accessible. There are so-called serial implementations of ILC where the feedforward signal is injected in the most outer loop, namely before the feedback controller C [21]. Hence, ILC is **widely applicable** to complex system dynamics and also actuation systems. **Stability** and **robustness** are further requirements on the actuator control for RTHS with contact. However, ILC is only able to monitor the closed loop stability of the controlled actuator but not of the RTHS loop. To fulfill all these requirements, ILC needs to be enhanced by a passivity-based control scheme, as presented in section 6.4.

The block diagram of RTHS featuring ILC is visualized in fig. 6.2. The main difference in comparison with fig. 6.1 is that the set-point trajectory (z_j and r) is not iteration-invariant anymore. This is because an altered tracking performance leads to different excitation of the experimental part. This in turn alters the measured/interface forces $F_{\mathrm{m},j}/F_{\mathrm{int},j}$ that are used in the simulation of the numerical part to generate the motion command z_j. As introduced in section 6.1, an iteration-invariant set-point trajectory belongs to the requirements for ILC. Hence, the convergence of ILC in an RTHS setup needs to be investigated and the convergence condition eq. (6.4) is not valid here.

General remarks: The goal using ILC is to find the appropriate feedforward signal for a specific motion task. After convergence, the feedforward signal can be stored and used for later tests. Preliminary studies of ILC in RTHS are also reported in [63, 96].

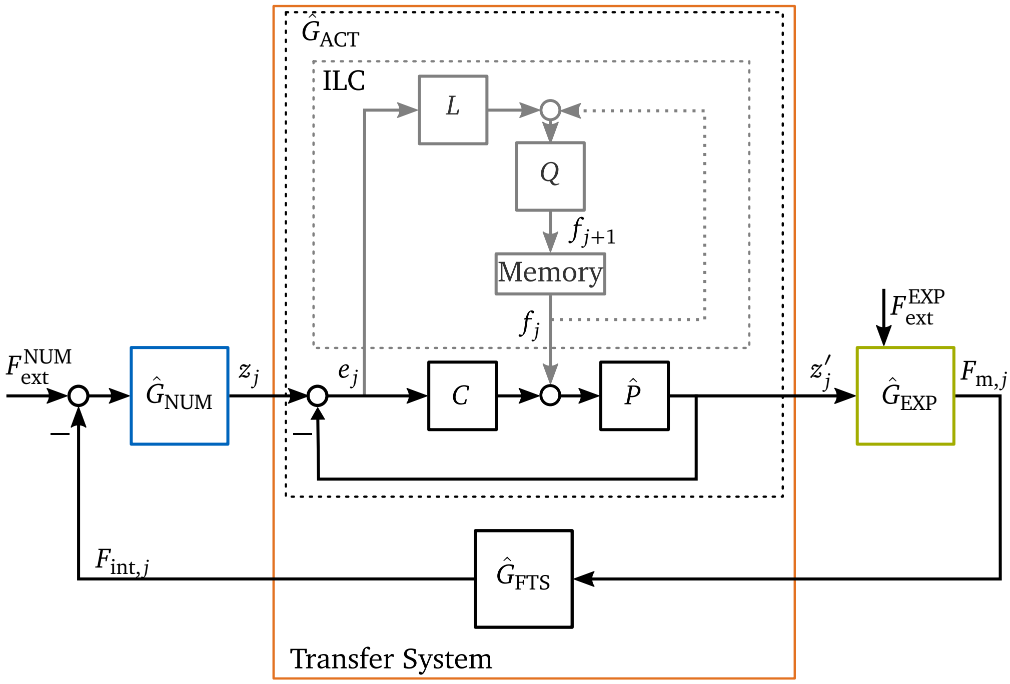

Figure 6.2: Signal flow using ILC in an RTHS setup. The tracking error $e_j = z_j - z'_j$ at iteration j is used to generate a feedforward signal for iteration $j+1$. Figure adapted from [108].

6.2.1 Convergence Condition

A convergence condition for ILC in the context of RTHS needs to be derived to understand how changes in the RTHS setup affect the ILC convergence and to properly select the learning filter L and the robustness filter Q. The following derivation is based on the block diagram visualized in fig. 6.2 and includes the following assumptions and simplifications:

- The actuator coordinates and the interface degrees of freedom are collinear and therefore the kinematic transformations are neglected.
- To derive a generally valid convergence condition, model knowledge of the transfer system and the experimental part is assumed. Usually, this knowledge is not available in an RTHS setup. Nevertheless, the derived convergence condition helps to get a feeling how changes in the respective parts affect ILC convergence. Hence, the following transfer functions are used: $\hat{G}_{NUM}$ is the transfer function of the numerical part, C denotes the feedback controller, $P \approx \hat{P}$ is the uncontrolled actuator transfer function, $G_{EXP} \approx \hat{G}_{EXP}$ models the transfer behavior of the experimental part and $G_{FTS} \approx \hat{G}_{FTS}$ is the transfer behavior of the FTS.
- The external forces F_{ext}^{NUM} and the interface forces $F_{int,j}$ are moved to the front of $\hat{G}_{NUM}$ to obtain a block diagram with single-input single-output blocks. The external forces F_{ext}^{EXP} are not considered.
- Dynamics introduced by communication/computation delays (DSP), A/D and D/A conversion are neglected.
- The derivation is done with continuous time transfer functions (Laplace variable s). In ILC, both discrete time and continuous time derivations of the convergence condition are used. Both are meaningful because the numerical part/controller is implemented in discrete time but interacts with the real actuator/experimental part (continuous time).

Discrete time representations may hide problems with robustness if the used sampling frequency is low.

To eliminate the effect of these assumptions and simplifications in the final application, a robust ILC design is targeted.

In the RTHS setup, the tracking error for iteration j writes

$$e_j = z_j - z_j' = G_{\text{NUM}}(F_{\text{ext}}^{\text{NUM}} - G_{\text{FTS}} G_{\text{EXP}} z_j') - z_j' \tag{6.6}$$

with the achieved displacement

$$z_j' = P(f_j + Ce_j). \tag{6.7}$$

Combining eq. (6.6) and eq. (6.7) and abbreviating the open loop dynamics of the coupled system with $G_{\text{DYN}} = G_{\text{NUM}} G_{\text{EXP}}$ yields

$$e_j = G_{\text{NUM}} F_{\text{ext}}^{\text{NUM}} - (G_{\text{FTS}} G_{\text{DYN}} P + P) f_j - (G_{\text{FTS}} G_{\text{DYN}} CP + CP) e_j, \tag{6.8}$$

Solving this equation for e_j gives

$$e_j = \frac{G_{\text{NUM}}}{1 + G_{\text{FTS}} G_{\text{DYN}} CP + CP} F_{\text{ext}}^{\text{NUM}} - \frac{G_{\text{FTS}} G_{\text{DYN}} P + P}{1 + G_{\text{FTS}} G_{\text{DYN}} CP + CP} f_j \tag{6.9}$$

$$e_j = S_{\text{in}} F_{\text{ext}}^{\text{NUM}} + S_{\text{f,in}} f_j, \tag{6.10}$$

with the inner sensitivity

$$S_{\text{in}} = \frac{G_{\text{NUM}}}{1 + G_{\text{FTS}} G_{\text{DYN}} CP + CP}. \tag{6.11}$$

The inner sensitivity maps the external excitation to the error. The inner feedforward sensitivity

$$S_{\text{f,in}} = -\frac{G_{\text{FTS}} G_{\text{DYN}} P + P}{1 + G_{\text{FTS}} G_{\text{DYN}} CP + CP} \tag{6.12}$$

maps the feedforward signal to e_j. Next, the ILC update equation eq. (6.1) ($f_{j+1} = Q \cdot (Le_j + f_j)$) is inserted into eq. (6.10) expressed at iteration $j+1$

$$e_{j+1} = S_{\text{in}} F_{\text{ext}}^{\text{NUM}} + S_{\text{f,in}} f_{j+1} \tag{6.13}$$

$$e_{j+1} = S_{\text{in}} F_{\text{ext}}^{\text{NUM}} + Q S_{\text{f,in}} f_j + Q S_{\text{f,in}} L e_j, \tag{6.14}$$

which can be expanded to

$$e_{j+1} = (1 - Q + Q) S_{\text{in}} F_{\text{ext}}^{\text{NUM}} + Q S_{\text{f,in}} f_j + Q S_{\text{f,in}} L e_j \tag{6.15}$$

$$= Q(S_{\text{in}} F_{\text{ext}}^{\text{NUM}} + S_{\text{f,in}} f_j) + Q S_{\text{f,in}} L e_j + (1 - Q) S_{\text{in}} F_{\text{ext}}^{\text{NUM}}. \tag{6.16}$$

The first term corresponds to the error in iteration j, see eq. (6.10), and insertion yields

$$e_{j+1} = Q(1 + S_{\text{f,in}} L) e_j + (1 - Q) S_{\text{in}} F_{\text{ext}}^{\text{NUM}}. \tag{6.17}$$

As discussed in section 6.1.2, the operator mapping the error between two successive iterations must contract all frequencies. Hence, the convergence condition for ILC in RTHS writes

$$\left| Q(e^{i\omega})(1 + S_{\text{f,in}}(e^{i\omega}) L(e^{i\omega})) \right| < 1 \ \forall \omega. \tag{6.18}$$

Using $f_1 = 0$, eq. (6.1) and eq. (6.10), the theoretical feedforward signal and error after convergence (compare to eq. (6.5) for ILC with iteration-invariant reference trajectory) write

$$f_\infty = \frac{QL}{1-Q} e_\infty \tag{6.19}$$

$$e_\infty = e_1 + S_{\mathrm{f,in}} f_\infty = \frac{1-Q}{1-Q(1+S_{\mathrm{f,in}}L)} e_1. \tag{6.20}$$

As could be seen in eq. (6.5), also eq. (6.20) reveals that the robustness filter Q increases robustness, on the one hand, but also deteriorates the final error, on the other hand. The appropriate choice of Q allows for uncertainties, modeling errors and the assumptions and simplifications made in the derivation of the convergence condition, while being as close to $Q = 1$ as possible to obtain minimum final error e_∞.

How different parameters of the PD-type ILC (β, γ and $f_{\mathrm{Q,cut}}$) and system partitioning (mass/stiffness experimental part) influence the frequency response eq. (6.18) is qualitatively shown in figs. 6.3 and 6.4. As can be seen in fig. 6.3, a higher P-gain ($\beta = 24\,{}^1/_\mathrm{s}$ here[3]) leads to a higher peak magnitude and hence less robustness. Smaller values of β decrease the convergence speed, which means that more iterations are needed to obtain the same error. Additionally, fig. 6.3 shows the influence of the robustness filter on the frequency response. As reported above, the robustness filter increases robustness and lowers the peak magnitude. Without the robustness filter ($Q = 1$), the ILC would not converge in this setup and an error component with a frequency of 6.5 Hz would grow throughout the iterations. Figure 6.4

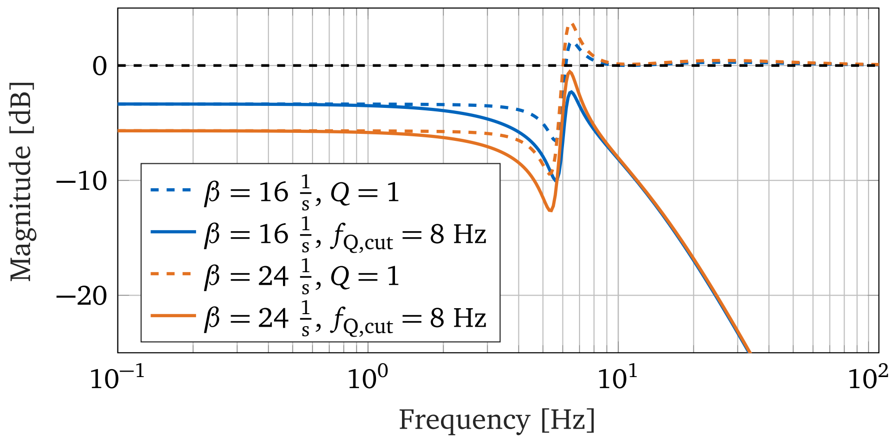

Figure 6.3: The influence of the P-gain β on the frequency response of eq. (6.18) for $\gamma = 0$ (P-type ILC). The black dashed line shows the 0 dB line.

shows the influence of the D-gain γ on the frequency response depending on the investigated dynamical system. If the experimental part consists solely of a spring ($m_{\mathrm{EXP}} = 0\,\mathrm{kg}$), a differential part ($\gamma \neq 0$) leads to an increased peak magnitude. The stabilizing influence of mass in the experimental part ($m_{\mathrm{EXP}} = 2\,\mathrm{kg}$, orange lines) as well as less experimental stiffness ($k_{\mathrm{EXP}} = 6000\,{}^\mathrm{N}/_\mathrm{m}$, green lines) lead to stability, which can be seen in the decreased peak magnitudes compared to stiffness experimental part (blue lines). Here, the D-gain γ results in smaller peak magnitudes and thus increased robustness.

[3] Why $\beta > 1\,{}^1/_\mathrm{s}$ is explained on p. 58.

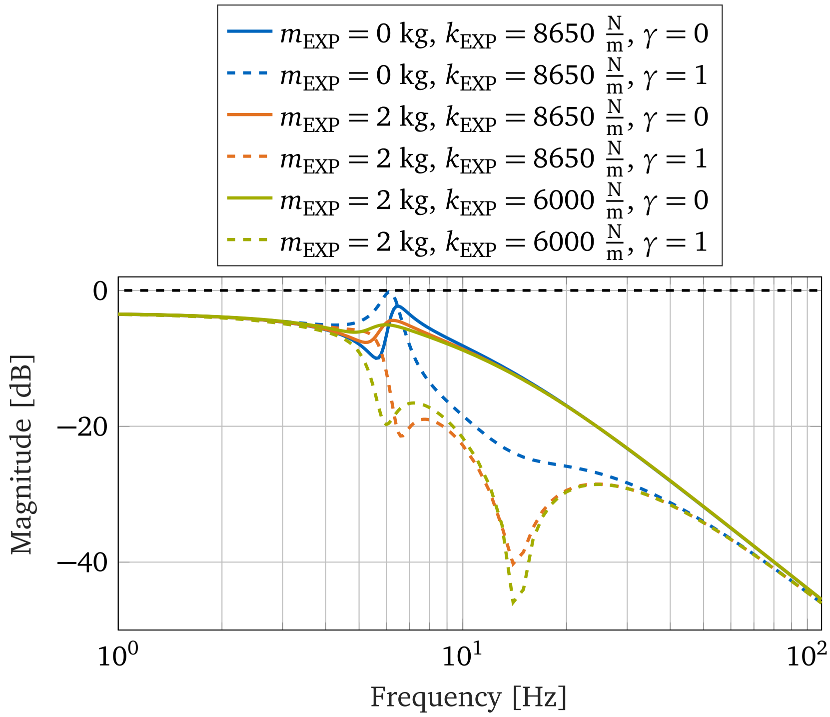

Figure 6.4: The influence of the dynamical system and the D-gain γ on the frequency response of eq. (6.18). A robustness filter with $f_{\mathrm{Q,cut}} = 8\,\mathrm{Hz}$ and a P-gain of $\beta = 16\,{}^{1}/_{\mathrm{s}}$ are used. The black dashed line represents the 0 dB line.

6.2.2 Application to RTHS Setup with Contact

Due to the simple and straightforward implementation, first order PD-type ILC is used for the RTHS setup with contact (introduced in chapter 4). The signal flow is depicted in fig. 6.5. In RTHS, one ILC iteration corresponds to one test and for the presented system with contact, this corresponds to one bump. Since the wall motion is a cosine trajectory with frequency f_{d}, the length of one iteration/test is $t_{\mathrm{end}} = \frac{1}{f_{\mathrm{d}}}$. ILC requires that the system states are reset between trials. Therefore, a pause time t_{pause} is implemented, where there is no motion of the suspension. Since the Stewart Platform is controlled with a decentralized feedback controller, also the ILC implementation is done for each leg ($i = 1 \ldots 6$) independently. Therefore,

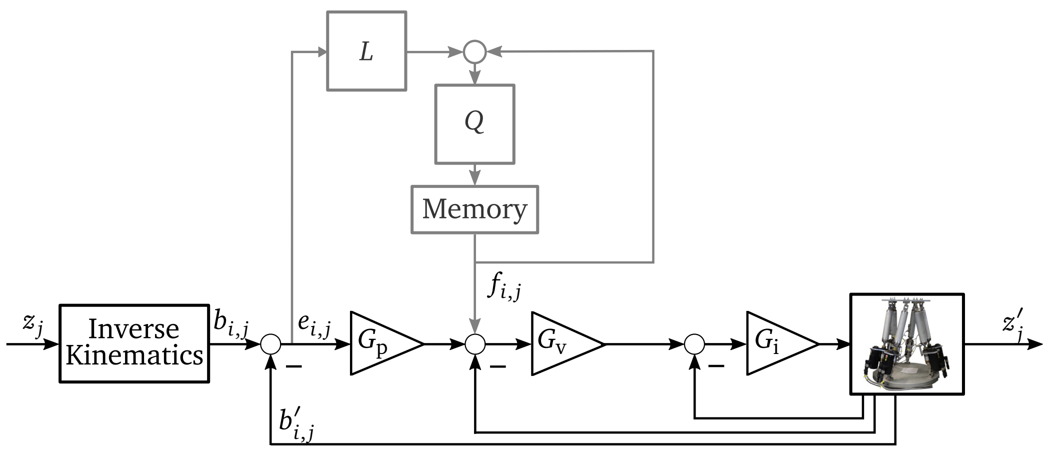

Figure 6.5: ILC in the RTHS setup used (presented in chapter 4). ILC is implemented for each leg $i = 1 \ldots 6$.

the iteration-dependent trajectory command z_j is transformed in the *Inverse Kinematics* block into the coordinates of the Stewart Platform $\boldsymbol{X}$ and then into the leg coordinates $b_{i,j}$ (leg i, iteration$j$). The tracking error of each leg i in iteration j is denoted by $e_{i,j}$. The ILC feedforward signal is injected on velocity level, i.e. after the position controller G_p. The signal could also be injected on current level or position level. Often in industrial robots, the inner loops are not accessible and therefore adding the feedforward signal in the outermost loop, which is the position control loop in this case, is necessary. This implementation is called serial implementation [31]. Mathematically, the injection on position and velocity level are equivalent [130]. This is for example the case if the feedforward signal $f_{i,j}$ in fig. 6.5 is inserted in the position control loop ($G_\mathrm{P} = K_\mathrm{Pp}$) and the proportional part β of the learning filter L is changed by $\frac{\beta}{K_\mathrm{Pp}}$. The robustness filter Q is implemented as a zero-phase Butterworth filter with cutoff frequency $f_\mathrm{Q,cut}$.

When the convergence condition eq. (6.18) is applied to the RTHS system with contact, only the contact phase is considered. This is because the dynamic coupling during the contact phase erodes the stability margin. During the contact phase, the open loop transfer function writes

$$G_\mathrm{DYN} = \frac{k_\mathrm{EXP}}{m_\mathrm{NUM}s^2 + d_\mathrm{NUM}s + k_\mathrm{NUM}}. \tag{6.21}$$

For a simple implementation of the convergence condition, collinearity between the leg axes and the interface DoFs (and respectively the Stewart Platform Z coordinate) is assumed. Hence, the transfer function P_2 (see table 4.1) is used representatively for the dynamics of the Stewart Platform in Z direction. In general, this assumption is only valid for actuators with centralized control. We assume that the leg dynamics along the leg axis are comparable to the Stewart Platform dynamics in Z direction. All other transfer functions (experimental part, numerical part, FTS) are also presented in chapter 4.

6.3 Investigation of ILC Efficacy in RTHS

Several investigations were performed to analyze the efficacy of PD-type ILC as actuator control scheme in RTHS. The shown data are results from RTHS tests performed with the RTHS setup presented in section 4.2.4 and the dynamical system from section 4.1. The presented studies were also conducted with the presented digital twin in vRTHS (section 4.3). The results are similar and the same fundamental behavior can be observed. Although the vRTHS setup offers a great opportunity to test novel control schemes preliminarily, the results are not shown here as they do not provide novel or disparate insights compared to the experimental results displayed. The RTHS experiments are better natured than the vRTHS simulations and respectively the convergence condition eq. (6.18) predicts (uses modeled transfer system and experimental part). This means that the RTHS test also converges if the peak magnitude is slightly above 0 dB. This appears unintuitive at first glance because the real RTHS test offers many more sources of uncertainty and errors, such as noise and the assumptions in the derivation. The reason is that the system identification and linear modeling of the actuator (section 4.3.1) is more conservative than the real nonlinear actuator transfer behavior, i.e. that the approximated dynamics are slower than the dynamics of the real Stewart Platform.

6.3.1 Convergence Condition in RTHS Tests

A convergence condition for ILC in RTHS is derived in section 6.2.1 and the general influence of the parameters of ILC and the dynamical system described. This section compares the behavior of ILC for the case that the convergence condition eq. (6.18) is fulfilled and respectively violated. The differences are presented in detail to introduce relevant physical quantities to the reader that are meant to facilitate the understanding of the complex interaction and error propagation in RTHS. The dynamical system parameters used are given in table A.2 and a PD-type ILC with $\beta = 16\,{}^{1}/_{\mathrm{s}}$ and $\gamma = 1$ was used[4]. The cutoff frequency of the robustness filter Q was tuned such that ILC converges ($f_{\mathrm{Q,cut}} = 2\,\mathrm{Hz}$, peak magnitude of eq. (6.18) at $-10\,\mathrm{dB}$, 30 iterations performed) and respectively diverges ($f_{\mathrm{Q,cut}} = 12\,\mathrm{Hz}$, peak magnitude of eq. (6.18) at $6\,\mathrm{dB}$, 10 iterations performed).

The relative RMS tracking error from eq. (4.4) is visualized for the iterations in fig. 6.6a. In case the convergence condition is fulfilled, the error decreases and levels off to the final error at iteration $j = 4$. After iteration $j = 4$, the ILC could not further improve the tracking performance and managed to keep the error small without transient growth or other detrimental effects. In contrast, for $f_{\mathrm{Q,cut}} = 12\,\mathrm{Hz}$, the relative RMS tracking error increases from the third iteration onward because the ILC diverges. The reference error e_{ref} (eq. (4.5)) is shown for ten iterations in fig. 6.6c. Better tracking performance results in a smaller ref-

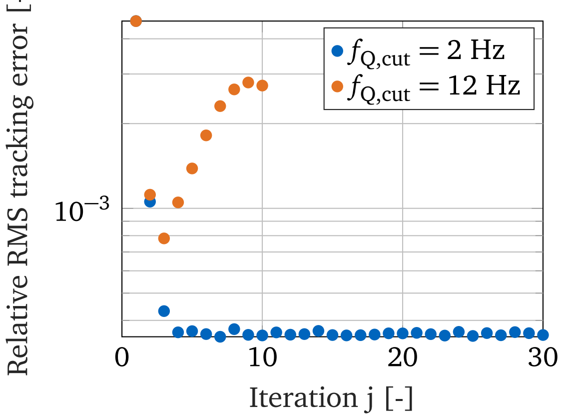

(a) Relative RMS tracking error $e_{\mathrm{track,rel}}$.

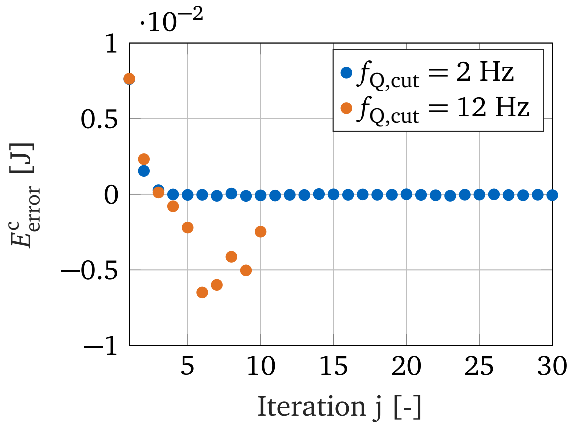

(b) Energy error during contact $E^{\mathrm{c}}_{\mathrm{error}}$.

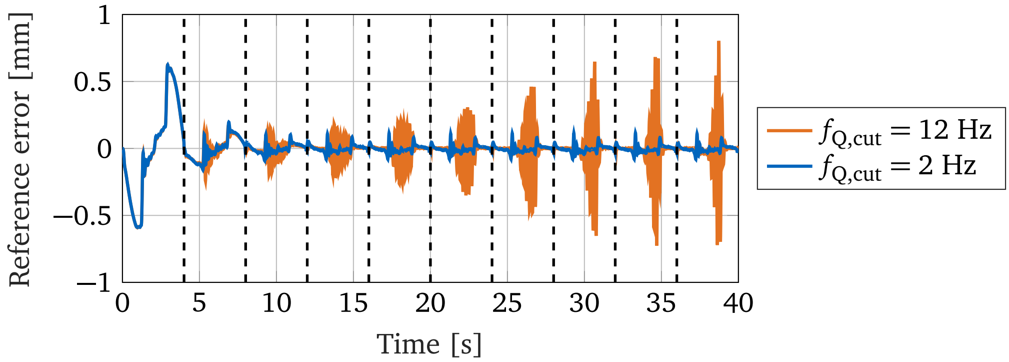

(c) Reference error over time. The pause times between the RTHS tests are not displayed in the figure.

Figure 6.6: RTHS test results with $f_{\mathrm{Q,cut}} = 2\,\mathrm{Hz}$ (convergence condition fulfilled, in blue) and $f_{\mathrm{Q,cut}} = 12\,\mathrm{Hz}$ (frequency response above $0\,\mathrm{dB}$, in orange). For the case with converging behavior, 30 iterations were conducted. The tests with diverging behavior had to be aborted after 10 iterations due to the high oscillations.

erence error and thus higher fidelity for the converging ILC implementation. However, for the diverging implementation, oscillations with growing amplitude can be seen. The oscillations have a frequency of $\approx 5\,\mathrm{Hz}$, which corresponds to the frequency where the frequency response of eq. (6.18) surpasses $0\,\mathrm{dB}$.

[4]Note that unlike explained in section 6.1.2, the proportional gain is $\beta > 1$. This is due to the conversion of a position error to a velocity feedforward signal and the factor $G_{\mathrm{P}} = K_{\mathrm{Pp}}$ between them.

To get a feeling how the RTHS result changes throughout ILC learning, figs. 6.7a and 6.7b show the interface displacement in different iterations during the contact phase. When the

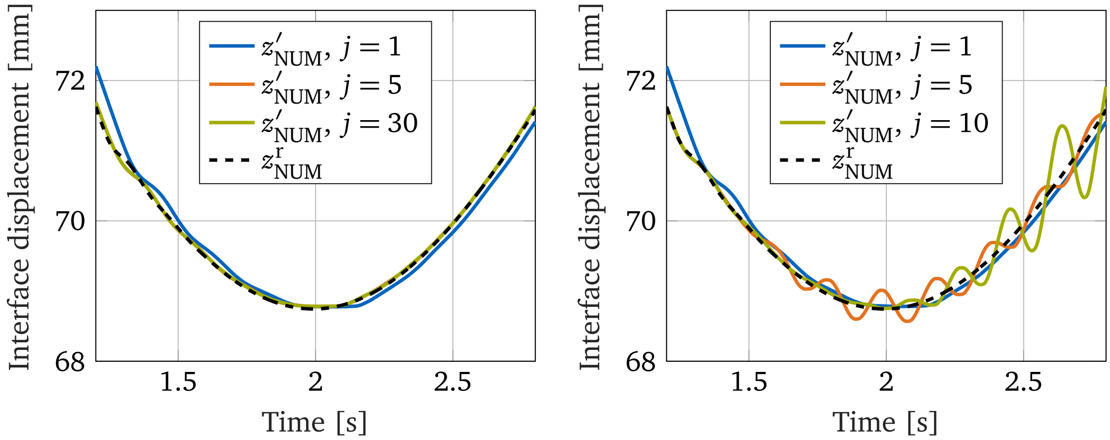

(a) Interface displacement in the RTHS test when the convergence condition is fulfilled. **(b)** Interface displacement in the RTHS test when the convergence condition violated.

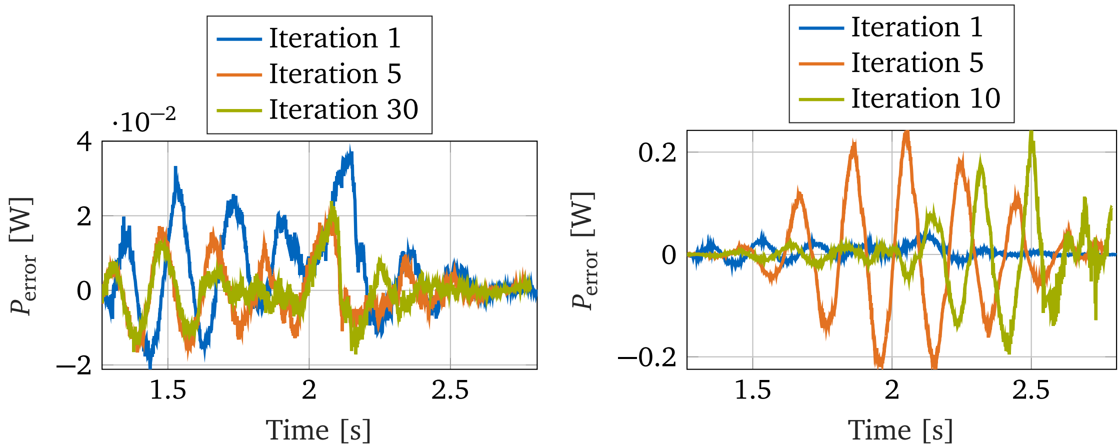

(c) The power error in the RTHS test when the convergence condition is fulfilled. **(d)** The power error in the RTHS test when the convergence condition violated.

Figure 6.7: The interface displacements and the power error P_{error} (eq. (5.3)) are shown during contact for different iterations j.

convergence condition is fulfilled (fig. 6.7a), ILC improves the phase error of the achieved displacement by shifting it to the front and thus more closely to the reference solution. No further improvement is visible after iteration $j = 5$, which corresponds to fig. 6.6a. When the convergence condition is violated, the phase error is also compensated and the interface displacement z'_{NUM} shifted to the front. However, oscillations develop and grow with a higher number of iterations, which is highly undesirable. As introduced in section 5.1, power/energy is exchanged between the components in an RTHS setup and it is an open challenge to determine the test stability in an ongoing RTHS test. One option is to monitor the power error P_{error} (see eq. (5.3)) of the transfer system, which is the difference between the power demand and the real power transmitted between the numerical and the experimental part. Figures 6.7c and 6.7d illustrate the power error during the contact phase and fig. 6.6b shows the energy error, i.e. the sum over the power error at the discrete time steps t_k (eq. (5.6)). The improved tracking performance for $f_{\mathrm{Q,cut}} = 2\,\mathrm{Hz}$ reduces the magnitude of the power error throughout the iterations. Furthermore, a phase shift to the front can be seen in fig. 6.7c which proves the ability of ILC to compensate for the actuator dynamics. A value of $E^{\mathrm{c}}_{\mathrm{error}} \approx 0\,\mathrm{J}$ can be inferred from fig. 6.6b after convergence, which indicates that the transfer system neither introduces nor dissipates energy to the investigated coupled dynamical system over the course of the whole RTHS test. For $f_{\mathrm{Q,cut}} = 12\,\mathrm{Hz}$, the magnitude of the power error increases from iteration to iteration. Due to the oscillations, the value of the energy error (fig. 6.6b) does not reveal the instability (in theory for $E^{\mathrm{c}}_{\mathrm{error}} > 0\,\mathrm{J}$) of the test. Hence, the power error should not be used as the sole indicator for test instability.

The goal of ILC is to reduce the error from iteration to iteration. More specifically, the frequency components of the error are contracted throughout the iterations depending on the value of eq. (6.18). Figure 6.8 shows the amplitude response of the tracking error e_{track}. For the converging ILC implementation shown in fig. 6.8a, the magnitude decreases throughout the ILC iterations for all frequencies, which complies with the fulfillment of the convergence condition. For $f_{\mathrm{Q,cut}} = 12\,\mathrm{Hz}$, however, the frequency response surpasses $0\,\mathrm{dB}$ at a frequency of $\approx 5\,\mathrm{Hz}$. As can be seen in fig. 6.8b, the magnitude of the error at $5\,\mathrm{Hz}$ and the adjacent frequencies grows while the magnitude for the other frequencies decreases.

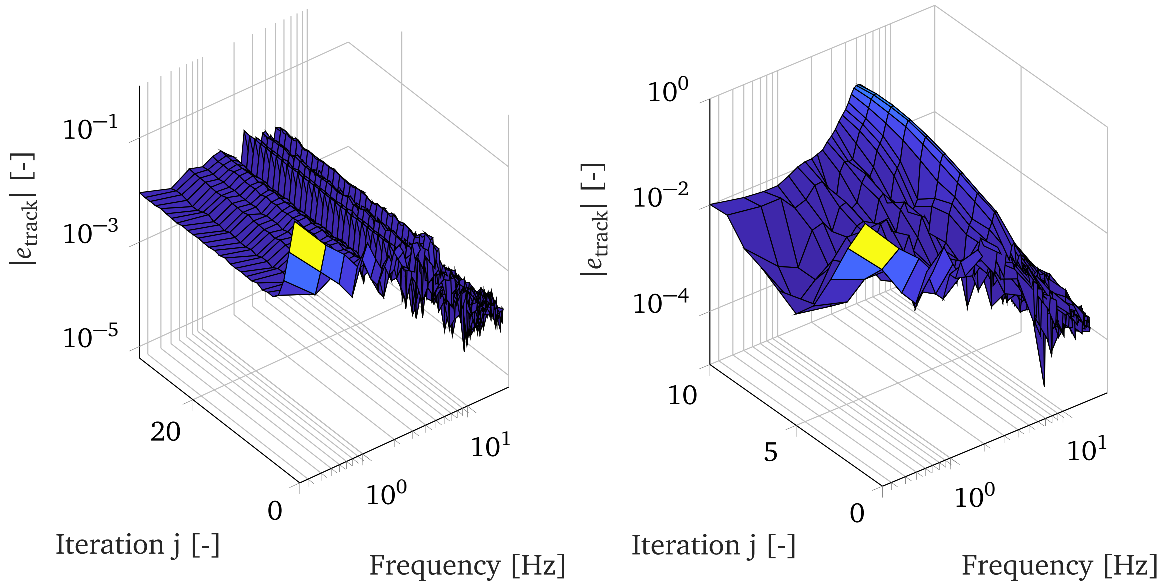

(a) Convergence condition fulfilled ($f_{\mathrm{Q,cut}} = 2\,\mathrm{Hz}$). **(b)** Convergence condition violated ($f_{\mathrm{Q,cut}} = 12\,\mathrm{Hz}$).

Figure 6.8: The fast Fourier transform (FFT) of the tracking error e_j is shown for all iterations. The frequencies that lie above $0\,\mathrm{dB}$ (eq. (6.18)) are amplified throughout the ILC iterations.

To sum up, ILC is able to compensate the actuator dynamics and improve the tracking performance in successive RTHS tests if the convergence condition is fulfilled. The better tracking performance improves the test fidelity (decrease reference error) and the energy exchange between the numerical and experimental substructure is more realistic.

6.3.2 Parameter Investigations

These first investigations show the efficacy of ILC in RTHS to compensate the actuator dynamics, requiring only little knowledge about the dynamics of the actuator and the experimental part. Throughout the iterations, ILC is able to improve the transfer behavior, which is not only visible in the time domain $z(t) \rightarrow z'(t)$ (e.g. figs. 6.6a, 6.6c and 6.8), but also in the frequency domain $Z(s) \rightarrow Z'(s)$. Figure 6.9 provides the FRF $\frac{Z'(s)}{Z(s)}$, which was approximated by a first order system. Through learning by ILC, the magnitude remains at $0\,\mathrm{dB}$ for a broader frequency range and the phase drop becomes less, which indicates the increased bandwidth through learning. However, the figure has to be interpreted with caution: The transfer behavior after learning is not as ideal as indicated by the figure and a controller bandwidth

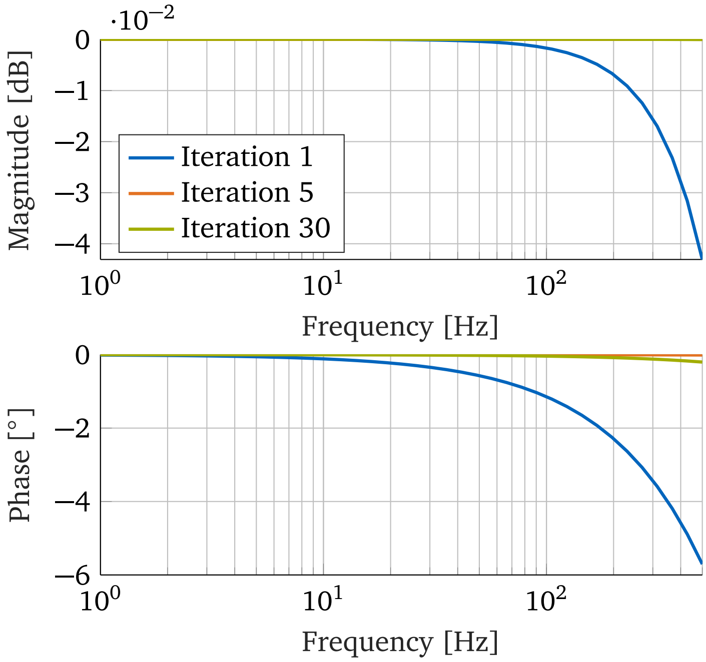

Figure 6.9: General influence of ILC on the transfer behavior of the actuator $Z(s) \rightarrow Z'(s)$ throughout the iterations.

up to 500 Hz is simply not realistic. Firstly, such a high controller bandwidth would indicate perfect tracking, which contradicts the remaining error in fig. 6.6a. Secondly, there are hardware limitations like maximum motor current/voltage, which restrict the achievable actuator bandwidth[5]. Nevertheless, the fundamental behavior, which is the increase of the actuator bandwidth through ILC, is correctly represented in the figure.

PD-type ILC has two tunable parameters, β and γ, and the robustness filter requires the choice of a cutoff frequency $f_{\mathrm{Q,cut}}$. The influence of these parameters is investigated next. The analysis is performed with parameter settings where the convergence condition is fulfilled and hence convergence of the ILC algorithm achieved. To see the influence of one specific variable on the convergence speed and tracking performance, only one parameter was varied at a time and the others remained constant.

Influence of the P-gain β

First, the influence of the P-gain β is investigated and the results are illustrated in fig. 6.10 ($\gamma = 0$, $f_{\mathrm{Q,cut}} = 6\,\mathrm{Hz}$). β took the values $5\,{}^1/_\mathrm{s}$ (30 iterations), $10\,{}^1/_\mathrm{s}$ (30 iterations) and respectively $16\,{}^1/_\mathrm{s}$ (15 iterations). The higher the value, the faster the rate of convergence and also the smaller the final error e_∞ (see fig. 6.10a). Nevertheless, the value cannot be chosen arbitrarily large since the frequency response of eq. (6.18) grows with higher values of β (cf. section 6.2.1). The final interface displacements after convergence are displayed in fig. 6.10b to visualize the discrepancy between the RTHS tests and the reference solution. The differences between the different RTHS tests are very small and lead to a similar test fidelity. In conclusion, β should be as high as possible to achieve low final errors and low enough to fulfill the convergence condition.

[5] The seemingly high actuator bandwidth could be caused by the short signals (few data) and the few excited frequencies used in the calculation of the FRF.

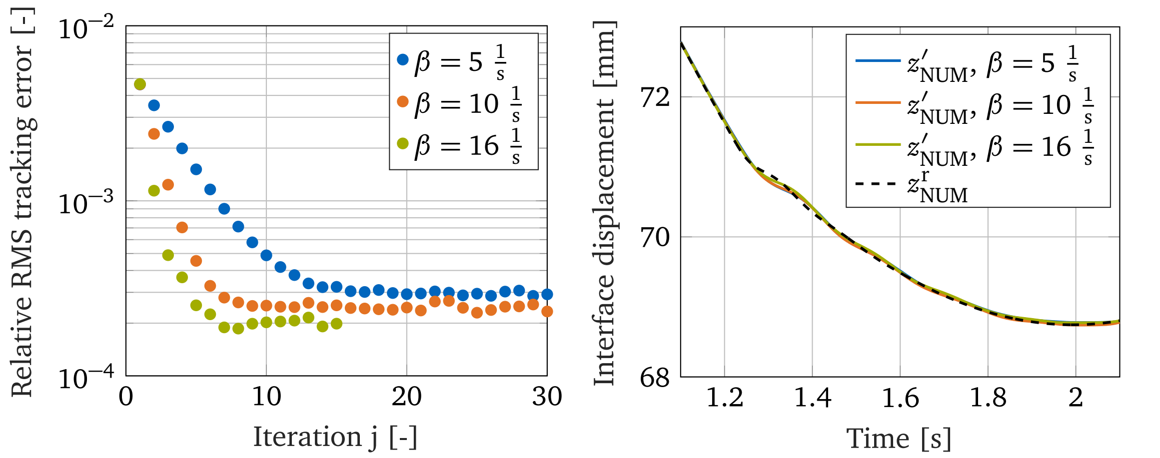

(a) Relative RMS tracking error $e_{\text{track,rel}}$. **(b)** Interface displacement after convergence.

Figure 6.10: The influence of the P-gain β is investigated.

Influence of the D-gain γ

Next, the influence of the D-gain γ is investigated ($\beta = 10\,{}^{1}/_{\text{s}}$, $f_{\text{Q,cut}} = 2\,\text{Hz}$). The used values were $\gamma = 0$ (P-type ILC), $\gamma = 1$ and $\gamma = 2$ (30 iterations each). In this case, not only the convergence of the position error $e_{\text{track,rel}}$, but also the convergence of the relative RMS velocity error is shown in fig. 6.11. The relative RMS velocity error is, similarly to eq. (4.4), calculated as

$$\dot{e}_{\text{track,rel}} = \frac{RMS(\dot{z}_{\text{NUM}} - \dot{z}'_{\text{NUM}})}{MAX(|\dot{z}_{\text{NUM}}|)}. \tag{6.22}$$

A tracking improvement can be seen on both, the position and the velocity level, and higher values of γ lead to smaller errors. In general, the RTHS results represent the reference dy-

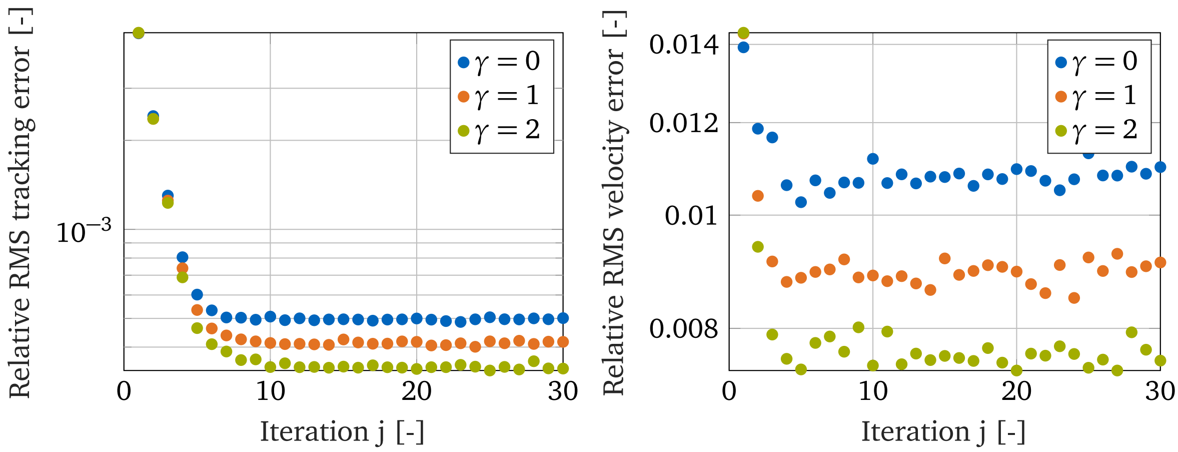

(a) Relative RMS tracking error $e_{\text{track,rel}}$. **(b)** Relative RMS velocity error.

Figure 6.11: The influence of the D-gain γ is investigated. The better tracking of the desired velocities lead to a smaller position tracking error.

namics very well and the difference between the specific values of γ is tiny. The comparison of the RTHS test results to the reference solution is visualized in fig. 6.12. Similar to the relative RMS tracking error (fig. 6.10a), also the reference error is smaller the higher γ. This is reasonable because a better tracking accuracy leads to better fulfillment of the compatibility condition and thus replication of the true system dynamics. The power error is shown

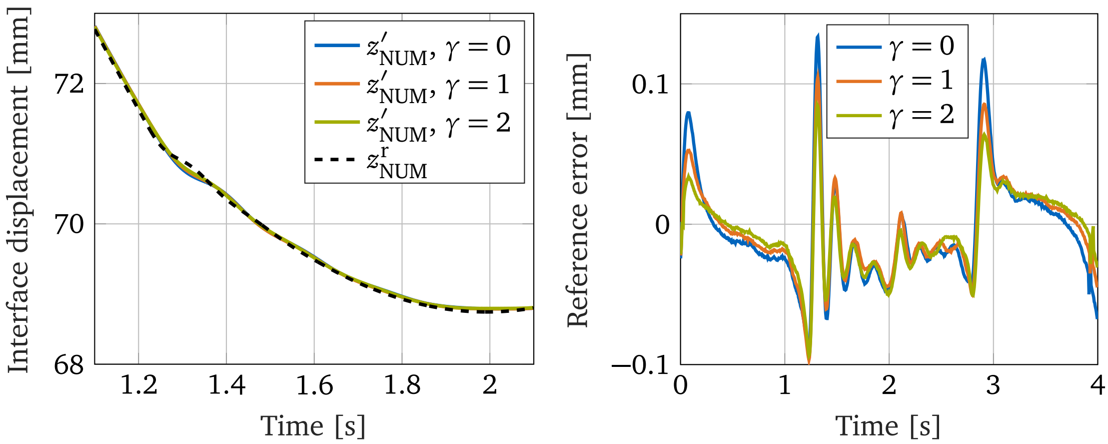

(a) Interface displacement during $t \in (1.1, 2.1)$ s. **(b)** Reference error during the RTHS test.

Figure 6.12: The reference error for different values of γ after 30 iterations.

in fig. 6.13. Compared to the sole feedback control using the cascaded controller, the power error magnitudes are smaller using ILC and the phase is shifted to the front, which indicates that the actuator dynamics are well compensated for by the ILC controller. Note that the power error (eq. (5.3)) is proportional to the velocity error $\dot{e}_{\mathrm{track}} = \dot{z}_{\mathrm{NUM}} - \dot{z}'_{\mathrm{NUM}}$. Hence, a better velocity tracking—as can be seen in fig. 6.11b—leads to smaller power error magnitudes. As was shown in fig. 6.4, higher values of γ increase the peak magnitude of the

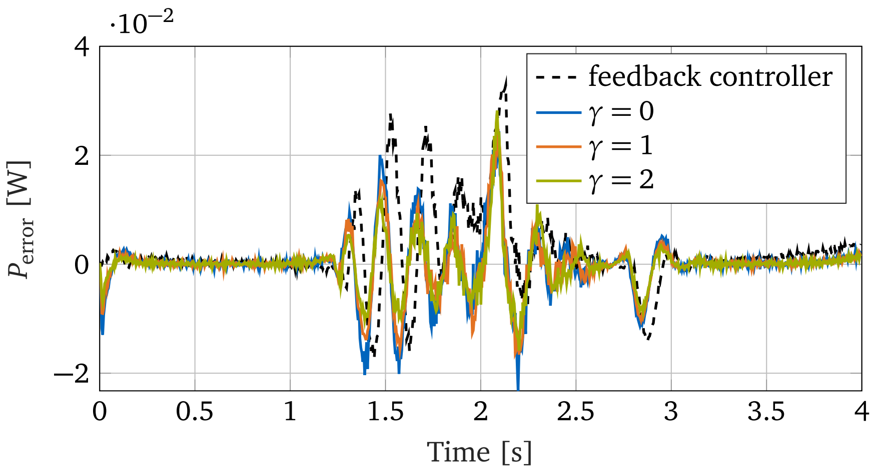

Figure 6.13: Power error for different values of γ. Due to better velocity tracking, the power error decreases for higher values of γ.

frequency response (eq. (6.18)) in case the experimental part solely consists of a spring (cf. section 6.2.1). During the contact phase, this is presumably the case if the mass of the spring is neglected and since the experimental mass is pushed to the ground and therefore does not undergo any motion. Hence, also γ ought to be chosen as high as possible for good tracking performance but low enough such that the convergence condition is fulfilled.

Influence of the Robustness Filter

The robustness filter Q is implemented as a zero-phase Butterworth filter with cutoff frequency $f_{\mathrm{Q,cut}}$. In general, signal filtering introduces delay, but zero-phase filtering circumvents this drawback. The principle of zero-phase filtering is that the filter is first applied forward and then backward in time to even the introduced delay out. A requirement is that the whole signal is available. Therefore, zero-phase filters are generally not applicable in real-time. In ILC, however, the feedforward signal for iteration $j+1$ is calculated in the pause time between iteration j and $j+1$, which means that the whole data from iteration j are already available and therefore zero-phase filters can be applied.

In the results displayed in fig. 6.14, $f_{Q,cut}$ took the values 2 Hz, 6 Hz and 10 Hz while $\beta = 5\,{}^1\!/\!_s$ and $\gamma = 0$. 30 iterations were performed. The results correspond well with the theory, see e.g. eq. (6.20), and show that the tracking performance improves more with higher cutoff frequency.

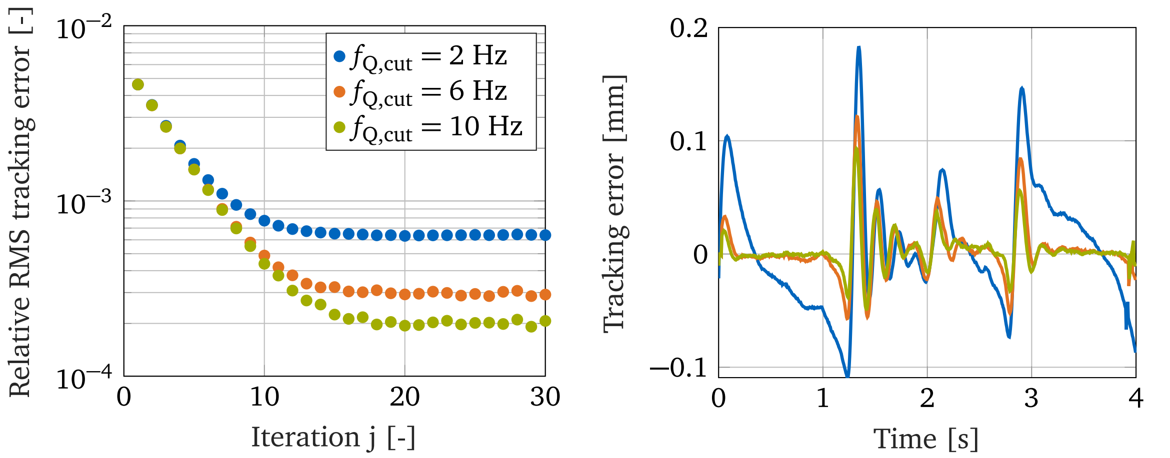

(a) Relative RMS tracking error. **(b)** Tracking error after convergence.

Figure 6.14: The influence of the cutoff frequency $f_{Q,cut}$ on the tracking performance. The legend is the same for both plots.

6.4 Combination of ILC with NPC

When ILC is applied to a system, a feedforward signal is injected from the second iteration onward. In the presented application, ILC enhances a decentralized feedback controller. In the first iteration, only this feedback controller is used to generate the actuator movement. In section 5.4.1, an investigation of the dynamical system properties on the test stability is presented. The results show that, for a damping in the dynamical system of $d_{NUM} = 200\,{}^{kg}\!/\!_s$, the RTHS test is stable when only the decentralized feedback controller is used. However, if $d_{NUM} = 50\,{}^{kg}\!/\!_s$, the RTHS test is unstable unless VFF is used as feedforward controller. Hence, an investigation is necessary how ILC performs if the test is unstable in the first iteration.

Based on the requirements in section 3.2, a powerful actuator control scheme does not only compensate the actuator dynamics effectively (high fidelity), but also ensures stability and robustness (safe tests). To achieve this, the combined use of NPC and ILC is proposed:

- **NPC** ensures test stability and introduces as much damping forces F_d as necessary to render the test stable. NPC is robust against disturbances because the damping force is calculated in real-time and the scheme is highly responsive.

- **PD-type ILC** improves the actuator tracking performance by compensating the actuator dynamics.

To investigate the efficacy of the combined use, RTHS tests were performed with the dynamical system properties given in table A.2, with $d_{NUM} = 50\,{}^{kg}\!/\!_s$, $\beta = 10\,{}^1\!/\!_s$, $\gamma = 2$, $f_{Q,cut} = 2$ Hz, $G_P = 1600\,{}^{kg}\!/\!_s$ and $T_{tot} = T_{error} = 0.1$ s. The convergence condition of ILC is fulfilled. The relative RMS tracking error and the relative RMS reference error are shown in fig. 6.15 and the corresponding time plots are given in fig. 6.16. If NPC is used, ILC is able to learn the appropriate feedforward signal, i.e. the tracking error and the reference error are reduced throughout the iterations, while having stable RTHS tests. Without NPC, the ILC does not manage to converge properly, even though the convergence condition is fulfilled. This is because the first RTHS test is unstable and exhibits large oscillations. ILC tries to track the desired oscillations better, rather than the true reference dynamics. In the presented results,

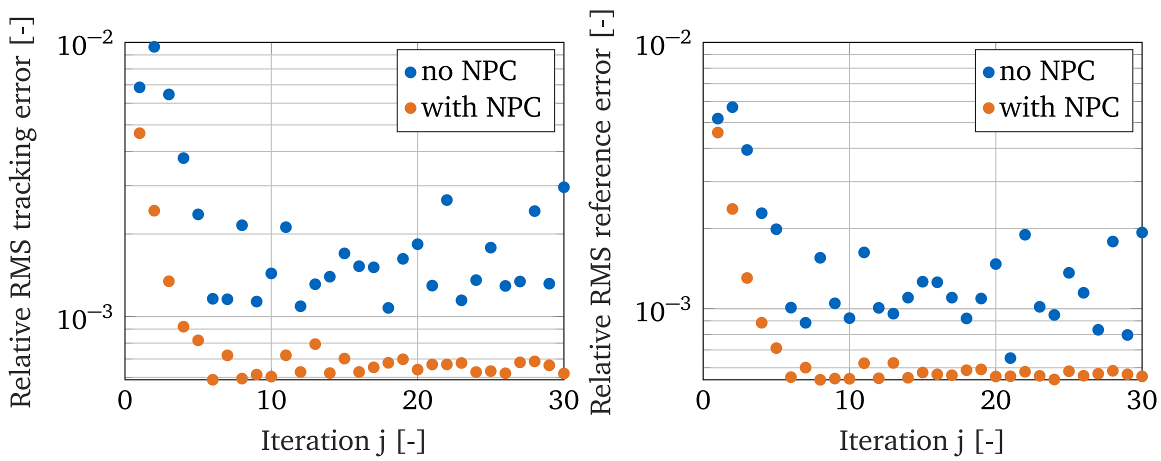

(a) Relative RMS tracking error. **(b)** Relative RMS reference error.

Figure 6.15: For $d_{\mathrm{NUM}} = 50\,\mathrm{kg/s}$, the test is unstable if only the decentralized feedback controller is used. Enhancing the RTHS control system with NPC renders the test stable.

the ILC managed to reduce the magnitude of the oscillations slightly even without NPC (see fig. 6.16b compared to fig. 6.16a). Note that, depending on the parameters of the ILC implementation, the oscillations might also grow and the test destabilized further by ILC learning. Further RTHS tests without NPC are presented in [107, 108]. In this work, the further focus is on the combined use of NPC and ILC as this offers safe and accurate RTHS tests. NPC introduces artificial damping forces to prevent the test from becoming unstable. These additional damping forces can be seen in fig. 6.17. During the first iteration, where only the decentralized feedback controller is active, the required damping forces have a magnitude up to $\approx 1.8\,\mathrm{N}$. As the ILC learning improves and the power error decreases, the additional damping force also decreases. This implies that a better actuator tracking performance leads to less NPC interference, i.e. the dynamic distortion decreases.

6.5 Discussion

This chapter proposes the use of ILC to compensate the actuator dynamics in RTHS. A convergence condition (see eq. (6.18)) is derived that facilitates the selection of the ILC tuning parameters. Furthermore, to achieve an actuator control scheme that enables safe and high fidelity RTHS tests, the combined application of NPC and ILC is proposed. This combination fulfills all requirements defined in section 3.2, maintains test stability and improves the actuator tracking performance. The successful application of NPC and ILC requires:

- **Repeatability of the RTHS test:** The RTHS tests must be repeatable with high reproducibility. Hence, the investigated system dynamics must not change between trials. Investigations like crack propagation are therefore not feasible.

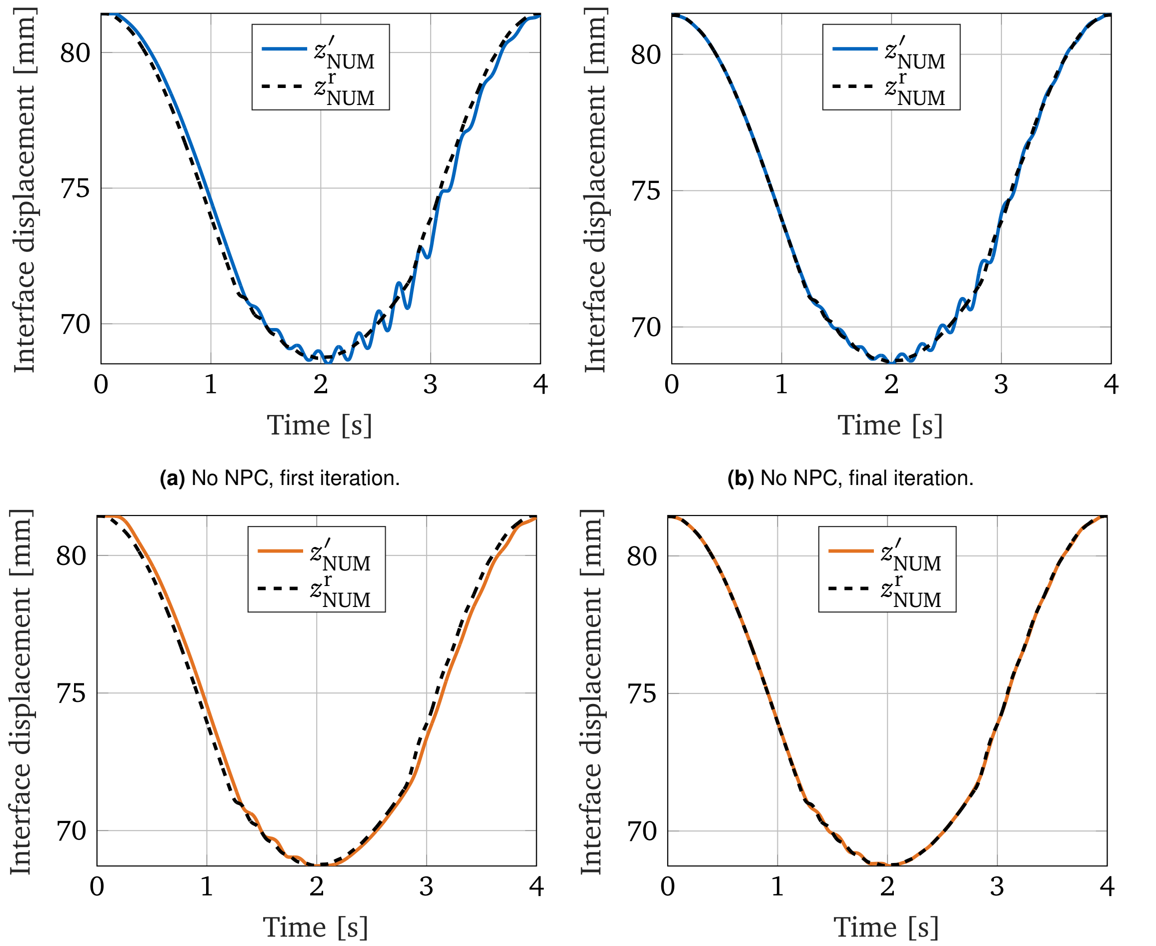

(a) No NPC, first iteration.

(b) No NPC, final iteration.

(c) With NPC, first iteration.

(d) With NPC, final iteration.

Figure 6.16: The test is unstable without NPC (blue) and can be stabilized using NPC (orange).

- **Test duration:** The performance of multiple successive tests required for ILC learning is time consuming. This should be considered when choosing this method.

PD-type ILC offers a simple implementation and overcomes highly nonlinear effects, like friction in the legs of the Stewart Platform and the changing dynamics during contact, effectively.

The derived convergence condition eq. (6.18) helps to select the appropriate values of ILC. If the dynamics of the actuator and the experimental part cannot be approximated easily, the following procedure is recommended to tune β, γ and $f_{\mathrm{Q,cut}}$:

1. Start with $\gamma = 0$ and $Q = 1$ and perform RTHS tests successively with increasing values of β. Following the literature about ILC, start with $\beta = \frac{1}{4}\,{}^{1}\!/\mathrm{s}$. If the ILC bypasses gains of the feedback controller or changes the physical unit of the signal, include this gain. Here, this is the case with the position gain K_{Pp} that transforms a position error into a velocity error.

2. Identify the frequencies that are amplified and tune the robustness filter to that frequency.

3. Adapt γ such that the relative RMS tracking error shows good convergence behavior and minimum final error.

4. Depending on the properties of the dynamical system, $f_{\mathrm{Q,cut}}$ can be raised due to the additional D-gain γ.

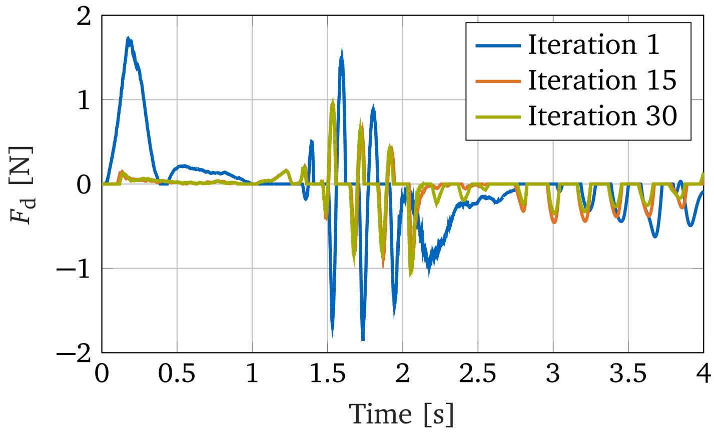

Figure 6.17: Damping force of the NPC throughout the ILC iterations.

The investigations in section 6.3 showed that different values of these variables change the ILC performance (e.g. final error) only slightly. Hence, an *optimum* tuning is ambiguous and, depending on the application, might not be required. Here, the parameters $\beta = 10\,{}^{1}/_{s}$, $\gamma = 1$ and $f_{Q,cut} = 6\,\text{Hz}$ are selected for the further investigations (see table A.4).

In literature, there exist more complex and potentially even more effective ILC schemes (see e.g. [31]) than PD-type ILC. Also, more effective passivity-based control schemes might be found in literature. Nevertheless, this work makes use of the simplicity of these methods and proves the efficacy of their combination.

Chapter 7

Adaptive Feedforward Filters (AFF)

The implementations and measurements shown in this chapter have been performed by Arian Kist and Henri Schwalm as research assistants.

In the PhD thesis by Andreas Bartl, adaptive filters were used to compensate for actuator dynamics in RTHS [15]. In adaptive control, controller parameters are adjusted so that the system output minimizes a cost function (see [111] for an introduction). In particular, the use of adaptive feedforward filters (AFF) has shown great potential in his work. There, not the controller parameters are adapted, but filter coefficients of a feedforward filter. The main focus in his work lay on dynamical systems with harmonic excitation to investigate the vibration response of structures. The applicability of AFF to the RTHS tests with contact is investigated in this chapter.

7.1 Introduction to AFF

A common application of adaptive control, or in particular AFF, is in active noise control (ANC) [120]. Here, the goal is to introduce an additional sound source (secondary noise) that cancels the noise (primary noise). The secondary noise, which is also called antinoise, is generated by a filter whose parameters are adjusted by an optimization algorithm. The optimization algorithm aims at minimizing the remaining noise. This principle is illustrated in fig. 7.1a. The primary path denotes the transfer path of the noise source to the location where noise should be canceled. For example, in case of noise canceling earphones, this is the path between surrounding noise and the user's ear. The secondary path includes the transfer path between the adaptive filter output and the considered target position. In the example, this is the transfer behavior of the loudspeaker and the path to the user's ear. The optimization algorithm adapts the filter parameters until the remaining noise is zero. The optimum solution, i.e. where the error is zero, is called Wiener solution.

The application of AFF requires the appropriate choice of the filter (e.g. harmonic basis functions, FIR filters), the optimization algorithm and the cost function. Often, a least-mean-square (LMS) algorithm is selected as optimization algorithm due to its simple implementation and low computational cost [120]. The LMS algorithm implements the concept of steepest descent, where the optimization follows along the direction of the negative gradient to find the minimum value. The LMS algorithm is considered in the remainder of the thesis. Appropriate choices of the cost function include the mean square error or the squared expected value [15].

If the secondary path follows the adaptive filter and the filter output does not act directly at the target location (cf. fig. 7.1a), the LMS algorithm must be modified to ensure conver-

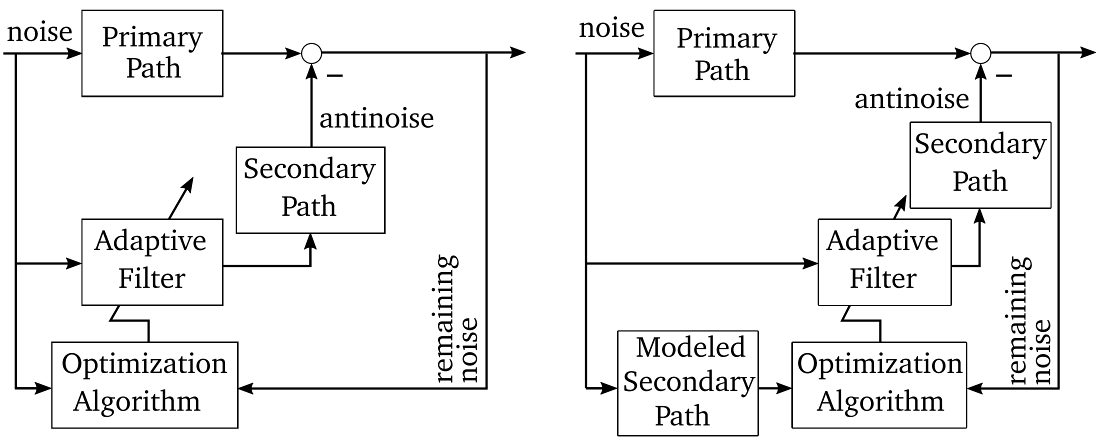

(a) Principle of ANC. **(b)** ANC with FXLMS.

Figure 7.1: In active noise control (ANC), the filter parameters of an adaptive filter are adjusted such that the remaining noise approaches zero. The diagonal arrows indicate that the filter coefficients are adapted. Figures adapted from [120].

gence. One option to do so is the filtered-X (FXLMS) algorithm [120, 168]. The input to the LMS algorithm is filtered by the transfer dynamics of the secondary path, see fig. 7.1b. In general, a correct representation of the secondary path is not available and a model has to be acquired. This model can be identified before the test and possibly adapted during the test.

Analogy for Sports Enthusiasts

ILC and adaptive control both incorporate the ability to learn and improve the performance by reducing an error. Nevertheless, they exhibit a significant difference: While ILC aims at finding the appropriate feedforward signal, adaptive controllers modify the controller parameters (the filter parameters in AFF), i.e. the transfer function. The following analogy from sports may help to understand the difference. In curling, the goal is to slide a stone on a sheet of ice as closely as possible toward the *house*, which is a circular target (right image in fig. 7.2). This is done by one player that throws the stone (left image). Then, the sweepers can influence the trajectory of the stone due to frictional heat and melting of the ice. The player that throws the stone needs to learn the delivery technique (signal) and can, after release, not further influence the motion trajectory of the stone, which is similar to ILC. The sweepers, in turn, influence the transfer path over which the stone glides and therefore, their work corresponds to adaptive control.

Figure 7.2: In curling, one player throws the stone and the rest of the team wipes the ice such that the stone approaches the target as closely as possible. Source: Martin Rulsch, Wikimedia Commons, CC BY-SA 4.0 and Panthermedia/imago images.

7.2 Application of AFF to RTHS

Adaptive control has been applied in RTHS, see e.g. [25, 40, 55, 206, 212]. In this work, the focus will be put on AFF, similar to the PhD thesis of Andreas Bartl [15]. In most of his work, structural modifications of the standard RTHS coupling (cf. in fig. 2.2) are employed, which are depicted in fig. 7.3. Here, the components are rearranged such that the control task is to minimize the difference between the output of the numerical part (z) and the experimental part (z'), which is called the gap $g = z - z' = e_{\text{track}}$. The adaptation algorithm adapts the filter parameters until $g \stackrel{!}{=} 0$, i.e. compatibility is achieved. This structure is also used in the publications by Stoten et al. with the name *Dynamically Substructured System (DSS)* [212, 213]. This rearrangement requires the knowledge of the dynamics of all involved parts for controller design. The advantage of the DSS structure compared to the RTHS structure is that the stability properties can be designed independently of the system dynamics [15, 213]. This is because a tuning of the controller parameters does not change the poles of the coupled system. With the change of the structure, also the viewpoint on the task of the actuator control is slightly changed: in the basic RTHS setup introduced in chapter 2, the control task can be described as *improve the actuator transfer behavior and minimize the tracking error*[1] and in DSS as *find the filter coefficients such that the interface of the experimental part is excited like the interface of the numerical part is excited by the external and interface forces*.

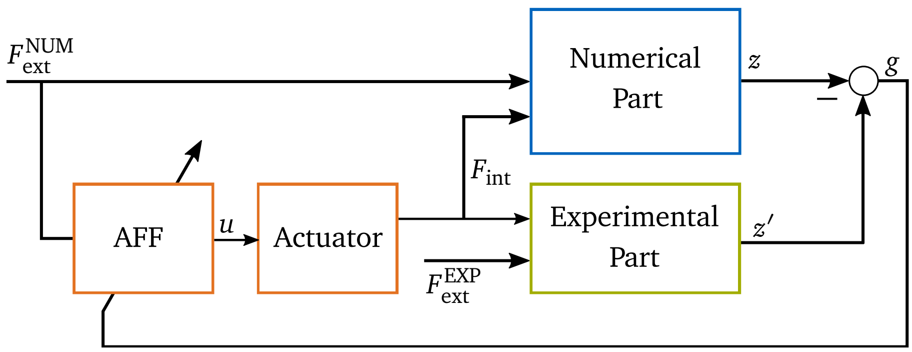

Figure 7.3: In feedforward based coupling, the RTHS structure can be modified. The rearranged structure is called DSS. The control task is to minimize the gap. Following the actio-reactio principle, F_{int} acts on the substructures with opposite sign. This is considered in the model of the numerical part. Figure adapted from [15].

One can see that the DSS structure in fig. 7.3 resembles the structure of disturbance rejection from fig. 7.1 and therefore Andreas Bartl [15] investigated the applicability of AFF to RTHS. The implementations included different filter types and optimization algorithms which are summarized in table 7.1. Filters based on harmonic basis functions can be used if a harmonic excitation and investigation of steady state can be assumed. While LMS is the simplest adaptation algorithm, more complex algorithms such as the recursive-least-squares (RLS) algorithm, can lead to faster convergence at the cost of higher complexity and higher computational cost. The specific implementation used in his work was the QR-RLS, which is an RLS algorithm utilizing a QR decomposition. Since the assumptions of harmonic excitation and steady state only hold for a limited number of engineering applications, [15] also proposed the use of finite impulse response (FIR) filters and investigated systems with arbitrary excitation and transient dynamics.

[1]This corresponds to an infinite impedance of the actuator, cf. section 2.4.

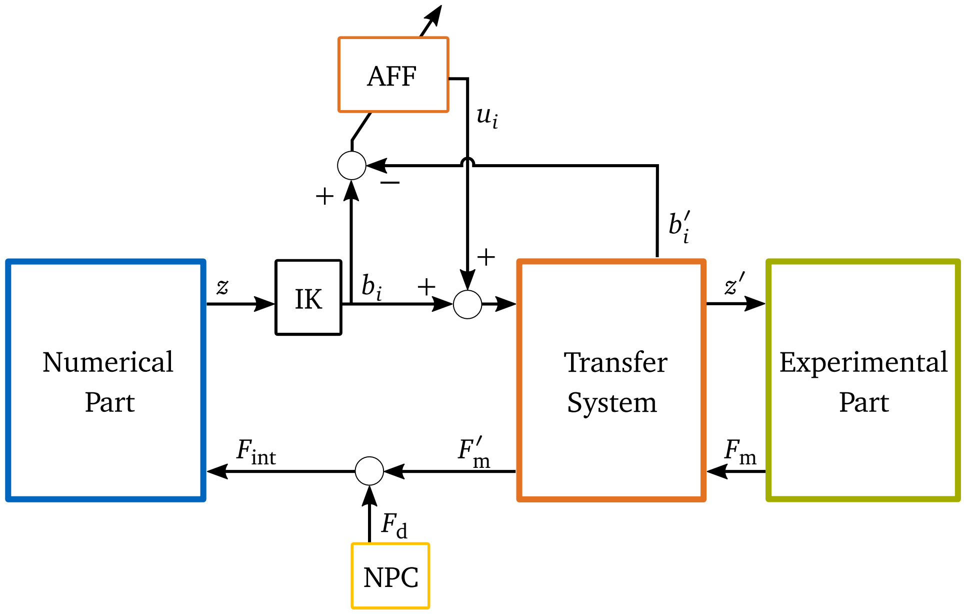

Figure 7.4: AFF used in conjunction with NPC in the RTHS setup with contact. The inverse kinematics module is denoted by IK. For the sake of clarity, the input signals to NPC are not drawn. Adapted from [15, 170].

7.3 Application of AFF to RTHS with Contact

The application of AFF to RTHS proved successful in the applications of [15, 17] and is therefore applied to the RTHS system with contact, in this work. Since the phenomenon of contact includes transient dynamics, FIR filters are selected for this application and the FXLMS algorithm is used to adapt the filter coefficients. Andreas Bartl [15] states that feedforward based coupling, which is the case when the DSS structure is applied, is not sufficient if transient dynamics cannot be neglected. Rather, enhancing the basic RTHS loop (fig. 2.2) by AFF as feedforward controller is proposed [15, 170]. To guarantee test stability, NPC should be applied. This implementation is selected in this thesis.

The resulting signal flow, where the RTHS setup (as explained in chapter 4) is enhanced with AFF and NPC, is visualized in fig. 7.4. The AFF outputs an additional displacement command u_i for each leg $i = 1...6$. The gap is defined for each leg as $g_i(t_k) = b_i(t_k) - b_i'(t_k)$ for a time instant t_k and the task of the AFF is to adapt the coefficients of the AFF such that the tracking error of the actuator is minimized. For the sake of clarity, the index i is omitted in the following equations. A FIR filter of length N_{FIR} is used, which is denoted by $\boldsymbol{\Theta}$ (vector of length N_{FIR}). A leaky FXLMS algorithm (see e.g. [120]) with the cost function

$$J(t_k) = g(t_k)^2 + \gamma_{\mathrm{LMS}} \boldsymbol{\Theta}(t_k) \boldsymbol{\Theta}(t_k)^{\mathrm{T}} \tag{7.1}$$

is used, where γ_{LMS} is a regularization term that minimizes the filter parameters $\boldsymbol{\Theta}$. Using the

Table 7.1: AFF implementations for the DSS structure presented in [15].

filter type	adaptation algorithm	comments
harmonic basis functions	LMS	simple and computationally efficient
	QR-RLS	faster adaptation
FIR filters	FXLMS	transient behavior can be investigated

adaptation gain μ_{LMS}, the general LMS algorithm writes

$$\boldsymbol{\Theta}(t_{k+1}) = \boldsymbol{\Theta}(t_k) - \frac{\mu_{\mathrm{LMS}}}{2}\nabla J(t_k), \tag{7.2}$$

where the derivative of the cost function J with respect to the parameter vector is

$$\nabla J(t_k) = -2\tilde{\boldsymbol{b}}(t_k)g(t_k) + 2\gamma_{\mathrm{LMS}}\boldsymbol{\Theta}(t_k). \tag{7.3}$$

In the FXLMS algorithm, the vector $\boldsymbol{b} = [b(t_k), b(t_{k-1}), \ldots, b(t_k - \Delta T \cdot (N_{\mathrm{FIR}} - 1))]$, which is a vector of length N_{FIR} containing the leg lengths from the previous time steps, is filtered by a model of the secondary path. The filtered vector is denoted by $\tilde{\boldsymbol{b}}$. The model of the secondary path is, in this case, the transfer function of each leg from desired to achieved displacement. In general, this transfer function can be identified during the test by a random excitation. Due to the vulnerable hardware setup, this is not done here, but the transfer function is obtained by taking the transfer functions from table 4.1 and combining them with the parameters of the cascaded feedback controller. $\tilde{\boldsymbol{b}}$ is a vector of length N_{FIR} with the components $\tilde{\boldsymbol{b}} = [\tilde{b}(t_k), \tilde{b}(t_{k-1}), \ldots, \tilde{b}(t_k - \Delta T \cdot (N_{\mathrm{FIR}} - 1))]$. Inserting eq. (7.3) into eq. (7.2) yields

$$\boldsymbol{\Theta}(t_{k+1}) = \nu_{\mathrm{LMS}}\boldsymbol{\Theta}(t_k) + \mu_{\mathrm{LMS}}\tilde{\boldsymbol{b}}(t_k)g(t_k), \tag{7.4}$$

with the leakage factor $\nu_{\mathrm{LMS}} = 1 - \mu_{\mathrm{LMS}}\gamma_{\mathrm{LMS}}$. In practice, a normalized value of $\bar{\mu}_{\mathrm{LMS}} = \frac{\mu_{\mathrm{LMS}}}{\delta + \tilde{\boldsymbol{b}}\tilde{\boldsymbol{b}}^{\mathrm{T}}}$ is desired instead of μ_{LMS}. δ is a small value such that a division by zero is excluded. The output of the AFF is the discrete convolution between the filter coefficients and the input signal

$$u(t_k) = \tilde{\boldsymbol{b}}(t_k)\boldsymbol{\Theta}(t_k)^{\mathrm{T}}. \tag{7.5}$$

The feedforward signal is calculated for each leg of the Stewart Platform, i.e. eq. (7.4) and eq. (7.5) are evaluated for each leg. This implementation can be interpreted as follows: similar to ANC, where a secondary source is tuned to cancel the noise at a target position, any position command b_i should not lead to a gap, i.e. the actuator should have infinite impedance such that $z' = z$. In comparison, for the pure feedforward based coupling in DSS from fig. 7.3, AFF tries to vanish the gap for any external excitation, which is to replicate the required dynamics.

7.4 Investigation of AFF Efficacy in RTHS with Contact

The application of AFF to the RTHS test with contact is analyzed next, similar to the investigations for ILC in section 6.3. The parameters of the dynamical system are given in table A.2 with $d_{\mathrm{NUM}} = 200\,\mathrm{kg/s}$. The Stewart Platform was controlled by the decentralized cascaded feedback controller with the controller parameters as stated in appendix A. The AFF is implemented as described previously in section 7.3. A FIR filter with N_{FIR} filter coefficients is adapted by the FXLMS algorithm for each leg $i = 1 \ldots 6$ and the filter coefficients are initialized with zeros at the beginning of the test. The filtering in the FXLMS algorithm is performed using the transfer function from desired to real leg length (see chapter 4). The implementation does not include specific knowledge about the contact scenario. The selected standard parameters are $\mu_{\mathrm{LMS}} = 0.1$, $\nu_{\mathrm{LMS}} = 0.99999$, $N_{\mathrm{FIR}} = 100$ and $\delta = 0.001$.

The tracking improvement using AFF compared to the sole use of the decentralized feedback controller is displayed in fig. 7.5a for one RTHS test. The tracking error has a maximum of 0.05 mm when the system switches from the flight to the contact phase. Figure 7.5b reveals

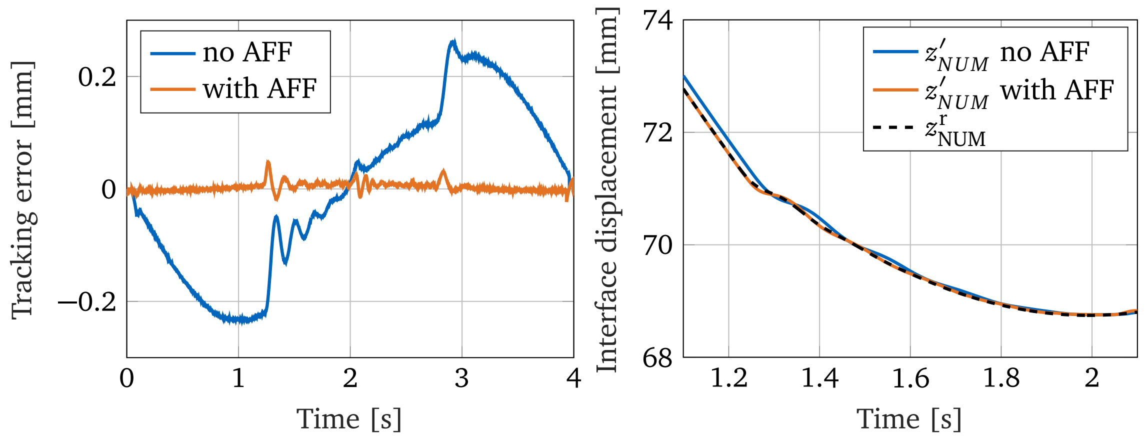

(a) Tracking error e_{track} during the whole test.

(b) Interface displacement of the reference and in the RTHS test during $t \in (1.1, 2.1)$ s.

Figure 7.5: Tracking performance and test fidelity with/without AFF.

that the improved tracking performance leads to a higher test fidelity. This figure shows the switch from the flight to the contact phase (at ≈ 1.25 s). In particular, the compensation of the delay due to AFF and the resulting high responsiveness after the switch into the contact phase is visible.

The improved tracking performance comes from an improved tracking of the desired velocity, which is shown in fig. 7.6. While the Stewart Platform is not able to achieve the maxima of the desired amplitude without AFF (left figure in fig. 7.6), there is even an overshoot visible when AFF is used (right figure in fig. 7.6). The FXLMS algorithm adapts the

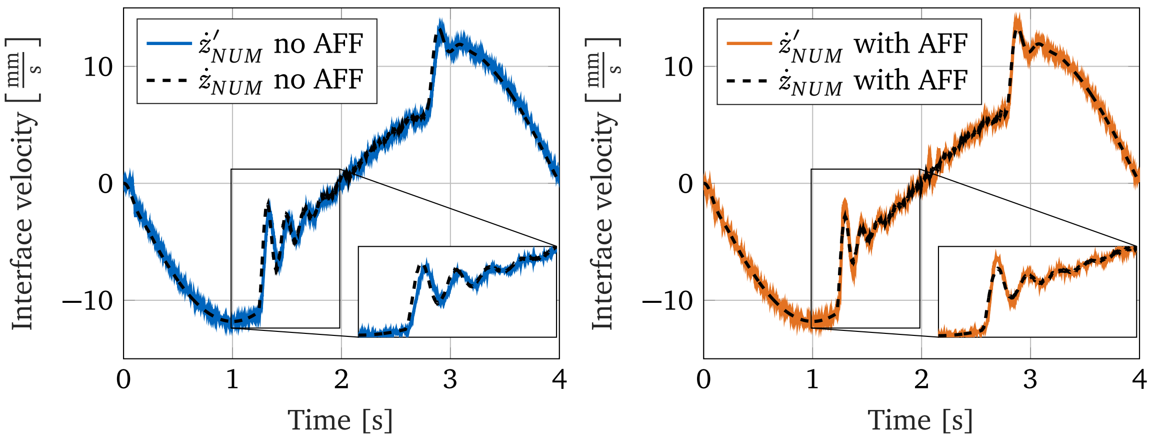

Figure 7.6: Velocity of the interface with and without AFF.

FIR filter coefficients by updating the parameter vector $\boldsymbol{\Theta}(t_k)$ at each time instance according to eq. (7.4). The adaptation process is visualized in fig. 7.7a, where only the first 20 of the $N_{\text{FIR}} = 100$ filter coefficients are shown for better visibility. The filter coefficients resemble the shape of the negative interface velocity. The remaining FIR coefficients that are not shown in the figure, show the same shape with reduced magnitude, i.e. the values that lie further in the past (e.g. $\tilde{b}\,(t_k - \Delta T \cdot (N_{\text{FIR}} - 1))$) are weighted less than the more recent samples.

The influence of the AFF on the power error is shown in fig. 7.7b. The magnitude of the power error is mostly reduced due to the AFF. Also here, the successful compensation of the time delay can be seen in the phase shift between the power error with/without AFF.

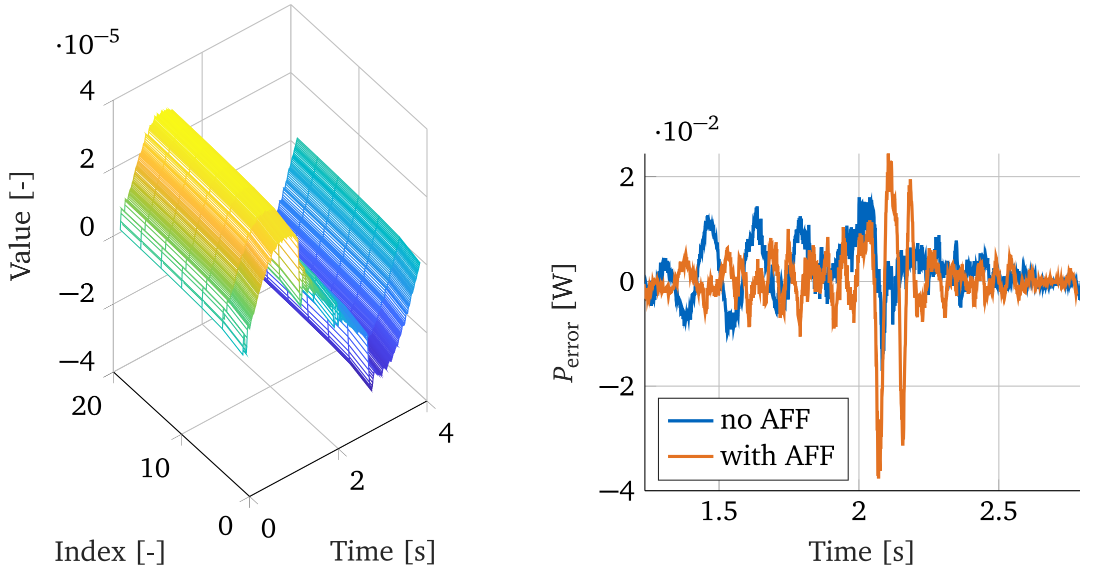

(a) Adaptation of the FIR filter coefficients during one RTHS test. The first 20 coefficients are shown.

(b) Power error with and without AFF during the contact phase.

Figure 7.7: The FIR filter coefficients and the power error are shown.

7.4.1 Parameter Investigations

The previously shown results were performed with the following AFF parameters: $\mu_{\mathrm{LMS}} = 0.1$, $\nu_{\mathrm{LMS}} = 0.99999$ and $N_{\mathrm{FIR}} = 100$, henceforth called standard parameters (see table A.5). The influence of these parameters on the RTHS results is investigated by successively changing one of these parameters. Specifically, the values of the adaptation algorithm were $\mu_{\mathrm{LMS}} = 0.01$, $\nu_{\mathrm{LMS}} = 0.999$ and $N_{\mathrm{FIR}} = 10$ and the results are presented in fig. 7.8. The results reveal that the influence of the adaptation gain μ_{LMS} is the largest. This relatively low value leads to a slow convergence rate and high remaining errors (orange in fig. 7.8). The influence of the filter length (black) and the leakage factor (green) is only barely visible and no clear distinction can be seen compared to the standard values.

7.4.2 Combination of AFF with NPC

Until now, there was no necessity to include NPC in the RTHS tests because the system with $d_{\mathrm{NUM}} = 200\,\mathrm{kg/s}$ is stable even if only the decentralized feedback controller is used. For $d_{\mathrm{NUM}} = 50\,\mathrm{kg/s}$, however, the RTHS test becomes unstable unless the actuator dynamics are appropriately compensated for. Hence, this section investigates the combined implementation of AFF and NPC for the RTHS system with contact and $d_{\mathrm{NUM}} = 50\,\mathrm{kg/s}$. The NPC was implemented using the parameters given in table A.2 and AFF was implemented using the standard parameters from table A.5.

Figure 7.9 shows the results with and without AFF (NPC is turned on in both cases). Similar to the results reported above, AFF manages to improve the tracking performance and reduce the tracking error to a maximum of 0.05 mm. The improved tracking performance also leads to significantly smaller power errors and hence smaller damping forces F_{d} that are introduced by NPC. In fig. 7.9b it is also visible that the AFF compensates for the actuator delay because a phase shift is visible between the damping forces with/without AFF during the contact phase. The figures imply that the test fidelity is increased by the combined use of NPC and AFF due to (i) the better tracking performance and (ii) the smaller additional damping forces that distort the RTHS test result (violation of the equilibrium condition).

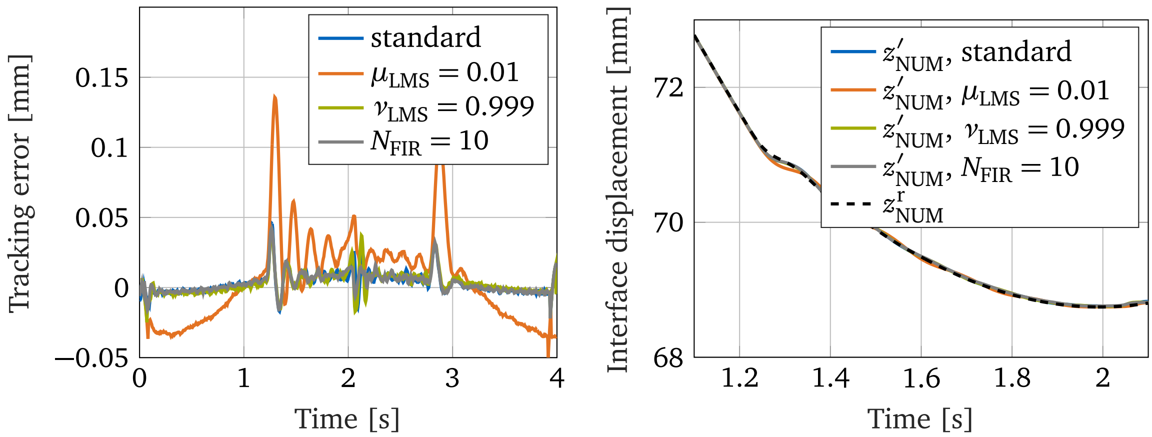

(a) Influence on the tracking error e_{track}.

(b) Influence on the test fidelity.

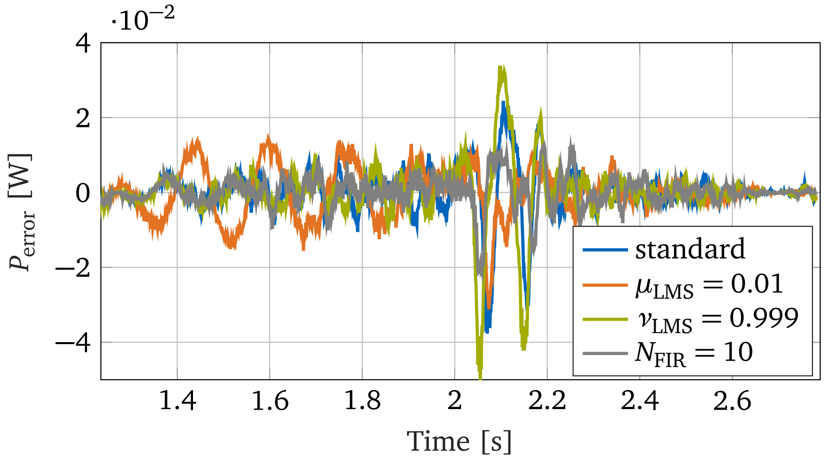

(c) Influence on the power error during the ocntact phase.

Figure 7.8: Investigation of the influence of μ_{LMS}, ν_{LMS} and N_{FIR} in the RTHS setup with contact.

7.5 Discussion

From these results it can be deduced that AFF effectively improves the tracking performance (position and velocity) and therefore the test fidelity. The AFF implementation has not been specifically adapted to RTHS with contact and can be optimized. For example, one could adapt a filter for the flight and the contact phase and switch between them. Learning the appropriate filter parameters for each phase could be done in an iteration-wise manner.

Even though AFF successfully compensates for actuator dynamics, a careful tuning of the parameters is necessary. If, for example, μ_{LMS} is too high, the filter adaptation is unstable. Results are i.a. reported in [15].

Also here, vRTHS simulations were performed and revealed similar behavior. In vRTHS, the maximum convergence rate μ_{LMS} is lower than in the real RTHS tests. Similar behavior could be observed in the vRTHS tests with ILC in section 6.3 and the reason is the modeling of the dynamics of the Stewart Platform. To improve the current implementation, a more detailed representation of the secondary path dynamics used for the FXLMS algorithm could be implemented. This involves a system identification procedure. Additionally, the pure feedforward based coupling (DSS structure) could be used in the future to make use of the improved stability properties.

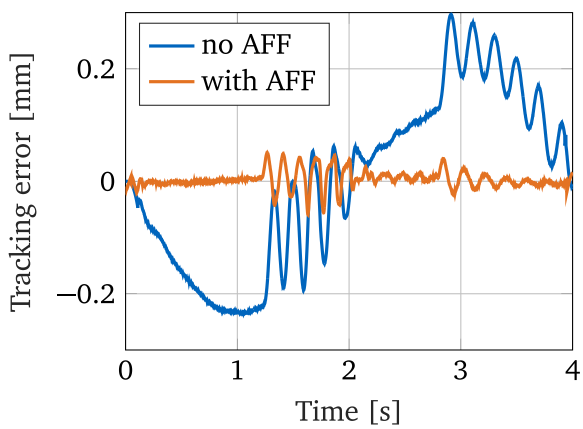

(a) Tracking error e_{track}.

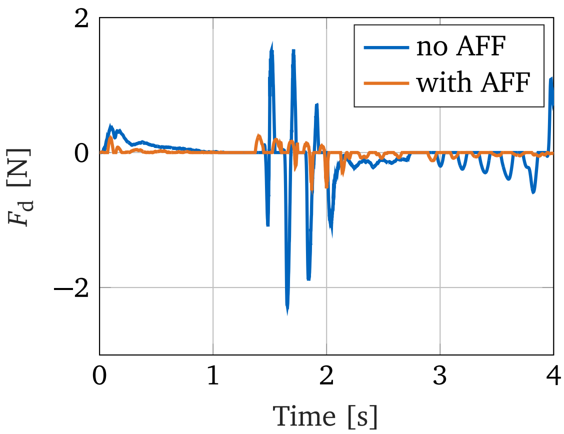

(b) The additional damping force by NPC.

Figure 7.9: The dynamical system with contact and $d_{\text{NUM}} = 50\,\mathrm{kg/s}$ is investigated using RTHS. The test is stabilized using NPC and the efficacy of AFF (without AFF in blue, with AFF in orange) is investigated.

Chapter 8

Benchmark of Control Schemes for RTHS with Contact

The results are partly published in the author's publication [108].

In the previous chapters 5 to 7, the individual efficacy of NPC, PD-type ILC and AFF for RTHS with contact was investigated. While NPC stabilizes RTHS tests and increases the test robustness, ILC and AFF are distinct feedforward control schemes to improve the actuator tracking performance—thus the test fidelity—of a feedback controlled actuator. In addition to ILC and AFF, also VFF has been introduced in chapter 4 as a simple implementation to improve the tracking performance. The goal is to find an appropriate control scheme for RTHS with contact, which is a control scheme that meets all requirements presented in section 3.2. To meet the key features of safe testing with high fidelity, NPC and the feedforward control schemes are combined. The following combinations of control schemes are highlighted in this chapter:

- NPC with PD-type ILC (cf. section 6.4)
- NPC with VFF (cf. section 5.4)
- NPC with AFF (cf. section 7.4.2)
- NPC with PD-type ILC and VFF

The damping of the dynamical system employed in the experiments in this chapter is $d_{\mathrm{NUM}} = 50\,\mathrm{kg/s}$. This RTHS test is unstable without proper actuator dynamics compensation, i.e. if only the decentralized cascaded feedback controller and the RTHS setup presented in chapter 4 are used. The same investigations were performed for the system with $d_{\mathrm{NUM}} = 200\,\mathrm{kg/s}$ (stable), but are not shown here as they do not offer novel insights. The parameters of the feedback controller used are given in appendix A.

8.1 Combination of NPC with PD-Type ILC and Velocity Feedforward

In section 6.4, PD-type ILC and NPC were combined to achieve robust and high fidelity tests. Both control schemes work independently on their distinct tasks, namely NPC stabilizes the test and PD-type ILC improves the tracking performance. To investigate how PD-type ILC interacts with additional feedforward control schemes to push the tracking performance even further, the combination of VFF and PD-type ILC in combination with NPC is investigated. The convergence results are shown in fig. 8.1. As can be seen, VFF achieves almost perfect tracking during the RTHS test. Nevertheless, ILC is able to slightly improve the tracking. In particular, ILC is able to reduce the tracking error where friction-effects dominate the actuator dynamics, which is at the start and at the turning point at $t = 2\,\mathrm{s}$. The combination of PD-type ILC with VFF combines the advantages of both control schemes: VFF achieves good tracking performance in highly dynamic phases, such as during contact, and ILC reduces the effect of iteration-invariant disturbances, like actuator friction.

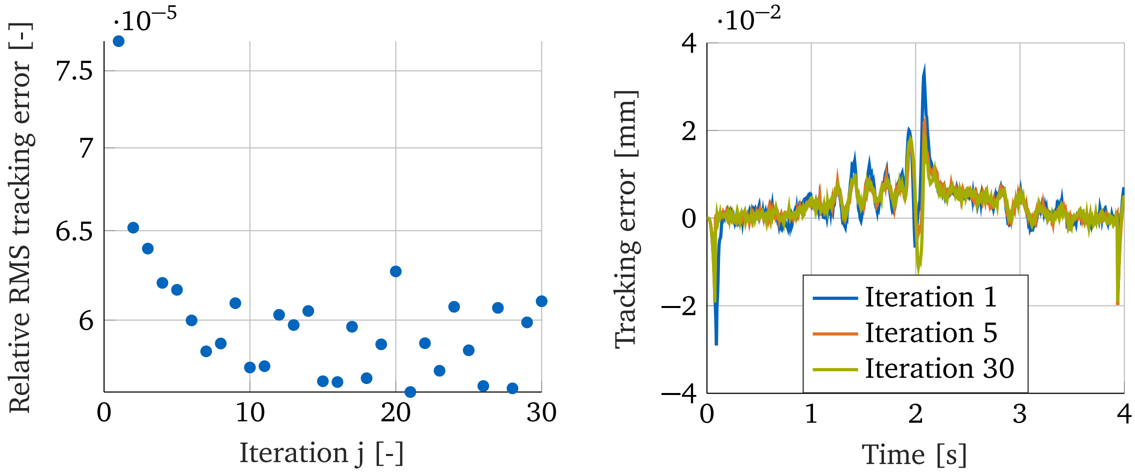

(a) Relative RMS tracking error throughout the iterations. **(b)** Tracking error for different iterations.

Figure 8.1: NPC is combined with PD-type ILC and VFF in this RTHS test.

8.2 Comparison of Different Feedforward Control Schemes

The parameters used for the implementation of the NPC, ILC and AFF are given in the tables of appendix A. These are the parameters that were determined based on the parameter studies in the respective chapters 5 to 7.

The tracking performance is shown in fig. 8.2a for the different feedforward control schemes combined with NPC. All feedforward controllers improve the tracking performance compared to the purely feedback controlled RTHS test. The magnitudes of the tracking error for ILC and AFF are comparable and have a maximum of 0.05 mm. Even though this error is already small, the tracking performance by VFF and the combination of VFF with ILC is significantly better with maximum errors of 0.03 mm and 0.02 mm at $t = 2\,\mathrm{s}$.

The interface displacements of the RTHS tests are compared with the reference solution $z^{\mathrm{r}}_{\mathrm{NUM}}$ in fig. 8.2b. The fidelity is the highest for VFF and the combination of ILC with VFF, as these displacements correspond best with the reference solution. ILC is the least responsive and lags behind the reference solution. AFF show high responsiveness and agile behavior, though the magnitudes of the oscillation are too high. This is due to the velocity overshoot which was shown in fig. 7.6. The power error is visualized in fig. 8.3 and matches with the tracking error: The better the tracking performance (VFF and ILC with VFF), the smaller the power error. The magnitudes of the power error for ILC and AFF are comparable, with the magnitude for AFF being slightly larger. Larger magnitudes result in larger forces F_{d} by the NPC and hence a higher deterioration of the test fidelity.

The feedforward schemes generate feedforward signals that are either injected on velocity level, which is the case for PD-type ILC and VFF, or on position level for AFF. To compare the feedforward signals, the AFF feedforward signal u needs to be multiplied by the gain of

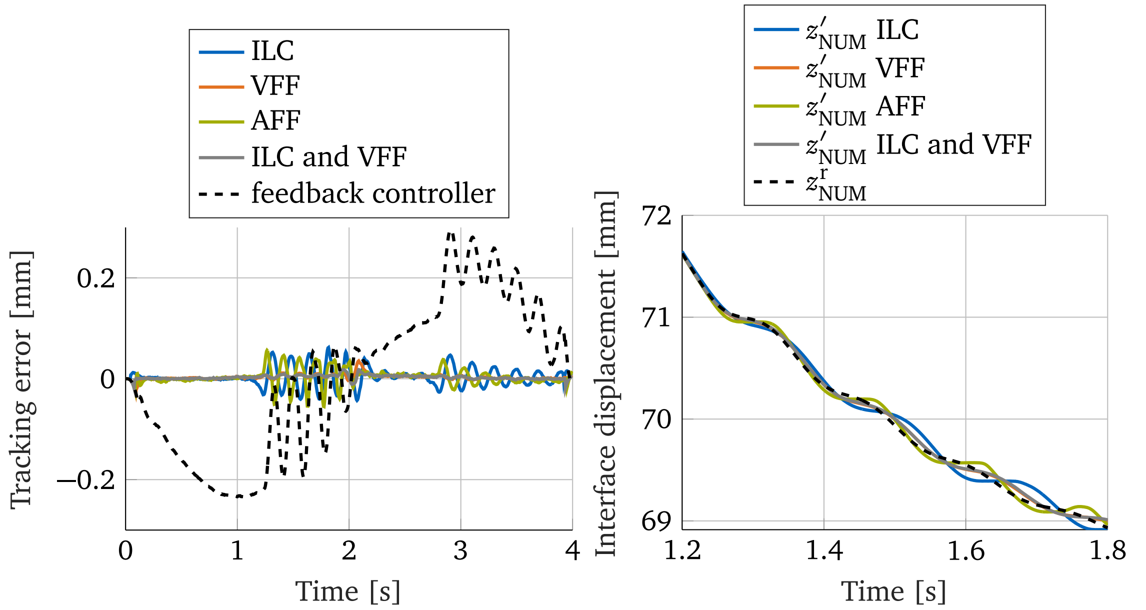

(a) Tracking error e_{track}.

(b) Interface displacement in the first part of the contact phase.

Figure 8.2: The influence of different feedforward control schemes in combination with NPC on the tracking error and the test fidelity. PD-type ILC (blue, solid line), PD-type ILC in combination with VFF (orange, solid line), VFF (green, solid line), and AFF (gray, solid line) are used to enhance the feedback controller (black, dashed line).

the position controller K_{Pp}. Figure 8.4 visualizes the feedforward control signal, where the ILC signal is given in the final iteration, i.e. after convergence. The fundamental shape and amplitude is similar for all feedforward control schemes and resembles the velocity of the interface $\dot{z}_{\mathrm{NUM}}$. This fundamental shape is superimposed by an oscillation, where the magnitude is the smallest for ILC and the largest for AFF. The oscillation frequency corresponds to the eigenfrequency of the coupled RTHS system (numerical part, experimental part and transfer system), as introduced in section 2.4.2 and will be detailed in Part II.

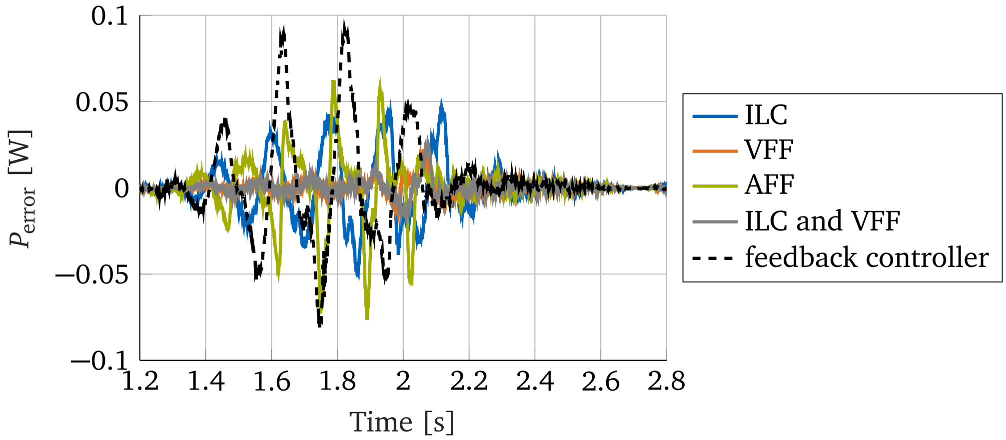

Figure 8.3: Power error during the contact phase for different feedforward control schemes in combination with NPC.

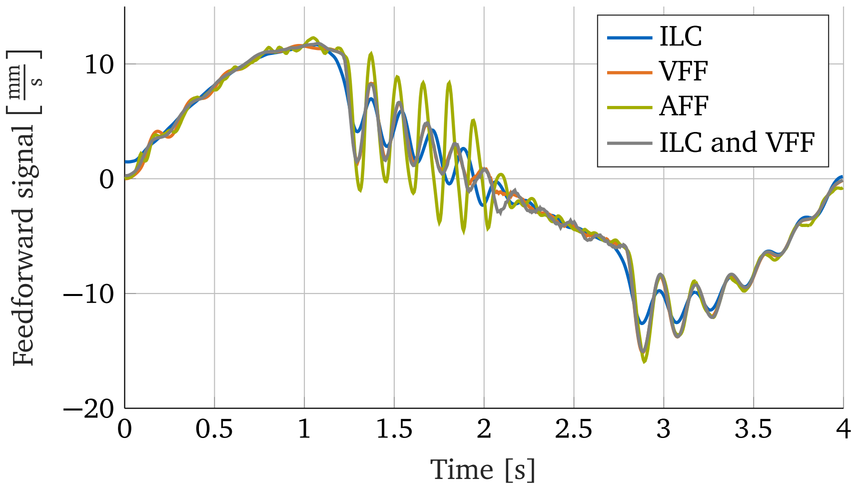

Figure 8.4: The feedforward signals for different feedforward control schemes on velocity level for leg $i = 1$.

8.3 Assessment for Contact Problems

The efficacy of the proposed control schemes and combination of them was investigated in multiple experiments. Apart from the results shown, also RTHS tests with different frequencies of the suspension ($f_d = 0.5\,\mathrm{Hz}$), different dynamical properties of the numerical mass (doubling and halving m_{NUM}, variation of k_{NUM}, reduction of damping to $d_{\mathrm{NUM}} = \{0, -10\}\ \mathrm{kg/s}$) and different h_0 (i.a. $h_0 = 0\,\mathrm{m}$ to obtain a continuous system without contact) were conducted, cf. section 4.1. Since the efficacy and the overall behavior of the presented control schemes is similar for all these results, they are not shown here.

All feedforward control schemes offer their advantages and disadvantages, which are summarized in table 8.1. In the presented application, VFF proves particularly efficient and offers high tracking performance while having little implementation effort. It is supposed that VFF performs not as well if CSI has to be taken into account and, unlike here, the actuator cannot be regarded as stiff compared to the experimental component.

To combine the advantages of different schemes, a combination of ILC and VFF, which gives the best result in the presented test, is beneficial. A general recommendation for RTHS with contact is to take the most simple implementation and to only use more complex control schemes if the required performance cannot be achieved. AFF shows highly dynamic behavior and might be further improved for RTHS with contact. The current implementation does not include knowledge about the occurring contact phenomenon. An implementation of a switching strategy, for instance, or a combination of AFF with another control scheme might improve the performance further. In case stochastic, non-repeatable dynamics such as friction (stick-slip) are present, AFF outperform ILC, which is only able to suppress repeating disturbances.

Table 8.1: Advantages and disadvantages of ILC, VFF and AFF.

	ILC	VFF	AFF
tunable	yes (β, γ, $f_{\mathrm{Q,cut}}$)	no	yes (μ_{LMS}, ν_{LMS}, N_{FIR})
system knowledge	approximation required for convergence condition	no	good knowledge required for FXLMS
time consumption	tuning, test execution	no	tuning
learning	in iteration domain	no	in time domain
contact handling	by learning	no	no
main benefit	handles nonlinearities and iteration-invariant disturbances	highly dynamic motion	high responsiveness
main limitation	requires iteration-invariant system dynamics (e.g. no crack propagation)	requires stiff actuator compared to experimental part	requires system knowledge

Chapter 9

Summary of Part I

Part I aims at improving the versatility of RTHS and expanding its application areas. This involves overcoming two major barriers in RTHS, which are **stability** even in the presence of destabilizing factors and uncertainties and **fidelity** to improve the confidence in the RTHS test. Both can be tackled by an appropriate choice of actuator control scheme—more specifically—actuator dynamics compensation.

In this work, the focus is put on dynamical systems with contact for which the attainment of stability and fidelity is particularly challenging. This is because the RTHS test should replicate all contact-induced dynamics, which are often highly dynamic. Additionally, these tests also require high responsiveness because the dynamics change depending on non-contact and contact state. The investigated dynamical system with contact as well as the hardware setup are described in chapter 4. Further requirements (see section 3.2 for a detailed summary) for methods to be widely used are their simple implementation with little system knowledge and applicability to a wide range of actuators and problems. Controlling complex dynamics with simple methods sounds contradictory, but novel control schemes incorporate the paradigm of learning or the ability to adapt and achieve high tracking performance while being simple to implement.

The application of Iterative Learning Control (ILC) to RTHS is proposed in chapter 6. In ILC, the tracking performance is improved in iteration domain by learning a feedforward signal specific for a certain task. A condition for monotonic convergence is derived, which facilitates parameter tuning. Specifically, PD-type ILC is used and the experimental results show that, if the convergence condition is fulfilled, ILC improves the tracking performance and hence the test fidelity substantially. Due to the iteration-wise learning, the changing dynamics at the instant of contact do not need to be implemented specifically, but the appropriate feedforward signal is learned automatically for the non-contact and contact phase. A limitation of ILC is that the investigated dynamics must be iteration-invariant.

Apart from ILC, also the applicability of Adaptive Feedforward Filters (AFF) is investigated for the first time in an RTHS setup with contact in chapter 7. AFF also manage to improve the tracking performance substantially. However, the implementation requires more accurate system knowledge compared to ILC. The AFF implementation used adapts the filter coefficients continuously in time and does not include any knowledge about the switch between non-contact and contact phase. As soon as the dynamics change, the tracking error increases before the adaptation algorithm is able to reduce the tracking error again. An adjustment of AFF in the future to include a switch ought to solve this problem. While feedforward controllers like ILC and AFF strive to compensate the actuator dynamics, they do not guarantee test stability. To this end, energy considerations and passivity-based control schemes are presented in chapter 5. Since Normalized Passivity Control (NPC) detects an energy increase early and only intervenes when necessary, its combined use with feedforward controllers is investigated. This combination exploits the strengths of both schemes: the feedforward control scheme deals with the actuator tracking (test fidelity) and NPC monitors the power flow from the transfer system into the coupled dynamical system and guarantees stable and robust testing. The joint use of ILC and NPC is presented in section 6.4 and of AFF with NPC in section 7.4.2. The results reveal that any feedforward control scheme and NPC work independently and stable tests (NPC) with high fidelity (ILC or AFF) can be achieved. For example, convergence of ILC is enabled when the test is stabilized with NPC, which is not possible without NPC.

In chapter 8, the efficacy of different feedforward controllers in combination with NPC is investigated. The use of ILC, AFF and the combination of ILC with velocity feedforward (VFF) is compared with respect to the tracking performance and resulting test fidelity. The combination of NPC with PD-type ILC and VFF achieves the best results, as it unites the benefits of all of them: NPC stabilizes the test, PD-type ILC improves the actuator tracking performance particularly for slow actuator movements and VFF improves the tracking performance during dynamic motion.

The presented control schemes enable robust and high fidelity testing and they can be applied to engineering applications where continuous and discontinuous dynamics are investigated as well as to stable and unstable RTHS setups. In particular, NPC, ILC and VFF do not require a system identification and only little system knowledge is necessary, which makes them easy to implement for different actuators. Hence, these schemes have the potential to be applied to many engineering applications and RTHS setups. Their application could also enable testing of complex systems, such as e.g. docking of satellites, testing of prosthetic feet or the interaction between pantographs and the overhead line.

Part II

Fidelity Assessment

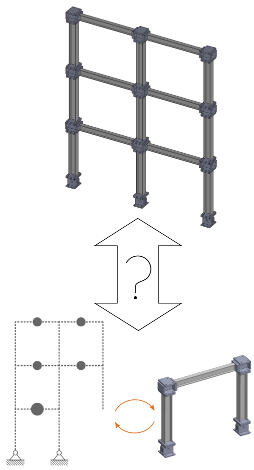

Chapter 10

Motivation for Fidelity Assessment

This chapter is based on the author's publications [109, 110].

The acceptance and broad application of RTHS for engineering applications in industry largely depends on the accuracy of the RTHS tests and their validity. The test results must replicate the dynamics of the final application sufficiently, such that the results can be trusted. Owing to the combination of numerical simulation and experimental testing and the multiple sources of errors and uncertainties in their respective space, the RTHS result will always differ from the reference solution. Accordingly, the assessment of the performed tests is of great importance and is called *fidelity assessment*. Fidelity measures tell the user how well the test emulates the true dynamical behavior of the coupled dynamical system. The major difficulty here is that usually no reference solution is available [43, 94, 145]. Therefore, the accuracy must be assessed without knowing the reference behavior—only from the known system properties and the measurable quantities during the experiment. Even though much understanding has been developed about RTHS (e.g., test stability), research and method development in the area of fidelity assessment is still quite limited. The proposed methods for fidelity assessment create a solid basis, but an all-encompassing and understandable measure has not yet been found. Hence, a long-term goal of the RTHS community is to develop acceptance criteria that tell the user whether the performed test emulated the reference dynamics accurately (accepted) or not (failed) [43].

10.1 Sources of Errors in RTHS

Errors in an RTHS test are inevitable—no matter how carefully the test is conducted. Since RTHS forms a feedback loop (see section 2.1), errors are propagated. This means that an error at time t_k influences all successive time steps $t > t_k$, which might be hundreds or even thousands. In general, the errors can be classified into systematic (epistemic) and random (aleatoric) errors and can stem from the numerical simulation or the physical components. Random errors are difficult to predict and control. They include noise (in displacement/force measurement), truncation in electrical signals at A/D conversion and they generally are of low amplitude. High frequency content of noise can excite higher modes in lightly damped structural systems unless it is compensated for by e.g. the appropriate numerical time integration scheme, added numerical damping or low-pass filters [151, 203]. In contrast, systematic errors occur with a regular pattern and include [126, 143, 151, 203]:

- Numerical Part
  - modeling inaccuracies
  - numerical integration algorithm and time step selected
- Physical Components
  - actuator control errors
  - transfer dynamics of the sensors (i.a. FTS and encoders)
  - sensor miscalibration and misalignment
  - communication and computational delays
  - flexibility of the specimen support

The detrimental effects of systematic errors are generally larger than those of random errors. In particular, a common assumption is that the transfer dynamics of the controlled actuator dominate them [42, 144]. Other systematic errors, such as sensor miscalibration/misalignment or flexibility of the specimen support can be reduced to insignificant levels by properly setting up the test bench.

The awareness for these sources of errors is already the first step to avoid them. Nevertheless, the question raises how the remaining errors influence the test fidelity. Not only the amount of these errors is of importance, but also the susceptibility of an RTHS setup. For example, the partitioning of the dynamical system (splitting ratio of mass and stiffness into numerical/experimental part) and the fastest eigenfrequency of the coupled dynamical system influence the susceptibility of the test [126, 137]. Hence, the amount of these errors as well as the dynamics of the investigated dynamical system ought to be considered in fidelity assessment.

10.2 Fidelity: A Philosophical Question

A widely accepted definition of fidelity is given in the PhD thesis by Thomas Sauder [191]: "[...] the degree to which it reproduces the behavior of the real system under study". Furthermore, a successful RTHS test is defined as "a system-level simulation that realistically incorporates experimentally-evaluated behavior [...]" by the MECHS community in [43]. These definitions leave room for interpretation and raise i.a. the following questions: What is the intended dynamic behavior and how is it measured? At what value of accuracy is the test considered accurate and acceptable? What does fidelity mean in case of chaotic dynamic behavior?

This room for interpretation is reflected in the research directions and method development found in the field of fidelity assessment. Basically there are two tracks to set up fidelity measures: the first idea is to use the desynchronization at the interface (equilibrium, compatibility) and evaluate the amount of error introduced. If the coupling of the substructures was perfect, both conditions would be fulfilled at all times. This viewpoint is chosen when the exact time response of a dynamical system to an excitation is of interest. In the case of earthquake engineering, this would correspond to knowing how a specific building responds to a specific earthquake. In contrast, for some applications, the general dynamic response is of importance rather than the specific time course. There, the test needs to replicate all system states, i.e. the RTHS test setup (specifically the QoI) must run through the same states as the reference system irrespective of the temporal ordering. This viewpoint is taken if the excitation is random and a statistical distribution should be replicated. For example, in earthquake engineering, this corresponds to the case where the failure of components during earthquake excitation is investigated. [11, 12, 58]

So the definition of fidelity depends on the goal of the test and the selected QoI [43, 58]. The present work aims at bringing together the two seemingly disparate tracks. The focus is put on the vibration response of structural systems including transient behavior. Therefore, the temporal aspect as well as the dynamic response (frequency, magnitude) are considered for fidelity assessment.

10.3 Current Assessment Measures

This section briefly reviews the state-of-the-art assessment measures that evaluate the test performance. *Assessment measures* comprise all methods validating the RTHS test performance, but do not necessarily relate the test results to the reference solution. Hence, *fidelity measures* are a subclass of *assessment measures*. Assessment measures can be classified into pre-test (before the test), online (during the test) and post-test (after the test) measures [134]. In general, pre-experiment measures evaluate the susceptibility of the RTHS configuration to errors, i.e. they indicate the minimum requirements on the transfer system to obtain a successful RTHS test. Online indicators monitor ongoing tests and if there are noticeable errors, the test can be interrupted (e.g. to avoid damaging the experimental part and the transfer system) [134, 142, 218]. Lastly, post-test measures often assess the test fidelity, i.e. how well the structural response was replicated [134, 238]. They require a reference solution.

10.3.1 Actuator Tracking Performance

As stated above, many existing assessment measures make use of the amount of local interface desynchronization. For example, the compatibility at the interface between the numerical and experimental part is used either in time or frequency domain. In this chapter, z and z' denote the time course of the commanded/achieved interface displacement (one DoF) during the whole test, i.e. $[z(t_1), z(t_2), ..., z(t_{\text{end}})]$.

The relative RMS tracking error $e_{\text{track,rel}}$ (cf. eq. (4.4))[1], the maximum tracking error (MTE) $e_{\text{track,MTE}}$ and the tracking peak error $e_{\text{track,peak}}$ are measures in time domain:

$$e_{\text{track,rel}} = \frac{RMS(z - z')}{RMS(z)} \tag{10.1}$$

$$e_{\text{track,MTE}} = \frac{max(|e_{\text{track}}|)}{max(z)} \tag{10.2}$$

$$e_{\text{track,peak}} = \left| \frac{max(|z|) - max(|z'|)}{max(z)} \right|. \tag{10.3}$$

Furthermore, the tracking error can also be assessed in frequency domain

$$e^{\text{f}}_{\text{track,rel}} = \frac{RMS(|Z| - |Z'|)}{RMS(|Z|)}, \tag{10.4}$$

where Z and Z' denote the Fourier transforms of the time course of the commanded and the real displacements z and z'.

Wallace et al. [226] proposed the visualization of the time domain tracking performance in the so-called Synchronization Subspace Plot (SSP), see fig. 10.1. In case of perfect tracking,

[1] In this part, the definition of $e_{\text{track,rel}}$ is slightly different from the definition used in Part I; the denominator is $RMS(z)$ vs. $max(z)$.

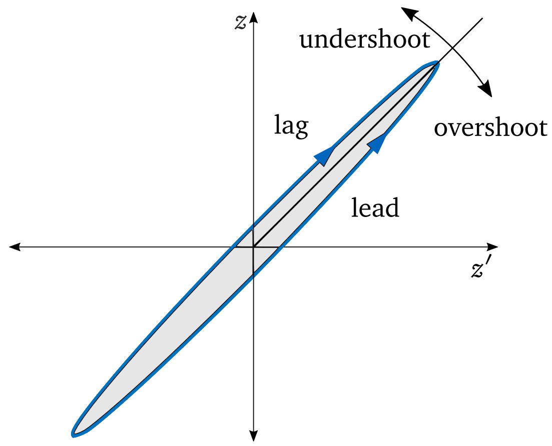

Figure 10.1: The commanded displacement z is plotted against the measured displacement z' in the Synchronization Subspace Plot (SSP). The shape of the ellipse represents the tracking performance of the actuator. Figure taken from [109].

a straight line with unit slope forms in the SSP plot. Amplitude over/undershoot affects the slope and phase lead/lag leads to an ellipse that evolves counterclockwise/clockwise. Hence, the actuator tracking performance can be inferred from the shape of the SSP plot. Based on the SSP plot and the shape of the ellipse, the tracking and amplitude indicators are set up [145]. The tracking indicator calculates the enclosed area in the SSP plot to quantify the phase lead/lag and the amplitude indicator measures the slope of the major axis of the ellipse to quantify the overshoot/undershoot.

The value of the tracking indicator depends on the magnitude of the displacement. If the actuator delay is kept constant and the magnitude of the interface displacement doubled, also the value of the tracking indicator doubles. This is undesirable because the amount of error is obviously the same. The Phase and Amplitude Error Indices (PAEI) extend the tracking indicator to circumvent this problem [94, 95]. An ellipse is fit into the SSP plot and the ellipse parameters are used to determine the phase lead/lag and the amplitude error.

The actuator tracking performance is also the basis of the Frequency Evaluation Index (FEI) [86, 238]. Also here, the tracking error is split into estimates of the phase delay and the amplitude error. The investigation uses weighted (weight l) frequency responses of the commanded and real displacements, i.e. $Z_l = |Z|^l$ and $Z'_l = |Z_l|^l$. The Fourier transforms are vectors of length n_t (length of the Fourier transformed signal vector) containing the frequency components (frequency vector f) up to the Nyquist frequency $\frac{1}{2\Delta T}$. The weighting implies that frequency content with higher magnitudes is weighted more. In Xu et al. [238], $l = 2$ was selected and found suitable. The FEI, which is a complex number, writes

$$FEI = \frac{\sum_{j=1}^{\frac{n_t}{2}} \frac{Z'_j}{Z_j} \cdot Z_{l,j}}{\sum_{j=1}^{\frac{n_t}{2}} Z_{l,j}} \tag{10.5}$$

$$A_{\mathrm{FEI}} = |FEI| \tag{10.6}$$

$$\Phi_{\mathrm{FEI}} = \tan^{-1}\left(\frac{\mathrm{Im}(FEI)}{\mathrm{Re}(FEI)}\right). \tag{10.7}$$

The amplitude and phase errors can be inferred from the FEI index as shown in eqs. (10.6) and (10.7). Perfect amplitude tracking is achieved if the actuator amplitude is $A_{\mathrm{FEI}} = 1$ and the phase error is $\Phi_{\mathrm{FEI}} = 0$. The phase error can be interpreted more easily if it is represented as a delay value τ_{FEI}. To transfer the frequency-dependent phase shift to a graspable scalar delay value, an equivalent frequency is evaluated and denoted by f_{eq}. The equivalent frequency serves as a scalar value representative for all involved frequencies in the commanded signal, which means that it is a weighted average where frequencies with a higher peak magnitude are weighted more heavily. It is calculated as

$$f_{eq} = \frac{\sum_{j=1}^{\frac{n_t}{2}} Z_{l,j} \cdot f_j}{\sum_{j=1}^{\frac{n_t}{2}} Z_{l,j}} \tag{10.8}$$

$$\tau_{FEI} = -\frac{\Phi_{FEI}}{2\pi f_{eq}}. \tag{10.9}$$

The actuator amplitude A_{FEI}, the phase error Φ_{FEI}, the equivalent frequency f_{eq} and the actuator delay τ_{FEI} are scalar values. The entire frequency range (up to the Nyquist frequency) is included in their calculation by weighting.

10.3.2 Energy Balance

As detailed in chapter 5, the substructures exchange energy/power between them at the interface. Accordingly, the interface energy can be used to set up an assessment measure. Observing the energy balance during an ongoing RTHS test was first proposed by Thewalt and Roman in [218] and elaborated on by Mosqueda et al. [150, 152] with the Hybrid Simulation Error Monitors (HSEM). In the calculation of the HSEM, the energy introduced by the transfer system E_{error} is normalized by the maximum strain energy E_{strain} $\left(HSEM^{S}\right)$ and the input energy[2] E_{input} $\left(HSEM^{I}\right)$:

$$HSEM^{S} = \frac{E_{error}}{E_{strain}} \qquad \text{with} \quad E_{strain} = \frac{1}{2} z_{max}^{T} k_{EXP} z_{max} \tag{10.10}$$

$$HSEM^{I} = \frac{E_{error}}{E_{strain} + E_{input}} \qquad \text{with} \quad E_{input} = \int F_{ext}^{NUM} \mathrm{d}z. \tag{10.11}$$

For the calculation of the strain energy, the maximum deformation during the test z_{max}, i.e. $max(z(t))$ for $t \in (0, t_{end})$, and the stiffness (in general: initial stiffness matrix) of the experimental substructure k_{EXP} are required.

A further accuracy measure using the energy balance at the interface is the Energy Error Indicator (EEI) [6]. The difference to HSEM is that the energy balance equation considers not only the energy at the interface but all energies in the numerical substructure (e.g. numerical time integration).

10.3.3 Susceptibility of RTHS Tests

How a specific amount of errors influences the RTHS dynamics depends on the dynamics of the investigated system and its partitioning. This is known as the *susceptibility*. The following characteristics are favorable and lead to less susceptible[3] RTHS tests following [28, 41, 76, 126, 133–135, 137]:

- high damping ratio (either in the numerical or the experimental part)
- low natural frequency

[2] Here, only an external force acting on the numerical substructure, i.e. F_{ext}^{NUM} is used.

[3] A susceptible test loses fidelity already in the presence of small errors/uncertainties and withstands less errors/uncertainties before becoming unstable.

- little stiffness in the experimental part
- mass in the experimental part (albeit within bounds, see section 2.2)

The influence of system partitioning into numerical and experimental part is i.a. investigated in the work of Maghareh et al. [134, 135, 137]. This research proposes the so-called Predictive Performance Indicator (PPI) and Predictive Stability Indicator (PSI), which are pre-test indicators to classify the experimental setup into extremely sensitive, moderately sensitive and slightly sensitive and gives guidelines about a favorable partitioning if one has the freedom to decide the location of the interface. The investigation uses DDE and the stability switch criterion to determine the critical delay of an RTHS system.

Apart from Maghareh et al., also Ersal et al. investigated the susceptibility of RTHS tests to partitioning in [62]. In this work, the frequency domain difference between the RTHS output and the reference solution is called distortion. A sensitivity function is set up that relates the distortion to perturbations in the data exchange due to the transfer system. The sensitivity function reveals that the best choice of the coupling point is where changes in the dynamics of the experimental part have the least effect on the dynamics of the coupled dynamical system. A further pre-test indicator to evaluate test susceptibility was proposed by Botelho and Christenson [27, 28], which makes use of robust stability analysis and the small gain theorem. Therein, an expression is derived that helps to evaluate the test stability and robustness including actuator dynamics. The condition writes

$$||T_o(s)\Delta(s)||_\infty < 1 \quad \text{robust stability} \tag{10.12}$$

$$||T_o(s)\Delta(s)||_\infty \ll 1 \quad \text{robust performance} \tag{10.13}$$

$$\text{with} \quad T_o = \frac{G_{\text{EXP}} G_{\text{NUM}}}{1 + G_{\text{EXP}} G_{\text{NUM}}}. \tag{10.14}$$

The nominal complementary sensitivity of the ideal RTHS loop is denoted by T_o and uses measured/simulated approximations of the true experimental transfer behavior $G_{\text{EXP}} \approx \hat{G}_{\text{EXP}}$. The actuator transfer behavior is modeled as a multiplicative uncertainty $\Delta(s) = G_{\text{ACT}} - 1 \approx \hat{G}_{\text{ACT}} - 1$ (again from measurements or modeling). Robust stability is fulfilled if the frequency response of eq. (10.12) does not exceed $0\,\text{dB} = 1$ and, following [28], robust performance is guaranteed if eq. (10.13) is $< -20\,\text{dB}$.

10.3.4 Surrogate Modeling

As outlined in section 10.2, there is a research track dealing with behavioral fidelity. Surrogate modeling is one of the employed methods [2, 3, 125, 191, 192]. Here, the idea is to generate a model (surrogate model) of the coupled system and validate the RTHS result against the results of a simulation with the generated models. Uncertainties (e.g. of dynamical properties or actuator tracking performance) are included and their propagation through the RTHS loop is investigated. In this approach, the susceptibility of RTHS tests to changes in system parameters is evaluated using uncertainty quantification.

10.3.5 Reference Errors

There are a few engineering applications where a reference solution is available. In case the Quantity of Interes (QoI) is the interface displacement $z^{\text{r}}_{\text{NUM}}$, fidelity measures similar to the tracking errors eqs. (4.4) and (10.2) to (10.4) can be set up. The relative RMS reference error is defined in eq. (4.6) and also the maximum reference error (MRE) $e_{\text{ref,MRE}}$, the reference peak error $e_{\text{ref,peak}}$ and the RMS reference error in frequency domain $e^{\text{f}}_{\text{ref,rel}}$ are obtained by replacing z by $z^{\text{r}}_{\text{NUM}}$ in eqs. (10.2) to (10.4).

10.3.6 Discussion of Current Assessment Measures

The presented accuracy measures attempt to evaluate the test performance in different ways. While the assessment measures based on the actuator tracking performance (see section 10.3.1) are easily applicable and evaluate the fulfillment of the compatibility condition between the numerical and experimental substructure, there are some limitations. For example, error propagation over the course of the RTHS test is not considered [238]. Furthermore, the influence on the system dynamics—which depends on the susceptibility of the test setup—is not deducible from the values of these accuracy measures and thus an interpretation of the values is difficult. The applications involving the SSP plot furthermore assume frequency-independent actuator delay, which is not true for many applications. Hence, a threshold value or an acceptance criterion cannot be inferred from them.

Similar shortcomings can be reported for the accuracy measures based on the energy balance (see section 10.3.2). Mosqueda et al. [152] proposed using a threshold of $HSEM^{S} \leq 0.05$, i.e. $E_{\text{error}} \leq 0.05 \cdot E_{\text{strain}}$, as a rule of thumb for an acceptance criterion. Nevertheless, an interpretation of the influence of a certain energy error on the test result is difficult and the specific values vary for different RTHS setups. Thus, a bridge between the numerical value of the indicator and the physical meaning needs to be built.

The pre-test indicators presented in section 10.3.3 address the influence of the partitioning and dynamical system properties on the success of a planned RTHS test. As these methods are applied before a test, they do only provide information about how critical the RTHS setup is, but do not assess the test result and the achieved test fidelity. Furthermore, they require knowledge/an approximation of the dynamics of the experimental part as well as of the transfer system.

Probably the most comprehensive approach so far is surrogate modeling (section 10.3.4), since both the coupled dynamical system and the possible errors and uncertainties are included. In addition, the approach considers error propagation. However, the implementation of this methodology requires a good understanding of the system dynamics (transfer system and experimental component), which is in general not available, as well as the magnitude and distribution of the expected occurring errors.

Lastly, reference errors were explained in section 10.3.5. Their largest drawback is that, in general, a reference solution is not available. Furthermore, similar to the accuracy measures based on the actuator tracking performance, the interpretation of the numeric values is difficult. Note that the relative RMS tracking/reference errors were used in Part I to assess the tracking/fidelity improvement by the proposed delay compensation schemes. They proved appropriate for that purpose, as these investigations did not focus on the specific values of the errors or the influence of the tracking error on the test result.

10.3.7 Requirements for Novel Assessment Measure

In view of the need for powerful fidelity measures and the drawbacks of the assessment measures that have been proposed so far, the following requirements can be formulated for a novel fidelity measure:

- **Fidelity assessment:** A novel method should assess the fidelity, which means relate the RTHS test result to the reference solution. This implies that the influence of several sources of errors on the QoI or system dynamics is investigated (in contrast to e.g. assessment of actuator tracking). Therefore, not only the amount of the errors, but also the system dynamics and the partitioning in the RTHS test must be included.

- **No reference solution:** Reference solutions are in general not available for RTHS setups. Therefore, novel fidelity measures should not require a reference solution.

- **No system identification:** System identification of the transfer system and the experimental part should not be required. This is not only because a system identification is cumbersome and time-consuming, but because the identification is often not accurately possible and the main reason why RTHS is performed in the first place.

- **Understandable:** The output of the fidelity assessment should be easily graspable. This includes that the influence of errors on the RTHS test result must be simple to interpret. It also means that the results can be compared among different RTHS setups.

- **Straightforward implementation:** The implementation must be simple so as to reduce the effort and make the application feasible without major hurdles.

- **Widely applicable:** The method should work for as many RTHS setups and dynamical systems as possible. Therefore, it should offer the possibility to be extended and adjusted for specific applications.

10.4 Objective of Part II

Even though current assessment measures offer a solid basis to understand the fundamental aspects of fidelity assessment, there are yet no powerful methods available that fulfill the above mentioned requirements. Many of them do not relate the amount of errors to the RTHS test result and thus the test fidelity. A long-term goal of the RTHS community is to find acceptance criteria to easily evaluate the test performance. This allows to give the user confidence that the test sufficiently emulates the real system dynamics of the final application and the test results can be trusted. Here, the objective is to work into this direction and set up a framework for fidelity assessment. The method ought to include not only information about the amount of errors, but also consider the susceptibility of a test setup and the influence on the test result. In particular, a novel method fulfilling the requirements stated in section 10.3.7 while circumventing the disadvantages of the presented methods is targeted in this work.

The vibration response of many engineering applications is of great importance. Therefore, the presented methodology is derived based on this type of problem. This means that the methodology is used to evaluate how well the real vibration behavior has been emulated using RTHS. Specifically, the vibration magnitude, frequency and damping are considered. Moreover, to show the application of the proposed methodology, the main assumption is that the dominating error source in the RTHS loop is the actuator dynamics. This assumption is not true for all RTHS setups but holds e.g. for the presented setup in Part I. Already at this point it should be mentioned that the presented methodology is not limited to the use cases *vibration behavior* and *actuator as main error source* and can also be applied to other QoIs and error sources.

The FACE (Fidelity Assessment based on Convergence and Extrapolation) method is developed in this thesis. In the following chapter 11, the key idea is presented. An investigation how actuator dynamics influence the observed vibration response of an RTHS test is presented. In particular, the special cases of a pure mass and spring experimental substructure are detailed.

Chapter 12 presents three different application examples of the FACE method. Firstly, a linear coupled mass-spring-damper system is investigated with vRTHS. Secondly, the Benchmark control problem, which is commonly used by the RTHS community, is used to investigate the applicability of the FACE method. This represents a three-story building under earthquake excitation. Finally, the FACE method is applied to the RTHS system with contact (real RTHS tests) presented in Part I.

A summary of the FACE method, the results and a discussion of its potential are given in chapter 13. This chapter details the benefits and shortcomings of the FACE method and gives a discussion about future research questions.

Chapter 11

Fidelity Assessment Based on Convergence and Extrapolation (FACE)

Parts of this chapter have been published in the author's publication [110].

The goal of Part II is to set up a fidelity measure without a reference solution required. This sounds contradictory, considering that *fidelity* refers to how well an RTHS test emulates the true dynamics. Accordingly, the question arises whether the reference solution can be determined. This is the fundamental idea of the presented methodology.

11.1 Key Idea: Convergence

When performing an RTHS test, one knows that there are inevitable errors in the RTHS loop. If the errors are small, they deteriorate test accuracy. If they are large, though, test stability is even jeopardized[1]. This implies that, within a certain range of errors, RTHS tests can be performed and the system behavior investigated. The presented idea is to extrapolate the system behavior outside the known area by thoroughly investigating within the known range.

This approach is illustrated in fig. 11.1. There, the susceptibility of the RTHS test result q to an error e shall be investigated. With prudent and best possible (for the hardware setup used) test execution, the minimum achievable error is e_{min}. Since the error cannot be smaller than e_{min}, the system behavior is unknown between $\mathrm{e} \in (0, e_{\mathrm{min}})$. The test tolerates a maximum error of e_{crit} before becoming unstable. Hence, the area $\mathrm{e} > e_{\mathrm{crit}}$ is also non-explorable and thus remains unknown. The area between e_{min} and e_{crit} is indicated as the explorable area (or further also called known area) because the error can take any (discrete) value within these bounds. This means that multiple RTHS tests can be performed and the RTHS result q changes depending on e. Hence, the influence of the error source on the system dynamics, that is the sensitivity with respect to this error, can be analyzed in this range. If e is the main error source and the other sources of errors are negligible, the RTHS test would yield the reference solution $\hat{q}$ for $\mathrm{e} = 0$. If the explorable area is investigated thoroughly, an interpolation can be done within this area. This means that the relation $q = h(\mathrm{e})$ can be learned, where $h(\cdot)$ denotes the functional interrelationship. Then, the value of the reference $\hat{q}$ can be approximated by extrapolation (q_{pred}) using the interpolated function $h(e)$.

The approach assumes that, as long as e_{min} is sufficiently small, the reference solution

[1] What is *small* and *large* depends on the investigated dynamical system.

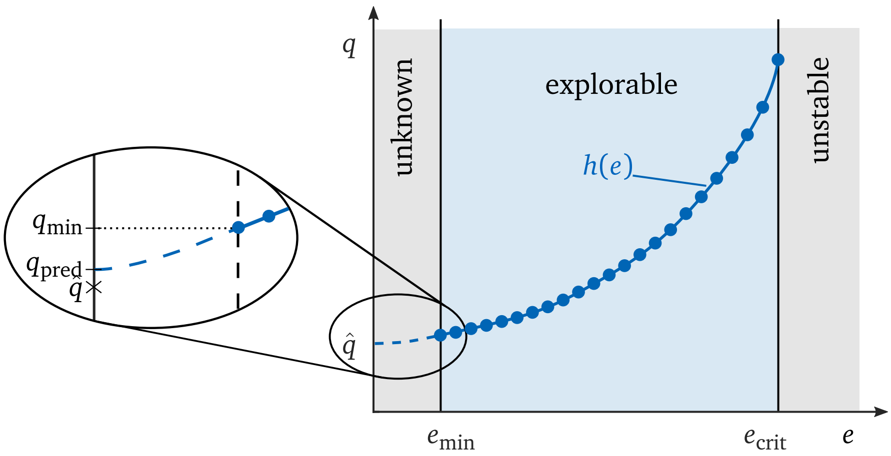

Figure 11.1: The key idea of the FACE method is to explore the area between the minimum achievable error e_{min} and the stability limit e_{crit} to investigate how the error influences the RTHS result q. The dots denote the measurement points that are used for interpolation to find $q = h(e)$. The true reference solution $\hat{q}$ is marked with a cross and the extrapolated reference is denoted by q_{pred}. Ideally, $q_{\text{pred}} = \hat{q}$. Then, the RTHS result at e_{min}, i.e. q_{min}, can be compared to q_{pred} and validated. Figure taken from [110].

is predicted accurately, i.e. $q_{\text{pred}} \approx \hat{q}$. Then, the RTHS result at the minimum error, which is $q_{\text{min}} = h(e_{\text{min}})$ can be validated against the predicted result q_{pred} and a decision taken, whether the test has sufficiently emulated the reference dynamics. Both, the amount of error e and the RTHS result q are scalars. The amount of error e could e.g. be the equivalent time delay or another accuracy measure from section 10.3 as well as a dynamic system property. The RTHS result is denoted by q and might be a measure of the system dynamics or of the QoI. The appropriate selection of e and q depends on the application, the desired RTHS result and the selected QoI.

Since this framework implements the idea of convergence towards the reference solution and makes use of extrapolation in the unknown area, this fundamental method is termed *Fidelity Assessment based on Convergence and Extrapolation*, or short *FACE*. In the current Part II, this idea is pursued and its applicability as novel fidelity measure is examined. In particular, a possible selection of the quantities e (error measure) and q (measure of test result) is presented and the creation of the convergence plot (fig. 11.1) shown. To this end, the following section illustrates how the dynamics of the transfer system affect the RTHS result.

11.2 Influence of Actuator Dynamics on RTHS Dynamics

In many engineering applications, the vibration response is of particular interest and often investigated with RTHS tests. Even though actuator dynamics might not be the major error source in every RTHS setup, their influence is crucial on the observable dynamic behavior in RTHS experiments. The importance of the actuator dynamics for the accuracy of RTHS tests is evident in the large amount of literature dealing with their compensation (cf. section 3.3). The understanding of how the actuator dynamics affect the observable vibration behavior in the RTHS experiment is now built. As briefly described in chapter 2, the coupled RTHS loop can be viewed from the Dynamic Substructuring perspective (see section 2.4.1) and also from a control theoretical perspective (see section 2.4.2). From both view points it is obvious that the actuator should have infinite impedance[2], which means compatibility should be fulfilled at all times and $\hat{G}_{\text{ACT}} = \frac{Z'(s)}{Z(s)} = 1$. Depending on the partitioning of the dynamical system in the RTHS test, the effect of actuator dynamics is different, see section 2.2.2. The two special cases of mass vs. spring experimental part are presented next. The investigated dynamical system is a coupled MSD system (numerical part: MSD system, experimental part: either spring or mass). For $t < 0$, the system is in static equilibrium. For $t \geq 0$, an external force $F_{\text{ext}}^{\text{NUM}} = -1\,\text{N}$ acts on m_{NUM} compressing the coupled MSD system. The results illustrated are from vRTHS simulations. The transfer behavior of the FTS is assumed to be ideal.

11.2.1 Spring Experimental Part

As described in section 2.2, actuator delay has a destabilizing effect if the experimental part consists of a stiffness (in position-based RTHS). Firstly, the influence of a pure actuator time delay $\tau = \{0.005, 0.01\}$ s is investigated. The nominal complementary sensitivity function of the coupled RTHS loop writes $\frac{\hat{G}_{\text{NUM}}\hat{G}_{\text{ACT}}\hat{G}_{\text{EXP}}}{1+\hat{G}_{\text{NUM}}\hat{G}_{\text{ACT}}\hat{G}_{\text{EXP}}}$. The dynamics of the coupled loop are defined by the characteristic function, which is the denominator of this transfer function. Figure 11.2a visualizes the magnitude of the complementary sensitivity function and fig. 11.2b the corresponding time domain course of the interface displacement and the reference solution. For such a single DoF (SDOF) system, [41, 98] reported that the delay has an effect like negative damping. This is visible in the growing oscillation magnitude for higher delay values in both the frequency and time domain.

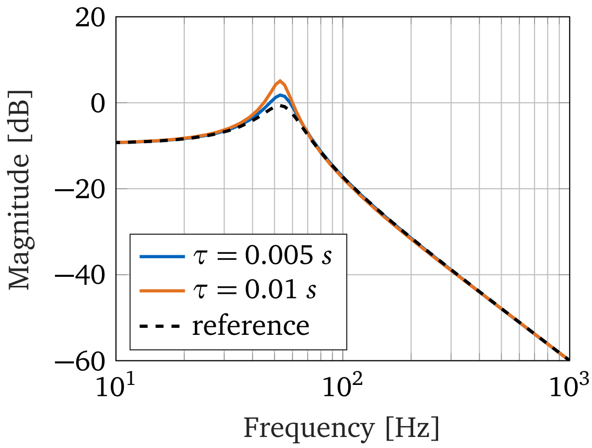

(a) Magnitude of the sensitivity function when the actuator is modeled as a pure time delay τ.

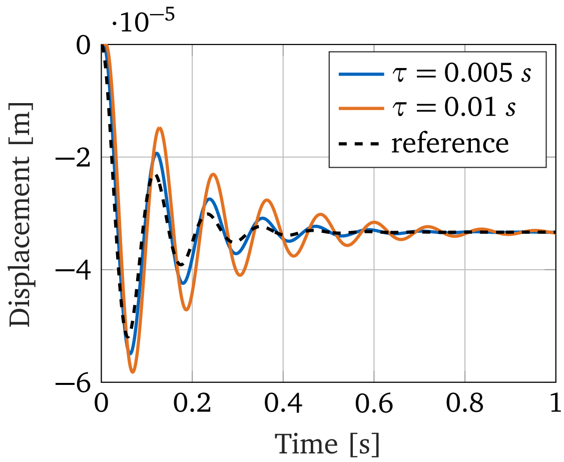

(b) Interface displacement over time.

Figure 11.2: The actuator dynamics are modeled as a pure time delay τ and the influence is shown for the case of a stiffness in the experimental part ($k_{\text{EXP}} = 10^4\,\text{N/m}$, $m_{\text{EXP}} = d_{\text{EXP}} = 0$). The numerically simulated part is a linear MSD system with $m_{\text{NUM}} = 10\,\text{kg}$, $k_{\text{NUM}} = 2 \cdot 10^4\,\text{N/m}$ and $d_{\text{NUM}} = 200\,\text{kg/s}$.

Secondly, the influence of frequency-dependent actuator dynamics $\hat{G}_{\text{ACT}}$ is investigated. The transfer behavior is modeled as a first order dynamical system $\hat{G}_{\text{ACT}} = \frac{1}{T_{\text{ACT}}s+1}$ with the time constants $T_{\text{ACT}} = \{0.001, 0.01, 0.03\}$ s. The smaller the time constant, the higher the actuator bandwidth: the corresponding corner frequencies are $\{159, 15.9, 5.3\}$ Hz. Figure 11.3a shows the magnitude of the complementary sensitivity function and fig. 11.3b the time domain response of a vRTHS test. One can recognize that the reference dynamics are met well for $T_{\text{ACT}} = 0.001\,\text{s}$ in frequency and time domain. This is because the actuator bandwidth

[2]In reality, it is sufficient if the condition $\hat{G}_{\text{ACT}} = 1$ is fulfilled within the frequency range of interest, i.e. if the actuator bandwidth is larger than the fundamental dynamics of the coupled dynamical system.

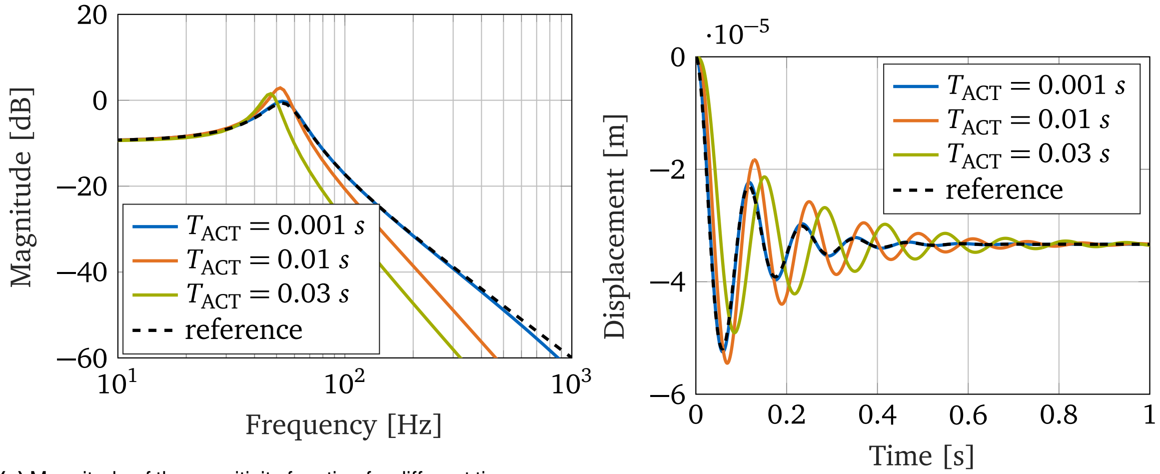

(a) Magnitude of the sensitivity function for different time constants T_{ACT}.

(b) Interface displacement for different time constants T_{ACT}.

Figure 11.3: The actuator dynamics are modeled as a first order system $\hat{G}_{ACT} = \frac{1}{T_{ACT}s+1}$ and the influence is analyzed for the case of a stiffness in the experimental substructure ($k_{EXP} = 10^4\,\mathrm{N/m}$, $m_{EXP} = d_{EXP} = 0$). The numerically simulated part is a linear MSD system with $m_{NUM} = 10\,\mathrm{kg}$, $k_{NUM} = 2 \cdot 10^4\,\mathrm{N/m}$ and $d_{NUM} = 200\,\mathrm{kg/s}$.

is much higher than the fundamental dynamics of the coupled system (analytical eigenfrequency of the reference system is 8.57 Hz). For larger time constants, however, the observable eigenfrequency decreases, which is visible both in frequency and time domain. This is because the controller bandwidth, i.e. the frequency range in which $\hat{G}_{ACT} \approx 1$, defines the frequencies that are transmitted between the numerical and the experimental substructure. Put in other words, the actuator acts like a filter. If the fundamental dynamics of the reference system are faster than the motion ability of the actuator, the frequency content is not replicated appropriately and the frequency behavior observable in the RTHS experiment is lower than the frequency content of the true dynamics.

11.2.2 Mass Experimental Part

When the experimental part comprises a mass, the effect of actuator time delay can be stabilizing, like positive damping (see section 2.2)[3]. Figure 11.4a shows the magnitude of the complementary sensitivity function for the case that the actuator is modeled as a pure time delay $\tau = \{0.005, 0.01\}$ s. The interface displacements for the corresponding vRTHS simulations are given in fig. 11.4b. In contrast to the figs. 11.2a and 11.2b, the oscillation magnitudes decrease in the presence of actuator time delay due to the effect of positive damping.

In case the actuator dynamics are that of a first order system (with time constant T_{ACT}), the observable dynamic behavior also differs compared to the case of a stiffness experimental substructure. Namely, an increase of the eigenfrequency can be observed in the figs. 11.5a and 11.5b and the actuator bandwidth cannot be interpreted as a filter anymore. This can be explained by the illustration of complex forces in section 2.2: in case of a mass experimental substructure, any actuator dynamics/delay lead to higher measurable interface forces. Disregarding the RTHS loop dynamics, this leads the numerical part to believe the experimental part had higher stiffness. Since stiffer dynamic systems have a larger eigenfrequency, consequently the coupled RTHS test also has a larger natural frequency. Hence, the overall effect of actuator dynamics in an RTHS test with a mass experimental substructure is twofold: Firstly, the RTHS test is stabilized due to added positive damping by m_{EXP}. Increased damping leads

[3]This statement is not valid without restrictions, see section 2.2.2.

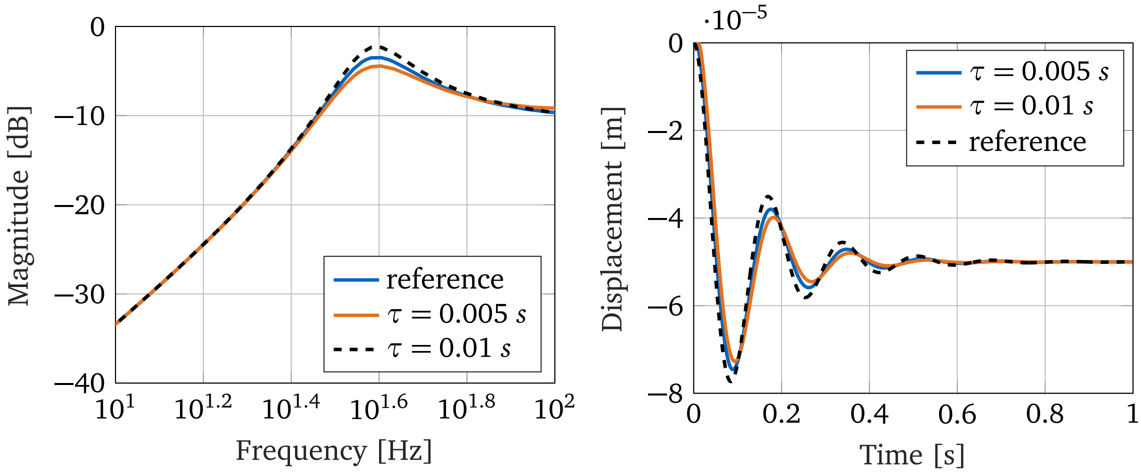

(a) Magnitude of the sensitivity function.

(b) Interface displacement over time.

Figure 11.4: The actuator is modeled as a pure time delay τ and the influence on a mass in the experimental part is illustrated ($m_{\text{EXP}} = 0\,\text{kg}$, $k_{\text{EXP}} = d_{\text{EXP}} = 0$). The numerically simulated part is a linear MSD system with $m_{\text{NUM}} = 10\,\text{kg}$, $k_{\text{NUM}} = 2 \cdot 10^4\,\text{N/m}$ and $d_{\text{NUM}} = 200\,\text{kg/s}$.

to a decrease of the eigenfrequency. Secondly, the dynamics effect is like increased stiffness, which causes an increase of the eigenfrequency. Depending on the specific value of T_{ACT}, the one or the other effect dominates: For example, the RTHS test with $T_{\text{ACT}} = 0.01\,\text{s}$ has a slightly smaller eigenfrequency (5.98 Hz) compared to the reference dynamics (6.02 Hz). For the other values of T_{ACT}, the eigenfrequency of the RTHS test is larger than the reference eigenfrequency. This means that the effect of added positive damping by the mass has a minor effect on the decrease of the eigenfrequency than the increase due to the added stiffness.

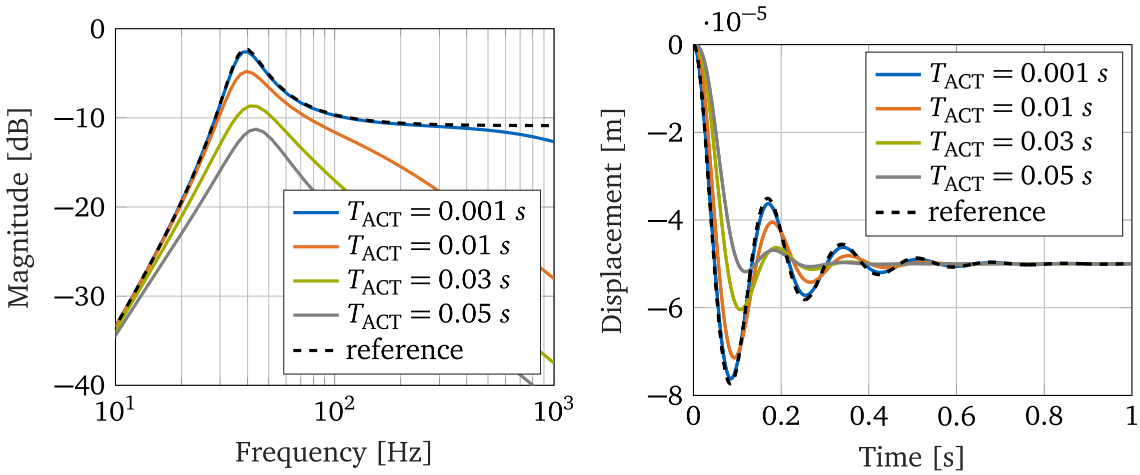

(a) Magnitude of the sensitivity function for different time constants T_{ACT}.

(b) Interface displacement over time for different time constants T_{ACT}.

Figure 11.5: The figures visualize the influence of the actuator dynamics for the case of a mass experimental substructure ($m_{\text{EXP}} = 0\,\text{kg}$, $k_{\text{EXP}} = d_{\text{EXP}} = 0$). The actuator is modeled as a first order system with $\hat{G}_{\text{ACT}} = \frac{1}{T_{\text{ACT}}s+1}$. The numerically simulated part is a linear MSD system with $m_{\text{NUM}} = 10\,\text{kg}$, $k_{\text{NUM}} = 2 \cdot 10^4\,\text{N/m}$ and $d_{\text{NUM}} = 200\,\text{kg/s}$.

To sum up, time delay at the interface influences the observable magnitude and consequently the damping of the frequency response in the RTHS experiment. In contrast, changes of the actuator bandwidth affect the frequency content, i.e. the poles of the complementary sensitivity function change depending on $\hat{G}_{\mathrm{ACT}}$.

11.3 FACE Method for Structural Vibrations

The focus in this work is put on the investigation of structural vibrations. Such tests possess high fidelity if they emulate the vibration response of the reference system well. The vibration response can be characterized by the oscillation magnitude, damping and frequency. In section 11.2, we showed that the actuator dynamics influence the vibration response of an RTHS test. To assess the test fidelity in the presence of inevitable actuator dynamics, the application of the FACE method (section 11.1) is proposed. The implementation of the FACE method requires an appropriate choice of q and e. The choice of q depends on the QoI (cf. definition on p. 12), that is, what is being investigated with the RTHS experiment. Based on the requirements set in section 10.3.7 and section 11.1, q is a scalar value that should be informative, easy to interpret and representative of the QoI. The oscillation magnitude (frequency domain), the overall system damping (transient behavior in time domain) and oscillation frequency (frequency domain) are appropriate measures of the RTHS result to assess the fidelity of vibration responses. In section 11.2, the frequency response was investigated using the complementary sensitivity function. The evaluation of the complementary sensitivity function is, however, often not possible in a real RTHS setup due to the lack of system knowledge about $\hat{G}_{\mathrm{ACT}}$ and $\hat{G}_{\mathrm{EXP}}$. Nevertheless, the characteristic dynamics are also visible in the displacement signals, see e.g. figs. 11.2b, 11.3b, 11.4b and 11.5b. Hence, a fast Fourier transform (FFT) of the achieved displacement[4] z' is used in the following to assess the oscillation magnitude and frequency. The damping characteristics are better visible in the transient response in time domain.

The choice of the error measure e depends on the major error source in an RTHS setup or the kind of error against which the sensitivity of the RTHS test is to be analyzed. This part assumes that the actuator dynamics are the most significant error source and other sources, like modeling errors or noise, are neglected. Section 11.2 showed how time delay and actuator bandwidth disparately influence the observable RTHS dynamics. While the variation of the delay enables exploring how the magnitude and the effective damping change, alterations of the actuator bandwidth vary the observable frequency content. To apply the FACE method, multiple measurements have to be performed to thoroughly explore the area between $e \in (e_{\mathrm{min}}, e_{\mathrm{crit}})$. Remember that the best available implementation of the actuator controller achieves the minimum error e_{min}. Hence, the delay and bandwidth of the controlled actuator can now be artificially degraded[5] as visualized in fig. 11.6. Delay can be introduced into the RTHS loop by simply delaying the displacement command that is sent to the controlled actuator by an additional delay τ_{add}. One option to change the controller bandwidth is to vary the controller parameters, which is denoted by the adaptation arrow at the feedback controller C in fig. 11.6. For example, if a PID controller is implemented as feedback controller, an increase/decrease of the position gain generally increases/decreases the controller bandwidth.

There are multiple possibilities to select the error measure e needed for FACE. The requirements are that it is a scalar value that represents the amount of error, or even less restrictive, the represents the quantity that is being varied to explore the area in fig. 11.1. If $e = 0$, the reference dynamics result (neglecting probable other sources of errors). For the application to vibration analysis, a measure of the time delay between z and z', such as e.g.

[4]The FFT is performed using the time course of the signal $z'(t)$ with $t \in (0, t_{\mathrm{end}})$.

[5]An improvement is usually not possible, since one has already designed the used controller in the best possible way.

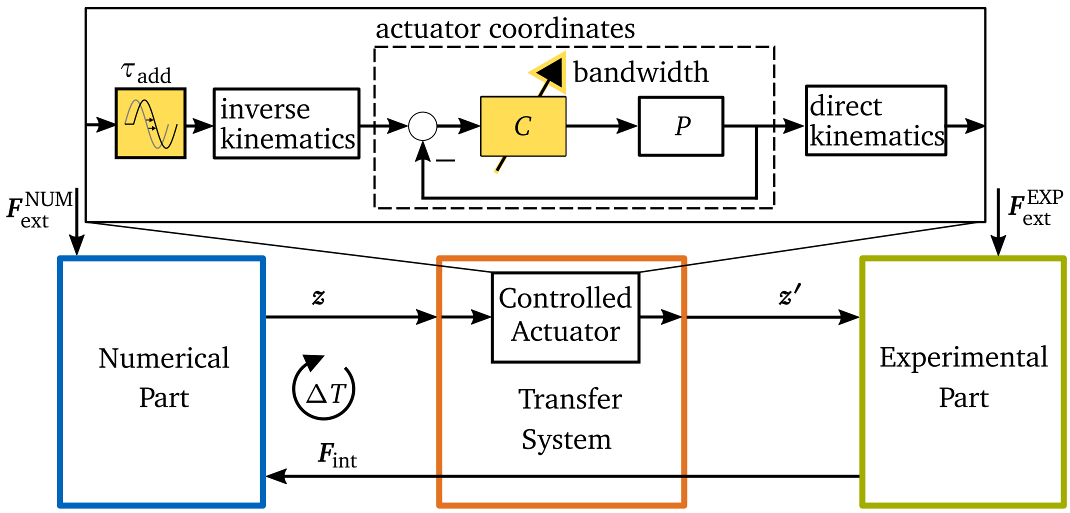

Figure 11.6: The dynamics of the RTHS test change depending on the actuator dynamics $\hat{G}_{ACT}$. To investigate the influence of them on the RTHS result, FACE can be applied. Firstly, the existing controller can be enhanced by an artificial additional delay and secondly by variation of the controller parameters C.

the equivalent time delay τ_{FEI} (eq. (10.9)), or a measure of the tracking performance, such as the relative RMS tracking error (eq. (4.4)), can be used. If the controller bandwidth is altered by variation of the position gain K_{Pp}, an appropriate measure of e is $\frac{1}{K_{Pp}}$.

The application of FACE to assess the fidelity of an RTHS test's vibration response is depicted qualitatively in fig. 11.7 for the case where $k_{EXP} \neq 0$ and $m_{EXP} = 0$. The measurement points for the peak magnitude and the overall system damping are obtained by adding additional delay τ_{add}. The peak magnitude is the maximum magnitude of $Z'(j\omega) = FFT(z'(t))$ with $t \in (0, t_{end})$. The frequency content of the RTHS experiments is investigated by changing the controller bandwidth, that is by varying the controller parameters. In case the controller bandwidth ω_{bw} is much higher than the fundamental frequency of the coupled dynamical system ω_{dyn}, a slight decrease of the bandwidth does not influence the observable frequency content in the RTHS test (in blue, see also fig. 11.3a). However, if the controller bandwidth is in the same range (smaller or only slightly above) as the fundamental frequency of the in-

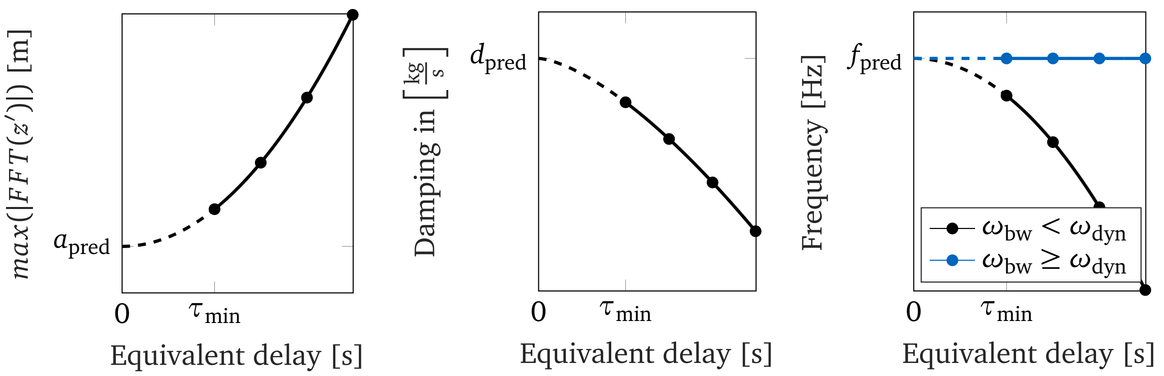

Figure 11.7: This figure qualitatively illustrates how the FACE method can be used for the fidelity assessment of the vibration response. The case of a stiffness experimental substructure (delay has a destabilizing effect) is visualized. The dots represent measurement points. At τ_{min}, the best available actuator is used and for equivalent delays $> \tau_{min}$, either additional delay τ_{add} is artificially introduced (magnitude and damping) or the controller bandwidth ω_{bw} (frequency) deliberately reduced. Interpolating between the measurement values and extrapolating to 0 yields the predicted values of the oscillation magnitude a_{pred}, the system damping d_{pred} and the frequency f_{pred}, which are ideally very close to the according values $\hat{a}$, $\hat{d}$ and $\hat{f}$ of the reference solution.

vestigated dynamical system, the frequency content visible in the RTHS experiment changes by variation of the controller parameters (in black). In this visualization, the equivalent time delay τ_{FEI} (eq. (10.9)) is used as e, but similar qualitative behavior is visible for other choices of e.

11.3.1 Frequency Evaluation Indices (FEI)

One of the possible choices of e is the equivalent time delay from the FEI indices, which is τ_{FEI}. The derivations are given in section 10.3.1 and the basic equation is eq. (10.9). The calculation of τ_{FEI} requires the determination of the equivalent frequency f_{eq}, which is based on the Fourier transforms of the commanded signal. Figure 11.8a displays the magnitude of the Fourier transform $Z(j\omega)$ of a vRTHS test of the coupled MSD system ($m_{\mathrm{NUM}} = 9.62\,\mathrm{kg}$, $k_{\mathrm{NUM}} = 2 \cdot 10^4\,\mathrm{N/m}$, $d_{\mathrm{NUM}} = 200\,\mathrm{kg/s}$, $k_{\mathrm{EXP}} = 8650\,\mathrm{N/m}$ and $m_{\mathrm{EXP}} = d_{\mathrm{EXP}} = 0$). The actuator is modeled as the Stewart Platform from section 4.3 with the identified leg transfer behavior and controller parameters (VFF was not used). The identified equivalent frequency using eq. (10.8) yields a value of 0.02 Hz. This is obviously too low, which is due to the fact that the summation is over the whole frequency range, i.e. for $\Delta T = 0.001\,\mathrm{s}$ up to 500 Hz (Nyquist frequency). The magnitudes that are lower than the eigenfrequency on the left hand side of the peak pull the equivalent frequency towards them. To circumvent this, the following idea is proposed: Firstly, detect the fundamental frequencies in $Z(j\omega)$ (here $\approx 8.3\,\mathrm{Hz}$). Then, only sum over the frequency bands that are close to these fundamental frequencies, e.g. in a range of 3 Hz around them. Using this adapted implementation, an equivalent frequency of 8.73 Hz is obtained. The equivalent frequency is the underlying quantity in the calculation of the equivalent delay. The standard implementation yields $\tau_{\mathrm{FEI}} = 0.007\,\mathrm{s}$ and the adapted implementation $\tau_{\mathrm{FEI}} = 0.011\,\mathrm{s}$, which is a much better approximation considering the commanded and real displacements shown in fig. 11.8b.

Next, additional delays $\tau_{\mathrm{add}} = \{0.002, 0.004, 0.006, ..., 0.022\}$ s were added in the vRTHS simulation and the equivalent delay τ_{FEI} was calculated with the standard and proposed, adapted implementation. The results are shown in fig. 11.8c. As the amount of added delay τ_{add} is known, a straight line with slope 1 starting from τ_{min} is expected. τ_{min} is the delay at $\tau_{\mathrm{add}} = 0\,\mathrm{s}$, where only the controlled actuator introduces dynamics/delay. While the standard implementation predicts delay values that are too low and flatten for higher τ_{add}, the adapted implementation leads to the desired behavior, i.e. $\tau_{\mathrm{FEI}} = \tau_{\mathrm{min}} + \tau_{\mathrm{add}}$. Henceforth, the adapted implementation is thus used and simply denoted by τ_{FEI}/equivalent time delay.

11.3.2 Interpolation and Extrapolation

The prediction accuracy of FACE, which is how well q_{pred} corresponds with $\hat{q}$, substantially depends on the approximation of $h(\cdot)$. This function is found by interpolation of the measurement points and used for extrapolation in the unknown area $e \in (0, e_{\mathrm{min}})$. Setting the fundamental shape of $h(\cdot)$ is crucial to include physical assumptions in the unknown area. Depending on the application, these are

- The magnitude of the gradient becomes smaller approaching $e = 0$. In a small area around $e = 0$, in the so-called linear regime, the gradient is even zero. How large this area is depends on the susceptibility of the QoI to e. In our experience, setting the gradient to zero at $e = 0$ is required for the prediction of the frequency f_{pred} (indicated in fig. 11.7). For the prediction of the magnitude, the gradient becomes smaller approaching $e = 0$ and for the prediction of the damping coefficient, no condition about the gradient can be specified.

- The sign of the curvature must not change in the unknown area.

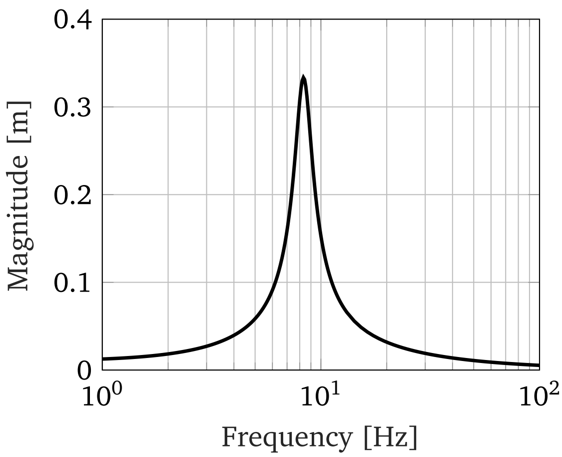

(a) Magnitude of $Z(j\omega)$ for $\tau_{\text{add}} = 0\,\text{s}$.

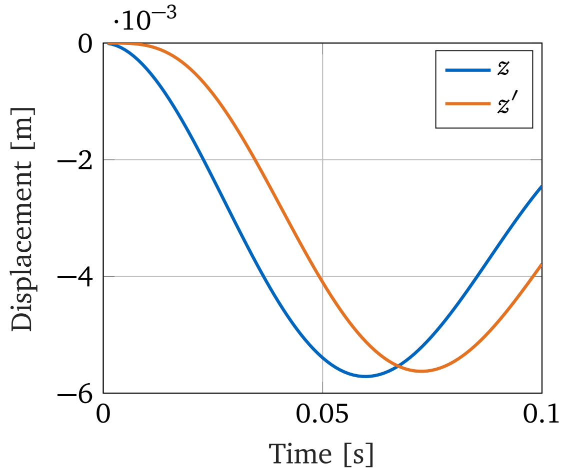

(b) Commanded z and real interface displacement z' in the first 0.1 s of the vRTHS simulation ($\tau_{\text{add}} = 0\,\text{s}$).

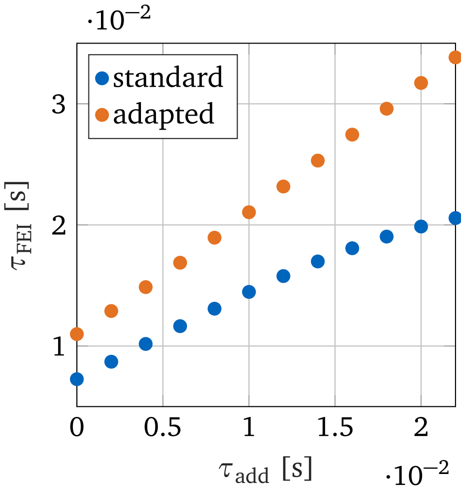

(c) Values of the equivalent time delay τ_{FEI} for the standard and adapted implementation.

Figure 11.8: These are the results from a vRTHS simulation of a coupled MSD system and the Stewart Platform presented in section 4.3 as transfer system.

Appropriate choices of $h(\cdot)$ include splines, polynomials and exponential functions. Later, recommendations are given.

In the presentation of FACE in section 11.1, measurement points are shown in the whole possibly explorable area $e \in (e_{\text{min}}, e_{\text{crit}})$. The size of this area depends on the susceptibility of the test to e. For example, introducing additional delay in highly sensitive tests, is only possible up to a few milliseconds. In this case, the user should try to get as many measurement points as possible. However, in order not to risk unstable tests, the use of NPC (see chapter 5) is especially recommended here. But only the measurement points should be used where NPC did not intervene because NPC distorts the investigated dynamics. For less susceptible tests, the explorable area is large. Then, not the whole area up to e_{crit} needs to be measured. Rather, many measurements with small intervals should be conducted in the vicinity of e_{min}. Based on the investigations in this work, as a rule of thumb, a minimum of four measurement points is required for a good prediction accuracy, but no more than 20 are necessary.

Chapter 12

Example Applications of FACE

Parts of this chapter have been published in the author's publication [110].

In this chapter, the introduced methodology is applied to three different application examples. The specific workflow for the application of the FACE method is elaborated using these examples and the performance is investigated. The analysis is performed on three different applications with the focus on vibration problems: vRTHS tests of a coupled linear SDOF system, the benchmark problem of the MECHS community and the RTHS system with contact from Part I. In all application examples, a reference solution is available and used to assess the performance of the FACE method. Hence, the reference solution is used to prove the efficacy of the method and gain trust in the method for applications where no reference solution is available.

12.1 Linear Virtual RTHS System

In order to understand the FACE method in more detail and to interpret the results, a linear RTHS system is chosen as an initial example. These first investigations are performed as vRTHS tests, which means that all components/substructures of the RTHS setup are modeled. The model of the Stewart Platform presented in section 4.3. is used as an actuator. As discussed in sections 2.2 and 11.2, the effect of errors on the RTHS loop differs fundamentally for mass and spring experimental parts. Hence, the applicability and efficacy of the FACE method to these two special cases and a combination of them is now studied. Furthermore, a relation to other accuracy measures presented in section 10.3 is built.

12.1.1 System Description

The coupled linear vRTHS system is visualized in fig. 12.1. Both, the numerical (NUM) and experimental part (EXP) consist of a linear MSD system. At time $t = 0\,\mathrm{s}$, both springs are in their rest position and external forces hold the masses in this position against gravity ($z_{\mathrm{NUM}} = 0\,\mathrm{m}$). For $t > 0\,\mathrm{s}$, the external forces are set to zero and the MSD system drops, oscillates and finally comes at rest (if $d_{\mathrm{NUM}} + d_{\mathrm{EXP}} > 0$) at the position where the restoring spring forces equal $(m_{\mathrm{NUM}} + m_{\mathrm{EXP}})g$. The oscillation frequency is the damped eigenfrequency of the reference system, i.e. $\omega_{\mathrm{dyn}} = \sqrt{\frac{k_{\mathrm{NUM}}+k_{\mathrm{EXP}}}{m_{\mathrm{NUM}}+m_{\mathrm{EXP}}} - \delta_{\mathrm{dyn}}^2}$ with $\delta_{\mathrm{dyn}} = \frac{d_{\mathrm{NUM}}+d_{\mathrm{EXP}}}{2\cdot(m_{\mathrm{NUM}}+m_{\mathrm{EXP}})}$. The transfer system is modeled using the controlled Stewart Platform (cf. fig. 4.4) as actuator. In the presented vRTHS tests, the standard controller parameters were $K_{\mathrm{Pp}} = 90\,\mathrm{1/s}$, $K_{\mathrm{Pv}} = 0.2\,\mathrm{As/m}$

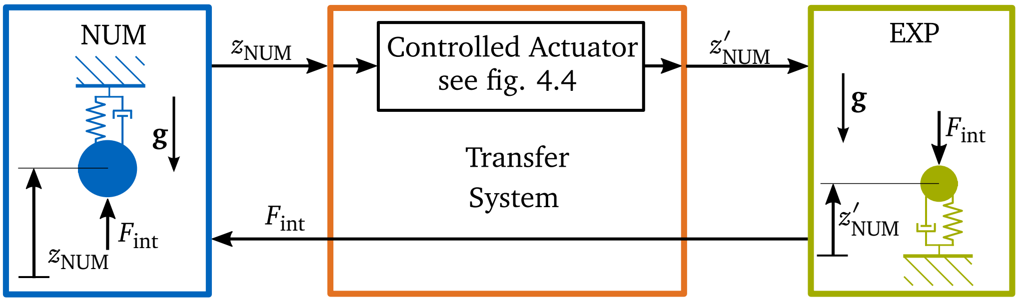

Figure 12.1: The coupled linear MSD system used for the vRTHS tests.

and $K_{\mathrm{Iv}} = 5\,\mathrm{A/m}$ and the VFF was switched off, if not indicated otherwise.[1] In a real RTHS setup, one should always take the best available controller when applying the FACE method. Here, a realistic test where the actuator might not be as well controllable as the Stewart Platform shall be simulated. Therefore, we keep the VFF switched off. The dynamics of the FTS and the DSP as well as any other errors/uncertainties are neglected. The sample time used for the vRTHS simulations is $\Delta T = 0.001\,\mathrm{s}$.

The FACE method can be applied to assess how well this vRTHS test replicates the vibration behavior of the system. The vibration response is characterized by the magnitude, the frequency and the damping. To investigate the prediction performance of the FACE method, which is how well the reference solution is predicted using the FACE method, the reference solution is required. The eigenfrequency is given above and the overall system damping is $d_{\mathrm{NUM}} + d_{\mathrm{EXP}}$. The magnitude is retrieved from the analytical solution of the oscillation response. The Fourier transform is taken over the whole transient response. Note that the Fourier transform is generally better suited to retrieve the harmonic components in stationary systems. Alternatively, a continuous wavelet transform could be used. Another possibility is to perform the Fourier transform piecewise on small snippets of the transient response, which is used in this thesis for the interpretation of the results.

12.1.2 Example: Spring Experimental Part

This first example goes through all steps of the FACE method in detail. Here, the parameters of the experimental part are $m_{\mathrm{NUM}} = 9.62\,\mathrm{kg}$, $k_{\mathrm{NUM}} = 2 \cdot 10^4\,\mathrm{N/m}$, $d_{\mathrm{NUM}} = 200\,\mathrm{kg/s}$, $k_{\mathrm{EXP}} = 8650\,\mathrm{N/m}$ and $m_{\mathrm{EXP}} = d_{\mathrm{EXP}} = 0$. Since the major source of error in this RTHS setup is the actuator dynamics, the sensitivity of the RTHS setup with respect to actuator dynamics should be analyzed. The experimental part only comprises a spring. Hence, any dynamics/delay have a destabilizing effect (see section 11.2.1). This implies growing oscillation magnitudes and an effect like negative damping. Firstly, additional delay is introduced $\tau_{\mathrm{add}} = \{0.001, 0.002, ..., 0.011\}$ s and vRTHS tests are performed for each additional delay value. Using these measurements, the convergence plot (cf. fig. 11.1) can be generated. The error measure e, which is plotted on the abscissa, should be representative for the main error source, which are the actuator dynamics here. Possible selections of e are the equivalent time delay τ_{FEI} (see eq. (10.9) and the proposed adaptations from section 11.3.1) and the relative RMS tracking error $e_{\mathrm{track,rel}}$ (see eq. (4.4)).

The results are illustrated in fig. 12.2. The magnitudes are the peak magnitudes of the frequency responses[2] of $z'_{\mathrm{NUM}}(t)$. The equivalent time delay τ_{FEI} is used as the error measure e

[1] NPC was never activated in Part II.

[2] The Fourier transform is performed over the first 5 s of the test. After 5 s, the system has come to rest and the spring forces balance the weight force of the masses. Note that the FFT is done for a transient signal. Nevertheless, the resulting (scalar) magnitude value captures the amount of damping/oscillation magnitude throughout the RTHS test and makes comparisons between RTHS tests possible.

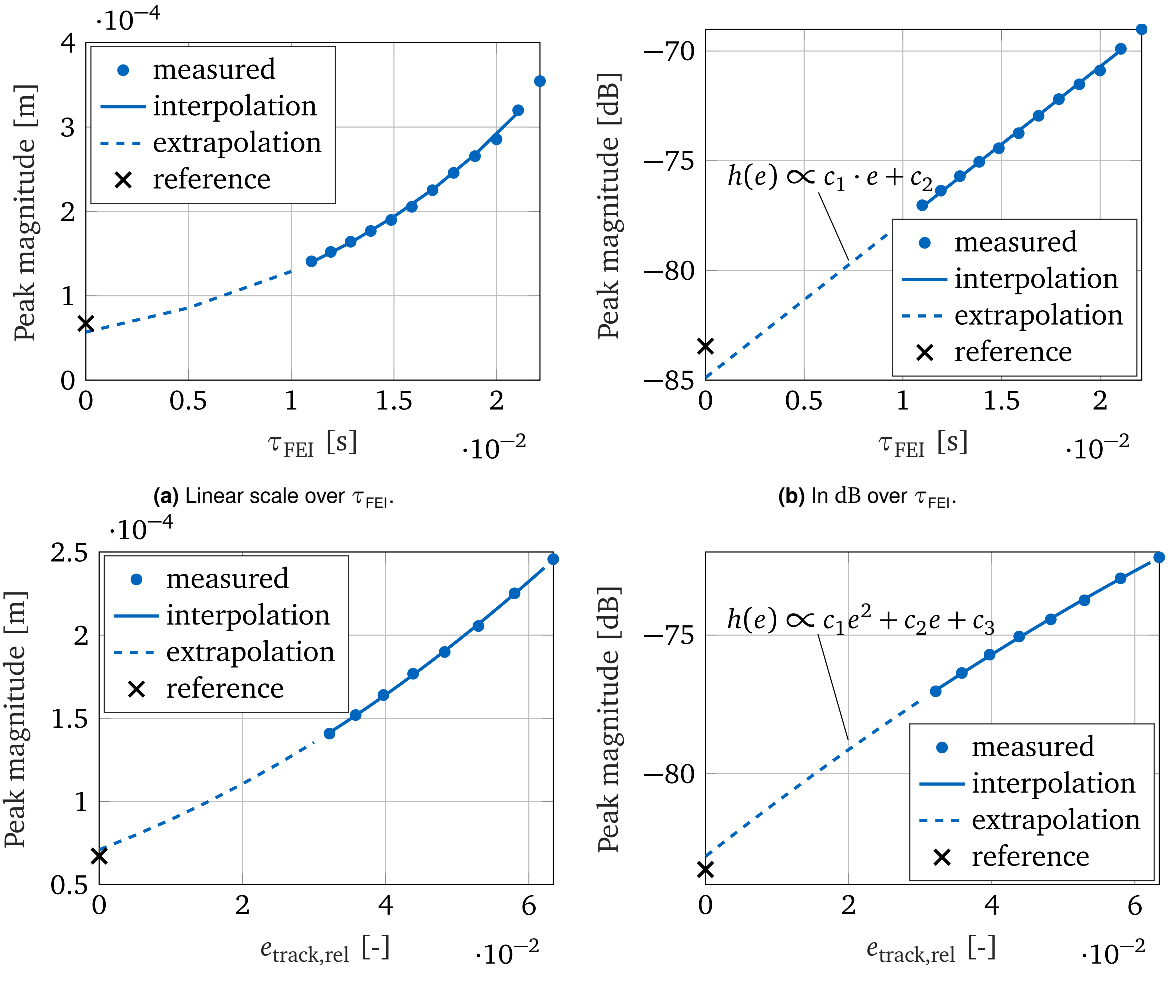

(a) Linear scale over τ_{FEI}.

(b) In dB over τ_{FEI}.

(c) Linear scale over $e_{\text{track,rel}}$.

(d) In dB over $e_{\text{track,rel}}$.

Figure 12.2: The peak magnitude $max(FFT(z'_{\text{NUM}}))$ varies depending on the dynamics/delay of the actuator. The blue dots indicate the results of the vRTHS tests with varying delay τ_{add}. The left-most measurement point corresponds to the actuator without any artificial deterioration. The interpolation $h(\cdot)$ between them is indicated by the solid blue line. The dashed line indicates the extrapolation to $\tau_{\text{FEI}} = 0\,\text{s}$ or respectively $e_{\text{track,rel}} = 0$. The reference amplitude $\hat{a}$ is given by the black cross. The function fit is performed with the representations in dB and the coefficients c_1, c_2, ... were identified.

in figs. 12.2a and 12.2b and the relative RMS tracking error $e_{\text{track,rel}}$ is used in figs. 12.2c and 12.2d. As can be seen for both cases, the relationship is almost linear if the magnitude is plotted in dB, that is $20 \cdot \log_{10}\left(\frac{\cdot}{1}\right)$. Hence, the logarithmic plots are used for the polynomial fit. The extrapolation with τ_{FEI} on the abscissa uses a linear polynomial (coefficients c_1 and c_2) for interpolation and in case of $e_{\text{track,rel}}$, a polynomial of degree two (coefficients c_1, c_2 and c_3) is used.

The appropriate degree for the selected polynomial is found using the considerations from section 11.3.2: the gradient at $e = 0$ must be smaller than at e_{min} (in the linear plot) and the curvature must not change in the extrapolated range. Additionally, overfitting must be avoided, i.e. the degree of the polynomial fit must be smaller than the number of measurement points used. Using these conditions, the fit can be performed with different polynomials. The user selects the function $h(\cdot)$ that fits the measurement points best.

The identified polynomials are used to extrapolate in the unknown areas $(0, \tau_{\text{min}})$[3] and

[3] τ_{min} is the minimum delay, that is τ_{FEI} for $\tau_{\text{add}} = 0\,\text{s}$.

$(0, min(e_{track,rel}))$. The values of the extrapolation at zero correspond to the predicted magnitude a_{pred}, which ideally corresponds to the magnitude of the reference solution $\hat{a}$. As can be seen in the figures, they are of the same order of magnitude and the relative prediction error is $\frac{|a_{pred}-\hat{a}|}{\hat{a}} \approx 15\,\%$ when τ_{FEI} is used and $\approx 6\,\%$ for $e_{track,rel}$. In figs. 12.2a and 12.2c, the extrapolated values are shown in linear scale of the magnitude. The constant curvature and the decreasing gradient in the extrapolated area are reasonable. The decreasing gradient is reasonable because a small error destabilizes the test less (i.e. at around zero) than when there are already other destabilizing errors in the loop (for $\tau_{FEI} > 0/e_{track,rel} > 0$).

As mentioned above, the Fourier transform is performed over the whole time course of the transient behavior. However, the magnitude can only be interpreted meaningfully for steady state oscillations, which are oscillations with constant magnitude. Therefore, the signal is now cut into snippets of length 0.25 s and the first snippet is used for the following analysis[4]. The interface displacement z'_{NUM} is visualized over time in fig. 12.3a and the results of the FACE method using τ_{FEI} on the abscissa in fig. 12.3b. A polynomial of degree three (c_1, c_2 and c_3) was used. The relative prediction error between $a_{pred} = 0.0012\,\text{m}$ and $\hat{a} = 0.0013\,\text{m}$ is 10%. The FACE method predicts that the error between the magnitude at $\tau_{min} = 0.002\,\text{m}$ and the reference is $8 \cdot 10^{-4}\,\text{mm}$. This result can be confirmed with the time domain course in fig. 12.3a. This implies a high prediction accuracy of FACE and shows how easy the results can be interpreted.

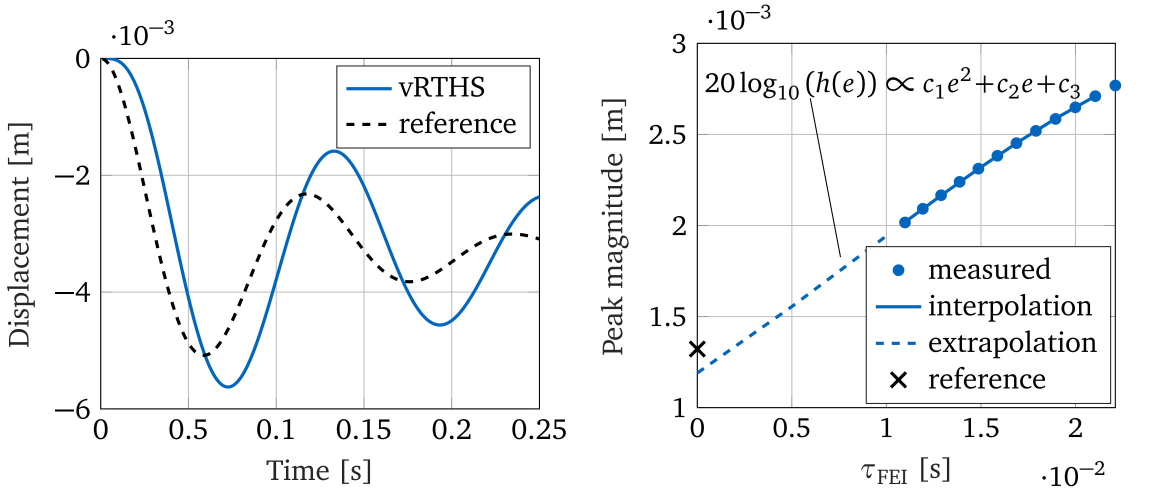

(a) Interface displacement of the vRTHS test (blue, solid) and z^r_{NUM} the reference solution (black, dashed).

(b) Measurement points of the FACE method using artificial delay τ_{add}.

Figure 12.3: In this figure, the first 0.25 s of the vRTHS test are used for the Fourier transform. In this short time span, the value of the magnitudes of the Fourier transform corresponds to the oscillation magnitude. Figures taken from [110].

A further characteristic quantity of the vibration response that is influenced by an artificial delay τ_{add} is the overall system damping. To obtain the damping for each vRTHS test, the time domain interface displacement is used. Figure 12.4a shows the interface displacement over time. The damping constant indicates the exponent with which the oscillation decays and the system damping can be determined by parameter tuning of the exponent. If the parameter tuning is performed for each vRTHS with artificially introduced time delay $\tau_{add} = \{0.001, 0.002, ..., 0.02\}$ s and drawn over τ_{FEI}, the convergence curve in fig. 12.4b results[5]. The best polynomial fit $h(\cdot)$ between the measurement points is found for a polynomial of degree

[4]Note that windowing (e.g. Hanning window) might be necessary to prevent leakage. For this application and the selected duration of the snippet, no window was necessary.

[5]Alternatively, $e_{track,rel}$ could be used here as well.

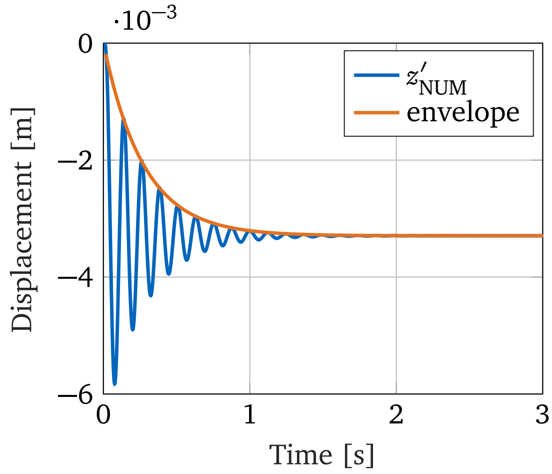

(a) The interface displacement of the vRTHS test with a controlled actuator is shown (blue) with $\tau_{\text{add}} = 0.004\,\text{s}$. The orange line indicates the exponential function with which the oscillation is damped.

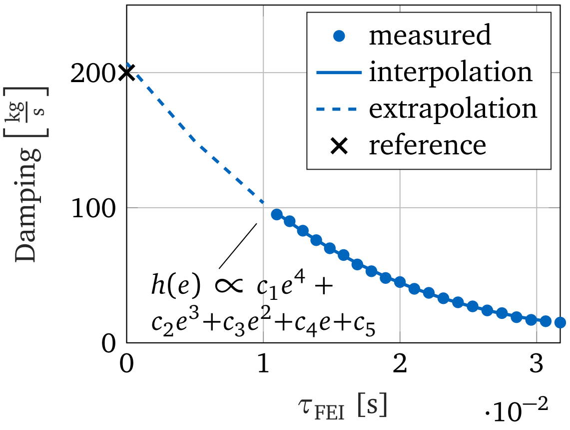

(b) The measurement points are indicated by blue dots, the interpolation is visualized as a solid line, the extrapolation in the area $\tau_{\text{FEI}} < \tau_{\text{min}}$ as the dashed blue line and the reference solution as the black cross. Figure taken from [110].

Figure 12.4: The FACE method is applied to predict the overall system damping $d_{\text{NUM}} + d_{\text{EXP}}$ in case of a stiffness experimental substructure. The equivalent damping parameter of the conducted vRTHS test is found by fitting an exponential function to the time domain interface displacement, as indicated in a. Combining several measurements with different τ_{add} yields the convergence plot b.

four (coefficients $c_1 - c_5$). The predicted value of the overall system damping is $d_{\text{pred}} = 207\,\text{kg/s}$, which is close to the reference solution $\hat{d} = 200\,\text{kg/s}$. As opposed to fig. 12.2, the convergence behavior between the measurement points indicates an increasing magnitude of the gradient in the range $\tau_{\text{FEI}} < \tau_{\text{min}}$. Hence, the only condition that can be set for $h(\cdot)$ for the extrapolation of the damping is that the sign of the curvature must remain the same.

The final vibration characteristic that is described here is the system eigenfrequency. Since the frequency behavior is altered by the actuator bandwidth, the controller parameters are adapted here and $\tau_{\text{add}} = 0\,\text{s}$. Specifically, the position gain $G_{\text{p}} = K_{\text{Pp}}$ was varied and took the values $\{20, 30, \ldots, 90\}\ 1/\text{s}$. In general, higher values of K_{Pp} lead to a higher actuator bandwidth. Figure 12.5 shows the results for the case when VFF is switched off or on. τ_{FEI} is used to create the convergence plot in fig. 12.5a. Note that higher values of K_{Pp} lead to smaller values of τ_{FEI}. If no VFF is used, the actuator bandwidth is too low to emulate the fundamental system dynamics correctly, which is visible in the lowered system eigenfrequency (cf. black line in the right figure of fig. 11.7). The FACE method was used with a polynomial of degree three (coefficients $c_1 - c_4$). This polynomial was selected because the gradient at $e = 0$ should be zero for the prediction of the eigenfrequency (cf. section 11.3.2). Using this polynomial, a frequency of the reference solution of $f_{\text{pred}} = 8.4\,\text{Hz}$ is predicted. The eigenfrequency of the reference solution is $\hat{f} = 8.5\,\text{Hz}$. When VFF is used, the values of the equivalent delay τ_{FEI} are considerably smaller and the frequency content of the RTHS loop is emulated better. The function course around e_{min} resembles the curve for $\omega_{\text{bw}} \geq \omega_{\text{dyn}}$ in fig. 11.7. This means that no interpolation is required and $f_{\text{pred}} = f_{\text{min}}$ is taken ($h(\cdot) = \text{const.}$). For $K_{\text{Pp}} = \{70, 80, 90\}\ 1/\text{s}$, the eigenfrequency of the RTHS test is slightly higher than the eigenfrequency of the reference solution. This might come from an amplitude overshoot of the actuator at a frequency slightly above the eigenfrequency of the reference system. The same analysis can be done for K_{Pp}^{-1} on the abscissa, see fig. 12.5b. Since the actuator bandwidth $\omega_{\text{bw}} \to \infty$ for $K_{\text{Pp}} \to \infty$, ideal coupling between the numerical and the experimental part is achieved for $K_{\text{Pp}}^{-1} \to 0$. Here, the predicted eigenfrequency when no VFF is used is $f_{\text{pred}} = 8.6\,\text{Hz}$ and when VFF is switched on $f_{\text{pred}} = 8.8\,\text{Hz}$.

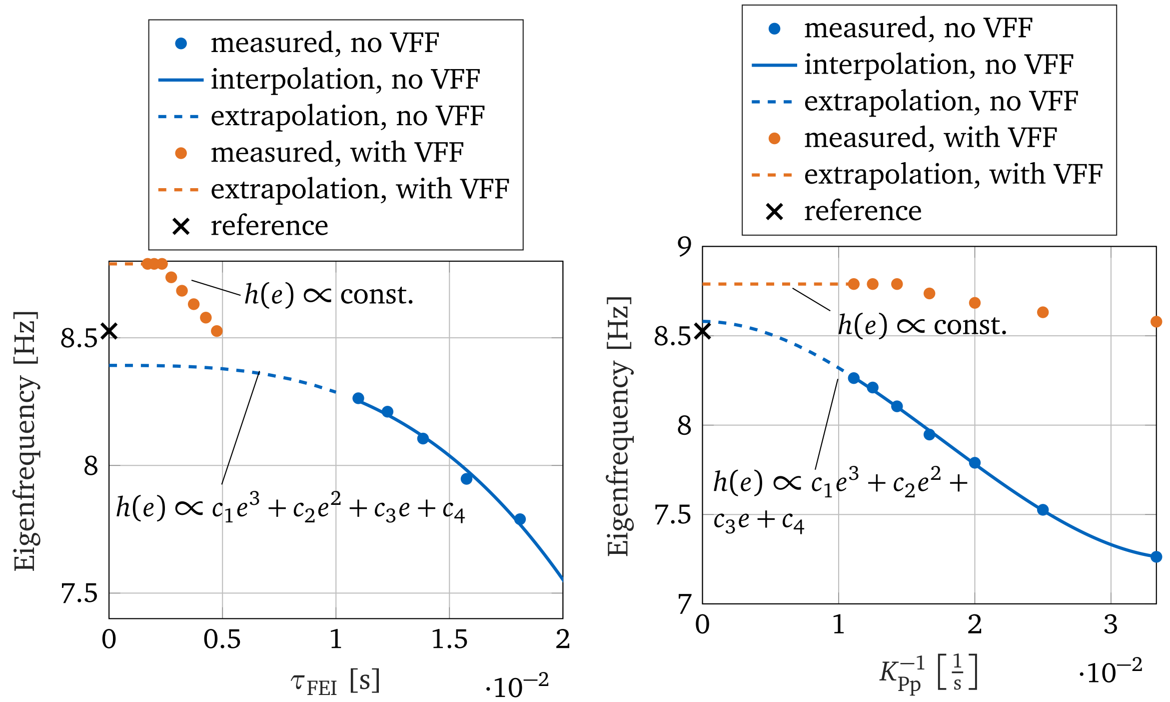

(a) The equivalent delay τ_{FEI} is used to measure the interface compatibility error.

(b) K_{Pp}^{-1} is used on the abscissa for the convergence plot. Figure taken from [110].

Figure 12.5: The FACE method is applied to predict the system eigenfrequency $\hat{f}$. The measurement points represent different values of the controller gain K_{Pp}. The cases when the VFF is switched on (in orange) and off (in blue) are investigated.

To sum up, the FACE method is applied in this section to predict the vibration response of the reference system characterized by the vibration magnitude, damping and eigenfrequency. To set up the required convergence plot, additional delay is added for the investigations of the magnitude and damping. The controller parameters are varied for the analysis of the system frequency. A good prediction accuracy for the reference solution can be achieved. The prediction accuracy depends significantly on the chosen interpolation function. The most important feature is that the sign of the curvature must remain the same in the extrapolated area as in the interpolated area. For the magnitude, the gradient at $e = 0$ must be smaller than at e_{min} and for the prediction of the eigenfrequency, the gradient must be zero at $e = 0$. Different quantities on the abscissa, e.g. τ_{FEI}, $e_{\mathrm{track,rel}}$ and K_{Pp}^{-1} led to the desired convergence behavior, but no clear difference can be seen among them regarding the prediction accuracy. After using the FACE method, the user has to decide how well the test went, i.e. whether the test results are acceptable (using the controlled actuator with τ_{min}). Knowing the reference solution or the approximated reference solution helps to make this decision. For example, the magnitude error is significant in the shown example, i.e. almost 0.8 mm in relation to the full oscillation magnitude, which is ≈ 2.5 mm. The large effect of the actuator dynamics is also visible in the effective damping, which is 96 kg/s and thus approximately half of the system damping in the reference solution. The frequency characteristics are emulated well with VFF.

12.1.3 Example: Mass Experimental Part

As was described in section 11.2.2, the effect of actuator dynamics is stabilizing in case the experimental component comprises a mass. In this example, the system parameters are $m_{\text{NUM}} = 1\,\text{kg}$, $k_{\text{NUM}} = 2 \cdot 10^3\,\text{N/m}$, $d_{\text{NUM}} = 10\,\text{kg/s}$, $m_{\text{EXP}} = 0.5\,\text{kg}$ and $k_{\text{EXP}} = d_{\text{EXP}} = 0$. Firstly, the prediction of the magnitude is described. Similar to the previous section, τ_{FEI} and $e_{\text{track,rel}}$ are used to visualize the convergence behavior. The results are presented in fig. 12.6. Again,

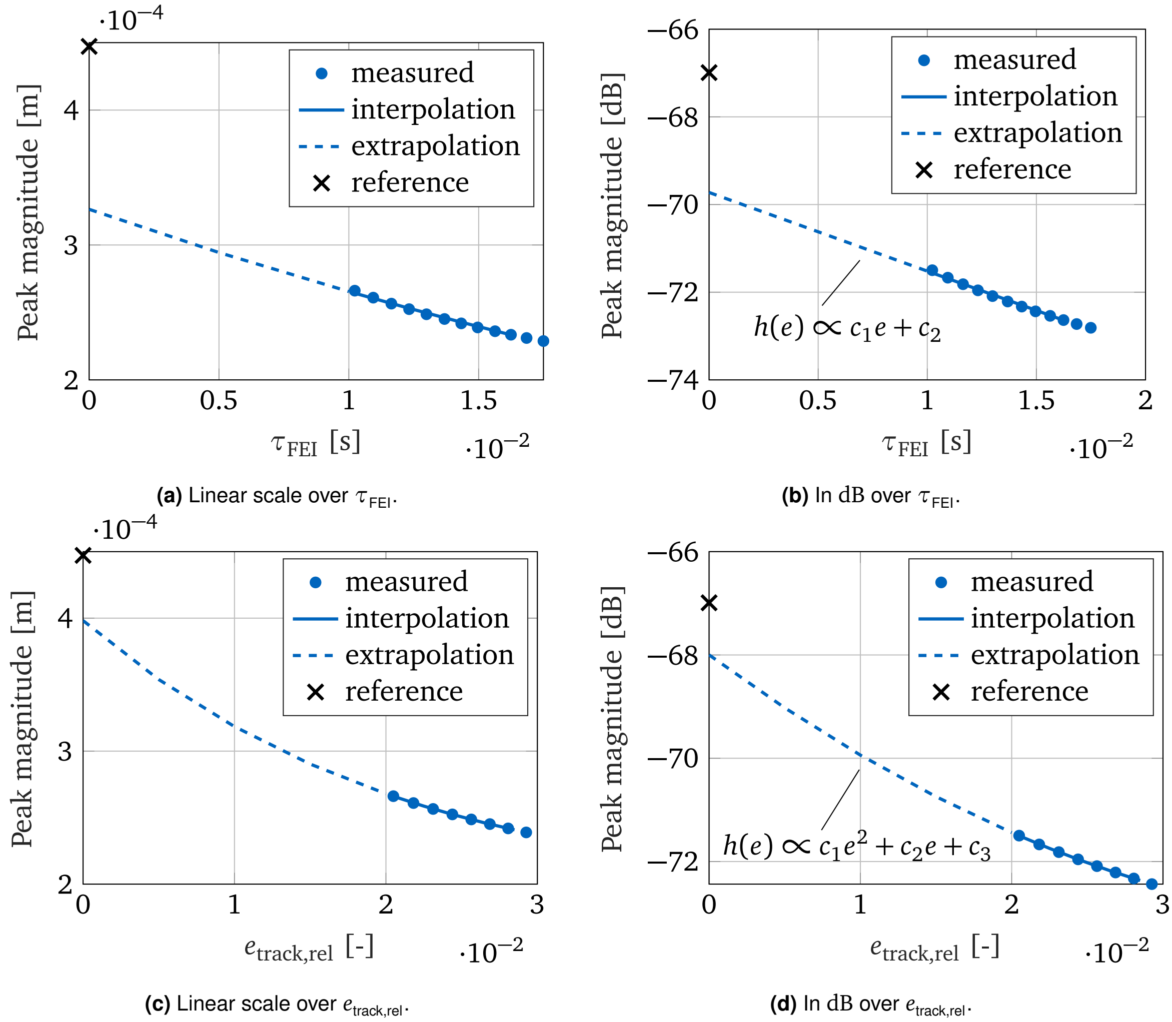

Figure 12.6: The blue dots indicate the measured peak magnitude $max(FFT(z'_{\text{NUM}}))$ of vRTHS tests with different values τ_{add}. The left-most measurement point corresponds to the controlled actuator without any artificial deterioration. The interpolation between the measurement points is indicated by blue solid lines and the dashed lines show the extrapolation to zero. The reference amplitude $\hat{a}$ is given by the black crosses.

the interpolation is done using the values of the magnitude in dB and a linear/quadratic polynomial is used. In contrast to fig. 12.2, the dynamics of the actuator and the artificial additional delay τ_{add} lead to smaller peak magnitudes due to the stabilizing effect of the delay in case the experimental part is dominated by the mass (see section 11.2.2). The relative prediction error between a_{pred} and $\hat{a}$ is 27 % for τ_{FEI} and 11 % if $e_{\text{track,rel}}$ is used. Using FACE it can be seen that the error between a_{min}, which is the error at τ_{min} or $min(e_{\text{track,rel}})$, and a_{pred} is large and therefore the magnitude values are not emulated sufficiently with the actuator control used.

Since the experimental mass has a stabilizing effect, any additional delay has an effect like added positive damping. From the individual vRTHS tests with varying τ_{add}, the damping values are found and given in the convergence plot fig. 12.7a, where the FACE method is applied. The prediction accuracy is high: using a polynomial interpolation of degree four, the predicted damping value is $d_{\text{pred}} = 10.6\,\text{kg/s}$ ($\hat{d} = 10.0\,\text{kg/s}$).

Finally, the frequency content is analyzed by variation of the controller gain $K_{\text{Pp}} = \{20, 30, ..., 90\}\ 1/\text{s}$. The results are visualized in fig. 12.7b. Similar to fig. 12.5a, the

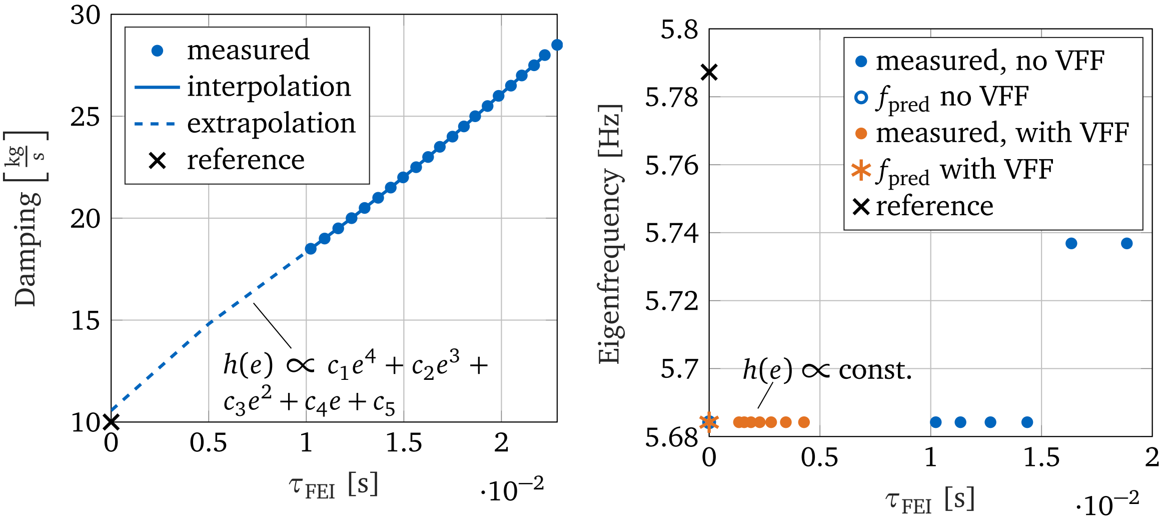

(a) The overall system damping is investigated. Each measurement point (blue dot) corresponds to a vRTHS test with a different value of τ_{add}.

(b) The system eigenfrequency is predicted using the FACE method with VFF switched on (in orange) and off (in blue).

Figure 12.7: The FACE method is applied in case of a mass experimental substructure.

equivalent time delay is much smaller if VFF is used. Following section 11.2.2, slightly increased eigenfrequencies are observed for lower actuator bandwidth (lower K_{Pp}, i.e. larger τ_{FEI}). The frequency content converges to $f_{\text{pred}} = 5.7\,\text{Hz}$ (with and without VFF). In comparison, the reference solution is $\hat{f} = 5.8\,\text{Hz}$. Hence, the frequency content is replicated well with the selected actuator controller ($h(e) = \text{const.}$).

To sum up, the fundamentally different influence of actuator dynamics/delay on RTHS tests with stiffness and mass experimental substructures can be seen in the application of the FACE method as well.

12.1.4 Example: General Experimental Part with Mass and Spring

To briefly show that the FACE method also effectively works for a general experimental part, which is with mass and spring in the experimental substructure, results are visualized in this section for the dynamical system with $m_{\text{NUM}} = 8\,\text{kg}$, $k_{\text{NUM}} = 11380\,\text{N/m}$, $d_{\text{NUM}} = 20\,\text{kg/s}$, $m_{\text{EXP}} = 2\,\text{kg}$ and $k_{\text{EXP}} = 710\,\text{N/m}$ and $d_{\text{EXP}} = 0\,\text{kg/s}$. The stiffness values are tuned such that the eigenfrequency of the numerical part is 6 Hz and of the experimental part 3 Hz. Figure 12.8 illustrates the results.

The FACE method is at first applied to predict the magnitude and the damping of the reference solution. This is done by introducing artificial delay $\tau_{\text{add}} = \{0.001, 0.002, ..., 0.014\}$ s. Since the interpretation of the magnitude is easier when short time spans are considered, only the first 0.35 s are taken for the calculation of the FFT. The time domain interface displacement is visualized in fig. 12.8a for the case when no additional delay is introduced. The convergence plot that forms from different vRTHS tests (no VFF) is shown in fig. 12.8b. The function fit is done in the logarithmic plot with a polynomial of degree two (coefficients $c_1 - c_3$). As the magnitude decreases for higher values of τ_{add}, the stabilizing effect of m_{EXP}

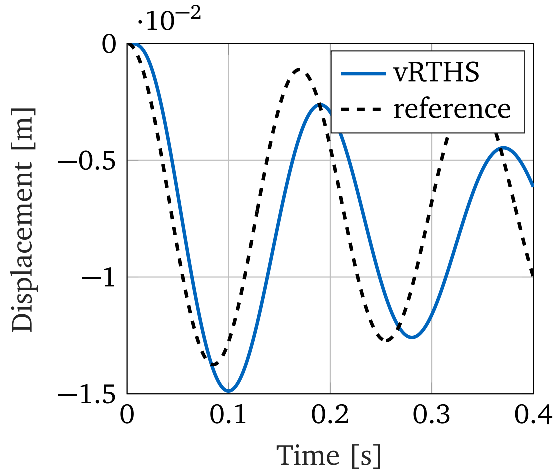

(a) Interface displacement of the vRTHS test (blue, solid) and the reference solution z^{r}_{NUM} (black, dashed).

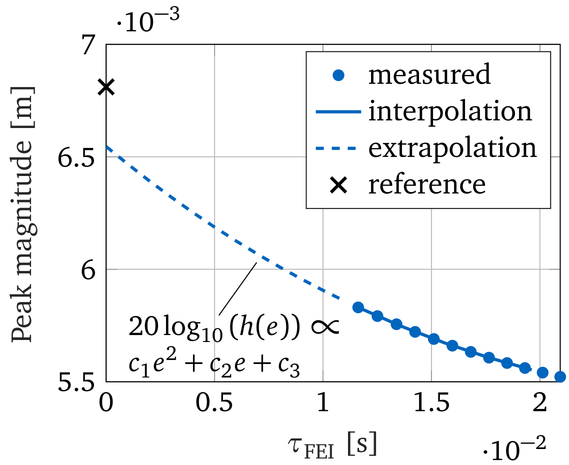

(b) The FACE method applied to the peak magnitude in the first 0.35 s of the vRTHS test.

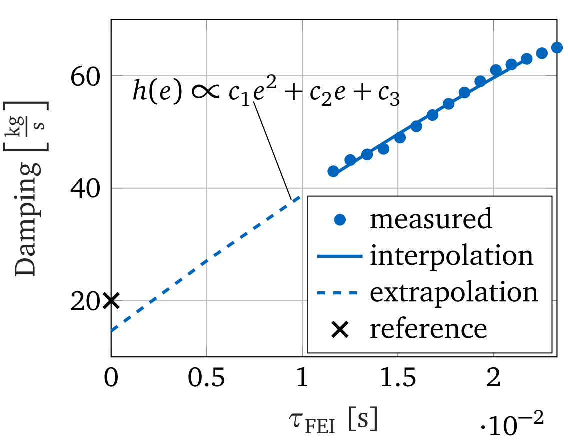

(c) The prediction of the overall system damping using τ_{FEI} on the abscissa.

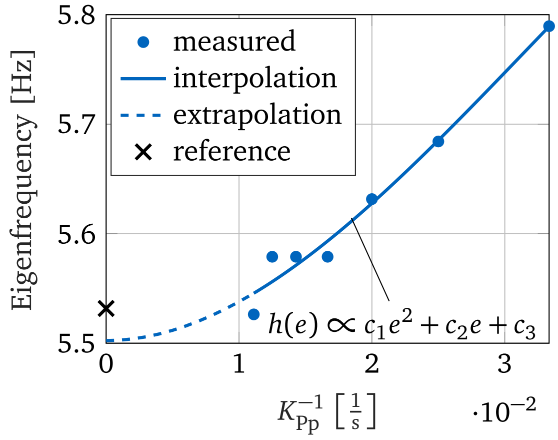

(d) Frequency content in vRTHS tests depending on the actuator control.

Figure 12.8: The FACE method is applied in case of a general experimental substructure, i.e. with mass and stiffness. The data from vRTHS tests are visualized as blue dots and the interpolation function $h(\cdot)$ is shown as blue solid line. The extrapolation with this interpolation function in the unknown area is indicated with blue dashed lines and the reference quantities $\hat{a}$, $\hat{d}$ and $\hat{f}$ are displayed as black crosses.

dominates the destabilizing effect of k_{EXP} in the presence of actuator dynamics in this example. The magnitude at τ_{min} is $a_{\text{min}} = 5.8\,\text{mm}$, the predicted magnitude of the reference is $a_{\text{pred}} = 6.5\,\text{mm}$ and the true reference solution is $\hat{a} = 6.8\,\text{mm}$. Hence, the relative prediction accuracy is $\approx 4\%$. Comparing a_{min} with a_{pred} (as an approximation of $\hat{a}$) yields an estimated amplitude error of 0.7 mm, which corresponds well with fig. 12.8a. This shows the high added value using the FACE method to understand how well the RTHS test emulates the reference dynamics. The FACE method is also applied to estimate the system damping, as can be seen in fig. 12.8c. A polynomial of degree two was taken because it meets the condition that the curvature remains the same in the extrapolated area. The predicted system damping of the reference solution is $d_{\text{pred}} = 15\,\text{kg/s}$ (reference solution $\hat{d} = 20\,\text{kg/s}$). Finally, the controller parameters are varied similar to the previous sections, i.e. $K_{\text{Pp}} = \{20, 30, \ldots, 90\}\ 1/\text{s}$ to investigate how well the test emulates the frequency content. The results are visualized in fig. 12.8d. If a polynomial of degree two (gradient at $e = 0$ is zero and curvature constant) is used for interpolation, $f_{\text{pred}} = 5.5\,\text{Hz}$ is obtained, which is very close to $\hat{f} = 5.53\,\text{Hz}$. Since the stabilizing effect of m_{EXP} dominates the destabilizing effect of k_{EXP} in this example, reduced actuator bandwidth (higher values of K_{Pp}^{-1}) leads to higher eigenfrequencies of the RTHS test.

In summary, the FACE method also works effectively in the case of a general experimental substructure. Whether the magnitude increases with additional actuator dynamics/delay depends on the ratio between the numerical/experimental masses/stiffnesses and can easily be investigated with the proposed methodology.

12.1.5 Influence of Test Sensitivity and Comparison with Accuracy Measures

Different accuracy measures were presented in section 10.3. The purpose of this section is to demonstrate the unique features of FACE with respect to some of these accuracy measures. For this purpose, the following two dynamical systems are investigated using vRTHS with and without VFF. System 1 is henceforth the dynamical system with $m_{\text{NUM}} = 8\,\text{kg}$, $k_{\text{NUM}} = 11380\,\text{N/m}$, $d_{\text{NUM}} = 20\,\text{kg/s}$, $m_{\text{EXP}} = 2\,\text{kg}$ and $k_{\text{EXP}} = 710\,\text{N/m}$ and $d_{\text{EXP}} = 0\,\text{kg/s}$ (like in the previous section). System 2 has a different partitioning of the mass and stiffness, namely $m_{\text{NUM}} = 9.5\,\text{kg}$, $k_{\text{NUM}} = 13512\,\text{N/m}$, $d_{\text{NUM}} = 20\,\text{kg/s}$, $m_{\text{EXP}} = 0.5\,\text{kg}$ and $k_{\text{EXP}} = 177\,\text{N/m}$ and $d_{\text{EXP}} = 0\,\text{kg/s}$. The stiffness values are tuned such that the eigenfrequency of the numerical part is 6 Hz and of the experimental part 3 Hz in both dynamical systems. In both dynamical systems, the stabilizing effect of m_{EXP} is larger than the destabilizing effect of k_{EXP}. Even though system stability is not jeopardized in the presence of delay, the fidelity of the RTHS result is deteriorated. System 1 is more susceptible to errors than system 2, which means that the fidelity decreases faster in the presence of delay.

Additional delay τ_{add} was introduced and the relative RMS tracking error $e_{\text{track,rel}}$, the $HSEM^{\text{S}}$ eq. (10.10) and the magnitude of the robust stability/performance indicator eq. (10.12) and eq. (10.13) were evaluated. The results are given in fig. 12.9. As VFF leads to better actuator tracking, all accuracy measures possess smaller values in case VFF is used. Figure 12.9a indicates that, for higher equivalent delay τ_{FEI}, the tracking error increases; this was expected. The eigenfrequency of the reference dynamics is slightly higher in system 2 than in system 1, and therefore $e_{\text{track,rel}}$ increases faster. From the value of $e_{\text{track,rel}}$ one could infer that system 2 would be more sensitive than system 1—which is not the case. Hence, $e_{\text{track,rel}}$ does not capture how susceptible the fidelity of an RTHS system is to errors.

Figure 12.9b shows the $HSEM^{\text{S}}$ values for the different vRTHS tests. Positive values indicate that the transfer system damped system energy, i.e. the stabilizing effect of m_{EXP} outweighs the destabilizing effect of k_{EXP}. This is in general beneficial regarding test stability, but any value $HSEM^{\text{S}} \neq 0$ means that the transfer system changed the system energy and thus deteriorated the fidelity. In this figure, system 1 has larger positive energy values, i.e. the experimental mass dissipates more energy in the presence of delay than system 2. Hence, $HSEM^{\text{S}}$ qualitatively captures the test susceptibility. Still, the effect of a specific value on the RTHS test result cannot be inferred.

The course of $||T_{\text{o}}||$ is visualized in fig. 12.9c. Remember that smaller values of $||T_{\text{o}}||$ imply robustness and if $< 20\,\text{dB}$, robust performance is achieved [28]. The figure implies that only system 2 with VFF has robust performance and that system 1 without VFF would be unstable. To understand the condition of robust stability and performance better, the interface displacement z'_{NUM} is shown for system 1 and system 2 with VFF in fig. 12.10. In both cases, the reference solution is emulated well with the vRTHS test. Therefore, the condition of $||T_{\text{o}}|| < -20\,\text{dB}$ for robust performance might be too conservative. Additionally, tests of system 1 without VFF were stable.

The FACE method was applied to these two systems with/without VFF. For the sake of simplicity, the results are not shown in detail here, as they resemble the results from section 12.1.4. The results are summarized in table 12.1, where the relative prediction error is calculated as $\frac{|a_{\text{pred}}-\hat{a}|}{\hat{a}}$, the test error as $\frac{|a_{\text{min}}-\hat{a}|}{\hat{a}}$ and the error estimate as $\frac{|a_{\text{min}}-a_{\text{pred}}|}{a_{\text{pred}}}$. In contrast

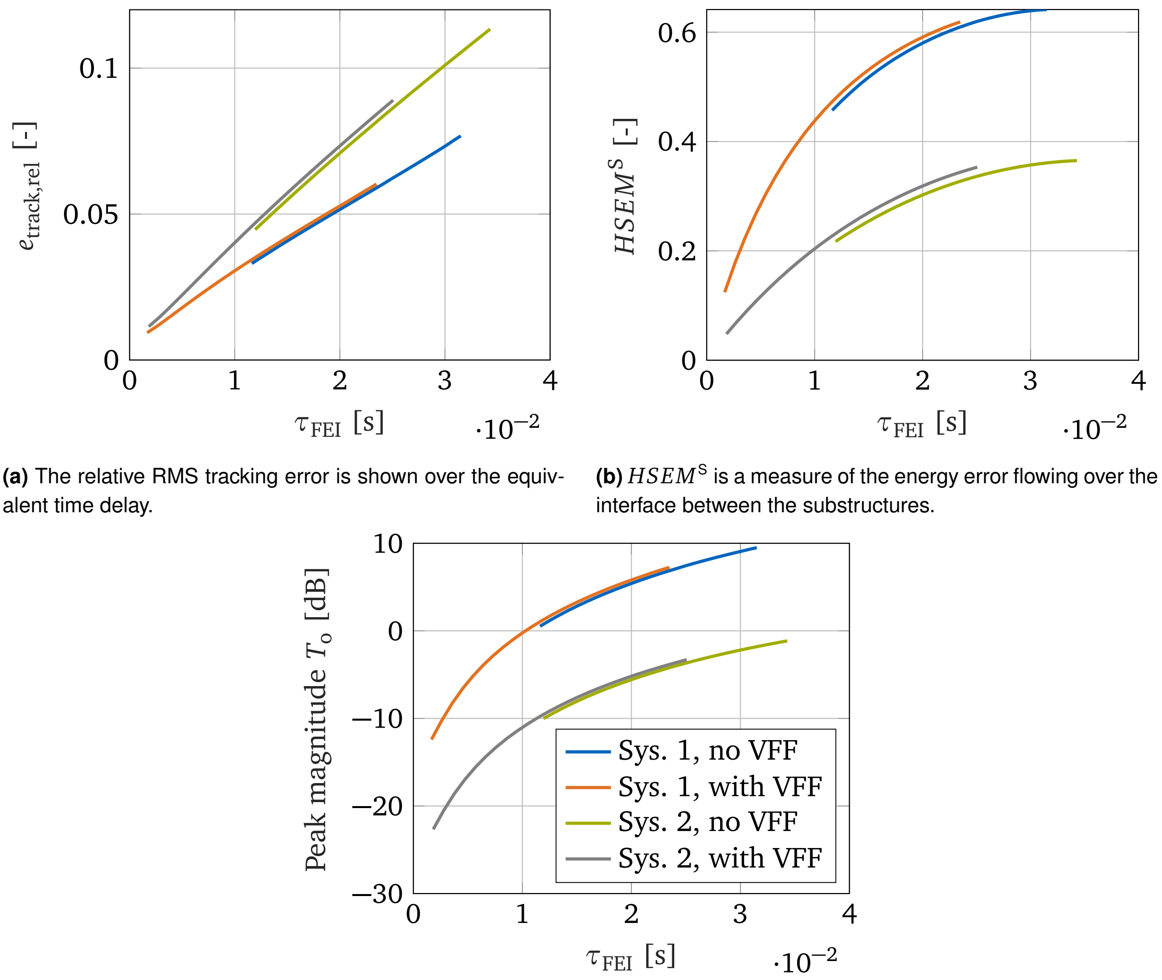

(a) The relative RMS tracking error is shown over the equivalent time delay.

(b) $HSEM^{\text{S}}$ is a measure of the energy error flowing over the interface between the substructures.

(c) If the magnitude of T_{o} is $< 20\,\text{dB}$, the condition of robust performance is fulfilled according to [28]. The condition for robust stability writes $||T_{\text{o}}|| < 0\,\text{dB}$.

Figure 12.9: Accuracy measures are visualized for vRTHS tests of different dynamical systems (system 1: blue and green vs. system 2: orange and gray) with artificial additional delay τ_{add}. The modeled Stewart Platform is controlled with (orange, gray) and without (blue, green) VFF.

to the accuracy measures above, the values of the amplitude error can be interpreted more easily. Also, the FACE method captures that the test fidelity is less susceptible for system 2 and that the tests with VFF are more accurate. Both conclusions can be drawn looking at the values of the error estimate or the function course in the convergence plot (not shown). In general, the prediction error of FACE is smaller, the higher the actuator bandwidth (i.e. higher with VFF than without) and the less susceptible the RTHS setup is (i.e. smaller for system 2 than system 1). Not only the prediction error is smaller, but also the error between a_{min} and $\hat{a}$ or a_{pred}.

This clearly demonstrates the added value of the FACE method compared to the other accuracy measures: the FACE method offers an experimental sensitivity analysis. This approach is therefore not only able to predict the reference solution quite accurately, but also to evaluate the susceptibility. This is unique compared to the state-of-the-art, where for such sensitivity analysis, models of the system dynamics need to be available. Furthermore, the quantitative values, i.e. the influence of an error on the test result (here a_{min} and a_{pred}), can be interpreted easily.

Table 12.1: Prediction performance for two differently sensitive dynamical systems.

Dynamical System	a_{min} [m]	a_{pred} [m]	$\hat{a}$ [m]	prediction error	test error	error estimate
System 1, no VFF	$4.72 \cdot 10^{-4}$	$8.65 \cdot 10^{-4}$	$9.92 \cdot 10^{-4}$	12.9 %	52.4 %	45.0 %
System 1, with VFF	$8.10 \cdot 10^{-4}$	$9.09 \cdot 10^{-4}$	$9.92 \cdot 10^{-4}$	8.4 %	18.4 %	10.8 %
System 2, no VFF	$6.72 \cdot 10^{-4}$	$8.40 \cdot 10^{-4}$	$8.93 \cdot 10^{-4}$	5.9 %	24.7 %	20.0 %
System 2, with VFF	$8.75 \cdot 10^{-4}$	$9.13 \cdot 10^{-4}$	$8.93 \cdot 10^{-4}$	2.3 %	2.0 %	4.2 %

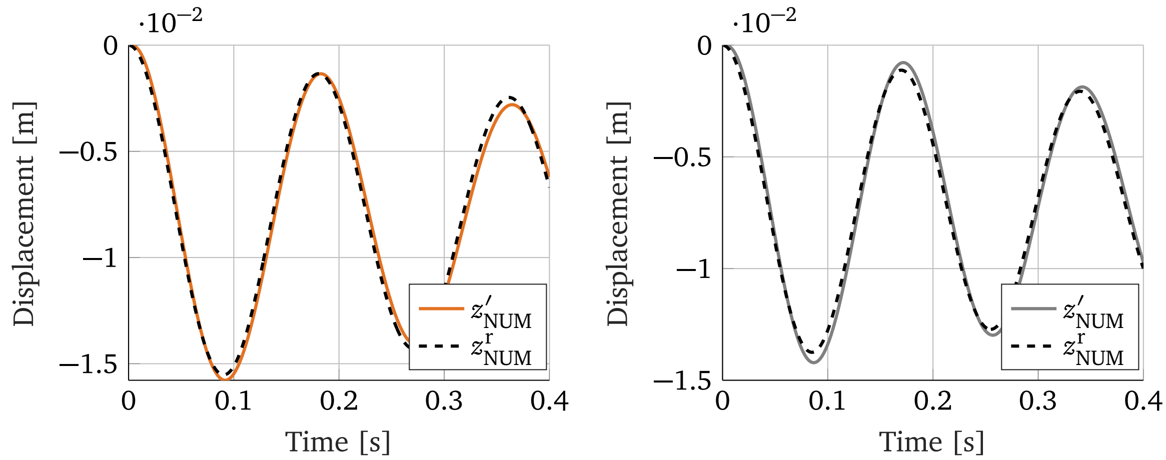

(a) System 1, where $||T_o|| \approx -12$ dB.

(b) System 2, where $||T_o|| \approx -23$ dB.

Figure 12.10: Interface displacement z'_{NUM} for system 1 and system 2 with VFF. The reference solution (black, dashed line) and the executed displacement z'_{NUM} (orange or gray) are shown.

12.2 Virtual RTHS Benchmark System

To evaluate the applicability and performance of the FACE method under more realistic conditions, the RTHS benchmark problem was used. This benchmark model is an initiative of the MECHS community and available for download via https://github.com/MECHS-RCN/BENCHMARKS [205]. The intention of this benchmark model, which is a vRTHS test, is to have a common framework to evaluate and compare controllers. In this work, the model is used to assess the FACE method, i.e. determine the test fidelity. The description of the model is based on [205] and further details can be found therein.

12.2.1 System Description

Since the origin of RTHS lies in earthquake engineering, the benchmark model[6] is a building structure. The structure has three stories and two bays (two-dimensional), as depicted in fig. 12.11, and is excited by horizontal ground accelerations due to an earthquake. The partitioning is as follows: the moment resisting frame is the experimental substructure and exists as hardware at the Intelligent Infrastructure Systems Lab (IISL) at the Purdue University. The numerical substructure comprises the remaining building, which is modeled assuming linear elastic behavior, negligence of vertical displacements and representation of the floors using lumped masses. The remaining, reduced numerical model consists of three DoFs. The transfer system consists of a servo-controlled hydraulic actuator, linear variable differential

[6] The used implementation of this vRTHS test was downloaded from https://github.com/MECHS-RCN/BENCHMARKS on February 24th, 2021.

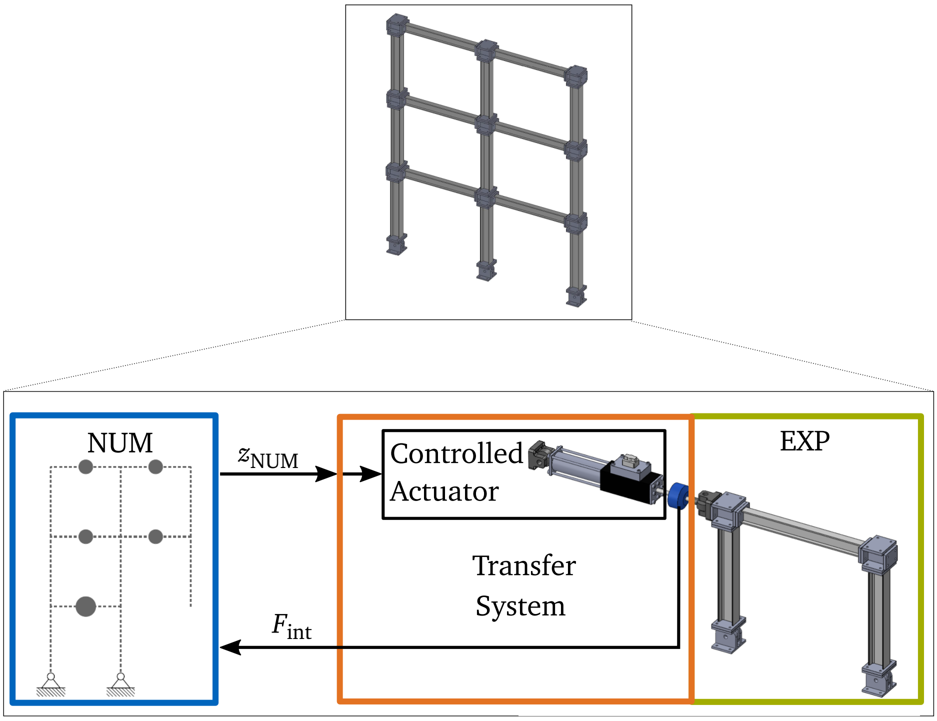

Figure 12.11: The benchmark control problem proposed by Silva et al. [205] investigates the dynamic response of a three-story, two-bay structure to earthquake excitation. The transfer system consists of a controlled servohydraulic actuator and a load cell. The vRTHS implementation can be downloaded from GitHub. Images are taken from [205].

transformers for displacement measurement and fatigue-rated low-profile load cells for force measurement. The controller input is the desired displacement of the first floor and the implemented controller consists of a PI controller and a phase-lead compensator. The PI controller was tuned using the Ziegler-Nichols closed loop method, where a position gain of $K_\mathrm{p} = 2$ and an integral gain of $K_\mathrm{i} = 95\,{}^1/_\mathrm{s}$ resulted. The phase-lead compensator is a zero-pole combination used to reduce the phase error.

The available model is a vRTHS test of this RTHS setup, which means that also the components of the transfer system, the experimental part and their dynamic interaction (CSI) are modeled. The controlled hydraulic actuator is modeled with identified dynamics of the servo-valve and the actuator itself. Furthermore, A/D and D/A conversion as well as noise on the displacement and force measurement are included. The vRTHS test runs with a fixed sampling time of $\Delta T = \frac{1}{4096}$ s and a fourth order Runge Kutta solver for time integration.

In the available model, the earthquake excitation as well as the partitioning can be selected. The partitionings differ in modal damping and the mass of each floor in the numerical part. This leads to differently sensitive RTHS tests, which are evaluated by the PSI (see section 10.3.3 and [134]). This research uses the El Centro 1940 earthquake as excitation and partitioning case 1, which is a slightly sensitive partitioning.

In general, the intent of an RTHS test in earthquake engineering is not necessarily to replicate exactly how a building reacts to a specific earthquake, but to guarantee that the general dynamic behavior has been emulated [12, 58]. Understanding the vibration response of buildings under earthquake excitation is important and must effectively be mitigated to avoid damage of the buildings. Hence, the vibration response is again of interest (QoIs magnitude and frequency) for the application of the FACE method. The reference motion of the building, which is the motion of the floors, is also available in the downloadable implementation and used in this section for the evaluation of the FACE method.

12.2.2 Application of the FACE Method to the Benchmark System

The selected QoIs for the benchmark problem are the vibration magnitude and frequency of the first floor. Note that, for example, also the motion of the second/third floor could be taken. In this case, the damping is not considered because, as could be seen previously, the damping is inversely proportional to the magnitude and does not offer novel insights at this point.

Firstly, the convergence of the magnitude is investigated. This is done by adding artificial delay[7] $\tau_{\text{add}} = \{0.001, 0.002, ..., 0.008\}$ s. The Fourier transform of the measured displacement data z'_{NUM} is performed with data from $\in (5.2, 36.8)$ s of the whole available measurement data, which is the time span where the earthquake shook the earth. The results are visualized over the equivalent time delay τ_{FEI} and the magnitude is plotted in dB in fig. 12.12a, as this proved to lead to an accurate prediction in the preceding section 12.1. The extrapolation (blue, dashed line) is performed using a polynomial of degree one for $\tau_{\text{add}} \in (0.001, 0.006)$ s. Larger values of τ_{add} are not considered because the slope of the magnitude increases, in other words, the linear relationship cannot be assumed. The mean magnitude of the vRTHS test without additional delay (just PI controller and phase-lead compensator) is $a_{\min} = 4.59 \cdot 10^{-4}$ m. The FACE method predicts a reference amplitude of $a_{\text{pred}} = 2.7 \cdot 10^{-4}$ m and the reference magnitude is $\hat{a} = 3.39 \cdot 10^{-4}$ m. This leads to a relative prediction error of $\frac{|a_{\text{pred}} - \hat{a}|}{\hat{a}} = 20.2\,\%$. The absolute difference between $a_{\min}$ and a_{pred} is $\approx 1.89 \cdot 10^{-4}$ m. The estimated amplitude overshoot in the vRTHS test is $\frac{|a_{\min} - a_{\text{pred}}|}{a_{\text{pred}}} = 69.9\,\%$ (as opposed to the true overshoot $\frac{|a_{\min} - \hat{a}|}{\hat{a}} = 35.6\,\%$). That this order of magnitude is correct can be seen in the arbitrarily selected time interval shown in fig. 12.12b, where the peak magnitude of the reference and of the vRTHS test differ approximately with this order. Whether this result is acceptable

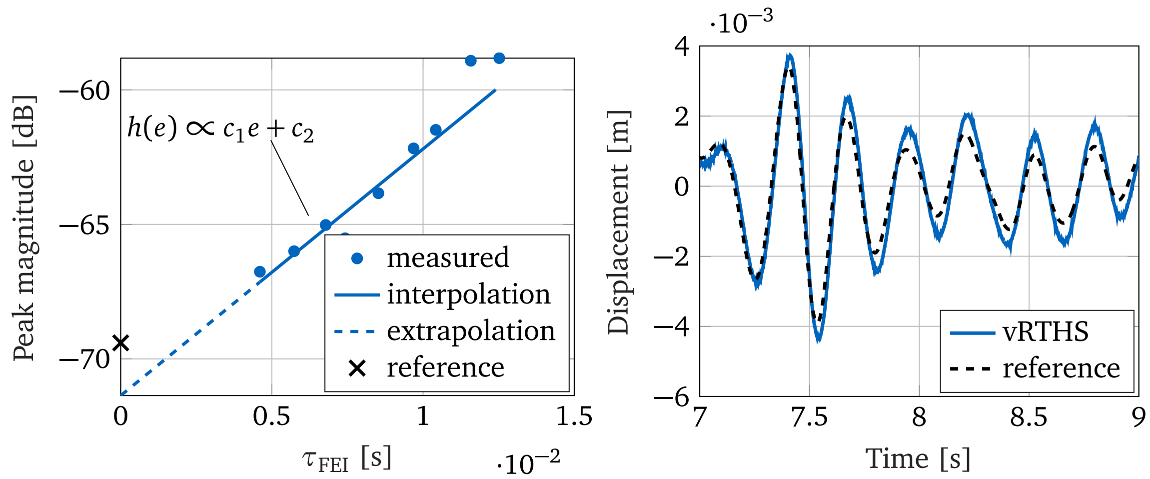

(a) Convergence plot of the magnitude for different values of τ_{add} (measurement points) over the equivalent time delay τ_{FEI}.

(b) Arbitrarily extracted time period showing the reference solution (black, dashed line) and the result of the vRTHS test (blue, solid line) for $\tau_{\text{add}} = 0$ s.

Figure 12.12: The FACE method is applied to predict the magnitude of the reference solution of the benchmark problem for the El Centro 1940 earthquake and partitioning case 1. For that purpose, additional artificial delay τ_{add} was introduced.

or not depends on the purpose of the test, i.e. which components should be tested. For the purpose of an earthquake, one might argue that if a critical component withstands the larger magnitudes that occur in the vRTHS test compared to the real load, this amplitude error is

[7] Note that smaller spacing between the τ_{add} values could have been taken due to the small sample time $\Delta T = 2.44 \cdot 10^{-4}$ s of the vRTHS test.

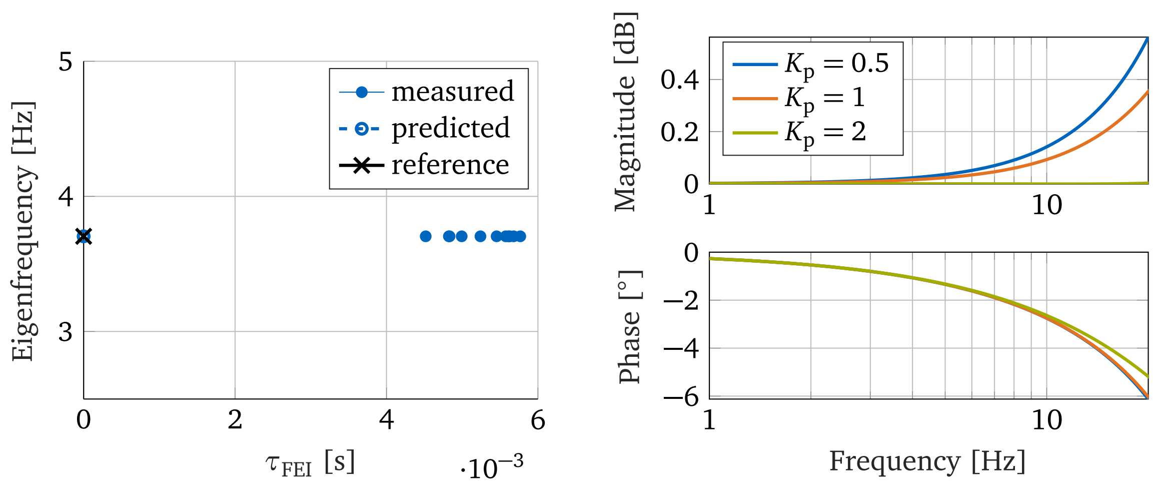

(a) The eigenfrequency of the vRTHS test is given over τ_{FEI}, which correspond to different values of K_p.

(b) The Bode plot of the controlled actuator for different values of K_p.

Figure 12.13: The FACE method is applied to investigate how well the frequency content is replicated by the vRTHS test of the benchmark structure (cf. fig. 12.11). To change the actuator bandwidth, the position gain K_p of the PI controller is varied.

acceptable. In general, however, this amplitude error is quite large. Note that the prediction accuracy is highly dependent on the measurement points taken for the interpolation. If, for example, only the values $\tau_{\mathrm{add}} \in (0.001, 0.004)$ s are taken, the slope of the interpolation function is smaller and the prediction more accurate (relative prediction error 5.7 %).

Next, the frequency content of the building vibration is investigated. This is done by changing the actuator bandwidth, i.e. the controller parameters K_p and K_i. The position gain K_p took the values $\{1.25, 1.4, 1.55, ..., 2\}$ and the results are depicted in fig. 12.13a. The figure indicates that a change of the position gain does not affect the frequency response of the vRTHS test. This corresponds to the case of $\omega_{\mathrm{bw}} > \omega_{\mathrm{dyn}}$ in section 11.2. This can also be seen in the transfer behavior of the controlled actuator given in fig. 12.13b: the transfer behavior of the controlled actuator is almost ideal in the shown frequency range of up to 20 Hz and a change of the position gain does not affect the actuator bandwidth in this frequency range. This implies that the chosen PI controller replicates the vibration response well and the results can be trusted.

Similar investigations have been performed varying the integral gain K_i and the results are displayed in fig. 12.14. The selected values were $\{30, 35, ..., 95\}$ 1/s. As can be seen in fig. 12.14a, decreasing the value of K_i (decreased K_i leads to higher delay τ_{FEI}) corresponds to the case $\omega_{\mathrm{bw}} < \omega_{\mathrm{dyn}}$. This is also obvious from the Bode plot in fig. 12.14c. The extrapolation of the reference frequency is done using a polynomial of degree two and $f_{\mathrm{pred}} = 3.8$ Hz results, which slightly overestimates the reference frequency of $\hat{f} = 3.7$ Hz. This is because the higher values of K_i (for $\tau_{\mathrm{FEI}} \in (0.004, 0.006)$ s) already have the correct frequency content, i.e. the final value has asymptotically been approached, but this is not implemented in the interpolating polynomial. Using K_i^{-1} on the abscissa (fig. 12.14a), a polynomial of degree two yields a very good prediction. Note that the step-wise changes of the eigenfrequencies comes from the Fourier transform and the limited duration of the time interval used. The longer the used time interval, the smaller the frequency spacing.

To sum up, the FACE method proves applicable in the benchmark problem, which is a vRTHS setup incorporating already some errors/uncertainties that also occur in a real RTHS test. The predicted quantities of the reference solution help to evaluate the test fidelity, i.e. offer a simple possibility to assess how well the test emulated the reference dynamics.

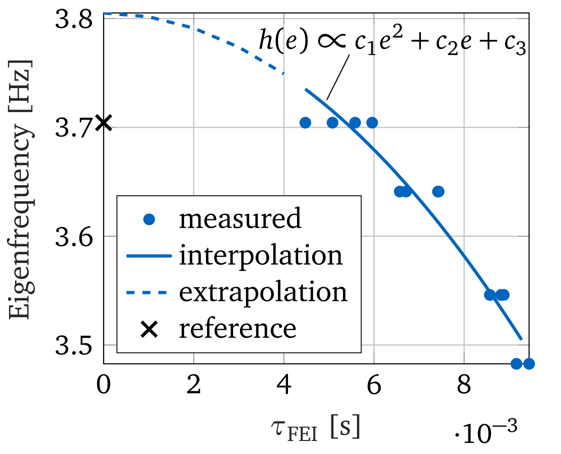

(a) The eigenfrequency of the vRTHS test is given over τ_{FEI}, which correspond to different values of K_{i}.

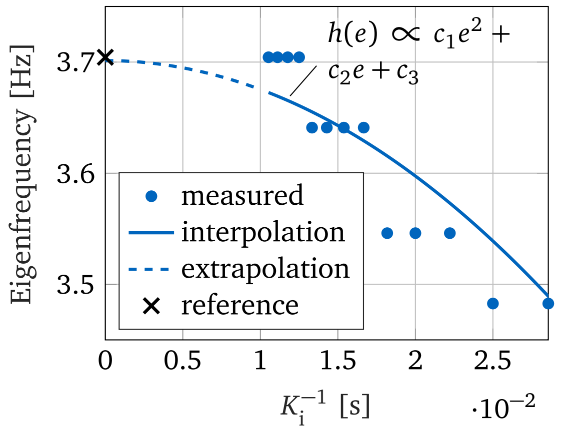

(b) The eigenfrequency of the vRTHS test is given over K_{i}^{-1}.

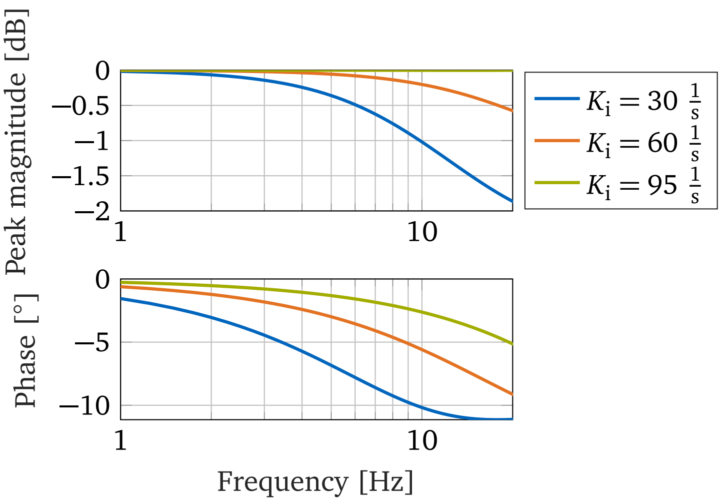

(c) The Bode plot of the controlled actuator for different values of K_{i}.

Figure 12.14: The FACE method is applied to investigate how well the frequency content is replicated by the vRTHS test of the benchmark structure (cf. fig. 12.11). To change the actuator bandwidth, the integral gain K_{i} of the PI controller is varied.

12.3 RTHS System with Contact

Finally, the FACE method is applied to a real RTHS test. Namely, the RTHS system with contact presented in fig. 4.5 and the dynamical properties given in table A.2 were used. The numerical damping was $d_{\mathrm{NUM}} = 50\,{}^{\mathrm{kg}}/_{\mathrm{s}}$ and the standard controller parameters $K_{\mathrm{Pp}} = 50\,{}^{1}/_{\mathrm{s}}$, $K_{\mathrm{Pv}} = 0.2\,{}^{\mathrm{As}}/_{\mathrm{m}}$ and $K_{\mathrm{Iv}} = 5\,{}^{\mathrm{A}}/_{\mathrm{m}}$ were used. Even though this system does not undergo large vibrations, i.e. exhibits only little vibration response during the contact phase, the QoI were the oscillation magnitude (see the reference solution in fig. 12.16a) during the contact phase and the frequency of this oscillation. The reference solution was obtained from a pure simulation of the overall system (see section 4.4).

To investigate the vibration magnitude and predict the reference, the controller performance was artificially deteriorated by additional delay τ_{add}. For RTHS tests with VFF, the additional delay was $\tau_{\mathrm{add}} = \{0.001, 0.002, \ldots, 0.009\}$ s and without VFF[8] $\tau_{\mathrm{add}} = \{0.001, 0.002, 0.003, 0.004\}$ s. For all tests, the equivalent time delay τ_{FEI} was evaluated, which is depicted

[8]Remember that the tests without VFF are unstable.

in fig. 12.15. Only those τ_{FEI} values are visualized that are $> 0\,\mathrm{s}$. The figure indicates that the VFF clearly improves the tracking performance (smaller τ_{FEI}) compared to solely using the cascaded feedback controller. Furthermore, the τ_{FEI} values show tendency to grow for larger τ_{add}. Nevertheless, a change in τ_{add} of $0.001\,\mathrm{s}$ does not change the value of τ_{FEI} by $0.001\,\mathrm{s}$, which would be expected. The reason lies in the implementation of the equivalent time delay. Firstly, the FFT is performed over a short time interval of $\approx 1.5\,\mathrm{s}$, i.e. just during contact, which leads to a low frequency resolution. Secondly, the magnitudes of the oscillation are small and the magnitudes at the frequencies surrounding the eigenfrequency are high and tilt the equivalent frequency f_{eq} to smaller values (see also section 11.3.1). Despite the inconsistency in the specific values of τ_{FEI}, they were used to predict the reference solution, which is the magnitude of the oscillation.

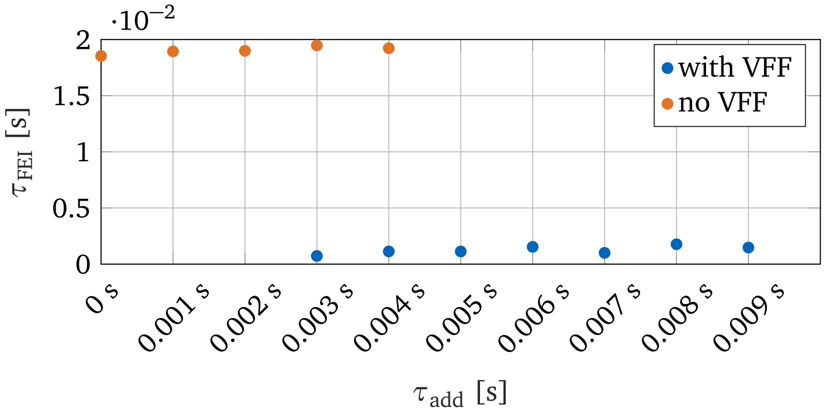

Figure 12.15: Value of τ_{FEI} in RTHS tests with different τ_{add} and with the VFF switched on/off.

The resulting interface trajectories are visualized in fig. 12.16a. As expected, the oscillations grow, the more delay is introduced. The convergence plots are shown in the figs. 12.16b and 12.16c. Figure 12.16b uses the measured data from the RTHS tests with and without VFF. The interpolation is done using the magnitude values in dB and a linear polynomial. Figure 12.16c just uses the measurements from the RTHS tests with VFF. Since here the interpolation is more precise for the measurement data with low τ_{FEI}, this prediction is used for the further explanations. The FACE method estimates a relative error of $\frac{|a_{\min}-a_{\mathrm{pred}}|}{a_{\mathrm{pred}}} = 37\,\%$ and the real error is $\frac{|a_{\min}-\hat{a}|}{\hat{a}} = 57\,\%$ ($a_{\min}$ with VFF and $\tau_{\mathrm{add}} = 0\,\mathrm{s}$). However, the results of the RTHS test are of high fidelity: the Stewart Platform has almost no time delay and further sources of dynamics/delay (sensors, DSP, numerical time integration scheme) are negligible. The deviation from the reference solution might come from a mis-identification of the experimental part (k_{EXP}, d_{EXP}) used to obtain the reference solution.

Since the vibration magnitude is rather small, it is arguable whether the investigation of the vibration behavior is the correct measure q for the fidelity assessment of this dynamical system or another choice of q might be more appropriate.

Furthermore, the fidelity with respect to the oscillation frequency can be investigated using the FACE method. This is done by changing the controller parameter K_{Pp} of the cascaded feedback controller. In the tests with VFF, the values were $K_{\mathrm{Pp}} = \{30, 35, ..., 80\}$ $^1/_\mathrm{s}$ and without VFF $K_{\mathrm{Pp}} = \{30, 35, ..., 70\}$ $^1/_\mathrm{s}$. Also this time, the values of τ_{FEI} were close together, since the delay with VFF is very small, $< 1\,\mathrm{ms}$. Since measurements with and without VFF are used, the choice of K_{Pp}^{-1} on the abscissa of the convergence plot is also not possible. Therefore, $e_{\mathrm{track,rel}}$ was selected here. The values of $e_{\mathrm{track,rel}}$ for different K_{Pp}, with and without VFF, are plotted in fig. 12.17. The figure illustrates that higher values of K_{Pp} lead to smaller tracking errors and the VFF reduces the tracking error even further. The convergence plot

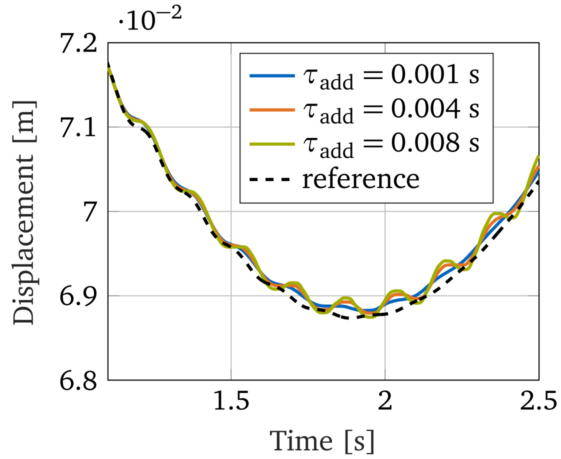

(a) Interface displacement of the reference z^r_{NUM} and the RTHS tests z'_{NUM} for different values of τ_{add}. VFF was turned on.

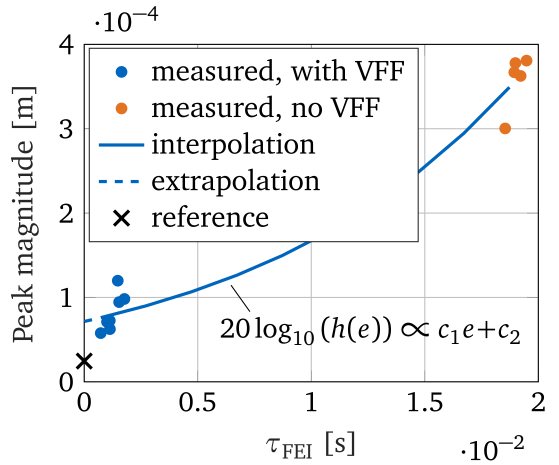

(b) The interpolation uses data from RTHS tests with VFF switched on/off.

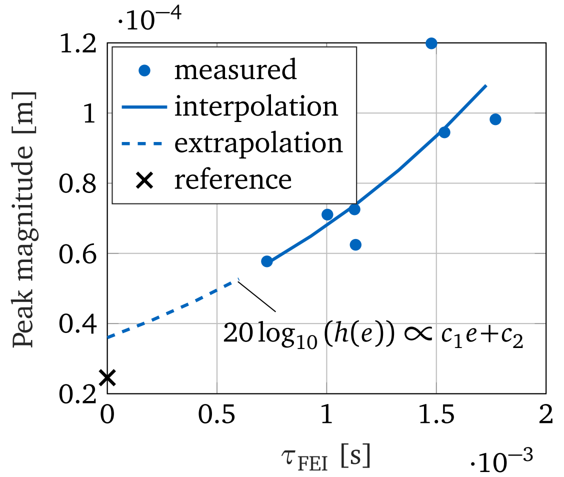

(c) The interpolation uses data solely from RTHS tests with VFF.

Figure 12.16: The FACE method is applied to the RTHS system with contact to predict the magnitude of the reference during the contact phase. In the lower figures, the measured data are represented as dots.

is shown in fig. 12.18a. The results with VFF all have a detected eigenfrequency of 6.7 Hz, which is higher than the detected eigenfrequencies without VFF at 6 Hz. This is as expected: the VFF increases the actuator bandwidth. For stiffness experimental substructure, an actuator bandwidth $\omega_{\mathrm{bw}} < \omega_{\mathrm{dyn}}$ leads to decreased observed eigenfrequencies (cf. section 12.1.2). Note that, in the contact phase, the dynamics of the RTHS system constitute just a spring. The figure also shows the analytical eigenfrequency, which is 7 Hz and the detected eigenfrequency of the reference simulation at 7.3 Hz. This reveals the difficulty using the Fourier transform to detect the eigenfrequencies, namely the limited time interval used and the resulting low frequency resolution. The algorithm detects the eigenfrequency at the frequency line closest to the analytical solution, i.e. the real oscillation frequency of the reference. Even though the measured frequencies lie on one horizontal line in fig. 12.18a, their true oscillation frequency is higher for smaller $e_{\mathrm{track,rel}}$. This is visible in time domain, but not caught by the Fourier transform. Therefore, a more appropriate method to determine the frequency needs to be found when dynamical systems with contact are investigated, i.e. when the time interval used for the Fourier transform is rather short. This could be done using a complex

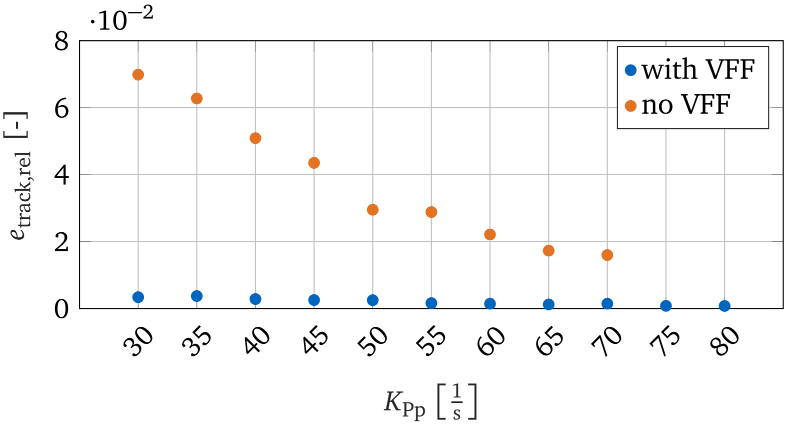

Figure 12.17: Tracking error $e_{\text{track,rel}}$ for different controller parameters K_{Pp}.

exponential fit in time domain. Due to this reason, no polynomial fit is performed with the data in fig. 12.18a.

In the benchmark of Part I, different feedforward controllers were compared to enhance the existing cascaded feedback controller. In these results, one could already observe that the oscillation frequency is different for different feedforward controllers. Therefore, the measurement data for the dynamical system with $d_{\text{NUM}} = 200\,\text{kg/s}$ are taken and compared with respect to their frequency content. The equivalent time delay τ_{FEI} was evaluated for each RTHS test and the results are given in fig. 12.18b. Here, PPI1 indicates the set of

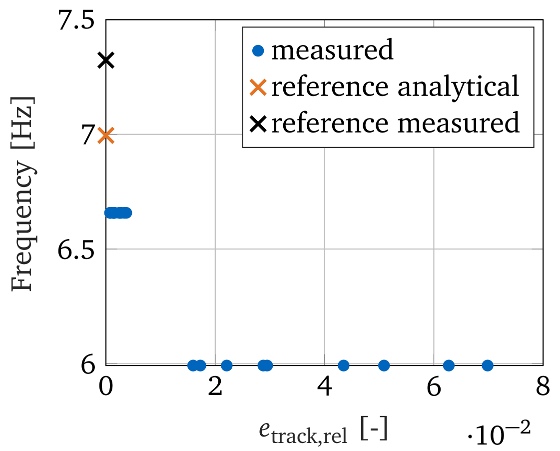

(a) The frequency during contact for different values of K_{Pp}.

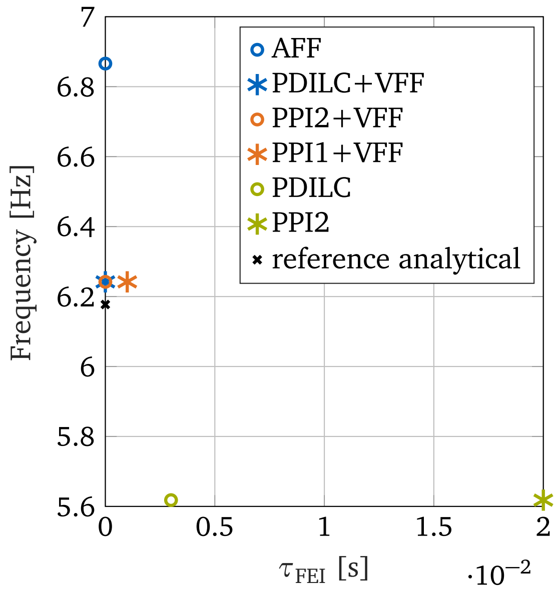

(b) The frequency during contact depending on the feedforward control scheme.

Figure 12.18: The FACE method is applied to the RTHS system with contact to predict the oscillation frequency of the reference during the contact phase.

controller parameters $K_{\text{Pp}} = 20\,\text{1/s}$, $K_{\text{Pv}} = 0.2\,\text{As/m}$ and $K_{\text{Iv}} = 1\,\text{A/m}$ and PPI2 the set $K_{\text{Pp}} = 50\,\text{1/s}$, $K_{\text{Pv}} = 0.2\,\text{As/m}$ and $K_{\text{Iv}} = 5\,\text{A/m}$. If not indicated specifically, PPI2 was used. The results imply that solely using the feedback controller (without any feedforward) leads to a large delay τ_{FEI} and a poor representation of the oscillation frequency. Using PDILC achieves smaller delay τ_{FEI}, however still the wrong oscillation frequency. The reason is that the cutoff frequency of the robustness filter was $f_{\mathrm{Q,cut}} = 6\,\mathrm{Hz}$ and therefore the feedforward signal is limited to the frequency range below. Consequently, the PDILC is able to compensate for low-frequency errors, but not for high-frequency errors. All combinations with VFF, specifically just using VFF or in combination with PDILC, lead to a perfect emulation of the oscillation frequency. Figure 12.18b depicts the analytically calculated frequency. Due to the frequency resolution of the Fourier transform, 6.2 Hz is the closest frequency to the analytical reference solution 6.18 Hz. Using AFF even leads to higher dynamic oscillations, which shows the potential of AFF to control highly dynamic processes. Nevertheless, further improvement of AFF is needed such that also these tests emulate the reference frequency more accurately.

Note that also during ILC learning, the oscillation frequency increases, which is visible e.g. in figs. 6.7 and 6.9. Also here, the frequency resolution in the Fourier transform is not high enough to detect those changes.

Chapter 13

Summary of Part II

Part II proposed the FACE method, which stands for *Fidelity Assessment based on Convergence and Extrapolation*. This novel method helps to assess the test fidelity while fulfilling the presented requirements from section 10.3.7. Using the FACE method, the reference solution of an RTHS test can be predicted and the test fidelity successively concluded. In principle, the FACE method uses the variation of a parameter to investigate the sensitivity of the RTHS setup, or specifically a QoI q, to uncertainties/errors e of this parameter. The variation is performed in the explorable area, which is between the minimum achievable amount of error e_{min} and the maximum, critical amount of error e_{crit} where the test becomes unstable. This approach corresponds to an experimental sensitivity analysis of a QoI to a system parameter/error. Interpolating between the measured data points in the explorable area yields the relation $q = h(e)$ and enables to evaluate the function at $e = 0$, which gives an estimate q_{pred} of the reference solution $\hat{q}$. Using q_{pred} and the RTHS result at e_{min}, i.e. q_{min}, the test fidelity[1] can be assessed. The application of the method requires that both, the source of error and the reference solution, are quantified as scalar values, i.e. values representing the characteristics of the whole RTHS test. Both quantities should be easy to interpret and representative of the system behavior.

In this thesis, the key idea of FACE (see section 11.1) is elaborated for the fidelity assessment of applications where the vibration response is of interest. Specifically, the vibration magnitude, damping and frequency were determined as the QoIs q describing the vibration response of a structural system. The actuator dynamics are assumed to be the dominating error source in the RTHS loop. Therefore, the influence of actuator dynamics on the RTHS dynamics is analyzed in section 11.2 for spring and mass experimental substructures. In this chapter, the conclusion is that the actuator delay can be arbitrarily changed by (i) introducing additional delay and (ii) altering the actuator bandwidth, which has disparate effects on the RTHS vibration response. Using the knowledge gained, the specific selection of e was made in section 11.3. Namely, using the equivalent time delay of the actuator τ_{FEI}, the relative RMS tracking error $e_{\mathrm{track,rel}}$ as well as the inverse of the controller parameters K_{p}^{-1} and K_{Pp}^{-1}, respectively, was found appropriate. If other sources of errors are neglected, the reference solution would be met if these quantities were zero. The overall workflow when applying the FACE method to determine how well the vibration behavior is replicated with the RTHS test (main error source: actuator dynamics) is illustrated in fig. 13.1.

Several application examples were presented in chapter 12. Firstly, vRTHS tests of a simple one-dimensional coupled mass-spring-damper system were performed and the FACE method applied. Then, the more complex benchmark example emulating the response of a three-story building under earthquake loads was investigated. Finally, the FACE method was applied to the RTHS system with contact from Part I. The overall results are promising and

[1] In this case, the test fidelity measures how well a certain QoI q has been emulated by the RTHS test.

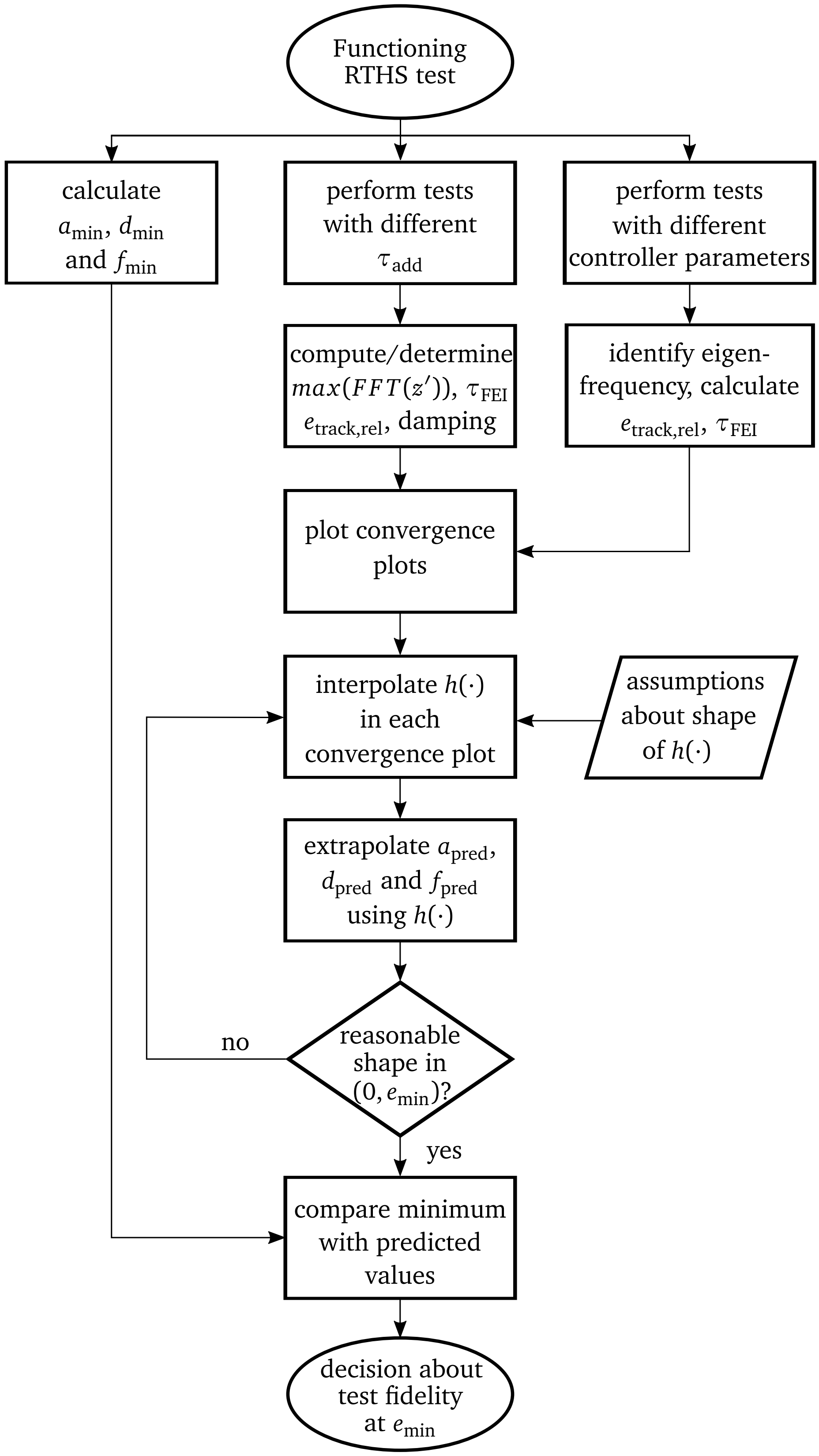

Figure 13.1: Part II proposes the FACE method and shows the efficiency for the special case, where the vibration response of a system is of interest and the actuator dynamics are regarded as the main error source. The detailed workflow when applying the FACE method for this kind of problem is shown in this figure.

show the potential that the FACE method offers. The prediction accuracy of the reference solution is higher, the smaller the error $e_{\min}$ and the less susceptible the RTHS test is to the investigated system parameter. Nevertheless, the results are easy to interpret and offer a good basis for fidelity assessment, i.e. to decide how well the RTHS test result $e_{\min}$ emulates the true system dynamics $q_{\text{pred}}/\hat{q}$. In these example applications, some limitations of the current implementation for the fidelity assessment of the vibration response could be identified: the extraction of the oscillation frequency using FFT and of the equivalent time delay τ_{FEI} is only accurate if the measuring period is sufficiently long. For the application to the system with contact, where the oscillation is rather small and the oscillation period short, other methods are required to extract the oscillation frequency with sufficient accuracy.

While the derivations in section 11.3 and chapter 12 assume the actuator dynamics as being the dominating error source and the vibration response of being the quantity of interest, this is not generally the case in all engineering applications. Nevertheless, the FACE method can still be applied. For example, modeling uncertainties in the numerical part or uncertainties of the test specimen might be much more important and influencing the RTHS result significantly. Then, not the dynamics of the actuator must be varied to obtain the convergence plot, but these dominating sources of error. For instance, the stiffness of the numerical part could be changed in the successive tests and the influence on the QoI investigated[2]. Then, the FACE method requires an appropriate choice of the error measure e. If just the sensitivity of the RTHS setup with respect to the system parameter is of interest, e could directly be k_{NUM} in the described example. This could be used to determine how important the accurate modeling of these system quantities is. If FACE should be used to determine the test fidelity, e must not only be a scalar quantity, but also satisfy that the reference solution is given when $e = 0$.

Advantages of using the FACE method include the simple and quick applicability, as no system knowledge (transfer system, experimental part) is required. Even though no reference solution is necessary, the fidelity can be estimated. Furthermore, the results are easy to interpret and the direct influence of an error/uncertainty on the RTHS result is seen. Due to monitoring the QoI q, the result is not just a numeric value but provides information about how the dynamics of the RTHS result are affected. The prediction accuracy of the FACE method, which tells how close the true reference solution is predicted, depends on several factors:

- The selection of the interpolation function $h(\cdot)$ is critical and the general shape should include as much physical information as possible (e.g. the gradient, curvature, maximum value, ...). Many measurement points in the vicinity of $e_{\min}$ help to understand the trend of the system behavior. These measurement points are more important for the interpolation than the measurement points close to e_{crit}.

- The smaller $e_{\min}$ and the less susceptible the RTHS test to the error e, the higher the prediction accuracy.

- The accuracy of the prediction also depends on the amount of other error sources. Since these are also in the RTHS loop, the best available prediction of the reference solution using FACE relies on these errors being negligible. This means that the FACE method just considers the influence of one error source. If the other error sources are not negligible, the reference solution is not obtained. Then, the FACE method just tells how sensitive the RTHS result is to the error source used for the analysis. One option to circumvent this is to combine several error measures in e.

[2] Also the choice of the QoI is not limited to the vibration magnitude, frequency and damping. Quantities like stresses, peak displacement values, etc. could be of interest.

The application of the FACE method requires the reproducibility of the test. For example, the fidelity of crack propagation cannot be investigated with this method. A further shortcoming of the method is that the system must permit additional error to build the convergence plot. With the current implementation, a skilled engineer is needed to interpret the results and determine the fidelity or acceptability of the test. This means, a decision needs to be taken whether the results q_{min} replicate the reference dynamics q_{pred} (best available knowledge of $\hat{q}$) accurately. The overall objective of the community is to set up an acceptance criterion and the FACE method could be used to achieve this goal. The idea is to combine the errors of the RTHS test on different QoIs (with weighting), such as e.g. the vibration magnitude, damping and frequency, as a scalar and determine a threshold—the acceptance criterion—for the RTHS setup. Further future steps could include the consideration of uncertainties, the application to nonlinear systems, multiple DoF (MDOF) systems, different QoIs and additional applications.

Part III

Testing Prosthetic Feet with RTHS

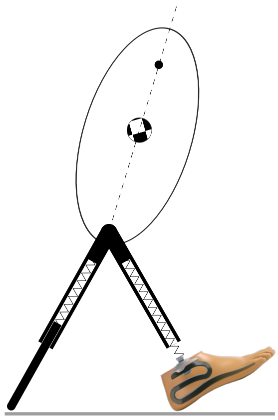

Chapter 14

Introduction to Foot Prostheses and Prostheses Testing

This chapter is partly based on the author's publication [102]. The content is further inspired by the co-supervised student thesis by Lisa-Marie Ballat [13].

Replacing a missing body part by prosthetics has been done for thousands of years. For example, a 3,000 year old toe made of wood and leather was found with an Egyptian noblewoman. The device assisted the balance and locomotion [32]. A prosthesis ought to mimic the function, appearance and feel of the lost limb [220]. This is important to increase the acceptance of the prosthesis by the amputee [10].

Amputations of the lower extremities are distinguished into transtibial and transfemoral amputations, where transtibial indicates an amputation below the knee and transfemoral above the knee. The less needs to be amputated, the more likely that normal movement can be regained [32].

In this work, the focus is put on foot prostheses. Building foot prostheses is critical because the function of the human foot needs to be emulated. The foot function is manifold during walking and standing: not only does it support the weight, but is also able to balance actively, adapt to different terrain and thus stabilize the human body [121]. On the one hand, the heel is compliant to absorb ground impact. On the other hand, due to the arch-type skeletal structure, the foot is rigid and acts like a rigid lever that returns energy at the end of the stance phase and propels the body forward together with the ankle [32, 121, 195, 207]. An ideal foot prosthesis would be able to fulfill these functions and generate the same gait pattern and forces as occur in an able-bodied human [32, 239].

14.1 Overview about Prosthetic Feet

Foot prostheses can be classified into conventional, energy storing and motor powered prostheses [220, 234]. An example for conventional foot prostheses is the solid-ankle cushioned heel (SACH) depicted on the left in fig. 14.1. The SACH foot is non-elastic and does not offer energetic support. During walking, the healthy side has to compensate for the energy loss. This kind of foot prostheses is used for people with limited mobility. [74, 220, 234]

Most commonly used are the so-called ESAR (energy storage and return) feet (see in the middle in fig. 14.1). These passive prosthetic feet consist of a carbon structure, which is loaded during stance and releases the stored energy during push off. The carbon structure provides compliance to absorb ground impact. [234]

Active prostheses introduce external power through motors and emulate human muscle activity [32, 234]. An example is shown on the right in fig. 14.1. The Cost of Transport (COT), which measures the energy required for locomotion, decreases with this kind of prosthesis, even though the mass increases due to the additional actuator [10]. This type of prosthesis is more expensive and relatively large, making it difficult to hide the prosthetic foot with a cosmetic cover.

Figure 14.1: Left: Prosthetic SACH foot 1S90 by Ottobock (© by Ottobock). Middle: Prosthetic Foot 1C40, C-Walk by Ottobock (© by Ottobock). The foot can be covered by a cosmetic cover. Right: Powered prosthetic foot Empower from Ottobock (© by Ottobock).

14.2 Gait Pattern of Amputees

The human foot is extremely complex with its multiple biomechanical functions. Despite great progress in prostheses development, technical replication of all these functions is challenging. The lack of functions leads to altered gait patterns of amputees: for example, the stance times on the prosthetic leg are shorter, they lift the hip during swing for ground clearance and they change their foot placement [32, 154, 193]. This results in a higher COT for amputees compared to non-amputees. In transfemoral amputees, the required energy is e.g. $30-60\,\%$ greater than in non-amputees and the self-selected walking speed is lower ($0.87-1.04\,\mathrm{m/s}$ [116] vs. $1.36-1.4\,\mathrm{m/s}$ [244]). The incorrect additional loading affects the whole body and leads to osteoarthritis, osteopenia, osteoporosis and back pain in the long run [74, 154]. The decreased balance additionally leads to increased falls. Especially walking on stairs and on uneven or soft ground can be challenging and decreases the level of independence of amputees [116, 154]. Hence, a proper prosthetic fit is relevant for both the physical and mental health. A targeted development of foot prostheses to ensure functionality in everyday life is therefore extremely important. This is achieved through functional tests, which can provide insights into the dynamic interaction between an amputee and the prosthesis already in the early development stage.

14.3 Testing of Prosthetic Feet: an Overview

Standardized test procedures for the approval of prostheses are defined in ISO 10328, ISO 22523, ISO 22675 and ISO 16955 [113, 114]. In these procedures, endurance tests are standardized, i.e. strength and material properties are tested. Also, tests of the complete heel to toe movement and dynamic loading conditions including the swing phase are defined [220]. Hence, these tests analyze the function of the prosthetic device, but lack to relate the measured quantities to the user benefit [114].

Apart from these standardized methods, further testing methods exist. A classification of these into model-based, human-based and further robot-based testing procedures has been proposed by [239].

In model-based testing, the prosthesis is simulated numerically. In the work of Tryggvason et al. [220], a Finite Element Model of a prosthetic foot is set up to optimize the stiffness characteristics of the prosthetic foot for different application scenarios. Another option is to model both the amputee and the prosthesis. This helps to analyze which parameters of the prosthetic foot influence the gait pattern and should therefore be tuned carefully [219, 239]. With model-based testing, investigations can already be performed in the early development stage since no prototype is required. Another advantage is that basic gait dynamics can be investigated without the need for test subjects. Nevertheless, modeling both the human and the prosthesis is cumbersome and the accuracy of the models needs to be validated.

Human-based testing, also called in-vivo testing, is an important step in prostheses testing [234, 239]. There, people are equipped with a prosthesis prototype. The tests are either done with an amputee or, using special modified devices, with able-bodied people to increase the number of potential test subjects [239]. These tests directly show the dynamic interplay between a user and the prosthesis and are valuable throughout the development process. Despite their importance in the final development stage of a prosthesis, these tests suffer from a poor safety level (hazardous conditions cannot be replicated), are subjective and not repeatable [139, 182].

Robot-based testing circumvents some of these problems, as it offers an objective and repeatable means of testing. Leg simulators are one option of robot-based testing. Leg simulators have for example been presented in [139, 182, 239], see fig. 14.2. The idea is to excite the tested prosthesis with the same motion (e.g. hip trajectories in [182]) or forces (e.g. ground forces in [239]) that are observable in human locomotion experiments. The correct functioning of controlled prostheses as well as the force and motion profiles can be investigated with these tests. For example, these tests can be used to see which forces/torques are required to reproduce normal gait [182]. While leg simulators already offer a good insight into these physical quantities, they do not take the dynamic interplay between a prosthesis and an amputee into account, that is how a human reacts to an inappropriate prosthesis and how the gait pattern is adapted. This can be illustrated by an example: Imagine having a pebble in your shoe. Although there are different forces than before, you can continue walking without falling over. Nevertheless, you probably adjust the posture, the walking speed and the stance time of the foot. This changes the trajectories and forces compared to your usual gait pattern. Hence, including this dynamic interplay in testing of prosthetic feet is important.

14.4 Requirements on Prostheses Testing

Based on the considerations in section 14.3, the following requirements can be set up for a novel testing procedure to fill the gap and improve prostheses development:

- **Objectivity and repeatability:** Robot-based testing offers an objective, repeatable and cost-efficient means to test prostheses [139, 182].
- **Early availability:** The testing procedure should be applicable as early as possible in the development stage.
- **Reproduce in-vivo conditions:** In-vivo working conditions should be reproduced and the dynamic interplay between humans and prostheses investigated. The prostheses

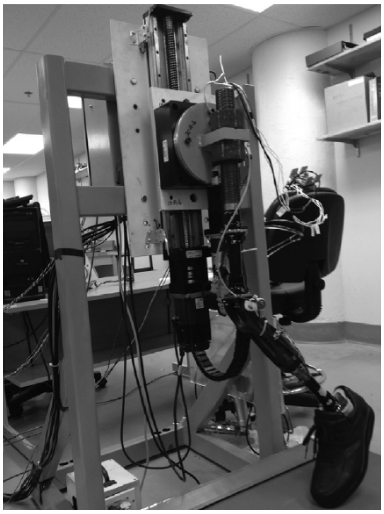

Figure 14.2: The leg simulator represents the hip motion from measured locomotion data in two DoFs [182].

should be evaluated compared to healthy subjects, since an ideal prosthesis leads to the same biomechanical functioning as the biological foot. [139, 234]

- **Safe:** The test ought to be safe while also investigating hazardous situations like tripping and stumbling [139, 182].

14.5 Objective of Part III

A novel testing method fulfilling the requirements of section 14.4 by combining the advantages of model-based, human-based and robot-based testing could be based on Real-Time Hybrid Substructuring (see also [239]). In RTHS, the amputee could be modeled while the prosthetic foot[1] is tested experimentally. This allows a dynamic analysis of the overall system *human with prosthesis* without having to perform potentially harmful subject studies or complex modeling of the prosthesis. Such an analysis would help to understand the dynamic interplay better and achieve a targeted prostheses development.

This part aims at investigating whether RTHS is in general applicable to investigate the dynamic coupling between a prosthetic foot on the test bench and a simulated modeled human. Hence, this part represents a proof-of-concept that the gait characteristics can be emulated using RTHS. The analysis investigates the potential of RTHS as a visionary test method for foot prostheses. This includes a survey of common human locomotion models and characteristic gait patterns that the RTHS test needs to be able to replicate.

In chapter 15, an understanding of human walking, the gait cycle and gait characteristics is built. Specifically, trajectories of the center of mass (CoM) and force profiles are presented. Based on these fundamentals, several conceptual models have been proposed, which are presented and investigated regarding their applicability to RTHS subsequently.

The application of RTHS is presented in chapter 16. This includes a presentation of the hardware setup used, where the controlled actuator is the Stewart Platform (see chapter 4). Additionally, an amputee model is set up based on a gait model and the required equations of motion (EoM) are derived. Relevant parameters of the gait model are optimized to achieve stable walking in compliance with hardware limitations.

[1] A prototype of the prosthetic foot needs to be available, which might contradict the requirement *early availability*.

Experimental investigations were performed and the results are outlined in chapter 17. Since the foot plays an important role during stance phase, only the stance phase is considered in the experiments. In particular, one step is performed with the presented RTHS setup. This chapter also discusses the potential of RTHS for prostheses testing critically.

Finally, chapter 18 summarizes the results and evaluates the achievements and presents future research directions.

The fundamental idea of using RTHS for testing of foot prostheses is also briefly outlined in [139, 239], but has not successfully been realized yet. Another use of RTHS in biomechanics is at the University of Rostock. There, researchers investigate the dynamics of hip and knee endoprostheses (experimental part) with a multibody simulation of the surrounding body parts (numerical part) [78, 92, 93].

Chapter 15

Human Gait and Gait Models

This chapter is inspired by the co-supervised student theses by Florian Holzberger [97], Lisa-Marie Ballat [13] and Felix Lorenz [131].

Human locomotion results from the complex action and interaction of bones, muscles and tendons as well as the interaction with the ground [197]. The human body is often viewed as a redundant system, which means that there are more muscles than actually needed to achieve a certain motion [4]. In this section, the fundamentals of human walking, the gait characteristics and commonly used walking models are outlined. This thesis focuses on walking on level ground. Neither running nor walking on inclines nor climbing stairs are considered here. The description of the gait cycle is given for non-amputees, since this is the targeted behavior of an ideal prosthesis. Descriptions of the gait characteristics with a prosthetic foot can e.g. be found in [32, 154, 239].

15.1 Gait Cycle

This section is based on the works of Whittle [231] and Murphy [153] if not indicated otherwise. Detailed studies of the gait cycle can also be found e.g. in [153, 173, 231, 235].

Walking is a symmetric[1], repetitive motion in which the left and right foot alternately contact the ground and swing forward. The gait cycle describes the movement and time interval between two repetitive events. Often, the heel contact of one leg is used as the starting point and the gait cycle includes the movement sequence until the next heel contact of the same leg, see fig. 15.1. During this gait cycle (also called stride), each leg goes through a stance phase (also support or contact phase) and a swing phase. For normal walking, the stance takes about 60 % ($\approx$ 600 ms) of the gait cycle and the swing phase the remaining 40 % ($\approx$ 400 ms). The stance phase starts with the touch down (TD, also called heel contact or heel strike) and terminates with the toe off (TO). After TD, the foot pivots about the heel until foot flat, where the whole foot is on the ground (at about 8 %) and accepts loads (loading response). Then, mid stance follows, which has multiple definitions [231]. In this thesis, mid stance denotes the point at which the full body weight has been taken over [153]. Heel off follows, where the foot starts to lift from the ground at about $40-45$ % of the gait cycle. The leg pivots about the ankle until the stance phase ends with the TO. The phase during mid stance when only one limb is in contact is called single support phase ($\approx$ 40 % of the gait cycle). During the double support phase, both legs are on the ground ($\approx$ 20 % of the gait cycle) and the force support is shifted from one to the other foot.

[1] Amputees, in contrast, exhibit an asymmetric gait pattern [32, 154, 193].

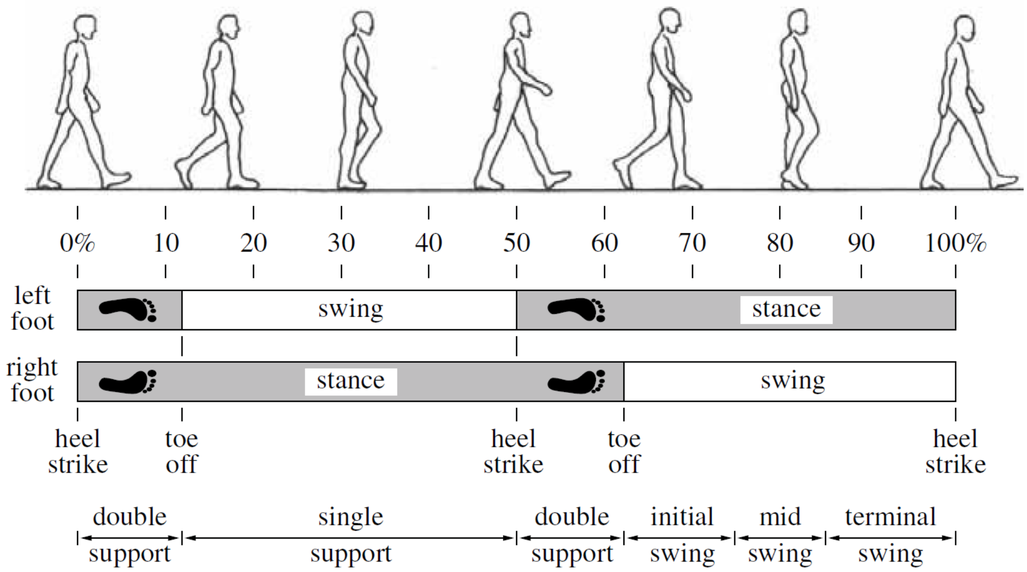

Figure 15.1: The gait cycle is shown between the heel strike of the right foot and the successive heel strike of the same foot. Each leg undergoes a stance and swing phase. [4]

During walking there is a steady energy conversion between kinetic and potential energy. During the single support phase, the body CoM rises until mid stance and after that descends [197]. A vertical sinusoidal movement of the CoM can be observed in walking humans with an amplitude of $\approx 2.5\,\text{cm}$, see fig. 15.2 [82]. The highest point of this trajectory, where the velocity in vertical direction is zero, is called apex. In biomechanics, the walking direction is commonly denoted as the x direction and the vertical direction as y. The motion of the human in fig. 15.2 is shown in the sagittal plane.

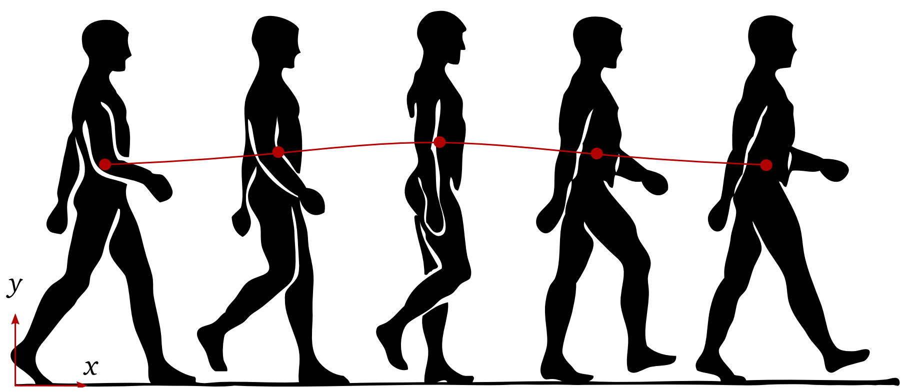

Figure 15.2: An illustration of the CoM trajectory of humans during stance phase of the left leg [97, 179].

The Ground Reaction Forces (GRFs) act on the body due to the interaction with the ground. They follow a characteristic pattern and are commonly analyzed in x and y direction. The GRFs are depicted for a woman walking at a speed of $1.5\,\mathrm{m/s}$ in fig. 15.3. The GRFs form an m-shaped curve in y direction, where the basin occurs approximately at mid stance. The faster humans walk, the lower the basin. The GRFs form an asymmetric curve in x direction, where decelerating forces act on the CoM in the first third of the stance phase and accelerating forces propel the body forward in the rest of the stance phase. The directions of the GRFs are visualized in fig. 15.4a. The Center of Pressure (CoP) is the point at the foot where the application of the GRFs on the body is assumed. Another important characteristic for humans is the shape of the hip, knee and ankle torques, as visualized in fig. 15.4b. In

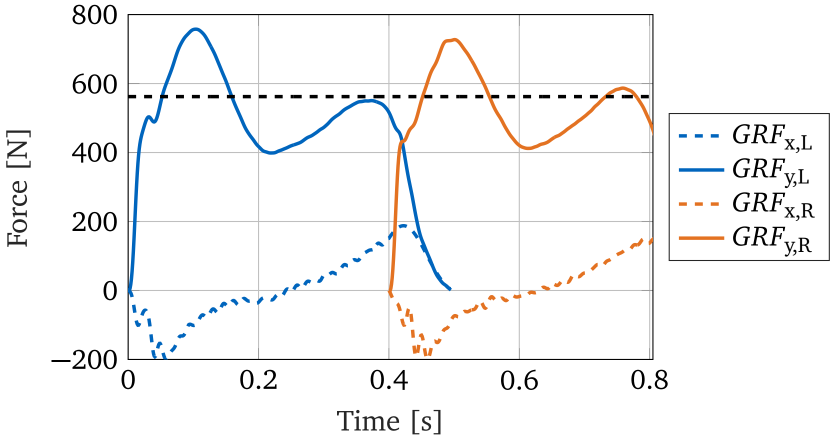

Figure 15.3: GRFs in x and y direction of a woman (27 years, 57.3 kg, 161 cm) walking on a treadmill at $1.5\,\mathrm{m/s}$. One gait cycle is shown, starting with the heel strike of the left foot (index $(\cdot)_L$). The black dashed line represents the body weight. In this figure, the second hump of the GRFs in y direction does not exceed the body weight, which is quite untypical. The data are taken from [237].

the first third of the stance phase, the hip exerts an extension moment, pushing the body over the foot. In the rest of the stance phase and the vast portion of the swing phase, the hip exerts a flexion moment and pulls the leg to the front. Several muscles contribute to the hip torque, i.a. the Gluteus maximus, the Iliopsoas, the Biceps femoris, Rectus femoris and Sartorius, but are represented here as one aggregate torque [186]. The ankle torque is vastly positive during the stance phase, indicating the forward and upward propulsion of the body.

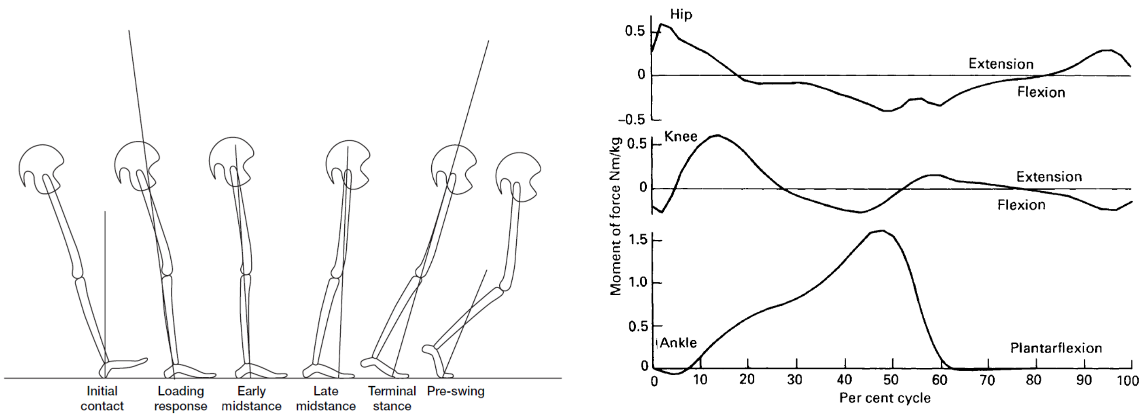

(a) The directions of the GRFs during stance phase. Until mid stance, they decelerate the CoM in x direction and afterwards propel the body forward. [153]

(b) The characteristic shape of hip, knee and ankle moment during one gait cycle starting with heel strike. The moments are normalized on the body weight. [235]

Figure 15.4: Kinetics during stance phase and during one gait cycle.

The stance phase is of particular importance for locomotion, since in this phase, decelerating and accelerating forces are generated. Hence, the further description of gait models focuses on the stance phase and the correct replication of the gait kinetics (CoM motion, GRFs and hip torques). The motion is only considered in sagittal plane.

15.2 Conceptual Models

To test foot prostheses with RTHS, models are needed that represent the mechanisms of human gait sufficiently accurate. How humans plan and control bipedal locomotion is still an open research question. Despite the high complexity, simple conceptual models are able to represent core observations in gait dynamics, such as the CoM motion, upper body stabilization or GRFs [197].

Over the last years, more complex multibody simulation models with many degrees of freedom and detailed modeling of muscles, joints, tendons and bones have been developed. Examples are OpenSim (https://opensim.stanford.edu/) [54, 198] and AnyBody (http://www.anybodytech.com/) [180]. However, their application to RTHS poses several difficulties: Firstly, these models are computationally intensive and may not be used for real-time application. Secondly, the model applied should not use any prescribed trajectories because this limits the movement options of the model in the RTHS experiment. However, these models use motion data that were e.g. measured in gait laboratories to calculate the dynamics.

Another way to simulate human gait is through the use of multibody simulation models of humanoid robots. This is especially possible and expedient if the humanoid robot exhibits human gait characteristics. Even though humanoid robots resemble humans morphologically, they do not necessarily implement biomechanical gait characteristics and rather balance/stabilize based on technical principles. One of the few examples implementing mechanistic human behavior is the robot ATRIAS [169]. At the Chair of Applied Mechanics, research is being conducted with the humanoid robot Lola and a multibody simulation model is available. In Staufenberg et al. [210], the forces and motions experienced by Lola are compared to those of humans. The results indicate that Lola's gait does not possess many biomechanical properties and, for now, cannot be considered suitable for biomechanical real-world testing of prosthetic feet.

15.2.1 Template Models

Full and Koditschek coined the classification of models into *templates* and *anchors* [73]. *Templates* denote models with the highest level of abstraction, featuring the aggregate locomotion behavior. Complexity is trimmed away such that the template model serves as a control target for locomotion [73, 197, 201]. In contrast, *anchors* are morphologically and physiologically more detailed, thus more realistic, and have the behavior of a template embedded. The so-called Inverted Pendulum (IP) and Spring Loaded Inverted Pendulum (SLIP) models indisputably serve as template models. The boundary which models belong to the anchors and which do not is not entirely clear [197].

As early as 1679, Borelli documented the first considerations on the transfer of mechanics to the human body [196, p. 218f.]. His investigations also involved the description of human walking and set the basis for a model, which we nowadays know as the IP model. In the IP model, which was proposed by Cavagna et al. [36] in detail, the whole body mass is concentrated in a single point mass and the legs are modeled as stiff rods. Even though this model represents the conversion between kinetic and potential energy well, neither the CoM trajectory nor the GRFs are represented correctly [167]. Blickhan proposed the SLIP model, where the legs are modeled by massless springs. He could show that the motion and GRFs of running are replicated well by this model [20]. To simulate walking, Geyer et al. extended this basic spring-mass model by a second leg [82]. This model is called Bipedal SLIP (BSLIP) model and is depicted in fig. 15.5. This model walks passively without any energy input: the CoM (position (x, y)) gets an initial push $\dot{x}_0$ at the initial height y_0 (e.g. in apex). The left and right leg (index $n = \{L,R\}$) have a resting spring length of $l_{0,n}$ and the angle of attack is α_0.

This is the angle with which the leg hits the ground (point contact between leg and ground). The CoM height is $y = l_{0,n} \cdot \sin(\alpha_0)$ at the moment of TD. During the stance phase, the leg pivots about the foot position $x_{\mathrm{FP},n}$ (angle during stance α_n). The GRFs always point along the leg axes to the CoM and are calculated as $GRF_n = k_n \cdot (l_{0,n} - l_n) = F_{s,n}$ (for $n = \{L, R\}$). The TO is triggered when the leg length exceeds the resting spring length, i.e. $l_n > l_{0,n}$. As the legs are massless, they do not contribute to the dynamics during swing phase. In general,

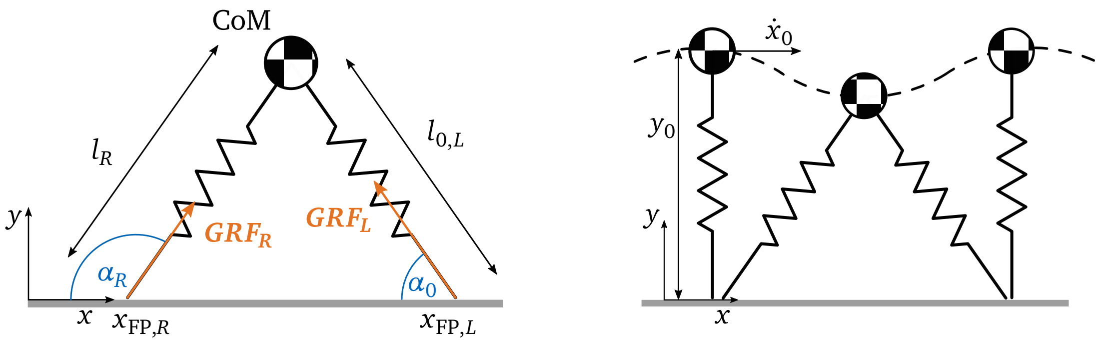

(a) The TD of a leg occurs with an angle of attack α_0. The GRFs point along the leg axes to the CoM.

(b) The CoM trajectory of the BSLIP model resembles the CoM oscillation of humans.

Figure 15.5: In the BSLIP model by Geyer et al. [82], the whole body mass is concentrated in the CoM and the legs are modeled as massless springs. The figures are adapted from [97].

while relatively simple, the BSLIP model is able to qualitatively predict the CoM trajectory and the GRFs (double-hump shape) very well. Lipfert at al. [128] compare the trajectories of the BSLIP model with those of humans in detail and point out limitations. The study reveals that e.g. the amplitudes of the CoM motion and the GRFs are overestimated and that the assumption of linear elastic leg behavior is only visible in a certain range of walking speed. Compared to human walking, where only 70 % of the energy can be recovered at best, the BSLIP model is energy conservative. Determining a suitable set of parameters k_n, α_0, $l_{0,n}$, $\dot{x}_0$ and y_0 is mandatory to achieve stable gait.

Stability of Walking models

Continuous running of a model is defined as the number of steps until fall in [199]. Often, a model is considered to walk/run continuously if it can walk 50 steps, where the velocity from step to step does not vary more than 5 %. Continuous walking/running also implies that the model does not fall after a perturbation occurs [49]. In a mathematical sense, the stability of walking models is often studied using Poincaré return maps. Here, stable walking solutions form a fixed point with a basin of attraction [178, 184, 197]. In practice, a suitable set of parameters is found via optimization. This means that the model is simulated for one gait cycle, e.g. from apex to apex, and the states (e.g. $(\dot{x}, y)$) are compared. The parameters are optimized such that the difference between the states is minimized.

In literature, multiple extensions of the BSLIP model can be found. For example, Maus et al. [141] extended the model with a trunk, which is called the TSLIP/BTSLIP model. The trunk represents the whole upper body with the arms and the head. Additionally, a knee joint was introduced and the legs segmented [185], or a foot element was added [197].

15.2.2 Virtual Pivot Point (VPP) Model

In locomotion experiments with dogs, chicken and humans, an interesting observation could be made. Namely—in a coordinate system fixed to the trunk—the GRFs intersect at a fixed location above the CoM, on the axis connecting the hip and the CoM [197]. This observation suggests that the stabilization of the upper body functions like the swinging of a pendulum, suspended at this point. This effect is called Virtual Pendulum (VP) and the intersection point Virtual Pivot Point (VPP). Small perturbations lead to torques restoring the posture and thus stabilizing the trunk [141].

Maus et al. [140, 141] implemented the VPP concept by extending the BTSLIP model (BSLIP model with trunk)[2]. The model is visualized in Figure 15.6. The trunk is inclined

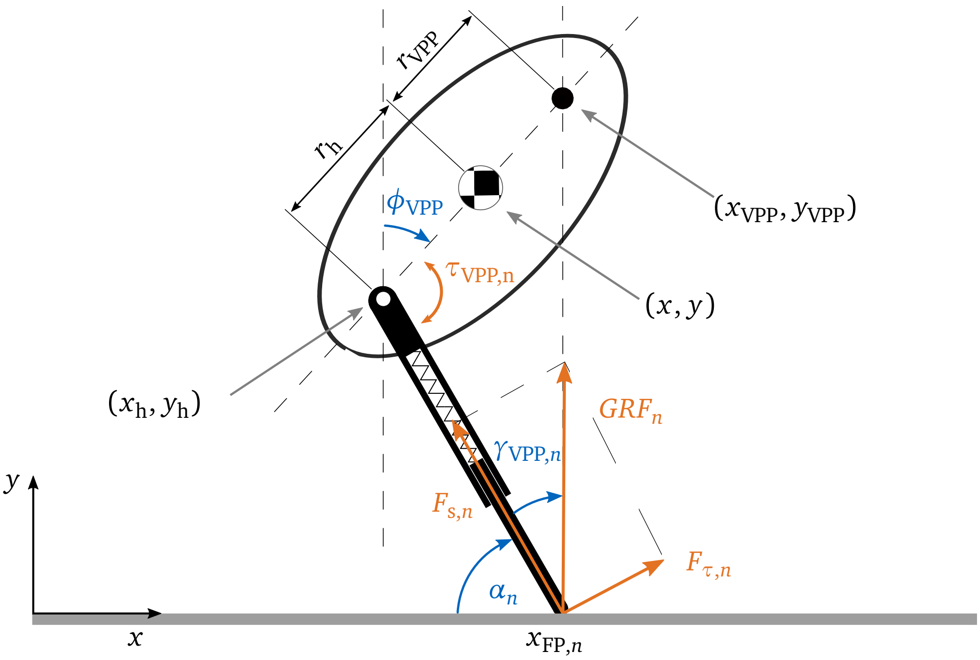

Figure 15.6: In the VPP model, the BSLIP model is extended by a trunk (angle ϕ_{VPP}) and a hip torque $\tau_{\text{VPP,n}}$ that redirects the GRFs of each leg $n = \{L, R\}$ into the VPP. Figure taken from [105].

by ϕ_{VPP} with respect to the vertical axis. An additional hip torque $\tau_{\text{VPP,n}}$ is introduced that redirects the GRFs to the VPP by

$$\tau_{\text{VPP,n}} = F_{\tau,n} \cdot l_n \quad \text{with } F_{\tau,n} = F_{\text{s},n} \cdot \tan\left(\gamma_{\text{VPP},n}\right) = k_n \cdot (l_{0,n} - l_n) \cdot \tan\left(\gamma_{\text{VPP},n}\right) \tag{15.1}$$

for $n = \{L, R\}$ if the leg contacts the ground[3]. The angle between the leg and the connection of the foot point $x_{\text{FP},n}$ with the VPP $(x_{\text{VPP}}, y_{\text{VPP}})$ is denoted by $\gamma_{\text{VPP},n}$. The total GRFs become [141]

$$GRF_n = \sqrt{F_{\text{s},n}^2 + F_{\tau,n}^2} = F_{\text{s},n} \cdot \sqrt{1 + \tan^2\left(\gamma_{\text{VPP},n}\right)} \tag{15.2}$$

$$GRF_{\text{x},n} = GRF_n \cdot \frac{x_{\text{h}} - x_{\text{FP},n}}{l_n} \tag{15.3}$$

$$GRF_{\text{y},n} = GRF_n \cdot \frac{y_{\text{h}}}{l_n} \tag{15.4}$$

for each leg $n = \{L, R\}$ and eqs. (15.3) and (15.4) are the projections of the GRFs into x and y direction. The distance between the hip and the CoM is r_{h} and between the CoM

[2]The VP concept can be understood as template. Hence, the VPP model implements the SLIP template and the VP template. [141]

[3]Note that the VPP in humans is only observed during single support phase, but not during double support phase [225], which is called the VPP controller. Nevertheless, the model assumes that the GRFs are redirected to the VPP during the whole stance phase.

and the VPP r_{VPP}. The distance between the CoM and the VPP r_{VPP} in humans is between 5 − 70 cm depending on the walking speed [141]. Hence, the walking speed of the model can be adjusted by varying r_{VPP}. To improve the robustness of the VPP model, the VPP position can be positioned with an angular offset between the VPP and trunk orientation [200]. Using the GRFs from eqs. (15.3) and (15.4), the mass m_{VPP} and the moment of inertia J_{VPP} of the trunk as well as gravitational forces, the EoM write

$$m_{\mathrm{VPP}}\ddot{x} = GRF_{\mathrm{x},L} + GRF_{\mathrm{x},R} \tag{15.5}$$

$$m_{\mathrm{VPP}}\ddot{y} = GRF_{\mathrm{y},L} + GRF_{\mathrm{y},R} - m_{\mathrm{VPP}}g \tag{15.6}$$

$$-J_{\mathrm{VPP}}\ddot{\phi}_{\mathrm{VPP}} = r_{\mathrm{VPP}}\left(\sin\left(\phi_{\mathrm{VPP}}\right)\left(GRF_{\mathrm{y},L} + GRF_{\mathrm{y},R}\right) - \cos\left(\phi_{\mathrm{VPP}}\right)\left(GRF_{\mathrm{x},L} + GRF_{\mathrm{x},R}\right)\right) \tag{15.7}$$

$$= r_{\mathrm{h}}\left(\cos\left(\phi_{\mathrm{VPP}}\right)\left(GRF_{\mathrm{x},L} + GRF_{\mathrm{x},R}\right) - \sin\left(\phi_{\mathrm{VPP}}\right)\left(GRF_{\mathrm{y},L} + GRF_{\mathrm{y},R}\right)\right) + \tau_{\mathrm{VPP,L}} + \tau_{\mathrm{VPP,R}} \tag{15.8}$$

Equations (15.7) and (15.8) are equivalent with the difference being that in the former, the principle of angular momentum is applied on the full dynamical system (VPP model) and in the latter with a free body force diagram on the trunk. Similar to the BSLIP model, the VPP model receives an initial velocity and height and walks passively with the only source of external energy being the hip torque. The VPP is not explicitly controlled in the model, but rather a mechanical behavior.

The VPP model shows good agreement with biomechanical data of the GRFs, CoM trajectory and hip torques [141]. In the first part of the stance phase, torques extending the hip are required to redirect the leg forces to the VPP and in the last part of the stance, torques flexing the hip are required. The additional $F_{\tau,n}$ reduce the horizontal force components $GRF_{\mathrm{x},n}$, i.e. the deceleration and acceleration, compared to the BSLIP model.

Based on the VPP model, the Force Modulated Compliant Hip (FMCH) was proposed by Sharbafi and Seyfarth [201]. Here, mechanical hip springs are used instead of the hip torques $\tau_{\mathrm{VPP,n}}$ to stabilize the trunk. The compliance of these hip springs is variable and adjusted based on the leg forces. They can be tuned such that the VPP forms, i.e. the FMCH and the VPP model are mathematically equivalent. [197, 201]

15.2.3 Neuromuscular Control Models

Neuromuscular control models are motivated by the fact that slow, variable-frequency locomotion is dominated by the nervous system in contrast to rapid, rhythmic locomotion that is dominated by mechanics [73]. Both, neural and mechanical systems are present in locomotion but appear on disparate spatial and temporal scales [73]. While the previously presented models rely on the mechanics, the neuromuscular control models try to mimic neural circuits. A comprehensive overview about neuromuscular control models is given in [81]. One of these models is the Neuromuscular-Skeletal (NMS) model by Geyer and Herr [80], which implements reflexes to determine the muscle activities. A visualization of the NMS model is given in fig. 15.7. The model is based on the BSLIP model, where the legs are segmented into three parts and the upper body (head, arms, trunk) are represented as a rigid trunk. Leg compliance is achieved by seven Hill-type muscles, which are controlled based on muscle reflexes. These muscles also enable the implementation of the swing phase. The model tolerates ground disturbances and is able to walk on inclines and uneven ground.

A further model combining both mechanical and neuromuscular representations has recently been proposed by Davoodi et al. [49]. This model is based on the FMCH model, where the hip springs are replaced by Hill-type muscles.

For this thesis, a simple model with sufficient complexity to represent basic gait characteristics is sought. The model should be able to react, more specifically, stabilize the trunk

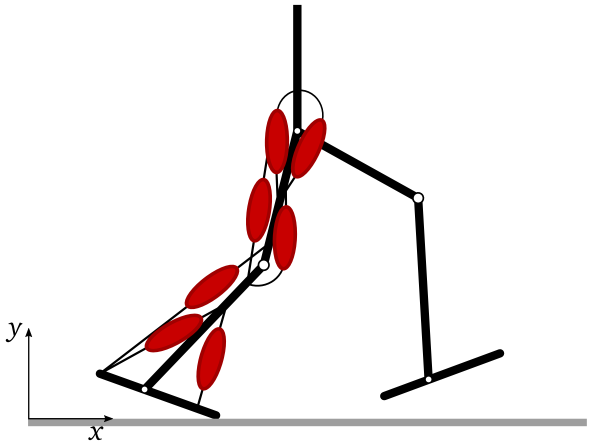

Figure 15.7: In the NMS model, the legs are segmented and the motor control is implemented based on muscle reflexes [80, 97].

in case of disturbances. In preliminary analyses, investigations with the BSLIP model have been performed by the co-supervised student Kaiyu Fan [66]. He found that the BSLIP model falls at realistic disturbance and is thus not suitable for RTHS tests. Hence, the VPP model, which is slightly more complex, is used for the investigations in this thesis. This model is able to represent human-like GRF patterns and CoM trajectories as well as hip torque patterns similar to those observed in humans. Still it is relatively simple to implement[4]. The motion is considered in the sagittal plane (three DoFs) and the whole body mass is represented in the rigid trunk.

[4]Another possible model would be the NMS model. This is not used in this thesis, because the modeling of the muscles at the ankle joint (connection to the prosthesis) is complex. However, this model can be regarded in the future.

Chapter 16

Application of RTHS for Gait Analysis

This chapter is inspired by the co-supervised student theses by Kaiyu Fan [66], Florian Holzberger [97], Lisa-Marie Ballat [13] and Felix Lorenz [131]. They implemented the VPP model [97] and the parameter optimization [66, 97].

Using RTHS, the dynamics of the amputee wearing a prosthetic device can be investigated. In this application, a reasonable choice of the interface location, which is where the dynamical system is split into numerical and experimental part, is at the stump of the amputee. This is often the ankle joint for prosthetic feet. The amputee is simulated based on the VPP model. The prosthetic foot 1C40 (ESAR foot, see section 14.1) from Ottobock, which is a right foot $n = R$, serves as the experimental part. The transfer system consists of the controlled Stewart Platform, a Kistler Dynamometer as FTS and a dSPACE 1202 (as DSP) system. All components are described in section 4.2. The resulting RTHS loop is visualized in fig. 16.1. The force adaptation block includes the transformation from the forces in the coordinate system of the FTS to the coordinate system of the simulated VPP model and could also include e.g. filtering of the force signal or the application of Normalized Passivity Control. As the VPP model is a two-dimensional model, the ankle joint of the model has three DoFs: the interface position $(x_{\mathrm{IFP}}, y_{\mathrm{IFP}})$ and the leg orientation α_R. The interface displacements $\boldsymbol{z}/\boldsymbol{z}'$ as well as $\boldsymbol{F}_{\mathrm{m}}/\boldsymbol{F}_{\mathrm{int}}$ (two planar forces and the torque about the (negative) z axis) therefore are vectors with three entries[1]. For this RTHS setup, no reference solution is available and the test can only be validated qualitatively. This is because the prosthetic foot has nonlinear dynamic behavior and thus modeling is cumbersome (cf. the stiffness characteristics depending on the angle of loading in appendix C).

16.1 Modeling an Amputee Using the VPP Model

The VPP model, as explained in section 15.2.2, cannot be used straightforwardly. For example, the model describes a human with two intact legs. Furthermore, the model neglects that the CoP moves from the heel to the toes during the stance phase. These required adaptations are derived and described below.

16.1.1 Interface Point

The numerical substructure should represent an amputee, i.e. a human with one intact leg with leg length $l_{0,L}$ (deformed length l_L) and stiffness k_L as well as one amputated leg with

[1] This is an MDOF RTHS setup in contrast to the SDOF applications discussed in Part I and Part II.

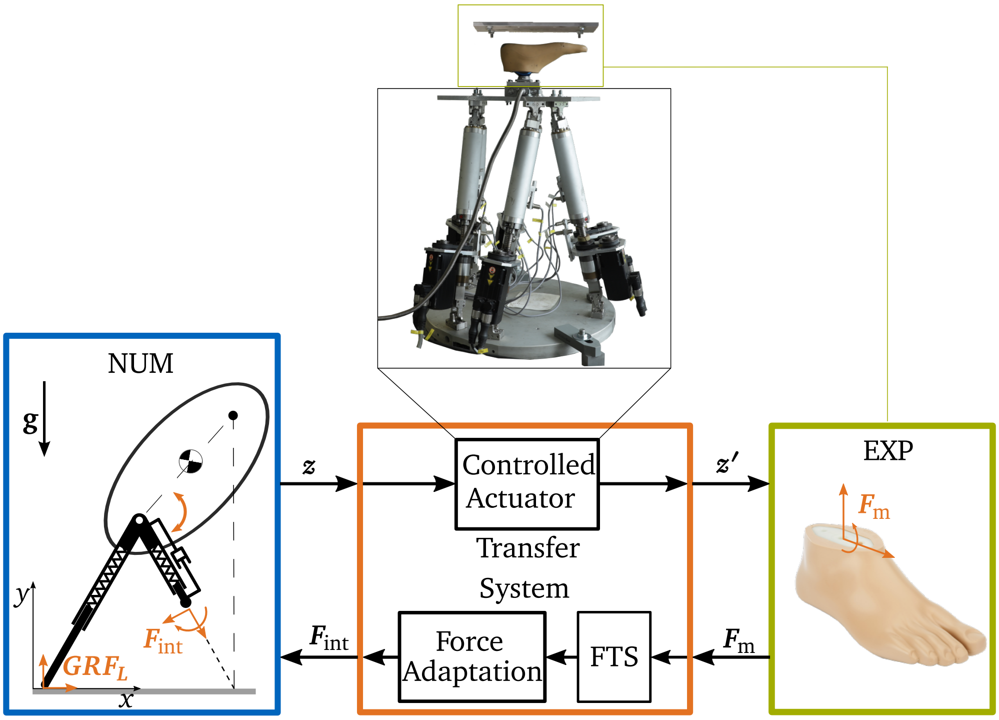

Figure 16.1: The RTHS setup for testing a prosthetic foot (© by Ottobock) with RTHS. The numerical part is a simulation of the walking human using the VPP model. For the sake of clarity, kinematic transformations and the DSP are omitted in the figure.

length $l_{0,\mathrm{u}}$ (deformed length l_u) and stiffness k_u. The prosthetic foot is tested experimentally and has a height $h_{0,\mathrm{f}} = l_{0,R} - l_{0,\mathrm{u}}$ (deformed height h_f). Its stiffness characteristics are nonlinear, depending on the loading angle.

The transfer system exchanges displacements/orientation and forces/torque at the ankle between the numerical and experimental substructure. Specifically, the measured forces are forces along the leg axis $F_{\mathrm{int},\|}$, orthogonal to the leg axis $F_{\mathrm{int},\perp}$ and a torque M_int about the z axis. The experimental part is positioned according to the end point position of the leg spring of the amputated leg in the VPP model. To determine the interface location $(x_\mathrm{IFP}, y_\mathrm{IFP})$, a DoF with a mass is inserted. This is necessary because—if the DoF had no mass—the stiffness of the amputated leg would be in series with the stiffness of the prosthetic foot and they would need to experience the same forces. However, this is numerically not trivial because the direct application of the measured interface forces on the numerical spring would lead to an infinite frequency in the hybrid model. Therefore, a mass needs to be added to regularize any discrepancies between the force in the prosthetic foot and in the spring of the VPP model. If the mass of the interface point (IFP) is small, that is m_IFP ($m_\mathrm{IFP} \ll m_\mathrm{VPP}$), the system dynamics are barely modified. The additional mass introduces artificial high-frequency dynamics and therefore a numerical damper with damping constant d_u is set in parallel to the spring in the amputated leg. The modified VPP model is illustrated in fig. 16.2. The GRFs of the intact leg $\boldsymbol{GRF}_L$ comprise the components $GRF_{\mathrm{x},L}$ and $GRF_{\mathrm{y},L}$ in x and y direction. The mass IFP can only move along the leg axis. In the further derivations, its weight force is neglected. The internal leg dynamics write

$$m_\mathrm{IFP}\ddot{l}_\mathrm{u} = F_{\mathrm{int},\|} - d_\mathrm{u}\dot{l}_\mathrm{u} - k_\mathrm{u}\left(l_\mathrm{u} - l_{0,\mathrm{u}}\right) = F_{\mathrm{int},\|} - F_\mathrm{u}, \tag{16.1}$$

where the acceleration and velocity of the mass IFP are $\ddot{l}_\mathrm{u}$ and $\dot{l}_\mathrm{u}$, respectively, and the forces in the spring-damper system of the amputated leg are abbreviated as F_u. The energy dissipated by the damper is not compensated for.

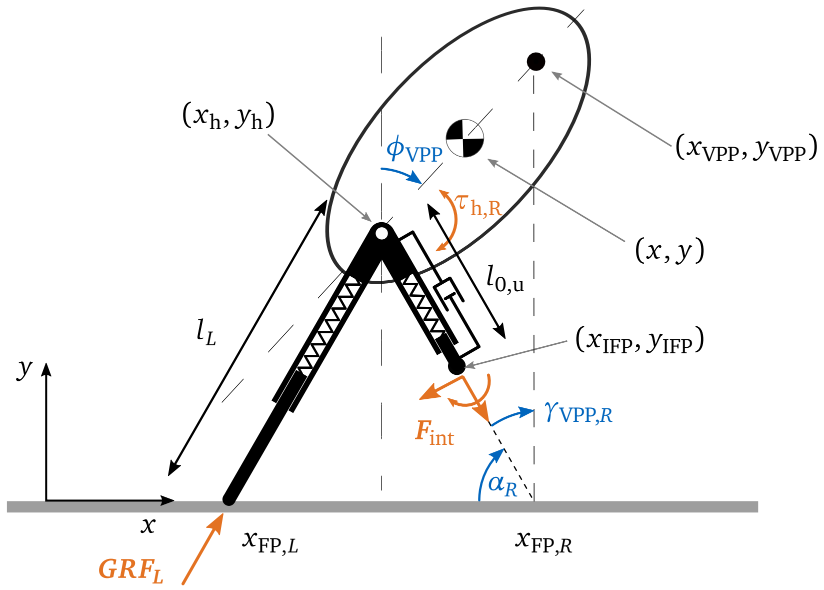

Figure 16.2: The VPP model is used as a basis for the model of the amputee. A mass IFP, which is required to numerically solve for displacements at the interface location, and a mechanical damper are introduced to the basic VPP model. Figure taken from [105].

The underlying idea of the VPP model is that a hip torque is applied such that the GRFs point into the VPP to stabilize the trunk (see section 15.2.2). The legs are represented as springs and any forces orthogonal to the leg axis solely occur due to the hip torque $\tau_{\text{VPP,n}}$ (cf. eq. (15.1)) of the VPP controller, i.e. $F_{\text{int},\perp} = 0$. However, when the three-dimensional prosthetic foot is tested, the perpendicular forces are not zero in general, which creates a hip torque $F_{\text{int},\perp} \cdot l_R$. The total leg length of the right leg is denoted by l_R, which is the distance between the hip and the mid foot point $x_{\text{FP},R}$ (the point where the leg axis intersects the ground). The total hip torque required to redirect the GRFs into the VPP writes

$$\tau_{\text{h,R}} = -F_{\text{int},\|} \cdot \tan\left(\gamma_{\text{VPP},R}\right) \cdot l_R \tag{16.2}$$
$$= \tau_{\text{VPP,R}} - F_{\text{int},\perp} \cdot l_R, \tag{16.3}$$

which is a combination of the contributions from the VPP controller and the torque due to $F_{\text{int},\perp} \neq 0$. The orthogonal forces resulting due to the hip torque from the VPP controller are

$$F_{\tau,R} = F_{\text{int},\perp} - F_{\text{int},\|} \cdot \tan\left(\gamma_{\text{VPP},R}\right). \tag{16.4}$$

Projected on the x and y axis, the forces by the VPP controller are denoted by $F_{\tau,\text{x},R}$ and $F_{\tau,\text{y},R}$. The left, intact leg has the same force/torque contributions as in section 15.2.2. To sum up, the EoM for the modified VPP model—modeling an amputee—write

$$m_{\text{VPP}}\ddot{x} = GRF_{\text{x},L} + F_{\text{u,x}} - F_{\text{int,x},\perp} + F_{\tau,\text{x},R} \tag{16.5}$$
$$m_{\text{VPP}}\ddot{y} = GRF_{\text{y},L} - F_{\text{u,y}} - F_{\text{int,y},\perp} + F_{\tau,\text{y},R} - m_{\text{VPP}}g \tag{16.6}$$
$$-J_{\text{VPP}}\ddot{\phi}_{\text{VPP}} = r_{\text{VPP}}\left(\sin\left(\phi_{\text{VPP}}\right)GRF_{\text{y},L} - \cos\left(\phi_{\text{VPP}}\right)GRF_{\text{x},L}\right) \tag{16.7}$$
$$+ r_{\text{h}}\left(\cos\left(\phi_{\text{VPP}}\right)\left(F_{\text{u,x}} - F_{\text{int,x},\perp} + F_{\tau,\text{x},R}\right)\right) \tag{16.8}$$
$$+ r_{\text{h}}\left(\sin\left(\phi_{\text{VPP}}\right)\left(F_{\text{u,y}} + F_{\text{int,y},\perp} - F_{\tau,\text{y},R}\right)\right) + \tau_{\text{h,R}}. \tag{16.9}$$

The angular momentum by the left leg is expressed in eq. (16.7) and of the right, amputated leg in eqs. (16.8) and (16.9).

To investigate how the additional mass IFP and damper change the system dynamics, a co-simulation is set up. Therein, the prosthetic foot needs to be modeled, which is done with a spring of stiffness k_f. All parameters of the model are summarized in table A.6. Figure 16.3 compares the results of the simulated VPP model according to section 15.2.2 with the results of the simulated modified VPP model (with mass IFP and additional damper).

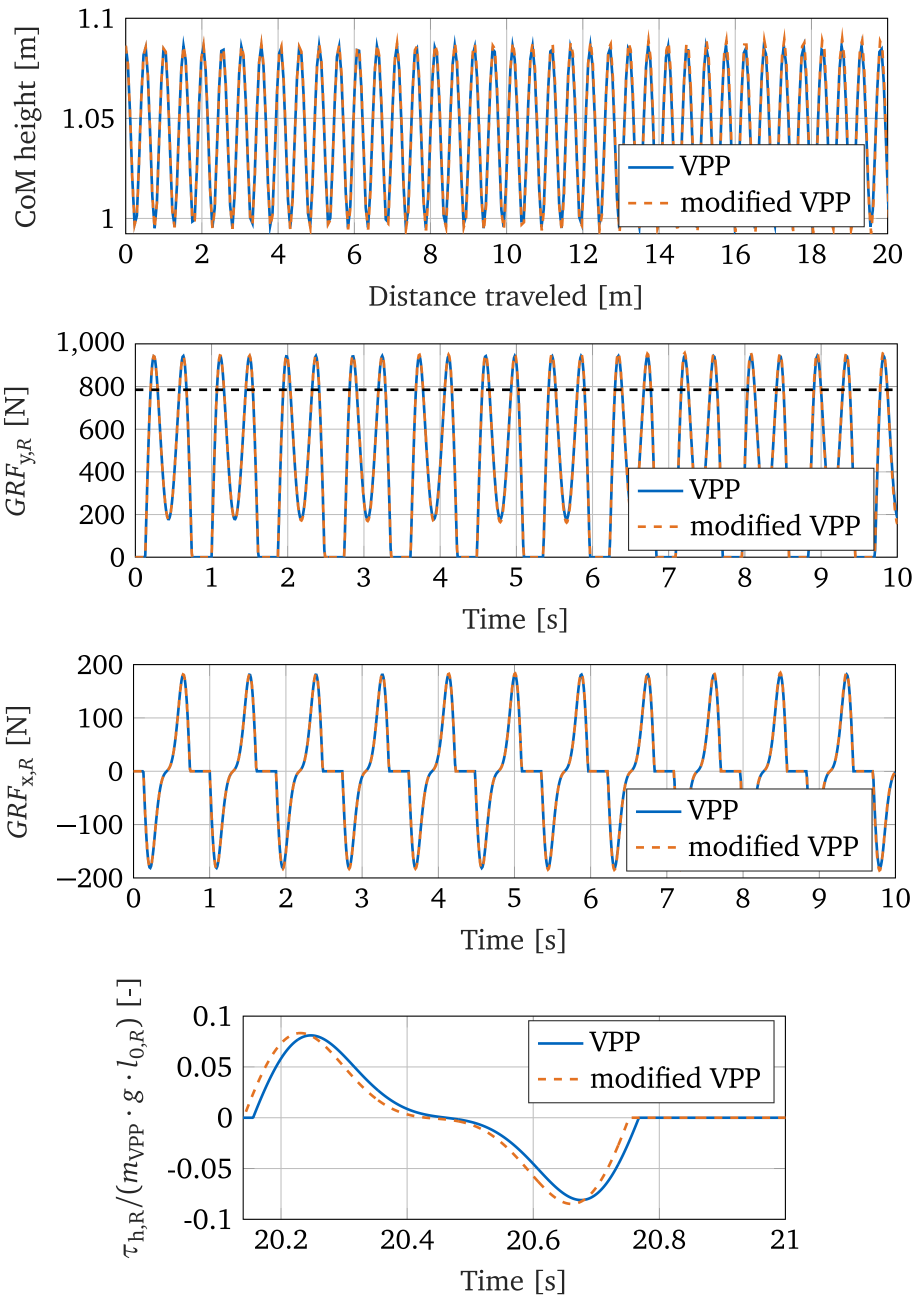

Figure 16.3: The CoM trajectory in y direction, the GRFs in x and y direction as well as the total hip torque (normalized on the body weight times the resting leg length) are visualized for the VPP model (blue, solid lines) and the modified VPP model (orange, dashed lines). The results are shown for the right leg, which is cut into two parts in the modified VPP model. The black, dashed line represents the weight forces.

The results of the modified VPP model and the basic VPP implementation match. Both models tend to diverge, as the amplitudes of the trajectories and forces slightly increase. This effect is a bit more pronounced in the modified VPP model. In conclusion, the results indicate that the modified VPP model displays the CoM trajectory, GRFs and hip torques similar to the basic VPP model[2].

16.1.2 Center of Pressure Shift

In the VPP model, the GRFs are applied at the foot point location $x_{\mathrm{FP},R}$, which is the intersection of the leg axis and the ground. In human walking, in contrast, a shift of the Center of Pressure (CoP)[3] from the heel to the toes during stance phase is observed [195]. To make the RTHS test more realistic, this forward shifting CoP is implemented in the numerical simulation of the amputee. The CoP location is denoted by $x_{\mathrm{CoP},R}$. Figure 16.4 depicts the forces acting on the foot (gravitational as well as inertia forces are omitted) as well as the geometry. The distance from the heel to the mid foot point is l_{h} and from the mid foot point to the toes l_{ff}. The angle between the horizontal ground and the connection of the CoP with the hip is denoted by α_R.

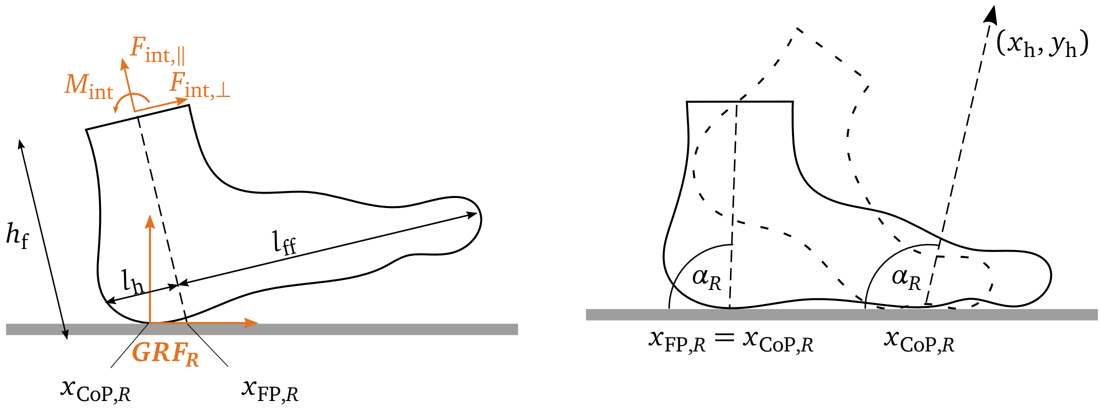

(a) The forces acting on the prosthetic foot while testing. Gravitational forces and inertial forces are neglected.

(b) The CoP location $x_{\mathrm{CoP},R}$ needs to be known such that the VPP model can redirect the GRFs into the VPP. Figure inspired by [97].

Figure 16.4: The GRFs act at the CoP, which shifts from heel to the toes during stance phase. The mid foot point $x_{\mathrm{FP},R}$ is the linear extension of the leg axis.

In this work, a linear shift of the CoP from the heel to the toes depending on the angle between the leg and the ground α_R is implemented. This approach requires knowledge about the TD angle α_0 and TO angle α_{TO} as well as the dimensions of the foot l_{h} and l_{ff}. For TD until foot flat, the CoP should shift from the heel to the mid foot point, i.e. travel a distance of l_{h} during a rotation of $\frac{\pi}{2} - \alpha_0$. For the phase between foot flat and TO, the CoP travels a distance of l_{ff} and the leg rotates about an angle of $\alpha_{\mathrm{TO}} - \frac{\pi}{2}$. Hence, the equations write

$$x_{\mathrm{CoP},R} = \begin{cases} \frac{l_{\mathrm{h}}}{\frac{\pi}{2} - \alpha_0} \cdot \alpha_R + c_1, & \text{if } \alpha_R \leq \frac{\pi}{2} \\ \frac{l_{\mathrm{ff}}}{\alpha_{\mathrm{TO}} - \frac{\pi}{2}} \cdot \alpha_R + c_2, & \text{if } \alpha_R > \frac{\pi}{2} \end{cases} \tag{16.10}$$

with c_1 and c_2 from the condition $x_{\mathrm{CoP},R} = x_{\mathrm{FP},R}$ for $\alpha_R = \frac{\pi}{2}$. This shift of the foot point is implemented for both, the left and right leg.

In conclusion, the model of the amputee presented in this chapter differs from the VPP model in literature (section 15.2.2) by the mass IFP, an additional damper and the moving

[2]This statement holds for the investigated set of parameters $\{m_{\mathrm{IFP}}, d_{\mathrm{u}}\}$, where $m_{\mathrm{IFP}} \ll m_{\mathrm{VPP}}$.

[3]The CoP is the location where the application of the GRFs is assumed. In able-bodied people, this results from an ankle torque and the rolling motion of the foot.

CoP position. The damper as well as the forward moving foot CoP imply an energy loss of the system. Hence, it is part of the investigations to find out whether the model has still enough energy to walk steadily due to the energy input by the hip torques $\tau_{\mathrm{VPP,n}}$ or whether an external energy source needs to be implemented to counteract this dissipation.

16.2 RTHS Implementation

The implemented model starts with foot flat of the left foot (single support). There, the initial conditions $x = 0\,\mathrm{m}$ and $\dot{y} = 0\,\mathrm{m/s}$ are set. The RTHS setup used has several limitations that have to be considered in the test setup and can be summarized as

- Stewart Platform:
  - The maximum leg velocity of each leg is $0.5\,\mathrm{m/s}$.
  - The work space of the Stewart Platform is limited by the leg length (maximum stroke 0.18 m) and joint limitations of the universal joints (maximum joint angles 45°) [183].
- Kistler Dynamometer: The maximum forces are $10^4\,\mathrm{N}$ and a maximum torque of 500 Nm.
- Reaction Frame: The maximum loading in vertical direction is estimated to be 500 N.

These conditions limit the gait speed, the TD and TO angles and the weight of the simulated human. Using optimization (see section 15.2.1), a set of model parameters leading to stable gait while staying within these limits needs to be found.

16.2.1 Parameter Optimization

Optimization algorithms try to minimize a cost function by changing the input parameters and simulating the model. Here, an optimization algorithm is used to find parameters that lead to stable walking, that is the deviations before and after one stride need to be minimal. The cost function contains the deviation of the following quantities: the CoM height y, the CoM vertical and horizontal velocities $\dot{y}/\dot{x}$ as well as the trunk orientation and angular velocity [13, 66, 97, 131]. The parameters that were optimized are $\dot{x}_0$, y_0 and $\dot{\phi}_{\mathrm{VPP},0}$ based on the given m_{VPP}, J, k_n, r_{VPP}, r_{h} and α_0. For the optimization, an evolutionary optimization algorithm called Covariance Matrix Adaptation Evolution Strategy (CMA-ES) was used [90]. Details about the implementation for this use case are given in [13, 66, 97, 131].

16.2.2 Selected Parameters and RTHS Setup

The optimization was performed using the VPP model. A parameter set was found, where the model is able to walk stably (> 50 steps). This parameter set is summarized in table A.7. Note that the model is highly sensitive to the exact choice of initial conditions. The leg stiffness k_n represents the leg stiffness of the intact and amputated legs $n = \{L,R\}$, where the stiffness of the right leg is constituted by k_{u} and k_{f}. Accordingly, approximate knowledge of the stiffness of the prosthetic foot k_{f} is necessary for the implementation in the RTHS setup. The required stiffness of the remaining leg k_{u} can be found with $\frac{1}{k_{\mathrm{u}}} = \frac{1}{k_R} - \frac{1}{k_{\mathrm{f}}}$. The prosthetic foot used is the 1C40 from Ottobock. This prosthetic foot poses nonlinear stiffness characteristics, as shown in fig. C.1, and one approximate value needs to be selected for the computation of k_{u}. In the RTHS implementation, an approximate value of $k_{\mathrm{f}} = 4950\,\mathrm{N/m}$ (cf. fig. C.1) is assumed and used to determine k_{u}.

Note that the found parameters do not represent a biomechanically meaningful adult ($m = 30\,\mathrm{kg}$, leg length $l_0 = 1\,\mathrm{m}$ and leg stiffness $k_L = 5.4 \cdot 10^3\,\mathrm{N/m}$), but the parameters of an average adult could not be chosen due to the hardware limitations. Nevertheless, these parameters suffice for these first RTHS tests to show the potential of RTHS to investigate the dynamic interplay between a prosthetic foot and an amputee.

The simulation of the VPP model includes the contact phenomenon of the intact (left) leg. When simulating contact dynamics, small numerical time integration steps are favorable in order to detect the contact event quickly and maintain a stable numerical simulation. But as the simulation needs to be real-time applicable, the time integration steps cannot be too small. As briefly mentioned in section 2.1, the numerical simulation can be solved with a different sample time than the synchronization time step between the numerical and experimental part or the actuator control. In the presented RTHS setup (chapter 4), the actuator control and synchronization time step are $\Delta T = 1 \cdot 10^{-3}\,\mathrm{s}$. This sample time is too large for a stable numerical simulation of the model and a time step size of $2 \cdot 10^{-4}\,\mathrm{s}$ was found suitable.

In human walking, a so-called toe-out or rarely a toe-in can be observed. This denotes a rotation of the toes outwards or inwards with respect to the x axis. Commonly, an angle of $7°$ is observed in locomotion experiments [173]. Thus, the prosthetic foot is mounted with approximately this angle on the Stewart Platform. The Stewart Platform was controlled with the parameters given in appendix A and with VFF.

Chapter 17

Experimental Investigations

The implementation used in this chapter is an adapted version of the implementation by Florian Holzberger [97] and Lisa-Marie Ballat [13]. The results have been published in the author's publication [105].

In chapter 16, the implementation of the RTHS setup with a modeled amputee (based on the VPP model) and a prosthetic foot was described. This setup is now used to investigate the applicability of RTHS to replicate human gait. The model starts at the position $x = 0\,\mathrm{m}$ with the left foot on the ground (single support left). Then, one stride is performed, which includes the following events: after the simulation start, the right prosthetic foot touches down. The body weight is then shifted from the simulated left leg to the amputated right leg. After that, TO of the left leg follows and the whole body weight is supported by the right leg. The left leg TD follows and the body weight is shifted from the right to the left leg before TO of the right leg occurs. The gait cycle is terminated at mid stance of the left leg. The Stewart Platform was controlled with the parameters given in appendix A and with VFF (no NPC).

17.1 Results of One Stride

The gait characteristics described in section 15.1 are now used to qualitatively compare the results of the RTHS test and to assess how well human gait is emulated with the RTHS test.

The CoM trajectory is illustrated in fig. 17.1a, which represents a sinusoidal shape. The maxima correspond to the mid stance positions of the left (at $x = 0\,\mathrm{m}$ and $x \approx 0.6\,\mathrm{m}$) and the prosthetic right foot (at $x \approx 0.3\,\mathrm{m}$). The amplitude of the CoM height is $\approx 0.04\,\mathrm{m}$, which relates very well to observations in humans. Though, while the general shape of the CoM height is as expected, the increasing amplitude is in contrast to steady human walking (cf. figs. 15.2 and 16.3). In human walking, the shape is sinusoidal with constant maxima and minima. The stance phase of the right leg is relatively long compared to human walking with 85 % of the gait cycle.

The CoM forward velocity $\dot{x}$ is depicted in fig. 17.1b. The model velocity decreases during the stride. In human walking, the body decelerates if the foot is in front of the body ($x_{\mathrm{CoP},R} > x$) and is propelled forward when the CoM is in front of the foot. Hence, alternating acceleration and deceleration would be expected. The results imply that the deceleration due to forces directed in the negative x direction outweigh the acceleration. The duration of the gait cycle is $\approx 0.6\,\mathrm{s}$. This is as expected because the duration is the same in a simulation of the VPP model with these parameters.

Furthermore, the trunk orientation is a characteristic quantity during walking and the results from the RTHS test are shown in fig. 17.1c. The results indicate that the model rotates backwards. The model has not fallen at the end of the first stride, but would probably not be able to walk stably for a second stride.

A visualization of the CoP location[1] is given in fig. 17.1d. The quantity $x_{\text{CoP},R}$ is given in relation to the foot point location $x_{\text{FP},R}$. The CoP location was found by setting up the torque equilibrium about the FTS using the measured interface forces $F_{\text{int},\parallel}$ and $F_{\text{int},\perp}$ as well as the interface torque M_{int}. Similar to the observation in humans, the CoP shifts from the heel to the toes in the RTHS test. In humans, however, the shift of the CoP stems from the ankle torque (actuated ankle). In contrast, the shift of the CoP in this RTHS experiment is solely due to the rolling motion of the foot.

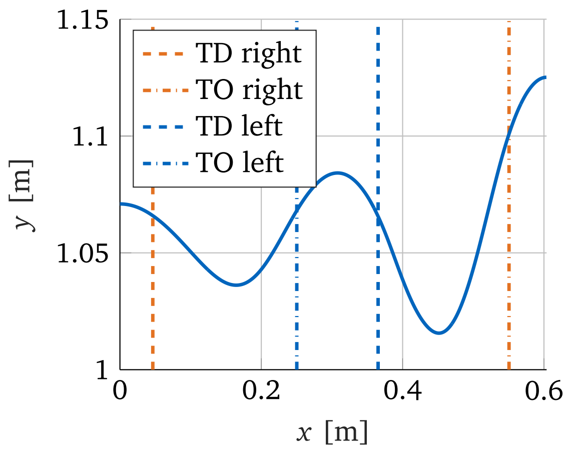

(a) CoM height.

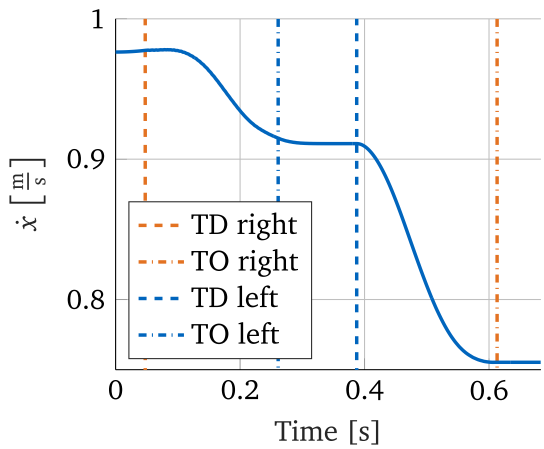

(b) Forward velocity of the model.

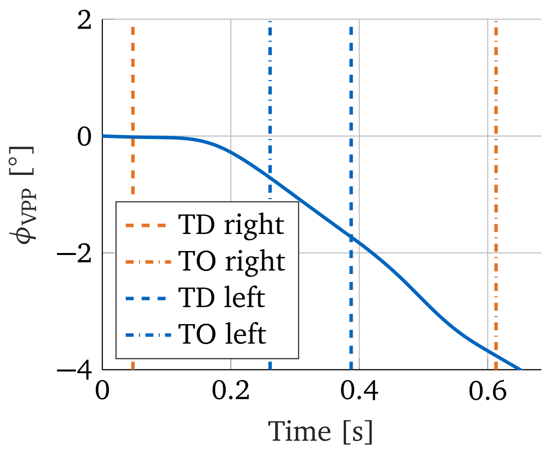

(c) Angle of the trunk.

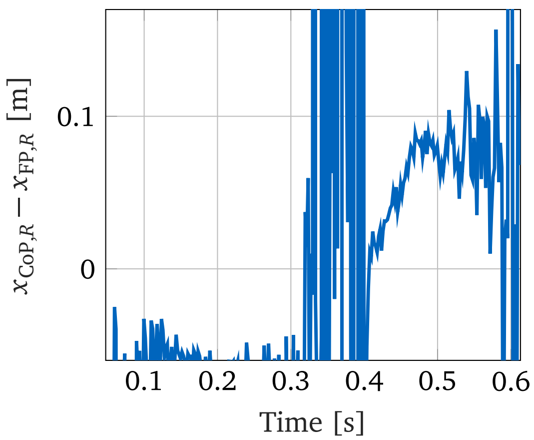

(d) Measured CoP during the stance phase of the prosthetic foot.

Figure 17.1: Kinetic quantities during one stride in the RTHS test with a prosthetic foot (right). The time instants of the left/right TD and TO are indicated by vertical lines. Figures taken from [105].

Apart from the trajectories shown, there are also characteristic force and torque profiles in human walking which should be represented realistically by the RTHS test. Firstly, the GRFs from the experiment are visualized in fig. 17.2a. The $GRF_{x,R}$ as well as $GRF_{y,R}$ qualitatively replicate the typical shapes observed in human walking (cf. figs. 15.3 and 16.3). The minimum of the vertical GRFs between the two maxima depends on the walking speed. In the RTHS experiment, the minimum was almost zero, which is untypical for a human walking at this speed. The maximum values are usually at about 110 % of the body weight, which is

[1]The force/torque measurements used are noisy and hence also the course of the CoP location is noisy.

the case in the results shown. In humans, the first peak is often higher than the second peak. In the experiment, the second peak is higher. Also, the force increase between the minimum and the second peak is more rapid than observed in humans and resembles an impact. The magnitude (in humans up to 25 % of the body weight) and shape of the forces in x direction are as expected. They are directly related to the forces in y direction by eq. (16.4). [173]

In the VPP model, a hip torque is applied to stabilize the trunk. The total hip torque (derived according to eq. (16.3)) is depicted in fig. 17.2b for the right leg. In the first half of

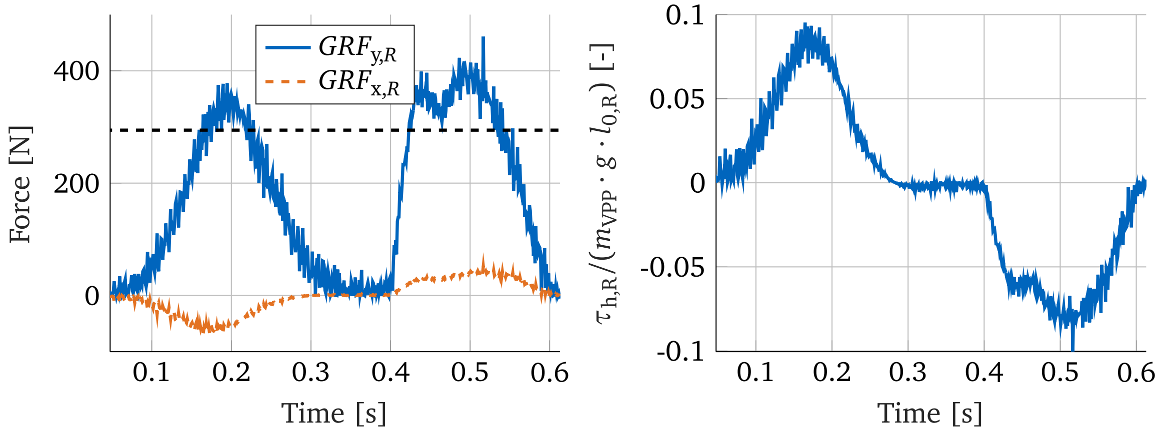

(a) The GRFs act on the human body (blue). The weight forces are represented by the dashed black line.

(b) The hip torque normalized over the body weight and leg length.

Figure 17.2: Forces and torques during the stance phase of the right, amputated leg. Figure taken from [105].

the stance phase, the hip torque hauls the CoM upwards and in the second half of the stance phase, the hip flexes. The magnitude and shape of the total hip torque $\tau_{h,R}$ correspond well with the observed hip torque in humans (cf. fig. 15.4b). Knee and ankle characteristics cannot be compared, as the VPP model does not have these joints.

A depiction of the whole motion during the stride is given in fig. 17.3. Perfect interface synchronization is assumed in the illustration, i.e. the displacements at the modeled interface and the ankle of the prosthetic foot are the same. When a leg is in swing phase, it does not contribute to the dynamics and is therefore not shown in the illustration.

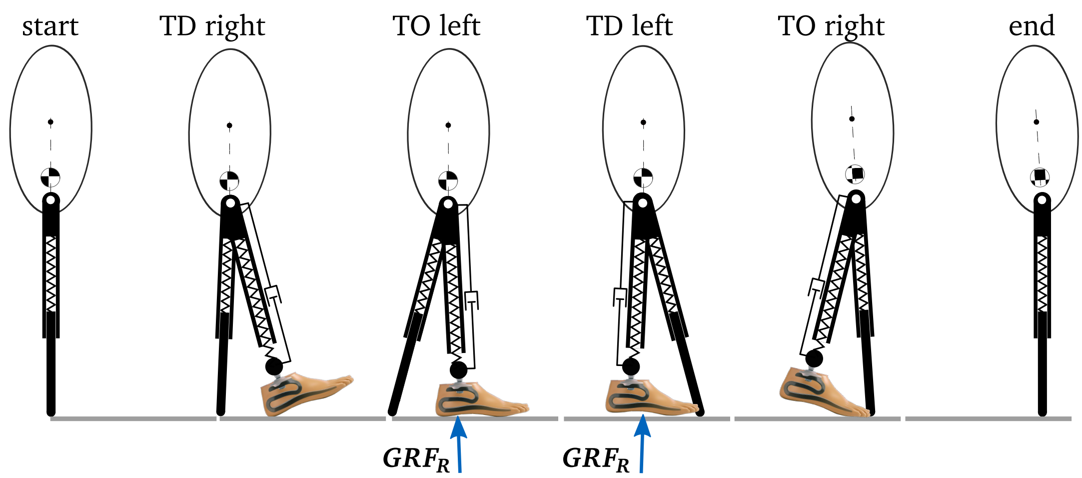

Figure 17.3: This figure depicts the motion of the model during the RTHS test of one stride. The model starts with the left leg on the ground. The GRFs are redirected by the hip torque such that they point towards the VPP. The right (prosthetic) leg does not influence the model dynamics during single support phase of the left leg. The visualized prosthetic foot is a 1D35 foot by Ottobock (© by Ottobock) rather than the 1C40 used in the RTHS test.

17.2 Test Reproducibility

One of the huge advantages of robot-based testing is the high reproducibility. To investigate how reproducible the RTHS tests with the prosthetic foot are, three different, independent trials with the same initial conditions were performed. The results are illustrated in fig. 17.4. In an RTHS test, errors accumulate throughout the test, which is also visible in the figure: the differences between the trials are smaller at the beginning of the test. Nevertheless, the magnitude of the motion/forces and the model behavior are similar among the trials. Differences are mainly of stochastic nature, such as measurement noise and friction between the prosthetic foot and the ground plate.

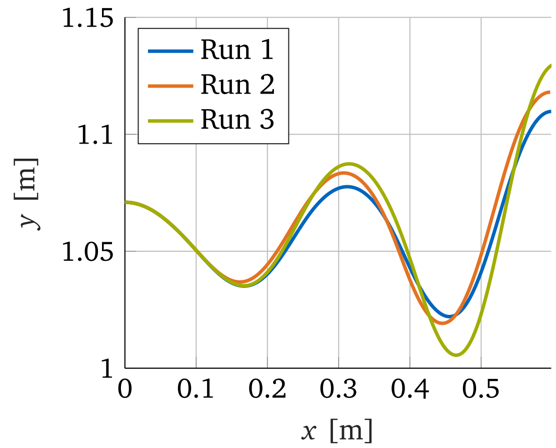

(a) The CoM trajectory during one stride.

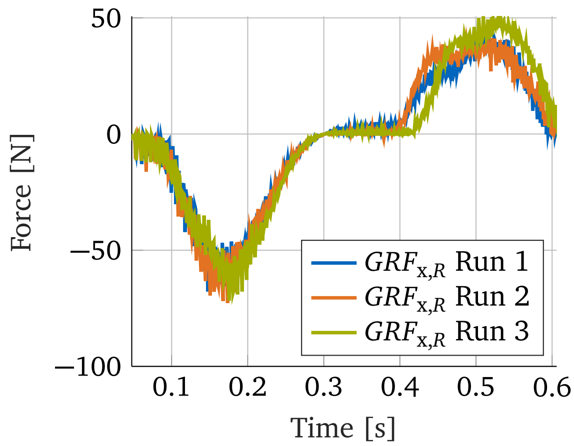

(b) The $GRF_{x,R}$ during stance phase of the prosthetic foot.

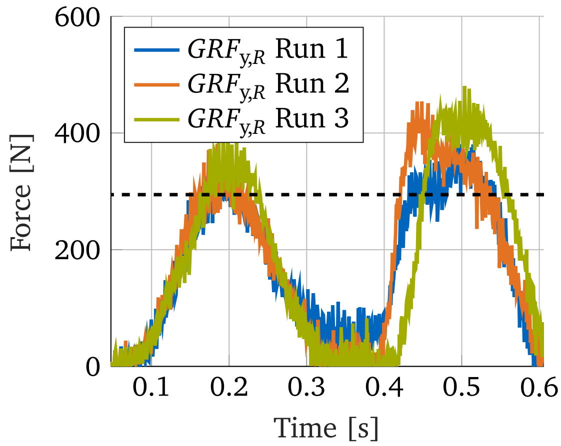

(c) The $GRF_{y,R}$ during stance phase of the prosthetic foot. The black dashed line indicates body weight.

Figure 17.4: Characteristic quantities of the gait cycle for different RTHS runs.

17.3 Discussion

From the results shown, several conclusions can be drawn: The performed RTHS test is in general able to qualitatively replicate human gait characteristics (CoM motion and forces/ torques) and is well reproducible. With the gait parameters used, no stable gait pattern could be achieved and the model would fall if a further stride would be performed. There are several reasons why the model would fall in a further step, even though a pure simulation of the VPP model with these parameters walks stably for more than 50 steps. Firstly, the

RTHS implementation used a forward shift of the CoP during stance phase for both feet (see section 16.1.2). As the body is decelerated when the CoM is behind the CoP, this phase is prolonged due to the forward shift, dissipating energy. This forward shift is not included in the pure simulation of the VPP model used for the parameter optimization. Secondly, the foot is three dimensional in contrast to the VPP model. This implies that, due to the relatively stiff prosthetic foot, the CoM has to be lifted while the body pivots about the foot. This is visible in figs. 17.1a and 17.4a by the growing amplitude of the CoM height. If the CoM velocity is too small, there is not enough kinetic energy to be converted into potential energy and the model falls backwards. Additionally, the introduced damper dissipates energy (≈ 5 %).

Apart from the changes made in the VPP model, there are also error sources in the RTHS setup itself. Even during walking high ankle velocities arise. For example, the foot lifts with a velocity of 4 m/s when humans walk at comfortable speed. The Stewart Platform used was driven at its limits for these RTHS tests (maximum motor voltage/current and actuator stroke). The tracking performance of the Stewart Platform is shown representatively for leg $i = 1$ in fig. 17.5. This leg undergoes the largest motion during the performed stance phase.

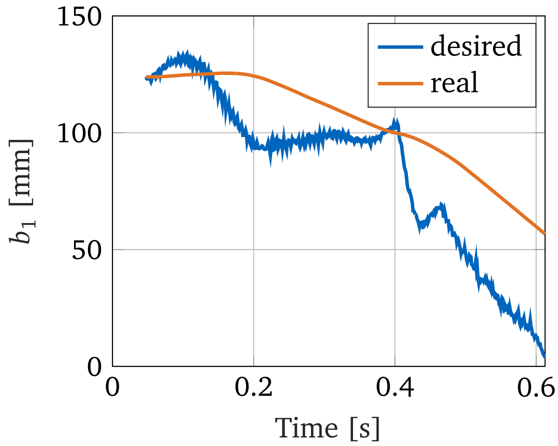

Figure 17.5: Representatively for all six legs, the desired and real displacement of Stewart Platform's leg 1 are shown. Large deviations can be seen between the commanded and the achieved displacement. The maximum leg velocity was set to 250 mm/s. Figure taken from [105].

The Stewart Platform is not able to follow the command sufficiently and responds with large time lag. This is the main reason why the stance phase of the right leg takes 85 % of the gait cycle rather than 60 % that is typical in human walking. Furthermore, the limited bandwidth of the Stewart Platform also explains the steep increase of the GRFs in y direction between the minimum and the second peak (at $t = 0.4$ s): The forefoot of the prosthetic foot is relatively stiff (see appendix C), that is, the forces increase rapidly when the foot is deformed. The simulated amputee reacts to these high forces by lifting the CoM (see fig. 17.1a), which leads to a changed motion command for the Stewart Platform. As fig. 17.5 illustrates, this motion command cannot be followed. Thus, the prosthetic foot is deformed further and high forces are measured. Since the Stewart Platform was already driven at its limits, an application of ILC or AFF as described in Part I would not achieve any advantages for the hardware setup used. The displacement command contains a high frequency oscillation (≈ 120 Hz), which is the vibration of the mass IFP. The Stewart Platform acted like a low-pass filter and the oscillation was not realized. For more powerful hardware setups, an additional low-pass filter may have to be implemented, the damping constant in the leg increased or the mass of the IFP reduced to dampen these oscillations. Another approach is to use Newmark time integration, as it offers the possibility to include massless DoFs.

A further limitation in the hardware setup is the support frame. Due to the horizontal friction forces, the frame started to oscillate and was not as stiff as a solid ground would be.

Chapter 18

Summary of Part III

Despite great progress in prostheses development, the gait pattern of amputees differs from that of able-bodied people. For a targeted prostheses development, a better understanding of the dynamic interaction between human and prosthesis is therefore necessary. In this part, a feasibility study was conducted to what extent RTHS can reproduce the dynamics of a human with a prosthetic foot and thus to be a visionary test method for foot prostheses.

Due to the complexity of human walking, this proof-of-concept study availed simplified models, focused on the stance phase and considered the motion only in two dimensions. Several conceptual models representing human gait characteristics were presented in chapter 15. The Virtual Pivot Point (VPP) model was selected as a basis to model the amputee. This model is able to replicate characteristic gait kinetics, such as the CoM motion, the GRFs and the hip torque. In chapter 16, a description was given how the VPP model is adapted to represent an amputee. The major changes were: (i) the right leg was cut by the height of the prosthetic foot (ii) a mass interface point and a damper were added to solve for the inserted DoF (iii) the CoP shift from heel to toe observed in human gait was modeled. In chapter 16, also the experimental setup and the prosthetic foot used were described.

In chapter 17, the RTHS test of one stride was performed. Compared with the biomechanical characteristics of human gait, the results correspond well. This implies that the RTHS setup is in general able to replicate gait characteristics according to the underlying VPP model and shows the potential of RTHS as a visionary test method for prosthetic feet.

Nevertheless, the current implementation suffers from some limitations:

- The gait parameters selected do not lead to stable gait. The trunk falls backwards because the initial conditions were found for the basic VPP model but not for the modified VPP model. The most influential difference lies in the shift of the CoP location, which reduces the system energy. To enable testing of several successive steps, the initial conditions of the gait model need to be adapted and ideally found for the modified VPP model.

- The Stewart Platform used was driven at its limits (maximum motor current), but still was not able to follow the motion command sufficiently. Hence, a more powerful actuator should be used. Alternatively, the Stewart Platform could be combined with an actuated ground plate to increase the workspace and maximum achievable relative motion between the prosthetic foot and the ground.

- The support frame is too flexible for the appearing shear forces and should be braced.

- Even though the parameters of the modeled amputee are in the range of parameters observed in humans, the combination of them is biomechanically not meaningful. The model has a mass of 30 kg, a leg length of 1 m and a leg stiffness of $5.4 \cdot 10^3$ N/m, which is a very light human on long, soft legs. The selection of a more realistic parameter set was not possible due to the limitations of the hardware setup used, but should be adapted to meaningful parameters in further research.

- The VPP model only considers the human motion in two dimensions and focuses on the stance phase. The swing phase and the foot geometry are not included. The ankle and the knee joint are also not included, but play an important role in locomotion.

The results that an ideal RTHS test—without errors in the execution—can produce are just as good as the underlying model. So, one should not expect that an RTHS test of prosthetic feet exactly replicates the motion of a specific amputee. RTHS could rather be used to determine how different prostheses or grounds influence the gait dynamics, e.g. whether the muscles need to be tensioned more, whether the energy consumption changes or how the loading in the hip/knee joint changes. In the VPP model, the hip torque could be such an indicator.

Part III presents the first ever RTHS test of a prosthetic foot and a modeled amputee. The results show the underlying potential of RTHS to replicate human gait dynamics. Nevertheless, the current implementation/hardware setup is not able to quantitatively emulate human gait data due to the limitations outlined above. Before RTHS can be used for testing of prosthetic feet, there are still many research questions that need to be solved. As a next step, implementing the amputee with the NMS model [80] is targeted. This model involves leg muscles, the knee joint, the swing phase and is able to withstand larger perturbations. Additionally, an improved hardware setup needs to be used.

Closure

Chapter 19

Conclusions and Outlook

The objective of this thesis was to develop methods that enable testing of prosthetic feet using RTHS. Successful testing of prosthetic feet requires a powerful implementation of RTHS because complex system dynamics need to be replicated with high fidelity. Prior to this work, the state-of-the-art methods were not sufficient to achieve this. Specifically, a high performance actuator control scheme able to handle contact dynamics stably and accurately and an informative fidelity measure were required. These two topics are addressed in Part I and Part II of this thesis. Furthermore, a proof-of-concept presented in Part III demonstrates that human gait dynamics can be replicated using RTHS. A detailed summary of the individual parts is given at the end of each part. The main findings with respect to the objective of the thesis to *lay the foundation for testing prosthetic feet using RTHS such that, in the future, the vision can be realized* (see section 1.1) are summarized in the following section. The emerging research questions for future work are also presented below.

19.1 Conclusions

An introduction to RTHS is given in chapter 2, where the method, the signal flow and the required components are explained. Furthermore, this chapter gives an overview about the effect of delay on the stability and fidelity of the RTHS test result. This chapter also introduces two possible view points of the coupling in RTHS that are used throughout the thesis, viz. as a control loop and as counterpart to dynamic substructuring.

In Part I, the focus was put on actuator control methods that are able to test various complex dynamical systems safely and accurately. For that purpose, requirements on the actuator control were defined in chapter 3 that make the developed scheme powerful while easy to apply. The actuator used at the Chair of Applied Mechanics and the one-dimensional RTHS setup with contact were presented in chapter 4.

Normalized Passivity Control (NPC) is able to stabilize RTHS tests with contact. One key issue in the execution of RTHS tests is keeping test stability. As introduced in chapter 5, this can be ensured by monitoring the energy/power flow in the RTHS setup and actively interfering when an energy increase is detected. Specifically, NPC was applied for the RTHS system with contact. This scheme monitors the power in- and outflow of the transfer system and introduces additional damping forces that augment the measured interface forces. NPC was proposed in [171], but has, to the authors knowledge, not been applied to RTHS with contact before. The influence of NPC on test stability and fidelity as well as the influence of the NPC parameters on the performance are analyzed. A recommendation about the appropriate parameter selection is given. In general, NPC is able to detect when test stability is jeopardized and dampens unwanted energy increase, also in RTHS tests with contact.

Iterative Learning Control (ILC) is a suitable feedforward control scheme to improve the test fidelity in successive RTHS trials. Any dynamics/delay of the transfer system do not only jeopardize test stability, but also deteriorate test fidelity. The development of powerful actuator control schemes concerns many researchers in RTHS. In chapter 6, the application of ILC to RTHS is proposed and the efficiency investigated. ILC is able to improve the tracking performance of the actuator in successive RTHS trials, which directly implies an increased test fidelity. Learning is successful if the ILC parameters are chosen such that the error converges. A convergence condition is derived and validated that helps to determine appropriate ILC parameters. Furthermore, the successful learning process of ILC requires test stability. For that purpose, ILC is combined with NPC and the proposed scheme is validated. Overall, ILC in combination with NPC is able to reduce the tracking error and the reference error.

Adaptive Feedforward Filters (AFF) are a powerful feedforward scheme for RTHS, but require further adaptation for the application to contact problems. AFF were proposed in [15, 17] as feedforward controller in RTHS. There, the application to linear and nonlinear systems was investigated, however, contact dynamics were not considered. In this thesis, AFF are applied to the RTHS system with contact and the influence of the hyper-parameters on the results are investigated. AFF show a high tracking performance and achieve a high responsiveness of the actuator during both, the non-contact and the contact phase. The tracking error is the largest at the instants of transition from non-contact to contact and vice versa, i.e. when the system dynamics change.

The combination of PD-type ILC and velocity feedforward (VFF) yields the best tracking performance and test fidelity in the conducted benchmark study. In chapter 8, different feedforward controllers (VFF, ILC and AFF) and their combinations were compared. All of them improve the tracking performance significantly compared to a pure feedback controller. The best results were achieved when VFF was involved because it achieves agility of the controlled Stewart Platform.

Developing fidelity measures to evaluate RTHS tests increases the acceptance of RTHS as a testing method. Fidelity measures tell the user how well the test performed emulates the true system dynamics. Part II deals with the development of a novel fidelity measure. Error sources in RTHS as well as a review of currently existing accuracy measures are given in chapter 10. Based on the benefits and shortcomings of the existing accuracy measures, requirements are set up for fidelity measures, which are incorporated in the presented method.

The key idea of the novel method for fidelity assessment is to explore how changes of errors in the RTHS setup influence the RTHS result. In chapter 11, a novel method for fidelity assessment called FACE (short for *Fidelity Assessment based on Convergence and Extrapolation*) is proposed. In this method, the main error in the RTHS setup is deliberately altered and its influence on the test result monitored, i.e. an experimental sensitivity study performed. Using the relation (found with a function fit) between the error and the RTHS result, the solution without this error can be extrapolated. If the investigated error is the only considerable error, the reference solution is obtained. A comparison between the approximated reference solution and the RTHS result helps the user to decide how accurately the true system dynamics are captured and how detrimental the errors are to this setup. The application of the FACE method requires that the error as well as the RTHS result are represented as scalar variables that are easy to interpret.

The fidelity of an RTHS test's vibration response can be assessed with the FACE method by monitoring the magnitude, frequency and damping. The FACE method was elaborated in detail for structural systems, where the vibration response is of interest and the main error in the RTHS setup came from the actuator dynamics (in section 11.3). The FACE method was further applied to a virtual RTHS test of a linear mass-spring-damper system, a virtual RTHS test of the MECHS benchmark control problem and experimentally to the RTHS system with contact in chapter 12. The investigations show the potential of the proposed method to predict the reference solution and to assess the test fidelity.

Testing prosthetic feet using RTHS is the vision underlying this work and literally a first step was taken in Part III. This part commenced with an introduction to prosthetic feet and prostheses testing in chapter 14. After that, human gait characteristics and locomotion models were presented in chapter 15.

The Virtual Pivot Point (VPP) model represents the characteristic gait pattern of humans and is therefore suitable to model an amputee. The numerical substructure of the envisioned RTHS test simulates an amputee. Based on the literature review in chapter 15, the VPP model was found to be a simple model which is able to replicate human gait dynamics (CoM motion and forces/torques) while having the option to stabilize the trunk and thus overcome some disturbances. Hence, the VPP model was used as basis for the modeled amputee. The right leg was cut at the ankle and enhanced by a mass interface point and a damper. Furthermore, the model was adapted such that the foot point shifts from the heel to the toes, as is observed in humans, and thus make the VPP model more realistic. All modifications and the final implementation are described in detail in chapter 16. This chapter also presents the used prosthetic foot.

One stride could be performed with RTHS, where the amputee was simulated with a modified VPP model and the prosthetic foot was tested experimentally. The stance phase was in the focus of the investigations in this thesis. With the hardware setup presented, one stride could be performed, which started in mid stance of the simulated, left leg. The right leg was modeled as the amputated one with the right foot mounted on the Stewart Platform. The center of mass trajectory as well as Ground Reaction Forces and the hip torque corresponded to human data. This indicates that the RTHS setup presented is able to replicate human gait dynamics.

In the introductory chapter 1, the parts of this thesis were depicted as three pillars representing the supporting function of the three individual parts for achieving the vision of testing prosthetic feet with RTHS. The methods were developed with the intention that they together form the basis for the intended achievement. However, the methods developed in Parts I and II have not yet been linked to the proof-of-concept in Part III. This is because the actuator used operates at its limits (maximum voltage/current exhausted). Hence, the application of ILC is not meaningful and would not achieve any tracking improvements. Neither the application of the FACE method to the prosthesis test would be meaningful: the tracking error by the Stewart Platform is very large. If the tracking performance is deteriorated even more, the execution of the motion command is so slow that the modeled amputee would fall before the full stride is executed. Note that when the FACE method is applied to the proof-of-concept, the measure q must be selected meaningfully for this application. The amplitude, frequency and damping, which were used for demonstration in Part II, are not meaningful in this case. Rather, e.g. the peak GRFs, the maximum/minimum CoM height or the take-off angle might be meaningful choices to represent the RTHS result. The FACE method would not tell how well the RTHS test emulates the true gait dynamics of a human amputee with the prosthetic foot but how much the RTHS result differs from the modeled amputee wearing the prosthetic foot.

Even though the achievements in this thesis offer a solid basis for the development of RTHS as a testing method for prosthetic feet, many open research questions remain. The steps until testing of prosthetic feet with RTHS can be put into practice are illustrated as a flow chart in fig. 19.1. The flow chart names just a few possibilities of the potential next research steps. The successful execution of prostheses testing requires a powerful hardware setup. How well the test emulates the true behavior of the amputee fundamentally relies on the accuracy of human gait models. Hence, literature about locomotion models should always be monitored in parallel to the execution of the next steps and alternative choices considered. The definition of the final stage (named "testing prosthetic feet with RTHS" in the figure) depends on the defined level of detail. RTHS as test method may already be helpful if the test result replicates human behavior, in other words, if the influence of certain prosthesis characteristics on the gait dynamics can be observed. In the long run, a patient-specific analysis including uncertainties in the investigation is desirable.

19.2 Future Directions of Research

In the course of this research, not only efficient methods were developed and issues resolved, but also new research questions emerged. These ideas are presented below.

NPC uses a monitor of the power throughput of the transfer system to decide whether test stability is jeopardized. In contrast, [53] or [75] use the energy flow to detect test instability. The efficiency of NPC to render the test stable varies depending on the selected energy/power observer. Different selections of threshold, i.e. when the passivity controller starts to augment the interface force and damp excessive energy, and different passivity controllers could be implemented for improved performance.

Even though the implementation of AFF presented in chapter 7 achieved good tracking performance, there is still some potential at the instant of contact. When the system dynamics change (non-contact to contact or vice versa), the tracking error is larger for a short time until the filter parameters have been adapted appropriately. Switching between filter parameters adjusted for each of the phases at the instant of contact could be one way to improve the tracking performance. First attempts to include changes of the filter at contact were investigated in a co-supervised Master thesis [72]. These implementations include time-domain adaptation (AFF) as well as iteration-wise learning (saving filter parameters for next trial).

The developed methods should also be generalized to and validated for nonlinear, MDOF systems and three dimensional contact. Due to the excellent performance of the developed schemes in Part I, it is assumed that they also work as intended in these more general applications. Another application example where ILC has already been used to improve the tracking performance is the RTHS test of a shock application [106]. A further idea—in contrast to these position-based control schemes—is to implement hybrid position-force control. At the moment of contact, the control scheme would switch to force control. Especially RTHS tests with stiff experimental structures are highly sensitive to actuator dynamics and a switch to force-based coupling is beneficial [15]. In force-based coupling, interface displacements are fed back and used for the next numerical time integration step rather than interface forces. This means that required velocities and accelerations are derived from the measured displacements. Preliminary experiments with hybrid position-force control showed that the derivation of the measured noisy displacements to obtain the velocity and accelerations quickly leads to test instability. So, even though the approach is promising, there are also some difficulties associated with it.

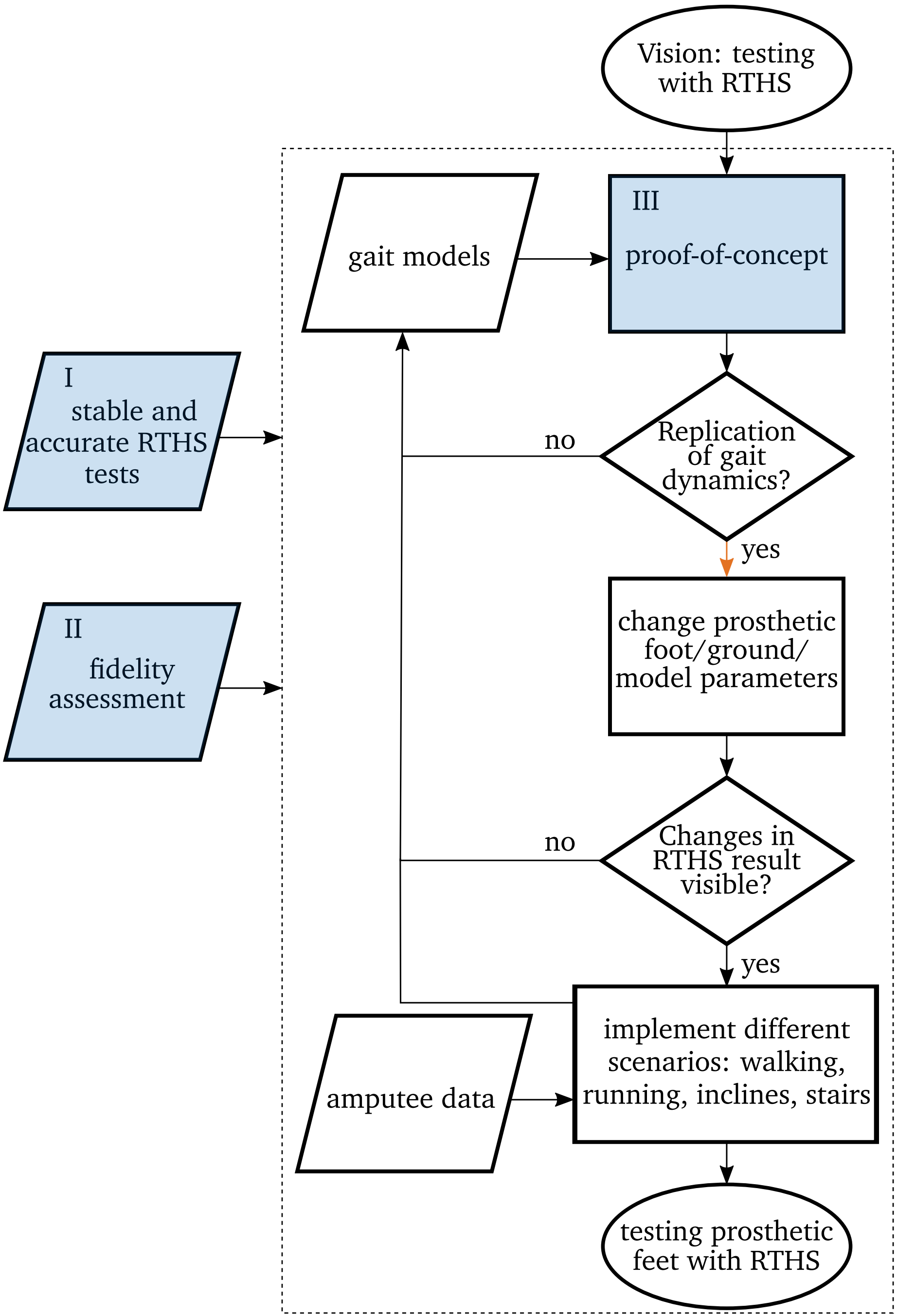

Figure 19.1: This flow chart represents the necessary steps until testing of prosthetic feet with RTHS is possible. In this thesis, a solid basis was set to enable testing of prosthetic feet with RTHS in the future: the method development of Part I and II is not limited to prostheses testing, but necessary to reliably run RTHS tests of complex dynamical systems. Part III specifically worked on that goal and one stride could be performed. The orange arrow indicates the current position in the flow chart. A lot of research still needs to be done before RTHS can be established for prostheses testing. In parallel to the upcoming steps, a constant comparison of the RTHS test with gait data and the evaluation of the amputee model used need to be done.

This thesis proposes the FACE method and its efficacy is examined for structural vibrations (RTHS result q) and the actuator dynamics as the main source of error (error represented with e) in the RTHS setup. As a next step, the FACE method needs to be validated for more dynamical systems and elaborated for different choices of q and e.

Apart from the FACE method developed for fidelity assessment in this thesis, further ideas for fidelity assessment include:

- Artificial Neural Networks (ANN) could be used to learn the relation between measurable quantities during the RTHS test and the test fidelity. A preliminary investigation of this approach was performed and published in [109]. This approach requires a lot of data from different RTHS setups and would therefore need the commitment of many researchers around the world to gather a large data set.

- Using frequency-based substructuring (FBS), dynamics of two independently measured substructures can be coupled to obtain the dynamic behavior of the overall system. Moreover, not only coupling, but also decoupling of substructures is possible, i.e. the dynamics of a substructure A can be determined when the dynamics of A+B and the dynamics of B are known. In RTHS, the dynamics of the coupled RTHS system, which comprises the numerical part (substructure A), the transfer system (substructure C) and the experimental part (substructure B) are known. If also the dynamics of the transfer system are identified, this influence can be quantified and the dynamics of the reference system (A+B) determined.

There are multiple ideas how to pursue the proof-of-concept study in Part III. Firstly, the hardware needs to be more powerful. This could be achieved by a different actuator or an additional actuation of the upper plate (the ground where the prosthetic foot is pushed against). Furthermore, the support frame needs to be braced. Apart from that, the Neuromuscular-Skeletal (NMS) model by Geyer and Herr [80] could be used to model the amputee rather than the VPP model. The advantage of this more complex model is that the legs and feet are modeled more realistically with segments and muscles. Moreover, the NMS model is less sensitive to disturbances and the swing phase is included. In the current implementation using the VPP model, a linear shift of the CoP from the heel to the toe is assumed. The real position of the CoP could be measured using pressure sensors at the sole and used for the calculations. Further steps until the envisioned test method is achieved are depicted in fig. 19.1.

Appendices

Appendix A

Parameters

This chapter summarizes the parameters used throughout the thesis.

The controller parameters of the decentralized cascaded feedback controller, which is described in section 4.2.1 are stated in table A.1. The position controller is a proportional controller, i.e. $G_\mathrm{p} = K_\mathrm{Pp}$, and the velocity control loop is controlled with a PI controller $G_\mathrm{v} = K_\mathrm{Pv} + \frac{K_\mathrm{Iv}}{s}$. The set of parameters PPI1 was used for the experiments in chapters 4 to 7. In chapter 8 and Part III, the parameters have been tuned to improve the performance further. These values are denoted by PPI2.

Table A.1: Controller parameters of the cascaded feedback controller.

variable	PPI1	PPI2
K_Pp	$20\,\mathrm{1/s}$	$50\,\mathrm{1/s}$
K_Pv	$0.2\,\mathrm{As/m}$	$0.2\,\mathrm{As/m}$
K_Iv	$1\,\mathrm{A/m}$	$5\,\mathrm{A/m}$

A.1 Parameters for Part I

This section summarizes the parameters used in Part I of this thesis. The parameters of the dynamical system are given in table A.2. The standard parameters of NPC were as given in table A.3, for the ILC table A.4 were chosen and the tests with AFF were conducted with the parameters given in table A.5.

Table A.2: Standard parameters of the RTHS system with contact.

variable	value	variable	value
h_0	$0.01\,\mathrm{m}$	m_EXP	$0.38\,\mathrm{kg}$
l_0	$0.071\,\mathrm{m}$	m_NUM	$9.62\,\mathrm{kg}$
k_NUM	$10^4\,\mathrm{N/m}$	f_d	$0.25\,\mathrm{Hz}$
d_NUM	$50\,\mathrm{kg/s}$, $200\,\mathrm{kg/s}$	Δz_max	$0.005\,\mathrm{m}$
k_EXP	$8650\,\mathrm{N/m}$	g	$9.81\,\mathrm{m/s^2}$
ΔT	$0.001\,\mathrm{s}$	Solver	ode8 (Dormand-Prince)

Table A.3: Standard NPC parameters.

variable	value
G_P	$1600\,\mathrm{kg/s}$
T_error	$0.1\,\mathrm{s}$
T_tot	$0.01\,\mathrm{s}$

Table A.4: Standard ILC parameters.

variable	value
β	$10\,\mathrm{1/s}$
γ	1
$f_\mathrm{Q,cut}$	$6\,\mathrm{Hz}$
t_pause	$1\,\mathrm{s}$

Table A.5: Standard AFF parameters.

variable	value
μ_LMS	0.1
ν_LMS	0.99999
N_FIR	100
δ	0.001

A.2 Parameters for Part III

The parameters used to investigate the influence of the IFP in chapter 16 are summarized in table A.6 and for the RTHS tests presented in chapter 17 in table A.7.

The model starts at $x = 0\,\mathrm{m}$ in its apex, i.e. $\dot{y} = 0\,\mathrm{m/s}$. The damping constant d_u in table A.6 and table A.7 is designed such that the remaining leg is critically damped, i.e. $d_\mathrm{u} = 2\cdot\sqrt{m_\mathrm{IFP} k_\mathrm{u}}$. The stiffness k_u is found using the leg stiffness $k_R = k_L$ and the approximated value $k_\mathrm{f} = 4950\,\mathrm{N/m}$ from fig. C.1. The Bogacki-Shampine solver is a Runge-Kutta scheme of order three.

Table A.6: Parameters of the VPP and modified VPP model for investigations about the influence of the IFP. Parameters taken from [97].

variable	value	variable	value
$l_{0,L}$, $l_{0,R}$	$1\,\mathrm{m}$	$l_\mathrm{0,u}$, $h_\mathrm{0,f}$	$0.5\,\mathrm{m}$
m_VPP	$80\,\mathrm{kg}$	m_IFP	$0.005\,\mathrm{kg}$
J_VPP	$5\,\mathrm{kgm}^2$	k_u	$15082\,\mathrm{N/m}$
k_L	$13\cdot 10^3\,\mathrm{N/m}$	k_f	$94176\,\mathrm{N/m}$
α_0	$69°$	d_u	$43.4\,\mathrm{kg/s}$
r_VPP	$0.25\,\mathrm{m}$	r_h	$0.1\,\mathrm{m}$
y_0	$1.086\,\mathrm{m}$	$\dot{x}_0$	$1.136\,\mathrm{m/s}$
$\phi_\mathrm{VPP,0}$	$0\,\mathrm{rad}$	$\dot{\phi}_\mathrm{VPP,0}$	$-0.145\,\mathrm{rad/s}$
Solver	Bogacki-Shampine	ΔT	$0.0001\,\mathrm{s}$

In the RTHS tests, the modeled amputee is simulated with a sample time of $0.0002\,\mathrm{s}$ while the sample time of the actuator control and the synchronization time step are $\Delta T = 0.001\,\mathrm{s}$. The parameters are summarized in table A.7. The implementation of the CoP shift (section 16.1.2) requires geometric data from the prosthetic foot. These are $l_\mathrm{h} = 0.06\,\mathrm{m}$ and $l_\mathrm{ff} = 0.19\,\mathrm{m}$. Furthermore, the leg angle at TO needs to be known for the evaluation of eq. (16.10), which is assumed to be $\alpha_\mathrm{TO} = 105°$. In the RTHS test, TO is detected when the upper leg extends above its resting spring length $l_\mathrm{0,u}$.

Table A.7: Parameters of the modified VPP model used for the RTHS test [13].

variable	value	variable	value
$l_{0,L}$, $l_{0,R}$	1 m	$l_{0,\mathrm{u}}$	0.84 m
m_{VPP}	30 kg	$h_{0,\mathrm{f}}$	0.16 m
J_{VPP}	3 kgm^2	m_{IFP}	0.005 kg
k_L	$5.4 \cdot 10^3$ N/m	k_{u}	$1.1 \cdot 10^3$ N/m
α_0	75°	d_{u}	4.69 kg/s
r_{VPP}	0.25 m	r_{h}	0.1 m
y_0	1.0709 m	$\dot{x}_0$	0.97633 m/s
$\phi_{\mathrm{VPP},0}$	0 rad	$\dot{\phi}_{\mathrm{VPP},0}$	−0.0071 rad/s
Solver	Euler	Sample Time NUM	$2 \cdot 10^{-4}$ s
		Sample Time RTHS	$1 \cdot 10^{-3}$ s

Appendix B

Dynamic Behavior of the Kistler Dynamometer

The dynamic behavior of the Kistler Multicomponent Dynamometer was tested using an impact test. The results can be seen in fig. B.1. The FTS was mounted on the measuring table in two configurations, first with the clamping tool carefully tightened (black) and then with high tension (orange). The measurements reveal that the FTS should be carefully mounted rather than too tight because this braces the sensor itself and leads to falsified measurements of the magnitude.

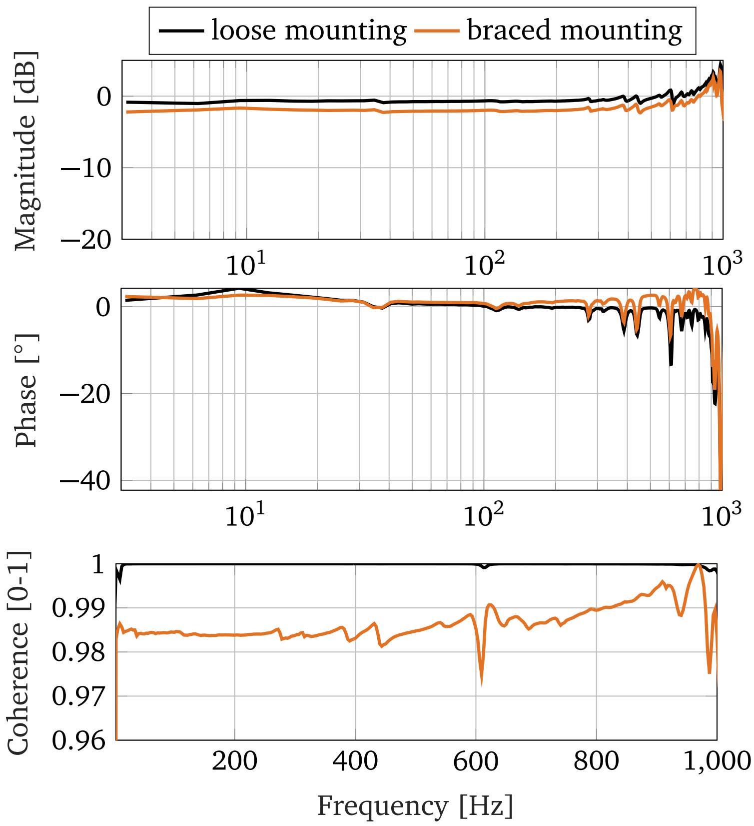

Figure B.1: The dynamic response of the Kistler Multicomponent Dynamometer in vertical direction was identified with an LMS data acquisition system. The magnitude and phase as well as the coherence of the measurements are shown.

Appendix C

Prosthetic Foot 1C40

The prosthetic foot used is of the type 1C40 and from Ottobock. Measured displacement-force characteristics of this prosthetic foot are given in fig. C.1. The angle α is measured between the shank and the ground. For an angle of 90°, both the forefoot and the heel are on the ground. Angles $> 90°$ indicate a tilt towards the toes and angles $< 90°$ towards the heel.

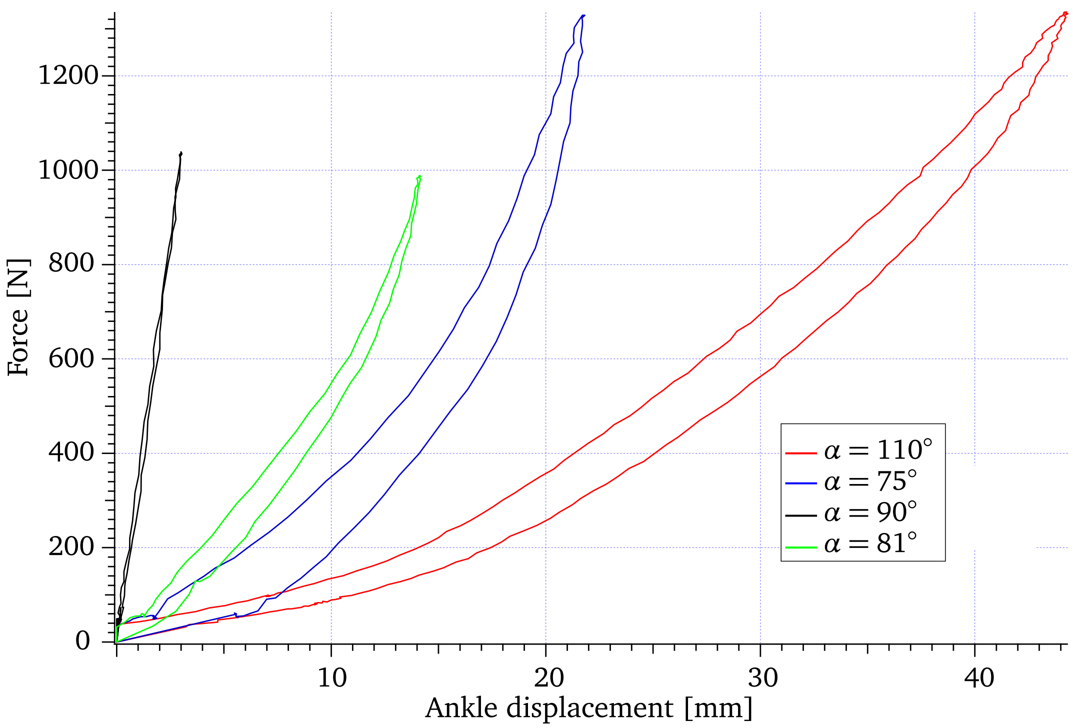

Figure C.1: Displacement-force characteristics of the used prosthetic foot 1C40 from Ottobock built in 1999. The characteristics are shown for different loading angles α between the shank and the ground. The measurements were performed barefoot by Ottobock.

Co-supervised Student Theses

Nouwens, S. "Realtime Substructuring of a Biped with a Prosthetic Foot". Semester thesis. Technical University of Munich, 2018.

Braesch, I. "RoBio Vibrations: Robot-driven Biomechanical Vibration Analysis". Master thesis. Technical University of Munich, 2019.

Göldeli, M. "Modellbasierte Regelung eines Hexapods". Semester thesis. Technical University of Munich, 2019.

Klotz, T. "Implementierung der Iterative Learning Control auf dem Hexapod". Semester thesis. Technical University of Munich, 2019.

Peters, J. "Implementation of Compliant Motion Control Schemes on the Stewart Platform". Semester thesis. Technical University of Munich, 2019.

Sorin, A. "Real-Time Hybrid Substructuring with Model Knowledge". Semester thesis. Technical University of Munich, 2019.

Xiang, J. "Konzept zur Umsetzung der Menschlichen Fußtrajektorie am Hexapod". Semester thesis. Technical University of Munich, 2019.

Zhou, D. "Implementation of Passivity Based Control on the Stewart Platform". Semester thesis. Technical University of Munich, 2019.

Fan, K. "Setting up a Hybrid Substructuring Test for Prosthetic Feet". Master thesis. Technical University of Munich, 2020.

Grassinger, D. "Accuracy Analysis of Real-Time Hybrid Substructuring (RTHS) Using Neural Networks". Semester thesis. Technical University of Munich, 2020.

Holzberger, F. "Comparison of Human Gait Models to be Used in Foot-Prostheses Testing". Semester thesis. Technical University of Munich, 2020.

Jain, S. "Fidelity Analysis of Real-Time Hybrid Substructuring (RTHS)". Bachelor thesis. Technical University of Munich, 2020.

Kist, A. "Implementierung der Iterative Learning Control für Real-Time Hybrid Substructuring". Semester thesis. Technical University of Munich, 2020.

Schwalm, H. "Robust Control for Real-Time Hybrid Substructuring Using Iterative Learning Control". Master thesis. Technical University of Munich, 2020.

Ballat, L.-M. "Umsetzung eines Hardware-in-the-Loop (HiL) Tests für Fußprothesen mit Verwendung des VPP-Modells". Semester thesis. Technical University of Munich, 2021.

Fuderer, S. "Adaptive Feedforward Filters for Hybrid Substructuring with Contact". Master thesis. Technical University of Munich, 2019.

Lorenz, F. "Umsetzung eines Hardware in the Loop Teststandes für Fußprothesen unter Verwendung des FMCH Modells". Semester thesis. Technical University of Munich, 2021.

Ochsenfarth, F. "Verwendung der Hybriden Kraft-Positionsregelung für Real-Time Hybrid Substructuring mit Kontakt". Semester thesis. Technical University of Munich, 2021.

Bibliography

[1] Abbiati, G., Marelli, S., Tsokanas, N., Sudret, B., and Stojadinović, B. "A global sensitivity analysis framework for hybrid simulation". In: *Mechanical Systems and Signal Processing* 146 (2021). ISSN: 0888-3270. DOI: https://doi.org/10.1016/j.ymssp.2020.106997.

[2] Abbiati, G. "Structural Reliability Analysis Using Deterministic Hybrid Simulations and Adaptive Kriging Metamodeling". In: *Proceedings of the 16th World Conference on Earthquake Engineering (16WCEE)*. 2017.

[3] Abbiati, G., Marelli, S., Bursi, O., Sudret, B., and Stojadinović, B. "Uncertainty propagation and global sensitivity analysis in hybrid simulation using polynomial chaos expansion". In: *Proceedings of the Fourth International Conference on Soft Computing Technology in Civil, Structural and Environmental Engineering*. Vol. 109. Civil-Comp Press, 2015. DOI: 10.4203/ccp.109.23.

[4] Ackermann, M. "Dynamics and Energetics of Walking with Prostheses". PhD thesis. University of Stuttgart, 2007.

[5] Aghili, F. "Robust Impedance-Matching of Manipulators Interacting With Uncertain Environments: Application to Task Verification of the Space Station's Dexterous Manipulator". In: *IEEE/ASME Transactions on Mechatronics* 24.4 (2019), pp. 1565–1576. DOI: 10.1109/TMECH.2019.2928281.

[6] Ahmadizadeh, M. and Mosqueda, G. "Online energy-based error indicator for the assessment of numerical and experimental errors in a hybrid simulation". In: *Engineering Structures* 31.9 (2009), pp. 1987–1996. ISSN: 0141-0296. DOI: https://doi.org/10.1016/j.engstruct.2009.03.002.

[7] Allen, M. S., Mayes, R. L., and Bergman, E. J. "Experimental modal substructuring to couple and uncouple substructures with flexible fixtures and multi-point connections". In: *Journal of Sound Vibration* 329.23 (2010), pp. 4891–4906. DOI: 10.1016/j.jsv.2010.06.007.

[8] Anderson, R. J. and Spong, M. W. "Bilateral control of teleoperators with time delay". In: *IEEE Transactions on Automatic Control*. Vol. 34. 1989. DOI: 10.1109/9.24201.

[9] Arimoto, S., Kawamura, S., and Miyazaki, F. "Bettering Operation of Dynamic Systems by Learning: A new Control Theory for Servomechanism or Mechatronic Systems". In: *The 23rd Conference on Decision and Control*. 1984, pp. 1064–1069. DOI: 10.1109/CDC.1984.272176.

[10] Au, S. K., Weber, J., and Herr, H. "Powered Ankle–Foot Prosthesis Improves Walking Metabolic Economy". In: *IEEE Transactions on Robotics* 25.1 (2009), pp. 51–66. DOI: 10.1109/TRO.2008.2008747.

[11] Bachmann, J. A., Strand, M., Vassiliou, M. F., Broccardo, M., and Stojadinović, B. "Is rocking motion predictable?" In: *Earthquake Engineering & Structural Dynamics* 47.2 (2018), pp. 535–552. DOI: https://doi.org/10.1002/eqe.2978.

[12] Bakhaty, A. A., Mosalam, K. M., and Govindjee, S. “Theoretical Development of Hybrid Simulation Applied to Plate Structures”. In: *Technical report 101422, California University, Berkeley* (2014).

[13] Ballat, L.-M. “Umsetzung eines Hardware-in-the-Loop (HiL) Tests für Fußprothesen mit Verwendung des VPP-Modells”. Semester thesis. Technical University of Munich, 2021.

[14] Barber, J. R. *Contact Mechanics*. Springer, Cham: Springer International Publishing AG, 2018. DOI: https://doi.org/10.1007/978-3-319-70939-0.

[15] Bartl, A. “Real-Time Hybrid Substructure Testing”. PhD thesis. Technical University of Munich, 2019.

[16] Bartl, A., Insam, C., and Rixen, D. J. “Stability Issues in Hardware-in-the-Loop Tests of Flexible Components”. In: *PAMM*. 2018.

[17] Bartl, A., Karamooz Mahdiabadi, M., Insam, C., Mayet, J., and Rixen, D. J. “A hybrid testing method based on adaptive feed-forward filters”. In: *Mechanical Systems and Signal Processing* 139 (2020). ISSN: 0888-3270. DOI: https://doi.org/10.1016/j.ymssp.2019.106586.

[18] Bas, E. E. “Advances in Nonlinear Computational Substructuring for Real-Time Hybrid Simulation”. PhD thesis. University of Nevada, Reno, 2020.

[19] Blakeborough, A., Williams, M. S., Darby, A. P., and Williams, D. M. “The development of real-time substructure testing”. In: *The Royal Society* 359.1786 (2001), pp. 1869–1891.

[20] Blickhan, R. “The spring-mass model for running and hopping”. In: *Journal of Biomechanics* 22.11 (1989), pp. 1217–1227. ISSN: 0021-9290. DOI: https://doi.org/10.1016/0021-9290(89)90224-8.

[21] Böck, M., Glück, T., Kugi, A., and Steinböck, A. *Fortgeschrittene Methoden der Nichtlinearen Regelung*. Vienna University of Technology, 2015.

[22] Boge, T. and Ma, O. “Using advanced industrial robotics for spacecraft rendezvous and docking simulation”. In: *Proceedings - IEEE International Conference on Robotics and Automation* (2011). ISSN: 10504729. DOI: 10.1109/ICRA.2011.5980583.

[23] Bolien, M. “Hybrid Testing of an Aerial Refuelling Drogue”. PhD thesis. University of Bath, 2018.

[24] Bonelli, A. and Bursi, O. S. “Predictor-corrector procedures for pseudo-dynamic tests”. In: *International Journal for Computer-Aided Engineering and Software* 22 (7 2005), pp. 783–834. DOI: 10.1108/02644400510619530.

[25] Bonnet, P. A., Lim, C. N., Williams, M. S., Blakeborough, A., Neild, S. A., Stoten, D. P., and Taylor, C. A. “Real-time hybrid experiments with Newmark integration, MCSmd outer-loop control and multi-tasking strategies”. In: *Earthquake Engineering and Structural Dynamics* 36 (2007), pp. 119–141. ISSN: 1096-9845. DOI: 10.1002/eqe.

[26] Bosse, D., Radner, D., Schelenz, R., and Jacobs, G. “Analysis and Application of Hardware in the Loop Wind Loads for Full Scale Nacelle Ground Testing”. In: *DEWI Magazin* 43 (2013), pp. 65–70.

[27] Botelho, R. and Christenson, R. “Robust Stability and Performance Analysis for Multi-actuator Real-Time Hybrid Substructuring”. In: *Dynamics of Coupled Structures, Volume 4*. 2015, pp. 1–7. DOI: 10.1007/978-3-319-15209-7_1.

[28] Botelho, R. M. "Real-Time Hybrid Substructuring for Marine Applications of Vibration Control and Structural Acoustics". PhD thesis. University of Connecticut, 2015.

[29] Bousias, S., Sextos, A., Kwon, O.-S. K., Taskari, O., Elnashai, A., Evangeliou, N., and Di Sarno, L. "Intercontinental Hybrid Simulation for the Assessment of a Three-Span R/C Highway Overpass". In: *Journal of Earthquake Engineering* 23.7 (2019), pp. 1194–1215. DOI: 10.1080/13632469.2017.1351406.

[30] Bristow, D. A. and Alleyne, A. G. "A manufacturing system for microscale robotic deposition". In: *Proceedings of the 2003 American Control Conference, 2003.* Vol. 3. 2003, pp. 2620–2625.

[31] Bristow, D., Tharayil, M., and Alleyne, A. "A Survey of Iterative Learning Control: A Learning-based Method for High-performance Tracking Control". In: *IEEE Control Systems Magazine* 3 (2006), pp. 96–114. DOI: 10.1109/MCS.2006.1636313.

[32] Brooker, G. "Active and Passive Prosthetic Limbs". In: *Introduction to Biomechatronics*. Materials, Circuits and Devices. Institution of Engineering and Technology, 2012. Chap. 10, pp. 523–586. DOI: 10.1049/SBCS003E_ch10.

[33] Bursi, O. S. and Wagg, D. *Modern Testing Techniques for Structural Systems: Dynamics and Control*. Vol. 502. International Centre for Mechanical Sciences. Springer Vienna, 2008. ISBN: 978-3-211-09444-0.

[34] Carrion, J. and Spencer, B. F. "Model-based Strategies for Real-time Hybrid Testing". In: *NSEL Report Series* (2007).

[35] Carrion, J. and Spencer, B. "Real-time hybrid testing using model-based delay compensation". In: *Smart Structures and Systems* 4 (6 2008). DOI: 10.12989/sss.2008.4.6.809.

[36] Cavagna, G. A., Thys, H., and Zamboni, A. "The sources of external work in level walking and running." In: *The Journal of Physiology* 262.3 (1976), pp. 639–657. DOI: https://doi.org/10.1113/jphysiol.1976.sp011613.

[37] Chabaud, V. "Real-Time Hybrid Model Testing of Floating Wind Turbines". PhD thesis. Norwegian University of Science and Technology, 2016.

[38] Chen, C. and Ricles, J. M. "Stability analysis of SDOF real-time hybrid testing systems with explicit integration algorithms and actuator delay". In: *Earthquake Engineering & Structural Dynamics* 37.4 (2008), pp. 597–613. DOI: 10.1002/eqe.775.

[39] Chen, C., Ricles, J. M., Marullo, T. M., and Mercan, O. "Real-time hybrid testing using the unconditionally stable explicit CR integration algorithm". In: *Earthquake Engineering & Structural Dynamics* 38.1 (2009), pp. 23–44. DOI: https://doi.org/10.1002/eqe.838.

[40] Chen, P.-C., Chang, C.-M., Spencer, B., and Tsai, K.-C. "Adaptive model-based tracking control for real-time hybrid simulation". In: *Bulletin of Earthquake Engineering* 13 (2015), pp. 1633–1653. DOI: 10.1007/s10518-014-9681-2.

[41] Chi, F., Wang, J., and Jin, F. "Delay-dependent stability and added damping of SDOF real-time dynamic hybrid testing". In: *Earthquake Engineering and Engineering Vibration* 9.3 (2010), pp. 425–438. DOI: 10.1007/s11803-010-0026-0.

[42] Christenson, R., Lin, Y. Z., Emmons, A., and Bass, B. "Large-Scale Experimental Verification of Semiactive Control through Real-Time Hybrid Simulation". In: *Journal of Structural Engineering* 134.4 (2008), pp. 522–534. DOI: 10.1061/(ASCE)0733-9445(2008)134:4(522).

[43] Christenson, R. E., Dyke, S. J., Zhang, J., Mosqueda, G., Chen, C., Nakata, N., Laplace, P., Song, W., Chae, Y., Marshall, G., Ou, G., Riascos Gonzales, C. A., and Song, C. “Hybrid simulation: a discussion of current assessment measures”. In: *Technical report, George E. Brown, Jr. Network for Earthquake Engineering Simulation (NEES), West Lafayette, IN* (2014).

[44] Covi, P., Abbiati, G., Tondini, N., Bursi, O. S., and Stojadinović, B. “A static solver for hybrid fire simulation based on model reduction and dynamic relaxation”. In: *SiF 2020 - The 11th International Conference on Structures in Fire*. 2020. DOI: https://doi.org/10.14264/2ed186c.

[45] Cryer, B., Nawrocki, P., and Lund, R. “A road simulation system for heavy duty vehicles”. In: *Technical report 760361, Society of Automotive Engineers* (1976).

[46] Darby, A. P., Blakeborough, A., and Williams, M. S. “Real-Time Substructure Tests Using Hydraulic Actuator”. In: *Journal of Engineering Mechanics* 125.10 (1999), pp. 1133–1139. DOI: 10.1061/(ASCE)0733-9399(1999)125:10(1133).

[47] Darby, A. P., Blakeborough, A., and Williams, M. S. “Improved control algorithm for real-time substructure testing”. In: *Earthquake Engineering & Structural Dynamics* 30.3 (2001), pp. 431–448. DOI: https://doi.org/10.1002/eqe.18.

[48] Darby, A. P., Williams, M. S., and Blakeborough, A. “Stability and Delay Compensation for Real-Time Substructure Testing”. In: *Journal of Engineering Mechanics* 128 (2002), pp. 1276–1284.

[49] Davoodi, A., Mohseni, O., Seyfarth, A., and Sharbafi, M. A. “From template to anchors: transfer of virtual pendulum posture control balance template to adaptive neuromuscular gait model increases walking stability”. In: *Royal Society Open Science* 6.3 (2019). DOI: 10.1098/rsos.181911.

[50] de Klerk, D., Rixen, D. J., and Voormeeren, S. N. “General Framework for Dynamic Substructuring: History, Review and Classification of Techniques”. In: *AIAA Journal* 46.5 (2008), pp. 1169–1181. DOI: 10.2514/1.33274.

[51] de Roover, D., Bosgra, O. H., and Steinbuch, M. “Internal-model-based design of repetitive and iterative learning controllers for linear multivariable systems”. In: *International Journal of Control* 73.10 (2000), pp. 914–929.

[52] de Rozario, R., Fleming, A. J., and Oomen, T. “Iterative control for periodic tasks with robustness considerations, applied to a nanopositioning stage”. In: *IFAC-PapersOnLine* 49.21 (2016), pp. 623–628.

[53] De Stefano, M., Balachandran, R., and Secchi, C. “A Passivity-Based Approach for Simulating Satellite Dynamics With Robots: Discrete-Time Integration and Time-Delay Compensation”. In: *IEEE Transactions on Robotics* 36.1 (2020), pp. 189–203.

[54] Delp, S. L., Anderson, F. C., Arnold, A. S., Loan, P., Habib, A., John, C. T., Guendelman, E., and Thelen, D. G. “OpenSim: Open-Source Software to Create and Analyze Dynamic Simulations of Movement”. In: *IEEE Transactions on Biomedical Engineering* 54.11 (2007), pp. 1940–1950. DOI: 10.1371/journal.pcbi.1006223.

[55] Dertimanis, V. K., Mouzakis, H. P., and Psycharis, I. N. “On the acceleration-based adaptive inverse control of shaking tables”. In: *Earthquake Engineering & Structural Dynamics* 44.9 (2015), pp. 1329–1350. DOI: https://doi.org/10.1002/eqe.2518.

[56] Dijkstra, B. G. “Iterative Learning control, with applications to a wafer-stage”. PhD thesis. TU Delft, 2004.

[57] Dijkstra, B. G. and Bosgra, O. H. "Extrapolation of optimal lifted system ILC solution, with application to a waferstage". In: *Proceedings of the 2002 American Control Conference (IEEE Cat. No. CH37301)*. Vol. 4. IEEE. 2002, pp. 2595–2600.

[58] Drazin, P. L. and Govindjee, S. "Hybrid simulation theory for a classical nonlinear dynamical system". In: *Journal of Sound and Vibration* 392 (2017), pp. 240–259. ISSN: 0022-460X. DOI: https://doi.org/10.1016/j.jsv.2016.12.034.

[59] Dyke, S. J., Spencer, B. F., Quast, P., and Sain, M. K. "Role of Control-Structure Interaction in Protective System Design". In: *Journal of Engineering Mechanics* 121.2 (1995), pp. 322–338. DOI: 10.1061/(ASCE)0733-9399(1995)121:2(322).

[60] El Mahmoudi, A., Rixen, D. J., and Meyer, C. H. "Comparison of Different Approaches to Include Connection Elements into Frequency-Based Substructuring". In: *Experimental Techniques* 44 (4 2020), pp. 425–433. DOI: 10.1007/s40799-020-00360-1.

[61] Elci, H., Longman, R. W., Phan, M. Q., Juang, J.-N., and Ugoletti, R. "Simple learning control made practical by zero-phase filtering: Applications to robotics". In: *IEEE Transactions on Circuits and Systems I: Fundamental Theory and Applications* 49.6 (2002), pp. 753–767.

[62] Ersal, T., Gillespie, R. B., Brudnak, M., Stein, J. L., and Fathy, H. K. "Effect of coupling point selection on distortion in Internet-distributed hardware-in-the-loop simulation". In: *Proceedings of the 2011 American Control Conference*. 2011, pp. 3096–3103. DOI: 10.1109/ACC.2011.5990934.

[63] Ersal, T., Brudnak, M., and Stein, J. L. "An Iterative Learning Control Approach to Improving Fidelity in Internet-Distributed Hardware-in-the-Loop Simulation". In: vol. 1. Dynamic Systems and Control Conference. 2012, pp. 373–382. DOI: 10.1115/DSCC 2012-MOVIC2012-8677.

[64] Facchinetti, A. and Bruni, S. "Hardware-in-the-loop hybrid simulation of pantograph–catenary interaction". In: *Journal of Sound and Vibration* 331.12 (2012), pp. 2783–2797. ISSN: 0022-460X. DOI: https://doi.org/10.1016/j.jsv.2012.01.033.

[65] Fallah, M. S., Bhat, R. B., and Xie, W. F. "Optimized Control of Semiactive Suspension Systems Using H-Infinity Robust Control Theory and Current Signal Estimation". In: *IEEE/ASME Transactions on Mechatronics* 17 (2012), pp. 767–778.

[66] Fan, K. "Setting up a Hybrid Substructuring Test for Prosthetic Feet". Master thesis. Technical University of Munich, 2020.

[67] Farhat, C. and Roux, F.-X. "A method of finite element tearing and interconnecting and its parallel solution algorithm". In: *International Journal for Numerical Methods in Engineering* 32.6 (1991), pp. 1205–1227. DOI: https://doi.org/10.1002/nme.162 0320604.

[68] Fermandois G. A. and Spencer, B. F. "Model-based framework for multi-axial real-time hybrid simulation testing". In: *Earthquake Engineering and Engineering Vibration* 16.4 (2017), pp. 671–691. ISSN: 1993-503X. DOI: 10.1007/s11803-017-0407-8.

[69] Föllinger, O. *Regelungstechnik*. 978-3-8007-3231-9. VDE Verlag, 2013.

[70] Franken, M., Stramigioli, S., Misra, S., Secchi, C., and Macchelli, A. "Bilateral Telemanipulation With Time Delays: A Two-Layer Approach Combining Passivity and Transparency". In: *IEEE Transactions on Robotics* 27.4 (2011), pp. 741–756. ISSN: 1552-3098. DOI: 10.1109/TRO.2011.2142430.

[71] Freeman, C. and Tan, Y. "Iterative learning control and repetitive control". In: *International Journal of Control* 84.7 (2011), pp. 1193–1195. DOI: 10.1080/00207179.2 011.596574.

[72] Fuderer, S. "Adaptive Feedforward Filters for Hybrid Substructuring with Contact". Master thesis. Technical University of Munich, 2021.

[73] Full, R. and Koditschek, D. "Templates and anchors: neuromechanical hypotheses of legged locomotion on land". In: *Journal of Experimental Biology* 202.23 (1999), pp. 3325–3332. ISSN: 0022-0949. DOI: 10.1242/jeb.202.23.3325.

[74] Gailey, R., Allen, K., Castles, J., Kucharik, J., and Roeder, M. "Review of secondary physical conditions associated with lower-limb amputation and long-term prosthesis use". In: *Journal of Rehabilitation Research & Development* 45 (1 2008), pp. 15–29. DOI: 10.1682/jrrd.2006.11.0147.

[75] Gálmez, C. and Fermandois, G. "Online Stability Analysis for Real-Time Hybrid Simulation Testing". In: *Frontiers in Built Environment* 6 (2020), p. 134. ISSN: 2297-3362. DOI: 10.3389/fbuil.2020.00134.

[76] Gao, X., Castaneda, N., and Dyke, S. J. "Real time hybrid simulation: from dynamic system, motion control to experimental error". In: *Earthquake Engineering & Structural Dynamics* 42.6 (2013), pp. 815–832. DOI: 10.1002/eqe.2246.

[77] Gawthrop, P., Wallace, M., Neild, S., and Wagg, D. "Robust real-time substructuring techniques for under-damped systems". In: *Structural Control and Health Monitoring* 14.4 (2007), pp. 591–608. DOI: https://doi.org/10.1002/stc.174.

[78] Geier, A., Kluess, D., Grawe, R., Herrmann, S., D'Lima, D., Woernle, C., and Bader, R. "Dynamical analysis of dislocation-associated factors in total hip replacements by hardware-in-the-loop simulation". In: *Journal of Orthopaedic Research* 35.11 (2017), pp. 2557–2566. DOI: https://doi.org/10.1002/jor.23549.

[79] Géradin, M. and Rixen, D. J. "Impulse-based substructuring in a floating frame to simulate high frequency dynamics in flexible multibody dynamics". In: *Multibody System Dynamics* (2017), pp. 1–31. ISSN: 1573-272X. DOI: 10.1007/s11044-017-9597-0.

[80] Geyer, H. and Herr, H. "A Muscle-Reflex Model That Encodes Principles of Legged Mechanics Produces Human Walking Dynamics and Muscle Activities". In: *IEEE Transactions on Neural Systems and Rehabilitation Engineering* 18.3 (2010), pp. 263–273. DOI: 10.1109/TNSRE.2010.2047592.

[81] Geyer, H. and Seyfarth, A. "Neuromuscular Control Models of Human Locomotion". In: *Humanoid Robotics: A Reference*. Ed. by Goswami, A. and Vadakkepat, P. Springer Netherlands, 2016, pp. 1–30. ISBN: 978-94-007-7194-9. DOI: 10.1007/978-94-007-7194-9_45-1.

[82] Geyer, H., Seyfarth, A., and Blickhan, R. "Compliant leg behaviour explains basic dynamics of walking and running". In: *Proceedings. Biological sciences* 273 (1603 2006), pp. 2861–2867. DOI: 10.1098/rspb.2006.3637.

[83] Ghaemmaghami, A. R. and Kwon, O.-S. "Nonlinear modeling of MDOF structures equipped with viscoelastic dampers with strain, temperature and frequency-dependent properties". In: *Engineering Structures* 168 (2018), pp. 903–914. ISSN: 0141-0296. DOI: https://doi.org/10.1016/j.engstruct.2018.04.037.

[84] Gough, V. E. and Whitehall, S. G. "Universal Tyre Testing Machine". In: *Proceedings of the 9th International Technical Congress*. 1962, pp. 117–137.

[85] Gross, R. *Psychology: The Science of Mind and Behaviour*. Taylor & Francis, 2010. ISBN: 978-1-4441-6436-7.

[86] Guo, T., Chen, C., Xu, W., and Sanchez, F. “A frequency response analysis approach for quantitative assessment of actuator tracking for real-time hybrid simulation”. In: *Smart Materials and Structures* 23.4 (2014). DOI: 10.1088/0964-1726/23/4/045042.

[87] Gutekunst + Co.KG. *Datenblatt Druckfeder VD-319*. 08.2018. 2018.

[88] Hakuno, M., Shidawara, M., and Hara, T. “Dynamic Destructive Test of a Cantilever Beam, Controlled by an Analog-Computer”. In: *Proceedings of the Japan Society of Civil Engineers* 1969.171 (1969), pp. 1–9. DOI: 10.2208/jscej1969.1969.171_1.

[89] Hannaford, B. and Ryu, J. “Time-domain passivity control of haptic interfaces”. In: *IEEE Transactions on Robotics and Automation* 18.1 (2002), pp. 1–10. ISSN: 1042-296X. DOI: 10.1109/70.988969.

[90] Hansen, N. “The CMA Evolution Strategy: A Comparing Review”. In: *Towards a New Evolutionary Computation: Advances in the Estimation of Distribution Algorithms*. Ed. by Lozano, J. A., Larrañaga, P., Inza, I., and Bengoetxea, E. Springer Berlin Heidelberg, 2006, pp. 75–102. ISBN: 978-3-540-32494-2. DOI: 10.1007/3-540-32494-1_4.

[91] Harris, M. J. and Christenson, R. E. “Experimental Test of Spacecraft Parachute Deployment Using Real-Time Hybrid Substructuring”. In: *Sensors and Instrumentation, Aircraft/Aerospace and Energy Harvesting, Conference Proceedings of the Society for Experimental Mechanics Series* 8 (2018), pp. 67–70.

[92] Herrmann, S., Woernle, C., Kaehler, M., Rachholz, R., Souffrant, R., Zierath, J., Kluess, D., and Bader, R. “HiL simulation for testing joint stability after total knee arthroplasty”. In: *Multibody System Dynamics* 28.1-2 (2012), pp. 55–67. ISSN: 13845640. DOI: 10.1007/s11044-011-9283-6.

[93] Herrmann, S. W. “Dynamic Testing of Total Hip and Knee Replacements under Physiological Conditions”. PhD thesis. University of Rostock, Sept. 2015.

[94] Hessabi, R. M. and Mercan, O. “A Practical Approach to the Phase and Amplitude Error Estimation for Pseudodynamic (PSD) Testing”. In: *Structures Congress 2013*, pp. 1938–1949. DOI: 10.1061/9780784412848.170.

[95] Hessabi, R. M. and Mercan, O. “Phase and amplitude error indices for error quantification in pseudodynamic testing”. In: *Earthquake Engineering & Structural Dynamics* 41.10 (2012), pp. 1347–1364. DOI: 10.1002/eqe.1186.

[96] Hochrainer, M. J. and Puhwein, A. M. “Investigation of Nonlinear Dynamic Phenomena Applying Real-Time Hybrid Simulation”. In: *Nonlinear Structures and Systems, Volume 1*. Springer International Publishing, 2020, pp. 125–131. ISBN: 978-3-030-12391-8.

[97] Holzberger, F. “Comparison of Human Gait Models to be Used in Foot-Prostheses Testing”. Semester thesis. Technical University of Munich, 2020.

[98] Horiuchi, T., Inoue, M., Konno, T., and Namita, Y. “Real-time hybrid experimental system with actuator delay compensation and its application to a piping system with energy absorber”. In: *Earthquake Engineering and Structural Dynamics* 28.10 (1999), pp. 1121–1141. ISSN: 00988847. DOI: 10.1002/(SICI)1096-9845(199910)28:10<1121::AID-EQE858>3.0.CO;2-O.

[99] Horiuchi, T. and Konno, T. “A new method for compensating actuator delay in real-time hybrid experiments”. In: *Philosophical Transactions of the Royal Society of London. Series A: Mathematical, Physical and Engineering Sciences* 359.1786 (2001). DOI: 10.1098/rsta.2001.0878.

[100] Horiuchi, T., Nakagawa, M., Sugano, M., and Konno, T. “Development of a real-time hybrid experimental system with actuator delay compensation (1st report)”. Japanese. In: *Transactions of the Japan Society of Mechanical Engineers* (1995).

[101] Huang, L., Chen, C., Guo, T., and Gao, X. “Stability Analysis of Real-Time Hybrid Simulation with Time-Varying Delay through a Delay Decomposition Approach”. In: *Journal of Engineering Mechanics* 146.10 (2020). DOI: 10.1061/(ASCE)EM.1943-7889.0001835.

[102] Insam, C., Bartl, A., and Rixen, D. J. “A Step Towards Testing of Foot Prostheses Using Real-Time Substructuring (RTS)”. In: *Special Topics in Structural Dynamics & Experimental Techniques, Volume 5*. Springer International Publishing, 2020, pp. 1–9. ISBN: 978-3-030-12243-0.

[103] Insam, C., Göldeli, M., Klotz, T., and Rixen, D. J. “Comparison of Feedforward Control Schemes for Real-Time Hybrid Substructuring (RTHS)”. In: *Dynamic Substructures, Volume 4*. Springer International Publishing, 2021, pp. 1–14. ISBN: 978-3-030-47630-4.

[104] Insam, C., Peiris, L. D. H., and Rixen, D. J. “Normalized Passivity Control for Hardware-in-the-loop with Contact”. In: *International Journal of Dynamics and Control* 9.4 (2021), pp. 1471–1477. DOI: 10.1007/s40435-021-00790-8.

[105] Insam, C., Ballat, L.-M., Lorenz, F., and Rixen, D. J. “Hardware-in-the-Loop Test of a Prosthetic Foot”. In: *Applied Sciences* 11.20 (2021). DOI: 10.3390/app11209492.

[106] Insam, C., Harris, M. J., Stevens, M. R., and Christenson, R. E. “Real-Time Hybrid Substructuring for Shock Applications Considering Effective Actuator Control”. In: *Proceedings of the 40th IMAC Conference & Exposition on Structural Dynamics*. 2022.

[107] Insam, C., Kist, A., and Rixen, D. J. “High Fidelity Real-Time Hybrid Substructure Testing Using Iterative Learning Control”. In: *ISR - 52nd International Symposium on Robotics*. VDE Verlag Berlin Offenbach, 2020. ISBN: 978-3-8007-5428-1.

[108] Insam, C., Kist, A., Schwalm, H., and Rixen, D. J. “Robust and high fidelity real-time hybrid substructuring”. In: *Mechanical Systems and Signal Processing* 157 (2021). ISSN: 0888-3270. DOI: https://doi.org/10.1016/j.ymssp.2021.107720.

[109] Insam, C. and Rixen, D. J. “Fidelity Assessment of Real-Time Hybrid Substructure Testing: A Review and the Application of Artificial Neural Networks”. In: *Experimental Techniques* (2021). DOI: 10.1007/s40799-021-00466-0.

[110] Insam, C. and Rixen, D. J. “Fidelity Assessment of Real-Time Hybrid Substructuring based on Convergence and Extrapolation”. In: *Mechanical Systems and Signal Processing* 175 (2022). ISSN: 0888-3270. DOI: https://doi.org/10.1016/j.ymssp.2022.109135.

[111] Ioannou, P. A. and Sun, J. *Robust adaptive control*. Upper Saddle River, NJ: PTR Prentice Hall, 1996.

[112] Isermann, R., Schaffnit, J., and Sinsel, S. “Hardware-in-the-loop simulation for the design and testing of engine-control systems”. In: *Control Engineering Practice* 7.5 (1999), pp. 643–653. ISSN: 0967-0661. DOI: https://doi.org/10.1016/S0967-0661(98)00205-6.

[113] International Organization for Standardization. *Prosthetics – Structural testing of lower-limb prostheses – Requirements and test methods*. Standard. ISO/TC 168 Prosthetics and orthotics, 2016.

[114] International Organization for Standardization. *Prosthetics – Quantification of physical parameters of ankle foot devices and foot units*. Standard. ISO/TC 168 Prosthetics and orthotics, 2016.

[115] Johnson, K. L. *Contact Mechanics*. Cambridge University Press, 1985. DOI: 10.1017/CBO9781139171731.

[116] Kahle, J. T., Highsmith, M. J., and Hubbard, S. L. "Comparison of nonmicroprocessor knee mechanism versus C-Leg on Prosthesis Evaluation Questionnaire, stumbles, falls, walking tests, stair descent, and knee preference". In: *Journal of Rehabilitation Research & Development* 45 (1 2008). DOI: 10.1682/jrrd.2007.04.0054.

[117] Kistler Group. *Instruction Manual, Multicomponent Dynamometer Type 9129AA*. 002-442e-03.15. 2015.

[118] Krenn, R., Boge, T., and Zebenay, M. "Passivity Control for Robotic Satellite Docking Simulators". In: *GNC 2014: 9th International ESA Conference on Guidance, Navigation & Control Systems*. 2014.

[119] Krenn, R., Landzettel, K., and Boge, T. "Passivity Control for Hybrid Simulations of Satellite Docking". In: *ICRA11 Space Robotics Workshop*. 2011.

[120] Kuo, S. M. and Morgan, D. R. *Active Noise Control Systems, Algorithms and DSP Implementations*. John Wiley & Sons, Inc., 1996. ISBN: 0-471-13424-4.

[121] Kwon, S. and Park, J. "Kinesiology-Based Robot Foot Design for Human-Like Walking". In: *International Journal of Advanced Robotic Systems* (2012). DOI: 10.5772/54763.

[122] Laghi, M., Ajoudani, A., Catalano, M., and Bicchi, A. "Tele-impedance with force feedback under communication time delay". In: *2017 IEEE/RSJ International Conference on Intelligent Robots and Systems (IROS)*. 2017, pp. 2564–2571. DOI: 10.1109/IROS.2017.8206078.

[123] Leisten, C., Jassmann, U., Balshüsemann, J., and Abel, D. "Model Predictive Speed Control of a Wind Turbine System Test Bench". In: *17th IFAC Workshop on Control Applications of Optimization CAO* 51.32 (2018), pp. 349–354. ISSN: 2405-8963. DOI: https://doi.org/10.1016/j.ifacol.2018.11.408.

[124] Li, X., Ozdagli, A. I., Dyke, S. J., Lu, X., and Christenson, R. E. "Development and Verification of Distributed Real-Time Hybrid Simulation Methods". In: *Journal of Computing in Civil Engineering* 31.4 (2017). DOI: 10.1061/(ASCE)CP.1943-5487.0000654.

[125] Ligeikis, C. and Christenson, R. E. "Identifying Stochastic Frequency Response Functions Using Real-Time Hybrid Substructuring, Principal Component Analysis, and Kriging Metamodeling". In: *Experimental Techniques* 44 (2020), pp. 763–786. DOI: 10.1007/s40799-020-00389-2.

[126] Lin, F., Maghareh, A., Dyke, S. J., and Lu, X. "Experimental implementation of predictive indicators for configuring a real-time hybrid simulation". In: *Engineering Structures* 101 (2015), pp. 427–438. ISSN: 0141-0296. DOI: https://doi.org/10.1016/j.engstruct.2015.07.040.

[127] Lindemann, U., ed. *Handbuch Produktentwicklung*. München: Hanser, 2016. Chap. III - 6. ISBN: 978-3-446-44518-5. DOI: 10.3139/9783446445819.

[128] Lipfert, S. W., Günther, M., Renjewski, D., Grimmer, S., and Seyfarth, A. "A model-experiment comparison of system dynamics for human walking and running". In: *Journal of Theoretical Biology* 292 (2012), pp. 11–17. ISSN: 0022-5193. DOI: https://doi.org/10.1016/j.jtbi.2011.09.021.

[129] Ljung, L. *System Identification: Theory for the User*. Prentice Hall information and system sciences series. Prentice Hall PTR, 1999. ISBN: 978-0-13-656695-3.

[130] Longman, R. W. "Iterative learning control and repetitive control for engineering practice". In: *International Journal of Control* 73.10 (2000), pp. 930–954. DOI: 10.1080/002071700405905.

[131] Lorenz, F. "Umsetzung eines Hardware in the Loop Teststandes für Fußprothesen unter Verwendung des FMCH Modells". Semester thesis. Technical University of Munich, 2021.

[132] Ma, O., Flores-Abad, A., and Boge, T. "Using Industrial Robots for Hardware-in-the-Loop Simulation of Spacecraft Rendezvous and Docking". In: *ASME, International Design Engineering Technical Conferences and Computers and Information in Engineering Conference, 36th Mechanisms and Robotics Conference*. Vol. 4. 2012, pp. 1059–1066. DOI: 10.1115/DETC2012-70917.

[133] Maghareh, A. "Nonlinear Robust Framework for Real-Time Hybrid Simulation of Structural Systems: Design, Implementation, and Validation". PhD thesis. Purdue University, 2017.

[134] Maghareh, A., Dyke, S. J., Prakash, A., and Bunting, G. B. "Establishing a predictive performance indicator for real-time hybrid simulation". In: *Earthquake Engineering & Structural Dynamics* 43.15 (2014), pp. 2299–2318. DOI: 10.1002/eqe.2448.

[135] Maghareh, A., Dyke, S. J., Prakash, A., and Rhoads, J. "Establishing a Stability Switch Criterion for Effective Implementation of Real-time Hybrid Simulation". In: *Smart Structures and Systems* 14 (2014). DOI: 10.12989/sss.2014.14.6.1221.

[136] Maghareh, A., Dyke, S. J., Prakash, A., and Rhoads, J. F. "Establishing Predictive Indicators for Stability and Performance of SDOF Real-time Hybrid Simulations". In: *Report IISL - 004* (2013).

[137] Maghareh, A., Dyke, S. J., Rabieniaharatbar, S., and Prakash, A. "Predictive stability indicator: a novel approach to configuring a real-time hybrid simulation". In: *Earthquake Engineering & Structural Dynamics* 46.1 (2016), pp. 95–116. DOI: 10.1002/eqe.2775.

[138] Maghareh, A., Dyke, S. J., and Silva, C. E. "A Self-tuning Robust Control System for nonlinear real-time hybrid simulation". In: *Earthquake Engineering & Structural Dynamics* 49.7 (2020), pp. 695–715. DOI: 10.1002/eqe.3260.

[139] Marinelli, C. "Design, Development and Engineering of a Bench for Testing Lower Limb Prosthesis, With Focus on High-Technological Solutions". PhD thesis. Politecnico di Milano, 2016.

[140] Maus, H.-M. "Stabilisierung des Oberkörpers beim Rennen und Gehen". Diplomarbeit. Friedrich Schiller University Jena, 2008.

[141] Maus, H.-M., Lipfert, S. W., Rummel, J., and Seyfarth, A. "Upright human gait did not provide a major mechanical challenge for our ancestors". In: *Nature Communications* 1.1 (2010). DOI: 10.1038/ncomms1073.

[142] MECHS (Multi-Hazard Engineering Collaboratory for Hybrid Simulation). "Hybrid Simulation for Multi-hazard Engineering, A Research Agenda". In: Version 1 (2018). Online: accessed 28 May 2019.

[143] Mercan, O. and Ricles, J. M. "Stability and accuracy analysis of outer loop dynamics in real-time pseudodynamic testing of SDOF systems". In: *Earthquake Engineering & Structural Dynamics* 36.11 (2007), pp. 1523–1543. DOI: 10.1002/eqe.701.

[144] Mercan, O. and Ricles, J. M. “Stability analysis for real-time pseudodynamic and hybrid pseudodynamic testing with multiple sources of delay”. In: *Earthquake Engineering & Structural Dynamics* 37.10 (2008), pp. 1269–1293. DOI: 10.1002/eqe.814.

[145] Mercan, O. and Ricles, J. M. “Experimental Studies on Real-Time Testing of Structures with Elastomeric Dampers”. In: *Journal of Structural Engineering* 135.9 (2009), pp. 1124–1133. DOI: 10.1061/(ASCE)0733-9445(2009)135:9(1124).

[146] Millitzer, J., Mayer, D., Henke, C., Jersch, T., Tamm, C., Michael, J., and Ranisch, C. “Recent Developments in Hardware-in-the-Loop Testing”. In: *Model Validation and Uncertainty Quantification, Volume 3*. Ed. by Barthorpe, R. Cham: Springer International Publishing, 2019, pp. 65–73. ISBN: 978-3-319-74793-4.

[147] MOOG. *Benutzerhandbuch für den digitalen Servoregler L180*. Rev. b 05/00. 2000.

[148] MOOG. *Bürstenlose Servomotoren Baureihe G 400*. G400 - D / 03.96. 2000.

[149] Moore, K. L., Chen, Y., and Ahn, H. “Iterative Learning Control: A Tutorial and Big Picture View”. In: *Proceedings of the 45th IEEE Conference on Decision and Control*. 2006, pp. 2352–2357.

[150] Mosqueda, G., Stojadinović, B., and Mahin, S. A. “Real-Time Error Monitoring for Hybrid Simulation. Part I: Methodology and Experimental Verification”. In: *Journal of Structural Engineering* 133.8 (2007), pp. 1100–1108. DOI: 10.1061/(ASCE)0733-9445(2007)133:8(1100).

[151] Mosqueda, G., Stojadinović, B., and Mahin, S. “Implementation and Accuracy of Continuous Hybrid Simulation with Geographically Distributed Substructures”. In: *Earthquake Engineering Research Center, University of California, Berkeley, CA, USA* (2005).

[152] Mosqueda, G., Stojadinović, B., and Mahin, S. A. “Real-Time Error Monitoring for Hybrid Simulation. Part II: Structural Response Modification due to Errors”. In: *Journal of Structural Engineering* 133.8 (2007), pp. 1109–1117. DOI: 10.1061/(ASCE)0733-9445(2007)133:8(1109).

[153] Murphy, D. “19 - Normal Human Gait”. In: *Fundamentals of Amputation Care and Prosthetics*. Demos Medical Publishing, 2013. ISBN: 978-1-936287-70-3.

[154] Murphy, D. “20 - Gait Deviations after Limb Loss”. In: *Fundamentals of Amputation Care and Prosthetics*. Demos Medical Publishing, 2013. ISBN: 978-1-936287-70-3.

[155] Nakashima, M., McCormick, J., and Wang, T. “Hybrid simulation: A historical perspective”. In: *Hybrid Simulation: Theory, Implementation and Applications*. Ed. by Saouma, V. and Sivaselvan, M. V. 1st ed. Taylor & Francis, Inc., 2008. Chap. 1, pp. 3–13.

[156] Nakashima, M., Kato, H., and Takaoka, E. “Development of real-time pseudo dynamic testing”. In: *Earthquake Engineering & Structural Dynamics* 21.1 (1992), pp. 79–92. DOI: 10.1002/eqe.4290210106.

[157] Nakashima, M. and Masaoka, N. “Real-time on-line test for MDOF systems”. In: *Earthquake Engineering and Structural Dynamics* 28.4 (1999), pp. 393–420. ISSN: 00988847. DOI: 10.1002/(SICI)1096-9845(199904)28:4<393::AID-EQE823>3.0.CO;2-C.

[158] Nakata, N., Dyke, S. J., Zhang, J., Mosqueda, G., Shao, X., Mahmoud, H., Head, M. H., Bletzinger, M. E., Marshall, G. A., Ou, G., and Song, C. “Hybrid Simulation Primer and Dictionary”. In: *George E. Brown, Jr. Network for Earthquake Engineering Simulation, Hybrid Simulation Task Force Meeting, U.S. National Science Foundation (NSF) Award Number CMMI-0927178* (2014).

[159] NASA. *STS-131 Shuttle Mission Imagery*. https://spaceflight.nasa.gov/gallery/images/shuttle/sts-131/html/iss023e020915.html. Online: accessed 03 May 2019. 2010.

[160] Niemeyer, G. and Slotine, J.-J. E. "Telemanipulation with Time Delays". In: *The International Journal of Robotics Research* 23.9 (2004), pp. 873–890. DOI: 10.1177/0278364904045563.

[161] Norrlöf, M. "Iterative Learning control: analysis, design, and experiments". PhD thesis. Linköping University, 2000.

[162] Norrlöf, M. and Gunnarsson, S. "Experimental comparison of some classical iterative learning control algorithms". In: *IEEE Transactions on Robotics and Automation* 18.4 (2002), pp. 636–641.

[163] Nykodym, M. *Saab JAS-39 of the Swedish Air Force undergoing inflight refuelling from a TP 84 Hercules*. https://upload.wikimedia.org/wikipedia/commons/c/ce/Saab_JAS-39_of_the_Swedish_Air_Force_undergoing_inflight_refuelling_from_a_TP_84_Hercules_%28cropped%29.jpg. Online: accessed 23 June 2021, CC BY-SA 2.0, 29 February 2012. 2012.

[164] Olma, S., Kohlstedt, A., Traphöner, P., Jäker, K.-P., and Trächtler, A. "Indirect Force Control in Hardware-in-the-Loop Simulations for a Vehicle Axle Test Rig". In: *14th International Conference on Control Automation Robotics & Vision (ICARCV)*. Phuket, Thailand, 2016. DOI: 10.1109/ICARCV.2016.7838676.

[165] Olma, S., Kohlstedt, A., Traphöner, P., Jäker, K.-P., and Trächtler, A. "Observer-based nonlinear control strategies for Hardware-in-the-Loop simulations of multiaxial suspension test rigs". In: *Mechatronics* 50 (2018), pp. 212–224.

[166] Owens, D. and Daley, S. "Iterative Learning Control - Monotonicity and Optimization". In: *Applied Mathematics and Computer Science* 18 (2008), pp. 279–293. DOI: 10.2478/v10006-008-0026-7.

[167] Pandy, M. G. "Simple and complex models for studying muscle function in walking". In: *Philosophical transactions of the Royal Society of London. Series B. Biological sciences* 358 (1437 2003), pp. 1501–1509. DOI: 10.1098/rstb.2003.1338.

[168] Paschedag, J. "Aktive Schwingungsisolation in Kfz-Motoraufhängungen - Systemkonfiguration und Methoden". PhD thesis. Technical University of Munich, 2008.

[169] Peekema, A. T. "Template-Based Control of the Bipedal Robot ATRIAS". Master thesis. Oregon State University, 2015.

[170] Peiris, L. D. H., Bartl, A., du Bois, J., and Plummer, A. "Passivity control with adaptive feed-forward filtering for real-time hybrid tests". In: *IFAC Journal of Systems and Control* 12 (2020). ISSN: 2468-6018. DOI: https://doi.org/10.1016/j.ifacsc.2020.100081.

[171] Peiris, L. D. H., Plummer, A., and du Bois, J. "Normalised Passivity Control for Robust Tuning in Real-time Hybrid Tests". In: *International Journal of Robust and Nonlinear Control* (2020).

[172] Peiris, L. D. H., Plummer, A., and du Bois, J. "Passivity Control in Real-time Hybrid Testing". In: *2018 UKACC 12th International Conference on Control (CONTROL)*. IEEE, 2018, pp. 317–322. DOI: 10.1109/CONTROL.2018.8516814.

[173] Perry, J. and Burnfield, J. M. *Gait analysis: Normal and pathological function*. 2. ed. Thorofare, NJ: Slack, 2010. ISBN: 978-1-55642-766-4.

[174] Peters, J. "Implementation of Compliant Motion Control Schemes on the Stewart Platform". Semester thesis. Technical University of Munich, 2019.

[175] Phillips, B. M. and Spencer, B. F. "Model-Based Multiactuator Control for Real-Time Hybrid Simulation". In: *Journal of Engineering Mechanics* 139.2 (2013), pp. 219–228. DOI: 10.1061/(ASCE)EM.1943-7889.0000493.

[176] Plummer, A. R. "Model-in-the-Loop Testing". In: *Proceedings of the Institution of Mechanical Engineers, Part I: Journal of Systems and Control Engineering* 220.3 (2006), pp. 183–199. DOI: 10.1243/09596518JSCE207.

[177] Popp, A. "Mortar Methods for Computational Contact Mechanics and General Interface Problems". PhD thesis. Technical University of Munich, 2012.

[178] Pratt, J. and Tedrake, R. "Velocity-Based Stability Margins for Fast Bipedal Walking". In: *Fast Motions in Biomechanics and Robotics: Optimization and Feedback Control*. Ed. by Diehl, M. and Mombaur, K. Springer Berlin Heidelberg, 2006, pp. 299–324. ISBN: 978-3-540-36119-0. DOI: 10.1007/978-3-540-36119-0_14.

[179] Predovic, J. *Walking Cycle Man*. https://svg-clipart.com/man/YS0etCS-walking-cycle-man-clipart. Online: accessed 7 May 2021.

[180] Rasmussen, J., Damsgaard, M., Surma, E., Christensen, S. T., de Zee, M., and Vondrak, V. "AnyBody - A Software System for Ergonomic Optimization". In: *World Congress on Structural and Multidisciplinary Optimization* (2003).

[181] Reinhorn, A., Sivaselvan, M., Liang, Z., and Shao, X. "Real-time Dynamic Hybrid Testing of Structural Systems". In: *13th World Conference on Earthquake Engineering, Vancouver, B.C., Canada*. 2004, p. 1644.

[182] Richter, H., Simon, D., Smith, W. A., and Samorezov, S. "Dynamic modeling, parameter estimation and control of a leg prosthesis test robot". In: *Applied Mathematical Modelling* 39.2 (2015), pp. 559–573. ISSN: 0307904X. DOI: 10.1016/j.apm.2014.06.006. URL: http://dx.doi.org/10.1016/j.apm.2014.06.006.

[183] Riebe, S. "Aktive Schwingungsisolierung und Bahnregelung von Hexapodsystemen". PhD thesis. Technical University of Munich, 2005.

[184] Rummel, J., Blum, Y., and Seyfarth, A. "Robust and efficient walking with spring-like legs". In: *Bioinspiration & Biomimetics* 5.4 (2010). DOI: 10.1088/1748-3182/5/4/046004.

[185] Rummel, J. and Seyfarth, A. "Stable Running with Segmented Legs". In: *The International Journal of Robotics Research* 27.8 (2008), pp. 919–934. DOI: 10.1177/0278364908095136.

[186] Rummel, J. and Seyfarth, A. "Passive stabilization of the trunk in walking". In: *Proceedings of SIMPAR 2010 Workshops, International Conference on Simulation, Modeling and Programming for Autonomous Robots* (2010), pp. 127–136.

[187] Rutzmoser, J. "Model Order Reduction for Nonlinear Structural Dynamics". PhD thesis. Technical University of Munich, 2018.

[188] Ryu, J., Kwong, D., and Hannaford, B. "Stable teleoperation with time-domain passivity control". In: *IEEE Transactions on Robotics and Automation* 20.2 (2004), pp. 365–373. ISSN: 1042-296X. DOI: 10.1109/TRA.2004.824689.

[189] Ryu, J. and Preusche, C. "Stable Bilateral Control of Teleoperators Under Time-varying Communication Delay: Time Domain Passivity Approach". In: *Proceedings 2007 IEEE International Conference on Robotics and Automation*. 2007, pp. 3508–3513. DOI: 10.1109/ROBOT.2007.364015.

[190] Saouma, V. and Sivaselvan, M. V., eds. *Hybrid Simulation: Theory, Implementation and Applications*. 1st. Taylor & Francis, Inc., 2008. ISBN: 0415465680. DOI: 10.1201/9781482288612.

[191] Sauder, T. "Fidelity of cyber-physical empirical methods - Application to the active truncation of slender marine structures". PhD thesis. Norwegian University of Science and Technology, 2018. ISBN: 978-82-326-3600-6.

[192] Sauder, T., Marelli, S., and Sørensen, A. "Probabilistic robust design of control systems for high-fidelity cyber–physical testing". In: *Automatica* 101 (2019), pp. 111–119. DOI: 10.1016/j.automatica.2018.11.040.

[193] Schaarschmidt, M., Lipfert, S. W., Meier-Gratz, C., Scholle, H. C., and Seyfarth, A. "Functional gait asymmetry of unilateral transfemoral amputees". In: *Human Movement Science* 31.4 (2012), pp. 907–917. DOI: 10.1016/j.humov.2011.09.004. URL: http://dx.doi.org/10.1016/j.humov.2011.09.004.

[194] Schwalm, H. "Robust Control for Real-Time Hybrid Substructuring Using Iterative Learning Control". Master thesis. Technical University of Munich, 2020.

[195] Scott, S. H. and Winter, D. A. "Biomechanical model of the human foot: Kinematics and kinetics during the stance phase of walking". In: *Journal of Biomechanics* 26.9 (1993), pp. 1091–1104. ISSN: 0021-9290. DOI: https://doi.org/10.1016/S0021-9290(05)80008-9.

[196] Sehnbruch, L. *Eine Mediengeschichte des Bildschirms*. 1st ed. Springer VS, Wiesbaden, 2017. ISBN: 978-3-658-19169-6. DOI: 10.1007/978-3-658-19170-2.

[197] Seipel, J., Kvalheim, M., Revzen, S., Sharbafi, M. A., and Seyfarth, A. "Chapter 3 - Conceptual Models of Legged Locomotion". In: *Bioinspired Legged Locomotion*. Ed. by Sharbafi, M. A. and Seyfarth, A. Butterworth-Heinemann, 2017, pp. 55–131. ISBN: 978-0-12-803766-9. DOI: https://doi.org/10.1016/B978-0-12-803766-9.00004-X.

[198] Seth, A., Hicks, J. L., Uchida, T. K., Habib, A., Dembia, C. L., Dunne, J. J., Ong, C. F., DeMers, M. S., Rajagopal, A., Millard, M., Hamner, S. R., Arnold, E. M., Yong, J. R., Lakshmikanth, S. K., Sherman, M. A., Ku, J. P., and Delp, S. L. "OpenSim: Simulating musculoskeletal dynamics and neuromuscular control to study human and animal movement". In: *PLOS Computational Biology* 14.7 (July 2018), pp. 1–20. DOI: 10.1371/journal.pcbi.1006223.

[199] Seyfarth, A., Geyer, H., Günther, M., and Blickhan, R. "A movement criterion for running". In: *Journal of Biomechanics* 35.5 (2002), pp. 649–655. ISSN: 0021-9290. DOI: https://doi.org/10.1016/S0021-9290(01)00245-7.

[200] Sharbafi, M. A., Maufroy, C., Ahmadabadi, M. N., Yazdanpanah, M. J., and Seyfarth, A. "Robust hopping based on virtual pendulum posture control". In: *IOPScience, Bioinspiration & Biomimetics* 8 (2013). DOI: 10.1088/1748-3182/8/3/036002.

[201] Sharbafi, M. A. and Seyfarth, A. "FMCH: A new model for human-like postural control in walking". In: *2015 IEEE/RSJ International Conference on Intelligent Robots and Systems (IROS)*. 2015, pp. 5742–5747. DOI: 10.1109/IROS.2015.7354192.

[202] Shing, P. B. "Integration schemes for real-time hybrid testing". In: *Hybrid Simulation: Theory, Implementation and Applications*. Ed. by Saouma, V. and Sivaselvan, M. V. 1st ed. Taylor & Francis, Inc., 2008. Chap. 3, pp. 25–34.

[203] Shing, P. and Mahin, S. "Experimental error propagation in pseudodynamic testing". In: *Report No. UCB/EERC-83/12, Earthquake Engineering Research Center, University of California, Berkeley* (1983).

[204] Siciliano, B. and Khatib, O. *Springer handbook of robotics*. Springer, 2016. Chap. 18.

[205] Silva, C. E., Gomez, D., Maghareh, A., Dyke, S. J., and Spencer, B. F. "Benchmark control problem for real-time hybrid simulation". In: *Mechanical Systems and Signal Processing* 135 (2020). ISSN: 0888-3270. DOI: https://doi.org/10.1016/j.ymssp.2019.106381.

[206] Simpson, T., Dertimanis, V. K., and Chatzi, E. N. "Towards Data-Driven Real-Time Hybrid Simulation: Adaptive Modeling of Control Plants". In: *Frontiers in Built Environment* 6 (2020), p. 158. ISSN: 2297-3362. DOI: 10.3389/fbuil.2020.570947.

[207] Song, S., LaMontagna, C., Collins, S. H., and Geyer, H. "The effect of foot compliance encoded in the windlass mechanism on the energetics of human walking". In: *2013 35th Annual International Conference of the IEEE Engineering in Medicine and Biology Society (EMBC)*. 2013, pp. 3179–3182. DOI: 10.1109/EMBC.2013.6610216.

[208] Stahl, K. and Leimbach, K. "Vehicle dynamics simulation by using hardware in the loop techniques". In: *17th International IEEE Conference on Intelligent Transportation Systems (ITSC)*. 2014, pp. 520–524. DOI: 10.1109/ITSC.2014.6957742.

[209] Statistisches Bundesamt. "23141-0101: Operationen und Prozeduren an vollstationären Patienten: Deutschland, Jahre, Operationen und Prozeduren". In: (2019). URL: https://www-genesis.destatis.de/genesis//online?operation=table&code=23141-0101&bypass=true&levelindex=0&levelid=1620194148891#abreadcrumb (visited on 05/05/2021).

[210] Staufenberg, N.-S., Vielemeyer, J., Müller, R., Renjewski, D., and Rixen, D. J. "Virtual Pivot Point Analysis of the Humanoid Robot Lola". In: *Dynamic Walking 2019*. 2019.

[211] Stewart, D. "A Platform with Six Degrees of Freedom". In: *Proceedings of the Institution of Mechanical Engineers* 180.1 (1965), pp. 371–386. DOI: 10.1243/PIME_PROC_1965_180_029_02.

[212] Stoten, D. P. and Hyde, R. A. "Adaptive control of dynamically substructured systems: The single-input single-output case". In: *Proceedings of the Institution of Mechanical Engineers, Part I: Journal of Systems and Control Engineering* 220.2 (2006), pp. 63–79. DOI: 10.1243/09596518JSCE171.

[213] Stoten, D. P., Yamaguchi, T., and Yamashita, Y. "Dynamically Substructured System Testing for Railway Vehicle Pantographs". In: *Journal of Physics: Conference Series* 744 (2016). DOI: 10.1088/1742-6596/744/1/012204.

[214] Sygulla, F. and Rixen, D. "A force-control scheme for biped robots to walk over uneven terrain including partial footholds". In: *International Journal of Advanced Robotic Systems* 17.1 (2020).

[215] Sygulla, F., Wittmann, R., Seiwald, P., Berninger, T., Hildebrandt, A.-C., Wahrmann, D., and Rixen, D. "An EtherCAT-Based Real-Time Control System Architecture for Humanoid Robots". In: 2018, pp. 483–490. DOI: 10.1109/COASE.2018.8560532.

[216] Takanashi, K. and Nakashima, M. "Japanese Activities on On-Line Testing". In: *Journal of Engineering Mechanics* 113.7 (1987), pp. 1014–1032. DOI: 10.1061/(ASCE)0733-9399(1987)113:7(1014).

[217] Tang, Z., Dietz, M., Li, Z., and Taylor, C. "The performance of delay compensation in real-time dynamic substructuring". In: *Journal of Vibration and Control* 24.21 (2018), pp. 5019–5029. DOI: 10.1177/1077546317740488.

[218] Thewalt, C. and Roman, M. "Performance Parameters for Pseudodynamic Tests". In: *Journal of Structural Engineering* 120.9 (1994), pp. 2768–2781. DOI: 10.1061/(ASCE)0733-9445(1994)120:9(2768).

[219] Timmers, N. "Simulating gait with the 3R60 knee prosthesis and a control moment gyroscope". Master thesis. TU Delft, Dec. 2020.

[220] Tryggvason, H., Starker, F., Lecompte, C., and Jónsdóttir, F. "Modeling and simulation in the design process of a prosthetic foot". In: *Proceedings of the 58th SIMS* (2016), pp. 398–404. DOI: 10.3384/ecp17138398.

[221] Tsokanas, N., Wagg, D., and Stojadinović, B. "Robust Model Predictive Control for Dynamics Compensation in Real-Time Hybrid Simulation". In: *Frontiers in Built Environment* 6 (2020). DOI: 10.3389/fbuil.2020.00127.

[222] Uchiyama, M. "Formation of High-Speed Motion Pattern of a Mechanical Arm by Trial". In: *Transactions of the Society of Instrument and Control Engineers* 14.6 (1978), pp. 706–712. DOI: 10.9746/sicetr1965.14.706.

[223] van Zundert, J. and Oomen, T. "Inverting Nonminimum-Phase Systems from the Perspectives of Feedforward and ILC". In: *IFAC-PapersOnLine* 50.1 (2017). 20th IFAC World Congress, pp. 12101–12106. ISSN: 2405-8963. DOI: https://doi.org/10.1016/j.ifacol.2017.08.2135.

[224] Veerasamy, S. and Hubbar, J. "Real-time berthing simulator for space station and space shuttle". In: *SIMULATION* 57.1 (1991), pp. 31–38. DOI: 10.1177/003754979105700108.

[225] Vielemeyer, J., Müller, R., Staufenberg, N.-S., Renjweski, D., and Abel, R. "Ground reaction forces intersect above the center of mass in single support, but not in double support of human walking". In: *Journal of Biomechanics* 120 (2021). ISSN: 0021-9290. DOI: https://doi.org/10.1016/j.jbiomech.2021.110387.

[226] Wallace, M. I., Sieber, J., Neild, S. A., Wagg, D. J., and Krauskopf, B. "Stability analysis of real-time dynamic substructuring using delay differential equation models". In: *Earthquake Engineering & Structural Dynamics* 34.15 (2005), pp. 1817–1832. DOI: 10.1002/eqe.513.

[227] Wallace, M., Wagg, D., and Neild, S. "An adaptive polynomial based forward prediction algorithm for multi-actuator real-time dynamic substructuring". In: *Proceedings of the Royal Society A, Mathematical, Physical and Engineering Sciences* 461 (2005), pp. 3807–3826.

[228] Wang, X., Kim, R. E., Kwon, O.-S. K., Yeo, I.-H., and Ahn, J.-K. "Continuous Real-Time Hybrid Simulation Method for Structures Subject to Fire". In: *Journal of Structural Engineering* 145.12 (2019). DOI: 10.1061/(ASCE)ST.1943-541X.0002436.

[229] Wang, Y., Gao, F., and Doyle, F. "Survey on Iterative Learning Control, Repetitive Control, and Run-to-run Control, Journal of Process Control". In: *Journal of Process Control*. Vol. 19. 2009, pp. 1589–1600.

[230] Wassink, M. B. G., Bosgra, O. H., Rixen, D. J., and Koekebakker, S. H. "Modeling of an inkjet printhead for Iterative Learning Control using bilaterally coupled multiports". In: *Proceedings of the 44th IEEE Conference on Decision and Control*. 2005, pp. 4766–4772. DOI: 10.1109/CDC.2005.1582915.

[231] Whittle, M. W. "2 - Normal Gait". In: *Gait Analysis*. Ed. by Whittle, M. W. Butterworth-Heinemann, 1991, pp. 48–90. ISBN: 978-0-7506-0045-3. DOI: https://doi.org/10.1016/B978-0-7506-0045-3.50007-0.

[232] Whyte, C. A., Mackie, K. R., and Stojadinović, B. "Hybrid Simulation of Thermomechanical Structural Response". In: *Journal of Structural Engineering* 142.2 (2016). DOI: 10.1061/(ASCE)ST.1943-541X.0001346.

[233] Williams, M. S. "Real-time hybrid testing in structural dynamics". In: *5th Australasian Congress on Applied Mechanics, ACAM 2007*. Vol. 1. 2007. ISBN: 0 8582 5862 5.

[234] Windrich, M., Grimmer, M., Christ, O., Rinderknecht, S., and Beckerle, P. "Active lower limb prosthetics: a systematic review of design issues and solutions". In: *BioMedical Engineering OnLine* 15 (3 2016). DOI: 10.1186/s12938-016-0284-9.

[235] Winter, D. A. *The biomechanics and motor control of human gait*. 2nd ed. University of Waterloo Press, 1987. ISBN: 0888980787.

[236] Wittmann, R., Hildebrandt, A. C., Ewald, A., and Buschmann, T. "An estimation model for footstep modifications of biped robots". In: *IEEE International Conference on Intelligent Robots and Systems* (2014), pp. 2572–2578. ISSN: 21530866. DOI: 10.1109/IROS.2014.6942913.

[237] Wojtusch, J. and von Stryk, O. "HuMoD - A Versatile and Open Database for the Investigation, Modeling and Simulation of Human Motion Dynamics on Actuation Level". In: *Proceedings of the IEEE-RAS International Conference on Humanoid Robots*. Seoul: IEEE, 2015, pp. 74–79. DOI: 10.1109/HUMANOIDS.2015.7363534.

[238] Xu, W., Chen, C., Guo, T., and Yang, X. "Reliability Assessment of Real-time Hybrid Simulation Under Worst-Case Scenarios Using Frequency-Domain Evaluation Indices". In: *Experimental Techniques* 41 (2017), pp. 237–249. DOI: 110.1007/s40799-017-0172-7.

[239] Yang, Z. "Development of a Gait Simulator for Testing Lower Limb Prostheses". PhD thesis. University of Bath, July 2020.

[240] Ye, Y., Pan, Y., Gupta, Y., and Ware, J. "A Power-Based Time Domain Passivity Control for Haptic Interfaces". In: *IEEE Transactions on Control Systems Technology* 19.4 (2011), pp. 874–883. ISSN: 1063-6536. DOI: 10.1109/TCST.2010.2062513.

[241] Zebenay, M., Boge, T., Krenn, R., and Choukroun, D. "Analytical and experimental stability investigation of a hardware-in-the-loop satellite docking simulator". In: *Proceedings of the Institution of Mechanical Engineers, Part G: Journal of Aerospace Engineering* 229.4 (2015), pp. 666–681. DOI: 10.1177/0954410014539290.

[242] Zebenay, M., Lampariello, R., Boge, T., and Choukroun, D. "A New Contact Dynamics Model Tool for Hardware-In-The-Loop Docking Simulation". In: *I-SAIRAS - International Symposium on Artificial Intelligence, Robotics and Automation in Space*. 2012.

[243] Zhang, R., Phillips, B. M., Taniguchi, S., Ikenaga, M., and Ikago, K. "Shake table real-time hybrid simulation techniques for the performance evaluation of buildings with inter-story isolation". In: *Structural Control and Health Monitoring* 24.10 (2017). e1971 STC-15-0249.R2. DOI: https://doi.org/10.1002/stc.1971.

[244] Zijlstra, W. "Assessment of spatio-temporal parameters during unconstrained walking". In: *European Journal of Applied Physiology* 92 (1 2004), pp. 39–44. DOI: 10.1007/s00421-004-1041-5.

[245] Zucca, S. and Firrone, C. M. "Nonlinear dynamics of mechanical systems with friction contacts: Coupled static and dynamic Multi-Harmonic Balance Method and multiple solutions". In: *Journal of Sound and Vibration* 333.3 (2014), pp. 916–926. ISSN: 0022-460X. DOI: https://doi.org/10.1016/j.jsv.2013.09.032.